

**Monte Carlo calculation and analysis
of neutron and gamma fields at
spallation neutron sources for
simulating cosmic radiation**

by

Qian Hong

A thesis submitted in partial fulfilment for the requirements for the degree

of

Doctor of Philosophy

at the University of Central Lancashire

September 2015

STUDENT DECLARATION FORM

Concurrent registration for two or more academic awards

Either *I declare that while registered as a candidate for the research degree, I have not been a registered candidate or enrolled student for another award of the University or other academic or professional institution

or ~~*I declare that while registered for the research degree, I was with the University's specific permission, a *registered candidate/*enrolled student for the following award:~~

Material submitted for another award

Either *I declare that no material contained in the thesis has been used in any other submission for an academic award and is solely my own work

or ~~*I declare that the following material contained in the thesis formed part of a submission for the award of~~

(state award and awarding body and list the material below):

** delete as appropriate*

Collaboration

Where a candidate's research programme is part of a collaborative project, the thesis must indicate in addition clearly the candidate's individual contribution and the extent of the collaboration. Please state below:

Signature of Candidate

洪茜 Hong Qian

Type of Award

Doctor of Philosophy

School

School of Engineering

Acknowledgements

I would like to thank my parents for their support and encouragement throughout my study. And I also wish to thank my supervisors, Dr. S. P. Platt and Dr. S. J. Mein who gave me valuable technical support on my study. Especially my Director of Study (DoS), Dr. S. P. Platt who provided many useful scientific guidance for research. Besides my supervisors, I would like to thank Prof. Alexander Prokofiev and his colleagues at The Svedberg Laboratory (TSL) who shared unpublished information about ANITA facility with me, which helped my Monte Carlo modelling. Advice given by Christian Kay has been a great help in familiar with High Performance Computer. I am particularly grateful for the assistance given by Dr X.X. Cai and Dr X.Y. Guan.

Abstract

The research of the neutron induced Single Event Effect (SEE) at aircraft altitudes or at ground level are very important since the neutron radiation is able to cause serious errors or damages on electronic components and system. The Weapons Neutron Research (WNR) facility at Los Alamos Neutron Science Center (LANSCE), and ANITA (Atmospheric-like Neutrons from thick Target) facility at The Svedberg Laboratory (TSL) both provide spallation neutron source for radiation testing of electronic components. A local beam monitoring system was successfully developed by S. Platt and L. Zhang in the University of Central Lancashire for measuring neutron dosimetry during accelerated SEE testing of electronic devices with using silicon photodiode. However, such silicon photodiode is sensitive to gamma-ray as well. For above reasons, characterization of neutron and gamma fields at spallation neutron sources used for accelerated SEE testing has become the purpose of this work.

Monte Carlo calculation of radiation fields at spallation neutron source was used to characterize neutron and gamma energy spectra for accelerated single event effect testing. Geant4 (GEometry ANd Tracking version 4) toolkit, using Monte Carlo method, was used to simulate a preliminary model of spallation neutron source at LANSCE (ICE House, WNR) and TSL (ANITA) for understanding physical mechanisms of neutron and gamma interactions with matter. At first, two preliminary spallation neutron sources on basis of WNR (ICE House) and ANITA facilities were modeled with using two intra-nuclear cascade models (bertini, binary) provided by Geant4 reference physics lists. The result of neutron spectrum with binary INC model agrees well with LANSCE measurement data and independent calculation results in each case. In this computation, gamma dose rates at

WNR and ANITA were calculated, and gamma dose rate from the simulation is consistent with the ANITA measurement results. The results of photon energy spectra with using Geant4 toolkit presents a continuum between 0.1 MeV and 10 MeV, and the annihilation peak at 0.5 MeV. However, calculation results of neutron spectrum at ANITA facility with using binary INC model match ANITA measurements less well in absolute neutron yield above 20 MeV, which is likely due to the missing geometry components in preliminary spallation neutron source simulation.

A more complex model of ANITA facility was constructed with adding bending magnet, shielding components, detector system, and collimator, which makes modelling as realistically as possible. The discrepancy in absolute neutron yield between simulation results and measurements data has improved at Standard User Position (SUP) of ANITA facility, in contrast with the preliminary modelling of ANITA neutron source. At the same time, a new position referred as Close User Position (CUP) was investigated in order to compare with ANITA measurement informed by Monte Carlo N-Particle eXtended (MCNPX) simulation results. The neutron spatial distribution, radius effect for neutrons, neutron beam profiles, and time of flight spectra were calculated at the SUP and CUP positions for different collimator apertures of 3 cm, 10.2 cm, and 30 cm, respectively. A comparison of simulated neutron beam profiles folded with $^{238}\text{U}(n, f)$ cross-section with ANITA measurements at the SUP and CUP-TOF positions was used for validating improved ANITA neutron source modelling. The neutron beam profiles in the horizontal direction were predicted with using Geant4, which filled the gap of geometrical limitation at ANITA facility for accelerated single event effect testing.

It is the first time to predict gamma dose rate at the SUP and CUP positions for 3 cm, 10.2 cm, and 30 cm collimators with using Geant4 modelling of ANITA neutron source. In addition, the gamma dose rate at the SUP position is consistent with ANITA measurement data. Finally, the gamma yield, photon spatial distribution, dose rate against energy are considered for gamma field at the SUP and CUP positions, which have contributed to understand and analyze gamma interactions with matter.

Table of contents

List of figures	ix
List of tables	xiii
List of abbreviations	xv
1 Introduction	1
1.1 Single-event effects	2
1.2 Atmospheric radiation environment	7
1.3 Neutron induced single-event effects testing	10
1.3.1 Real-time testing	11
1.3.2 Accelerated soft error rate testing	12
1.4 Monte Carlo simulation for single event effect studies	18
1.5 Aims and calculations	20
2 Monte Carlo method for neutron spallation source	22
2.1 Nuclear spallation reaction	23
2.2 Neutron interactions with matter	25
2.3 Photons interactions with matter	28
2.4 A brief modelling with using Geant4 toolkit	32
2.4.1 Physics list chosen	39
2.4.2 Summary	42

3	Preliminary simulation of two spallation neutron sources	43
3.1	General description of the LANSCE WNR and TSL ANITA spallation sources and their models	43
3.2	Neutron field calculations	47
3.2.1	Neutron field calculations at LANSCE WNR	48
3.2.2	Neutron field calculations at TSL ANITA	55
3.3	Gamma field calculations	58
3.3.1	Gamma field calculations at LANSCE WNR, ICE House (4FP30L)	60
3.3.2	Gamma field calculations at TSL ANITA	60
3.4	Summary	63
4	Detailed calculation of neutron and gamma fields in the ANITA facility at TSL	66
4.1	Geant4 modelling of the ANITA facility	67
4.2	Neutron fields at the Close User Position and the Standard User Position of the ANITA facility	73
4.2.1	Spatial distribution of neutron field at the CUP and the SUP	73
4.2.2	Calculation of effective radius	78
4.2.3	Spectral neutron fluence at the CUP and the SUP for different collimator size	87
4.2.4	Components distribution to CUP	97
4.2.5	Time of flight spectra of fission events $^{238}\text{U}(n, f)$	100
4.2.6	Neutron beam profiles at the CUP, and SUP	106
4.2.7	Neutron beam spatial profiles folding with $^{238}\text{U}(n, f)$ cross-section at the CUP-TOF, and SUP	112
4.3	Gamma field at the Close User Position and the Standard User Position of the ANITA facility	117
4.3.1	Gamma spatial distribution at the CUP and SUP	117
4.3.2	Calculation of effective radius for γ ray at the CUP and SUP	119

Table of contents	viii
4.3.3 Photon spectra at the CUP and SUP	128
4.4 Summary	135
5 Conclusions	136
5.1 Summary of results	136
5.2 Contributions to knowledge	138
5.3 An evaluation of the limitations of work	139
References	141
Appendix A Los Alamos calculation using MCNP(X) and measurement data	149
Appendix B Uncertainty of counting	158
Appendix C TSL facility	164
Appendix D WNR calculation data with using Geant4	167

List of figures

1.1	Natural radiation events captured by CCD at Jungfraujoch	6
1.2	Events induced by a neutron beamline at ISIS VESUVIO	6
1.3	Atmospheric neutron flux against neutron energy	9
1.4	Altitude against 1 to 10 MeV neutron flux in the atmosphere	9
1.5	Latitude against 1 to 10 MeV neutron flux in the atmosphere	10
1.6	Neutron and Nuclear Science (WNR) Facility Layout	14
1.7	TRIUMF Neutron Facility Layout	16
1.8	ISIS Neutron and Muon Source Layout	16
1.9	Neutron beam spectra from Los Alamos, TRIUMF, and terrestrial	18
2.1	Role of Monte Carlo simulation	23
2.2	The scheme of spallation reaction of high energy proton with heavy nuclei	25
2.3	Neutron interactions with matter: scattering	27
2.4	The mechanism of neutron fission	28
2.5	The mechanism of photoelectric effect	29
2.6	The mechanism of Compton scattering	30
2.7	The mechanism of pair production	32
2.8	Spallation neutron source modelling frame	34
2.9	DetectorConstruction() code for SNS at ANITA facility	34
2.10	Core code of the main() function for preliminary SNS	36
2.11	Preliminary spallation neutron source model at ANITA facility	37

2.12	A comparison of neutron spectra at sea level with Geant4 and MCNPX after air shower	40
2.13	A comparison of neutron spectra at sea level with MCNPX and Measurement	41
3.1	A schematic drawing of the flight paths of Target 2 and Target 4 at the LANSCE neutron sources	44
3.2	Geometry drawing of spallation neutron source	46
3.3	Neutron yield at LANSCE WNR, ICE House	50
3.4	Neutron yield spectrum in the lethargy scale at LANSCE WNR, ICE House	52
3.5	Neutron yield in lethargy scale at LANSCE	53
3.6	Neutron yield spectrum at ANITA facility	56
3.7	Normalised neutron yield in the lethargy scale at TSL ANITA	57
3.8	γ ray flux to dose rate conversion factor	59
3.9	Photon yield spectrum at LANSCE WNR, ICE House	61
3.11	Prediction of dose rate versus energy at the WNR and ANITA facility . .	64
4.1	Real ANITA and QMN facilities overview seen from above	68
4.2	Simulated ANITA facility overview seen from above	68
4.3	Simulated ANITA facility close up view seen of target region from above	69
4.4	Simulated ANITA facility looking downstream from the target area	70
4.5	Simulated ANITA facility overview seen from the side	70
4.6	Simulated ANITA facility looking upstream towards the target area	71
4.7	Geant4 modelling of neutron field at TSL ANITA	72
4.8	Neutron spatial distribution at the CUP with 3 cm collimator	75
4.9	Neutron spatial distribution at the CUP with 10.2 cm collimator	76
4.10	Neutron spatial distribution at the CUP with 30 cm collimator	77
4.11	Neutron spatial distribution at the SUP with 3 cm collimator	79
4.12	Neutron spatial distribution at the SUP with 10.2 cm collimator	80
4.13	Neutron spatial distribution at the SUP with 30 cm collimator	81
4.14	Radius effect of neutrons at the CUP	83

4.15	Radius effects for neutron above 10 MeV at the SUP	84
4.16	Radius effect of neutrons at the SUP	86
4.17	Simulated spectral fluence at the CUP	89
4.18	Simulated spectral fluence at the CUP-TOF position	90
4.19	Comparison of neutron fluence rate at the CUP	91
4.20	Simulated spectral yield at the SUP	92
4.21	Comparison of simulated neutron spectra at the standard ANITA SUP field	94
4.22	Comparison of Geant4 simulated spectral fluence with analytical model at the SUP and the CUP with 10.2 cm collimator	96
4.23	Schematic diagram of neutron direction	98
4.24	Simulated neutron yield with 3 cm collimator at the CUP-TOF position and three components	99
4.25	$^{238}\text{U}(n, f)$ cross-section	101
4.26	Time of flight spectrum at the CUP-TOF position	102
4.27	Time of flight spectrum at the SUP	104
4.28	Comparison of experimental and Geant4 simulated TOF spectra	105
4.29	Neutron beam profile at the CUP with 3 cm collimator	108
4.30	Neutron beam profile at the CUP with 10.2 cm collimator	109
4.31	Neutron beam profile at the CUP with 30 cm collimator	110
4.32	Neutron beam profile at the SUP with 3 cm collimator	111
4.33	Neutron beam profile at the SUP with 10.2 cm collimator	112
4.34	Neutron beam profile at the SUP with 30 cm collimator	113
4.35	Neutron beam profiles folding with $^{238}\text{U}(n, f)$ cross-section at the CUP- TOF position	115
4.36	Comparison of neutron beam vertical profile at the CUP-TOF position . .	116
4.37	Neutron beam profile folding with $^{238}\text{U}(n, f)$ cross-section at the SUP . .	118
4.38	Gamma spatial distribution at the CUP with 3 cm collimator	120
4.39	Gamma spatial distribution at the CUP with 10.2 cm collimator	121
4.40	Gamma spatial distribution at the CUP with 30 cm collimator	122

4.41	Gamma spatial distribution at the SUP with 3 cm collimator	123
4.42	Gamma spatial distribution at the SUP with 10.2 cm collimator	124
4.43	Gamma spatial distribution at the SUP with 30 cm collimator	125
4.44	Radius effect of gamma at the CUP	127
4.45	Radius effect of gamma at the SUP	129
4.46	Comparison of differential photon yield at the CUP and SUP	130
4.47	Comparison of integral photon yield at the CUP and SUP	131
4.48	Dose versus energy at the CUP and SUP	133
4.49	Comparison of gamma dose rate at the SUP and the CUP	134
A.1	Calculated neutron yield spectra at LANSCE WNR Target4	157
C.1	Standard User Position for devices under testing at ANITA facility in TSL	165
C.2	Right above over Close User Position at ANITA facility in TSL	166

List of tables

1.1	Categories of Single Event Effect	3
2.1	Characteristic of neutron sources	24
2.2	Neutron classification	25
2.3	Geant4 version and release date	33
2.4	Geant4 physics list abbreviation	39
3.1	Geant4 modelling parameters	45
3.2	Simulated detector parameters	45
3.3	Integral neutron yield above 10 MeV, below 10 MeV, and for all energies, with respect to off-axis angles	54
3.4	Ratio comparison of projected area of the target to neutron flux at about 1 MeV with respect to the off-axis angles	54
3.5	Ratio of evaporation peak to intra-nuclear cascade peak for binary, Bertini, and TSL analytical model curves	58
4.1	Detection systems	71
4.2	Umbra and penumbra dimensions at the standard user position	73
4.3	Neutron yield under the umbra region at the standard user position	87
4.4	Neutron flux above 10 MeV at the SUP	95
4.5	Ratio of evaporation peak to intranuclear cascade peak in ANITA modelling	95
4.6	Three components percentage over neutron yield below 10 MeV with 3 cm collimator at the CUP-TOF position	99

4.7	γ yield for each collimator in a radius of 5 cm at the CUP	128
4.8	γ yield for each collimator in umbra region at the SUP	128
4.9	γ dose rate for each collimator at the CUP and SUP	132
A.1	Los Alamos measurement of WNR Target-4 neutron flux at ICE House . .	149
A.2	Calculation of WNR Target-4 neutron flux at 15° and 30°	153
A.3	Calculation of WNR Target-4 neutron flux at 60° and 90°	155
A.4	Projected area of the target from the view of the off-axis angle of 90°, 60°, 30°, and 15°	157
B.1	Poisson single sided upper limits	158
B.2	Poisson single sided lower limits	161
D.1	Geant4 calculation of WNR Target4 differential neutron yield at ICE House with binary INC cascade at 15° and 30°	167
D.2	Geant4 calculation of WNR Target4 differential neutron yield at ICE House with binary INC cascade at 60° and 90°	172

List of abbreviations

ANITA	Atomospheric-like Neutron from thIck TArget
AS	Atmospheric Showers
ASTEP	Altitude SEE Test European Platform
CCD	Charge-Coupled Device
CI	Confidence Interval
CMOS	Complementary Metal-Oxide-Semiconductor
DRAM	Dynamic Random Access Memory
DUT	Devices Under Testing
GEANT	GEometry ANd Tracking
JEDEC	Joint Electron Devices Engineering Council
LANL	Los Alamos National Laboratory
LANSCE	Los Alamos Neutron Science Center
MBU	Mutiple Bit Upset
MC	Monte Carlo
MCU	Multiple Cell Upset
MCNP	Monte Carlo N-Particle Transport Code
MCNPX	Monte Carlo N-Particle eXtended
MOSFET	Metal Oxide Semiconductor Field Effect Transistor
PSI	Paul Scherrer Institute
RAL	Rutherford Appleton Laboratory
SEB	Single Event Burnout
SEE	Single Event Effect

SEFI	Single Event Functional Interrupt
SEGR	Single Event Gate Rupture
SEL	Single Event Latchup
SET	Single Event Transient
SEU	Single Event Upset
SER	Soft Error Rate
SHE	Single Event Hard Error
SNS	Spallation Neutron Source
STFC	Science and Technology Facilities Council
TFBC	Thin-Film Breakdown Counter
TRIUMF	Tri-University Meson Facility
TSL	The Svedberg Laboratory
WNR	Weapons Neutron Research

Chapter 1

Introduction

There was a potential problem looming, which has been considered by electronic equipment manufacturers, called soft error. Soft error was noticed in Dynamic Random Access Memory (DRAM) in 1970s, and since then this sort of problem began to get attention. These soft errors are intermittent, random, and non-destructive. They are different from hard errors, which are irreversible and permanent. Charged particles are the major reasons to cause soft errors, and they are likely to interact with memory element, and then generate pairs of electron-hole along the tracks and change the stored bits in memory cell. These charged particles come from either high energy cosmic ray and solar particles or radioactive trace isotopes in packaging materials. These high-energy charged particles may interfere with chips and electronic equipment, especially semiconductor devices. With the development of semiconductor technology, the density of memory chip is higher but the size is smaller for high efficiency. In other words, Soft Error Rate (SER) sensitivity is increased with the development of technology and continuous growth.

This chapter is divided into five sections. Section 1.1 introduces the discovery of Single Event Effect (SEE). Then natural radiation environment induced SEE will be discussed in Section 1.2. Methods for testing soft error rate of electronic devices will be described in Section 1.3. Section 1.4 presents Monte Carlo (MC) simulation used for investigation and calculation of radiation fields. The aim of this work will be introduced in the last Section 1.5.

1.1 Single-event effects

With the development of semiconductor industry, the feature size of a device and power supply voltage are decreasing. It is more likely to cause single event effect in the natural radiation environment, along with critical charge reduction. Single event effect is caused by a single, energetic particle such as heavy ion (alpha particle), proton, and neutron, always influence performance of electronic components, circuits, and systems, and even worse, make electronics failed [Gaillard, 2011; JEDEC, 2006]. Such change or failure can be classified as two categories: soft errors and hard errors. Non-destructive, recoverable errors are soft errors. Non-reversible and permanent destructive errors are called hard errors.

In 1962, failures phenomena (during use and manufacture) were mentioned by Wallmark and Marcus in the paper about reduction in size of non-redundant semiconductor devices and they also predicted that failures might be caused by cosmic rays [Wallmark and Marcus, 1962]. As far back as 1975, Binder reported that interaction of galactic cosmic rays with sensitive transistors induced flip flop circuit that resulting in satellite anomalies [Binder et al., 1975]. In 1978, it has been proved that upsets in DRAMs and Charge-Coupled Device (CCD) due to alpha particle from radioactive decay of uranium or thorium existing in packaging material as impurities by May and Woods [May and Woods, 1978]. In the same year, Pickel and Blandford reported that errors in dynamic MOS semiconductor memory cells were caused by heavy cosmic rays particles ionization [Pickel and Blandford, 1978]. In 1979, Ziegler of IBM analyzed that secondary particles (photons, neutrons, electrons, muons, protons, pions) resulting from interaction of cosmic rays with atmosphere atoms induced soft errors in computer memories at sea level [Ziegler and Lanford, 1979]. Ziegler has pointed out that protons emitting from air shower are the mainly radiation particle to result in SEE at high altitude, neutrons and muons dominate at sea level [Ziegler and Lanford, 1979]. While it was in the same year that Guenzer observed upsets induced by high energy neutrons of 6.5, 9, and 14 MeV and protons of 32 MeV in experiments [Guenzer et al., 1979]. Much later, it was found that rather than

Table 1.1 Categories of Single Event Effect

Abbreviation	Name	Type
SEU	Single Event Upset	Soft
MCU	Multiple Cell Upset	Soft
MBU	Multiple Bit Upset	Soft
SET	Single Event Transient	Soft
SEFI	Single Event Functional Interrupt	Soft
SEL	Single Event Latchup	Hard
SEB	Single Event Burnout	Hard
SEGR	Single Event Gate Rupture	Hard

upsets problems have been discovered in spacecraft. In 1987, it was found that heavy ion could lead to semiconductor burnout [Fischer, 1987]. For a very long being, IBM has been published about upsets in terrestrial electronics due to alpha particle and terrestrial cosmic rays [Ziegler, 1996; Ziegler and Lanford, 1979, 1981]. Until 2003, Dirk and Ziegler indicated terrestrial neutrons were more significant than alpha particle contamination which was able to induce soft errors in electronic components at sea level [Dirk et al., 2003]. Single Event Upset (SEU) could still be regarded as a threat to digital devices even though radiation hardening and error correction could reduce soft error rate somewhat.

In the outer space, SEU in the natural environment is caused by the heavy ion from either solar flares or galactic cosmic rays and the proton from either solar flares or trapped proton in the Van Allen radiation belts [Petersen, 2011]. For ground electronic systems, SEU in the aircraft is caused by neutrons and protons from Atmospheric Showers (AS) (A chain of nuclear reactions as cosmic rays penetrate the atmosphere and react with atoms in the atmosphere) [Petersen, 2011]. Single Event Effect, happened through either direct ionization by a single energetic charged particle (heavy ion, proton) or indirect ionization by secondary particles emitting from neutron-induced nuclear reaction in devices, then generates electron-hole pairs along the tracking path in the sensitive volume which lead to alteration in logical state, or even permanent damage phenomenon. Table 1.1 shows a variety of possible SEEs caused by a single energetic particle.

Single Event Upset, a single energetic particle is incident on sensitive volume which make logical state change to opposite state resulting in memory errors or even worse. For

example, since bit flips were observed on satellites, and then Kolasinski et al. mentioned SEU induced by relativistic heavy ions in the laboratory in 1978. In general, SEU is dependent upon critical charge which is defined as minimum charges collected in sensitive node that is able to cause state change. As charges deposited in sensitive node are greater than critical charge which results in transient signal, it is considered that a single event upset has occurred.

Single Event Transient (SET), the transient pulses induced by within bias condition a single energetic particle collides with sensitive node of circuit. In general, SET occurs in operational amplifier, comparator, digital analog converter, and optoelectronic coupler [Gaillard, 2011].

Single Event Functional Interrupt (SEFI) is caused by a single energetic particle, which results in a temporary non-functionality malfunction of device [Koga et al., 1997]. It will not last very long and not require to restart power.

Multiple bit errors occurred at the same time and lead to the failure of circuit, was named after Multiple Cell Upset (MCU) [JEDEC, 2006]. Multiple Bit Upset (MBU) is a subset of MCU, more than two error bits are existed in the same word [JEDEC, 2006], has been frequently found in Harris HM-6508 Complementary Metal-Oxide-Semiconductor (CMOS) RAMs and 93L422 bipolar RAMs after single bit upset was discovered in satellite [Martin et al., 1987].

Single Event Latchup (SEL), to put it simply, a logical state latchup is caused by an energetic particle induced a bit upset through direct ionizing or nuclear reaction [Adams, 1983]. It cannot be reset except shutting down the power and then turning it back on. More seriously, it will cause irreversible permanent error if the current is higher than device limit [Adams, 1983; Petersen, 2011].

Single Event Gate Rupture (SEGR) and Single Event Burnout (SEB) are belong to hard errors for single event effect. Waskiewicz tested the performance of Metal Oxide Semiconductor Field Effect Transistor (MOSFET)s could be influenced by a single particle with high energy and lead to the complete failure in device [Waskiewicz and Groninger, 1990]. The gate leakage current will rise when the energetic particle strikes into the MOS-

FETs. Titus mentioned SEB induced by heavy ion in bipolar junction power transistors in 1991 [Titus et al., 1991]. When the power device runs in a high voltage, SEB is likely to occur.

Figure 1.1 shows montage events caused by natural cosmic radiation and captured by CCD in Jungfraujoch, in the Swiss Alps [Torok et al., 2007]. It shows neutrons interact with matter in or near sensitive region of CCD, and then emit secondary charged particles which induces ionization. In Figure 1.1, three bright tracking records are observed and they are located at top left, top right, and lower right of the figure. These bright tracking records are named as Blooming Artefacts. The reason why they are so bright is that the deposited charge due to ionization is greater than the pixel charge capacity. For example, the top right blooming artefact is about 80 μm and around 7.6 MeV 0.34 pC is collected in the CCD [Torok et al., 2007].

Figure 1.2 shows that events caused by synthetic neutron beam at VESUVIO¹ at ISIS² by Imaging Single-Event Effects Monitor (ISEEM) [Platt et al., 2008]. The difference between Figure 1.1 and Figure 1.2 is that the former due to neutrons resulting from natural cosmic radiation and the latter due to neutrons resulting from spallation reaction. These strong blooming artefacts show neutron interactions in active region of CCD, and records of charge particle resulting from neutron interactions.

Energetic neutrons that are generated in cascades shower become the major particles which induced terrestrial SEEs. Neutrons can produce secondary particles in electronic components through indirect ionization to cause SEE (secondary ions such as D, T, α , Mg, Al have been created) [Messenger, 1997]. To take semiconductor as an example, those neutrons with sufficient high energy strike on silicon atoms in sensitive region of Integrated Circuit (IC) through strong nuclear interactions, which produce secondary particles such as protons, alpha particles, and heavy recoil nuclei via nuclear reaction or scattering [Gaillard, 2011]. Those secondary products produce sufficient couples of free electron-holes on active microcircuit which will induce a device to change state or performance. Electron-hole pairs

¹Vesuvio is a unique neutron spectrometer used in ISIS.

²ISIS is a world well known facility, which is located at STFC Rutherford Appleton Laboratory, and provides neutron and muon sources.

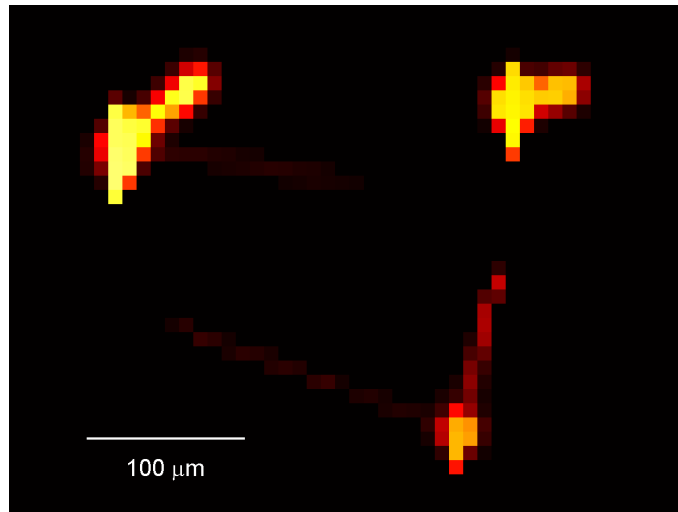


Fig. 1.1 Natural radiation events captured by CCD at Jungfraujoch [Torok et al., 2007]

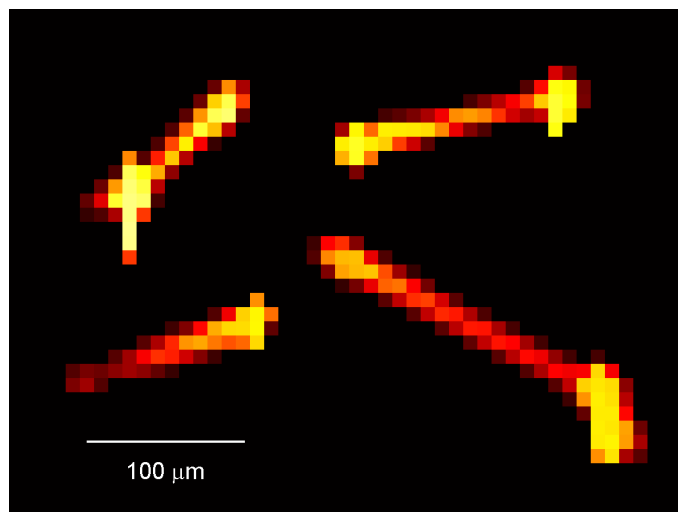


Fig. 1.2 Events induced by a neutron beamline at ISIS VESUVIO [Platt et al., 2008]

will be generated along the path of secondary particles produced by interaction between neutron with the nuclei [Rocheman et al., 2008], on average 3.6 eV of ionising energy in silicon is required to emit one pair of electron-hole (1.6×10^{-19} C) from valence band. The critical charge is about in the order of a tenth of a picocoulombs (0.1 pC) which contains about 6.25×10^5 charge carriers. It assumed that a single energetic particle with 10 MeV could enable to transfer all energies into ionization of semiconducting silicon at 3.6 eV per electron-hole pair [Guenzer et al., 1979]. Therefore, a 10 MeV neutron particle is capable of producing a maximum of 2.8×10^6 electron-hole pairs (0.44 pC of charge carriers). According to this conclusion, 1 MeV of ionising energy can liberate 4.4×10^{-2} pC charges or 2.78×10^5 electron-hole pairs which can result in SEE in semiconductor. The single particle energy having greater than 10 MeV is most likely to induce SEE. The terrestrial electronic devices are little affected by neutrons with energy less than 10 MeV, except for SEE caused by interaction of thermal neutron and ^{10}B .

According to elastic scattering condition, the recoiling Silicon atom could carry away up to 13.3% of kinetic energy of incident neutron. For $^{28}\text{Si}(n, p)^{28}\text{Al}$ reaction, with threshold energy above 13 MeV which measured at IRMM [Plompen et al., 2005]. Neutron energy can be transferred to ionizing energy efficiently. It is the reason that neutrons with energy over 1 MeV region are being studied for SEE field.

1.2 Atmospheric radiation environment

Most of natural radioactive particles in the atmosphere or on the ground are induced by galactic cosmic rays (GCRs), a few by solar cosmic rays (SCRs). Galactic cosmic rays are composed of 98% atomic nuclei and about 2% electrons with energy up to 10×10^{19} MeV [Goldhagen, 2003; Ziegler and Lanford, 1979]. 90% percent of these energetic particles are hydrogen nuclei, 9% are helium nuclei, and the others are nuclei heavier than helium nucleus [Goldhagen, 2003]. The earth magnetic field and atoms in the atmosphere have shielding effect to primary galactic cosmic rays (GCRs) particles. The GCRs and SCR (from the sun, solar-particle events) with a sufficiently high energy are ca-

able of penetrating the earth's atmosphere and colliding with atomic nuclei of atmosphere (nitrogen, oxygen) and generating a cascade of secondary radioactive particles, including hadrons, leptons, photons, which this phenomenon is called Air Shower (AS) [Gaillard, 2011; Goldhagen, 2003; Ziegler and Lanford, 1979].

Neutrons, protons, electrons, gamma rays, muons, pions are mainly radioactive particles to constitute natural radiation environment at aviation altitude, and each type particle flux varies with time, altitude, latitude, and longitude. The particles which are able to reach the ground, neutrons account for 96%, protons account for 3% and pions for 3%, refer to Ziegler's paper published in 1998 [Ziegler, 1998]. However, particle proportion at an altitude of 10 km will be changed to 36% pions and 12% protons [Ziegler, 1998]. The atmospheric neutron flux variation with altitude, latitude, and longitude independently is studied to illustrate the influence of various factors. See Figure 1.3, which presents that two main peaks in atmospheric neutron spectrum, cascade peak at about 100 MeV and evaporation peak at about 1 MeV. Nakamura et al. indicated three peak components on neutron energy spectra in 3 days measurement with using Bonner ball, thermal peak below about 1×10^{-6} MeV, evaporation peak at about 1 MeV, and cascade peak at about 100 MeV. The term cascade came from AS, which illustrated a cascade of secondary particles produced when the energetic particle collides with an atom in the atmosphere. Many of those secondary particles' flight direction is consistent with that of primary particle [Autran and Munteanu, 2015].

In Figure 1.4, it is presented that neutron flux increases with altitude until around 60000 ft, then neutron flux begins to decrease with altitude. However, the major atmospheric radiation source, neutrons, appearing at the altitudes of 30000 ft to 35000 ft are likely to induce SEE [Frost et al., 2009]. The relation between latitude and neutron flux illustrates the main concentration of neutrons are near the poles, see Figure 1.5. It is because the earth geomagnetic field makes flight path of galactic particles bended.

The reason why it happened is that the charged particles such as protons, electrons are likely to stop either by ionization in atmosphere or by nuclear reaction. Neutron has no charge so that ionization has no effect on it. Neutrons have very high penetrating

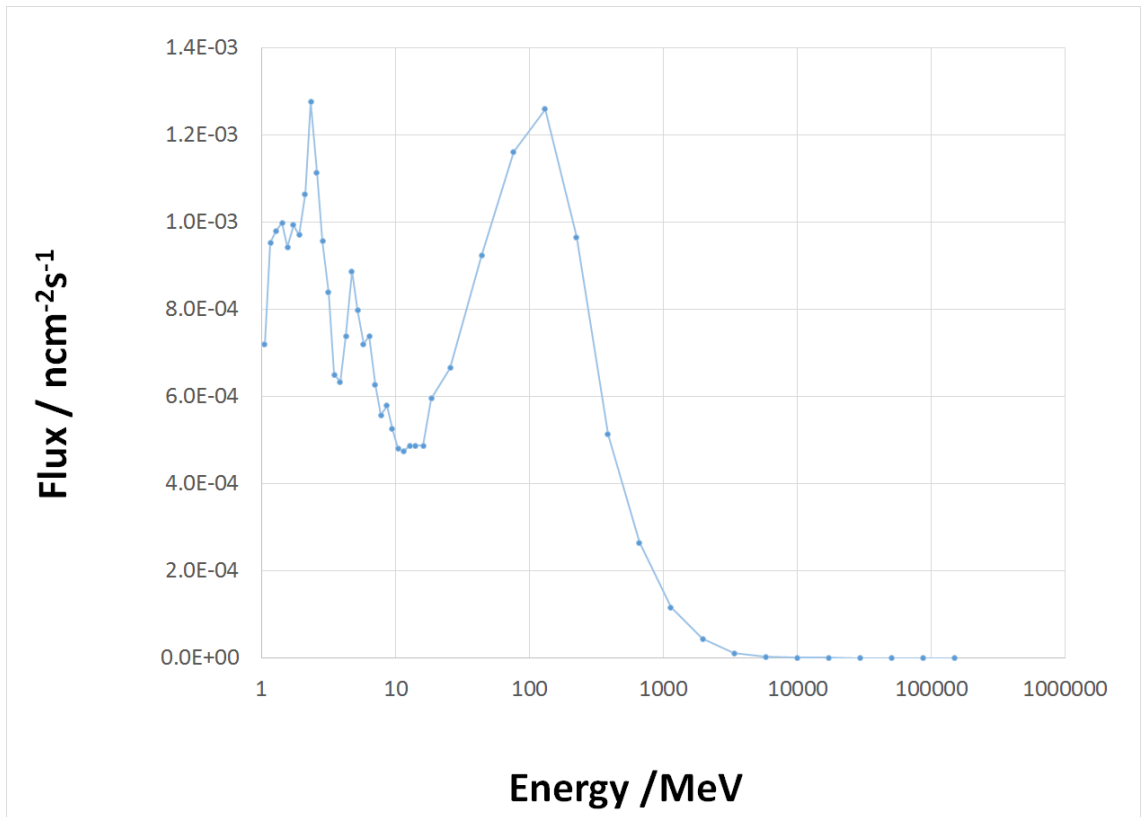


Fig. 1.3 Atmospheric neutron flux against neutron energy [JEDEC, 2006]

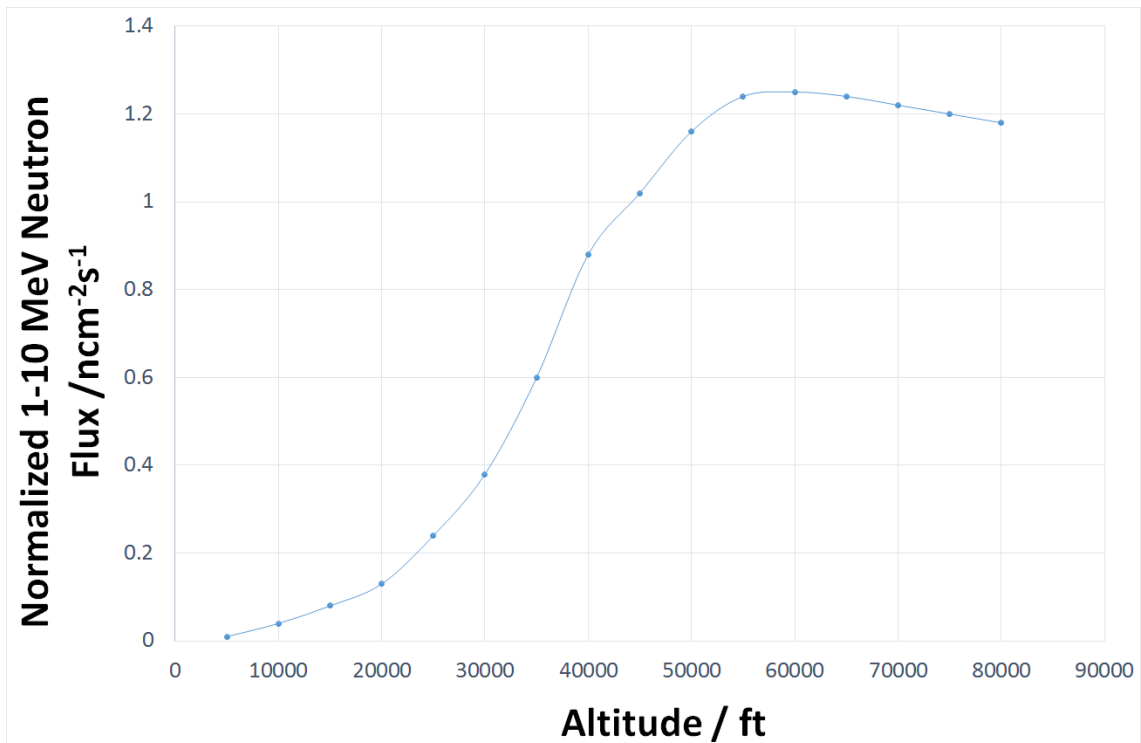


Fig. 1.4 Altitude against 1 to 10 MeV neutron flux in the atmosphere [BSI, 2012]

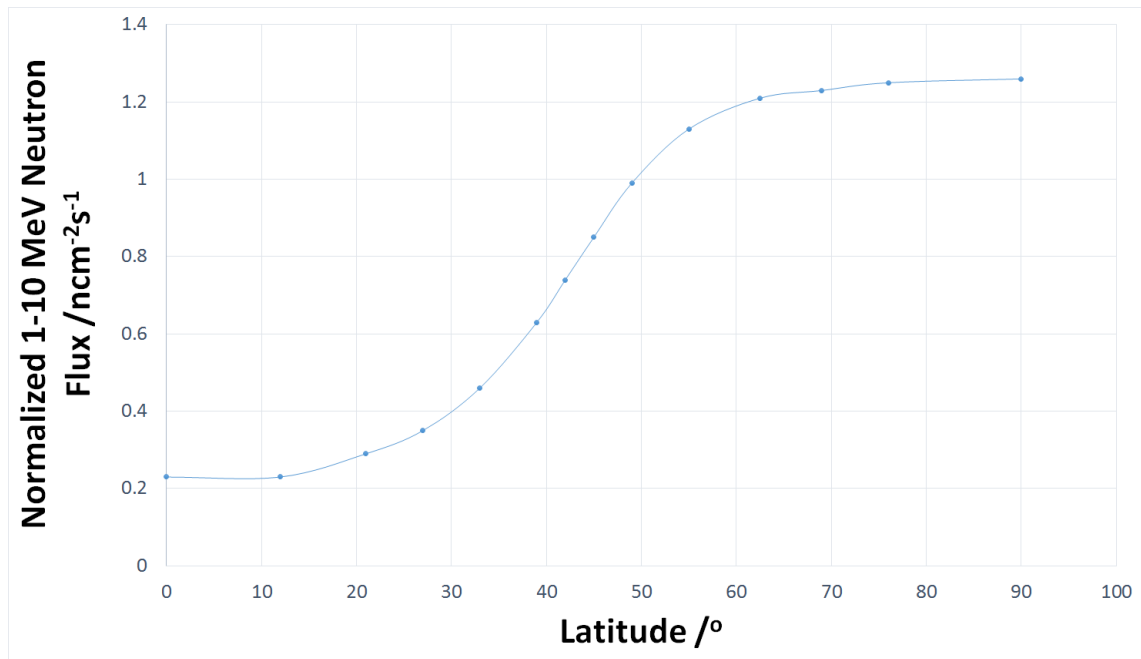


Fig. 1.5 Latitude against 1 to 10 MeV neutron flux in the atmosphere [BSI, 2012]

power so that shielding material cannot stop them to reach sensitive volume of the device. In addition, alpha particle (emitting from radioactive decay of uranium or thorium in packaging material) has a low penetration depth due to the big molecules and it can be stopped by a sheet of paper. Alpha particle induced SEE can be reduced by improving characteristics in packaging material. Atmospheric neutrons are considered the major radioactive particles to cause SEE in the atmosphere and on the ground.

1.3 Neutron induced single-event effects testing

The JEDEC Solid State Technology Association is a standardization organization, which is used to establish criteria and specifications that meet technical and developmental needs of microelectronics industry and guarantee product interoperability [JEDEC, 2006], for example JESD89A. JESD89A standard is published by JEDEC, introduces two fundamental approaches to test soft error sensitivity of a particular product: Real-Time Soft Error Rate (RTSER) testing and Accelerated Soft Error Rate (ASER) testing [JEDEC, 2006].

At Earth's surface and aircraft altitude, the major radiation sources that caused soft errors in electronic components are either from energetic neutron and low energy neutron

created by atmospheric showers or from alpha particle radiated from radioactive element in the package and chip materials. Compare to package contaminants, cosmic ray radiation is harder to control for electronic industry. According to JESD89A standard, it is specified two approaches to test and gain soft error rate of the electronic devices or components, one is unaccelerated SER testing and the other is accelerated SER testing. Unaccelerated SER testing always takes a long period time and large amount of money to measure soft error rate in device. Accelerated SER testing can make use of nuclear reaction to imitate the source of unaccelerated SER testing to achieve the same purpose and shorten the time. The merit of RTSER testing is that the device is being tested and exposed to in the actual radiation environment. By comparison, ASER testing is a time-saved testing and already known radiation source. However, the intensity of radiation source used in ASER testing is greater than that in RTSER testing. ASER testing does require extrapolations to use conditions for the actual field product soft error rate so that two radiation sources (alpha-induced and neutron-induced) caused errors have to be tested individually.

1.3.1 Real-time testing

The RTSER testing is applied to estimate SER of the electronic device in a natural radiation environment. This testing is involved in amount of devices and very long time to complete SER measurement [JEDEC, 2006]. It is difficult to distinguish radiation source induced failures during RTSER testing with using same devices in actual world. In addition, RTSER testing costs a great deal of money and devotes time to measure SER of device but with really low SER rate. For example, Autran et al. reported that only 38 SEU and 3 MBU errors have been detected at the French Alps 2552 m in half year with using 3.6Gbit of SRAMs manufactured in 1.3×10^{-7} m feature size [Autran et al., 2007]. The ASTEP, a mountain laboratory, which is set up in the French alps on the Plateau de Bure at 2552 m and start running since 2006 [Autran et al., 2007]. This laboratory is support for academic research, and has a neutron monitor and a muon monitor [Autran et al., 2008]. RTSER testing of various size CMOS SRAMs such as 130 nm, 65 nm, and 40 nm were measured in

ASTEP [Autran et al., 2007, 2008, 2012]. The radiation sources at the ground are neutrons and alpha particle. For the RTSER testing, the position of devices should be considered such as latitude, longitude, and altitude. In addition, experimental environment factors such as weather condition, and building construction [JEDEC, 2006].

1.3.2 Accelerated soft error rate testing

The radiation source induced SEU on the ground is either alpha particle from uranium and thorium impurities existing in packaging material or neutron created by atmospheric shower. The radiation source of ASER testing can be classified into alpha and neutron. The device is irradiated in an accelerated environment with high intensity radiation source. The device's SER in the actual field can be measured by using extrapolating results from accelerated testing [JEDEC, 2006].

The neutron radiation source induced SEU on terrestrial electronic devices has high energy. In the ASER testing, neutron facilities of SEE testing can be categorized into three according to radiation source: quasi-monoenergetic neutron source, spallation neutron source, and monoenergetic proton source [JEDEC, 2006]. The spallation neutron source is capable of providing a broad range of neutron energies above 1 eV [Autran and Munteanu, 2015; Rinard, 1991]. The spectrum from spallation neutron source facility is similar to that of actual atmospheric neutron spectrum produced by interaction of primary cosmic ray with molecules in the air [Autran and Munteanu, 2015; JEDEC, 2006]. The quasi-monoenergetic neutron source and monoenergetic proton facilities are capable of providing several nominal energies such as 14, 50, 100 and 200 MeV with a wide range tail of lower energies [JEDEC, 2006].

The radiation effect on electronic components resulting from protons (50 MeV) is similar to that induced by neutrons (50 MeV) [JEDEC, 2006; Normand and Dominik, 2010]. If neutron energy and proton energy both are greater than 50 MeV, either of two will be likely to interact with semiconductor material elements such as silicon, oxygen and then produce similar secondary particles like alpha particle or charged particle with

energies over 5 MeV. In other words, SEU cross-section caused by neutron is close to that caused by proton when incoming particle's energy over 50 MeV. While those secondaries are able to induce SEU and in consequence proton would be considered as a radiation source being used in accelerated SEE testing.

The typical spallation neutron source facilities, e.g., the ICE House at Los Alamos Neutron Science Center (LANSCE) in United States, TRIUMF at the University of British Columbia in Vancouver, Canada [Blackmore et al., 2003], Spallations-Neutronenquelle (SINQ) at Paul Scherrer Institute (PSI) in Switzerland [PSI, nd], and ISIS facility at the Rutherford Appleton Laboratory (RAL) in United Kingdom [Frost et al., 2009], are producing "white" neutron spectrum by bombarding a heavy atom material such as tungsten, lead with protons in the energy range from several hundred MeV to several GeV [Prokofiev et al., 2005]. The representative quasi-monoenergetic neutron source facilities, e.g., The Svedberg Laboratory (TSL) in Uppsala, Sweden [Prokofiev et al., 2009, 2005], and the Japan Atomic Energy Research Institute (JAERI) [JAEA, nd]. For TSL facility, it has a broadband source (with energies up to 200 MeV) likewise, which similar to the natural atmospheric spectrum [Prokofiev et al., 2005].

Neutron and Nuclear Science (WNR) Facility at LANSCE provides a broadband neutron spectrum (less than 800 MeV) by firing 800 MeV pulsed proton beam on tungsten [LANSCE, nd]. Time-of-Flight (TOF) technique is used to calculate neutron energy and the shape of the spectrum is close to that of terrestrial neutron spectrum [Frost et al., 2009; JEDEC, 2006; Prokofiev et al., 2005]. Six flight path directions are produced in WNR (Target 4) facility, which are 60° right, 30° right, 15° right, 15° left, 30° left, and 90° left, with respect to incident direction of proton beam. ICE House (T4FP30L¹) and ICE House II (T4FP30R) are two experimental stations about 20 m away from the production target, are used for measurement of neutron induced soft errors or hard errors. Figure 1.6 shows several targets' positions and flight paths from each target [LANSCE, nd]. The integrated neutron flux above 10 MeV is about $4.6 \times 10^5 \text{ cm}^{-2} \text{ s}^{-1}$.

¹T4FP30L: a Flight Path origins from Target 4 and is 30° to the Left with respect to the incoming proton beam.

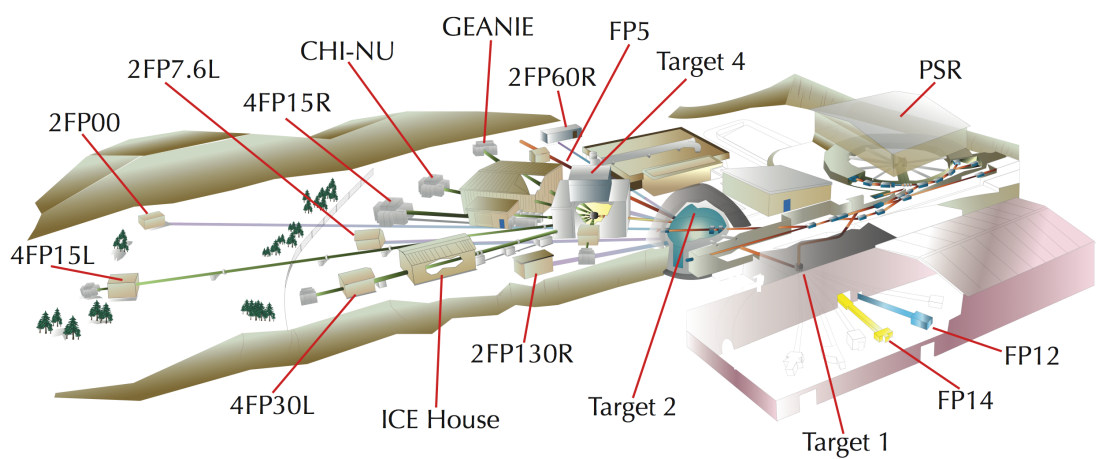


Fig. 1.6 Physical layout of WNR at Los Alamos Neutron Science Center [LANSCE, nd]

The TRIUMF has been used for production of proton beams (65-500 MeV) and neutron beam (0.025 eV-above 20 MeV) after it has been improved. The TRIUMF Proton Irradiation Facility (PIF) has been used for production of monoenergetic proton beams. The TRIUMF Neutron Facility (TNF) is based on neutron production in a lead or steel absorber irradiated by the incoming proton beams from 450 MeV to 500 MeV [Blackmore et al., 2003]. The incoming protons will be fully stopped in the meson production target and four neutron beam flight paths are produced [Blackmore et al., 2003]. The neutron spectrum from TRIUMF facility is close to that available at WNR facility at LANSCE. The TRIUMF neutron beam is intended to characterize SER of integrated circuit that induced by terrestrial cosmic ray [Blackmore et al., 2003]. With comparison of TNF neutron beam and WNR neutron beam, it shows that the access of thermal neutron can be controlled in TNF neutron beam but WNR does not [Blackmore et al., 2003]. Figure 1.7 shows neutron beam flight path from the target [Blackmore et al., 2003]. The TRIUMF can provide neutron flux of $2.6 \times 10^5 \text{ cm}^{-2} \text{ s}^{-1}$ with energies above 10 MeV, which is lower than ICE House does.

ISIS facility, a pulsed spallation neutron source facility located at the RAL in the UK, used for investigation of the internal microscopic structure of the matter and material study [STFC, nd]. All instruments in the ISIS can be classified as three categories according to target: "Muons", "Target Station 1" and "Target Station 2". ChipIR, a new SEE facility is designed for accelerated SER testing of electronic devices [Frost et al., 2009]. Figure 1.8 shows ChipIR is sited on the Second Target Station [STFC, nd]. It is able to provide atmospheric neutron spectrum with energy from 0.1 MeV to 800 MeV by using 800 MeV proton beam bombard on tungsten target [Frost et al., 2009]. The production of neutron flux in ISIS is more than $1.0 \times 10^6 \text{ cm}^{-2} \text{ s}^{-1}$ with energies above 10 MeV.

Monoenergetic neutron and proton sources facilities have also been used for accelerated SER testing on electronic devices at particular energies. To some extent, this is due to limited access of these spallation neutron source facilities [JEDEC, 2006]. To research neutron induced SEEs, two neutron beam sources at TSL are introduced, one is ANITA, the other is Quasi-monoenergetic neutrons (QMN). ANITA, a method to generate spallation neutron

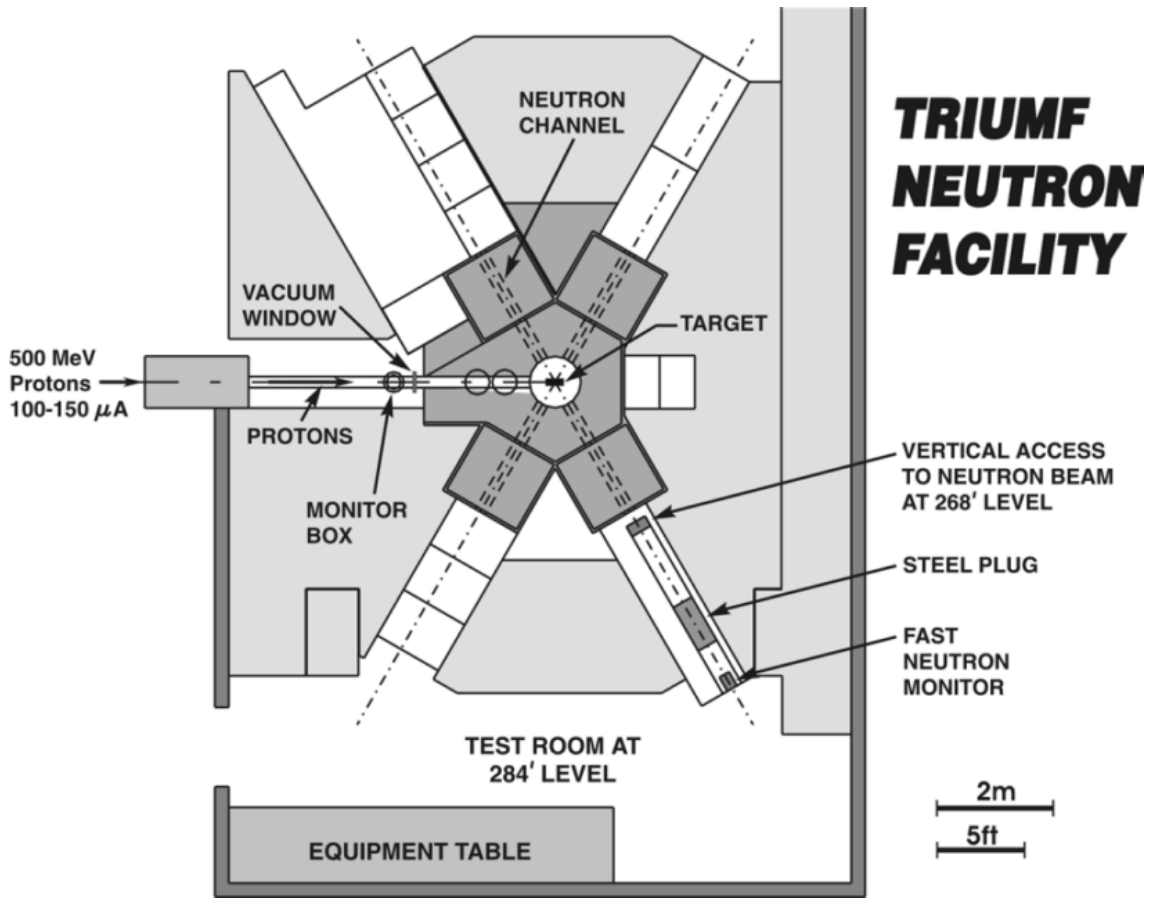


Fig. 1.7 Physical layout of TRIUMF Neutron Facility [Blackmore et al., 2003]

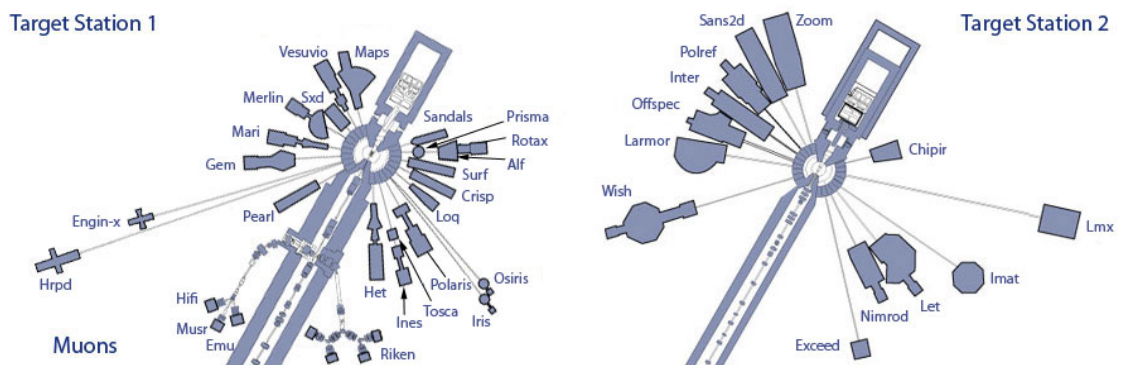


Fig. 1.8 ISIS Neutron and Muon Source Layout [STFC, nd]

source by bombarding the tungsten target with a beam of 180 MeV proton [Prokofiev et al., 2009, 2014]. Protons will be fully stopped in the target and neutrons will be diverged, scattered into user area. The neutron flux above 10 MeV is about $1.0 \times 10^6 \text{ cm}^{-2} \text{ s}^{-1}$ at the ANITA Standard User Position (SUP) (where devices under testing is about 2.5 m from the target) with using 215 nA current [Prokofiev et al., 2014]. The flux (10 MeV) at the Close User Position (CUP) is about 11 times higher than that at the SUP [Prokofiev et al., 2014]. QMN, a method to produce quasi-monoenergetic neutron source with energies from about 20 to around 175 MeV according to nuclear reaction ${}^7\text{Li}(p,n){}^7\text{Be}$ [Frost et al., 2009; Prokofiev et al., 2009]. For such quasi-monoenergetic neutron source, the devices should be at least tested with four beam energies used for SEU rate measurement shown in JEDEC Standard JESD89A [JEDEC, 2006]. QMN beam facility provides some selectable energies, for example, 22, 47, 59, 65, 75, 88, 95, 110, 143, 160, and 175 MeV [TSL, nd].

There is a proton facility with different energies of incident beam, for instance, Paul Scherrer Institut (PSI) Proton Irradiation Facility (PIF) provides monoenergetic proton source with several energies, 74 MeV, 100 MeV, 150 MeV, 200 MeV, and 230 MeV [PSI, nd]. The maximum initial proton beam energy is 230 MeV at current of 2 nA [PSI, nd]. The maximum irradiation region is a circle of radius 4.5 cm and the DUT are positioned on a square holder of $25 \times 25 \text{ cm}^2$ [PSI, nd].

In the real life, spallation neutron sources were applied in ASER testing to generate a similar atmospheric neutron spectrum covering wide energy range. Figure 1.9 [JEDEC, 2006] shows comparisons of neutron energy spectra from spallation neutron beams and terrestrial neutron energy spectrum: the blue diamond from Los Alamos measurement based on spallation neutron source, the pink solid line from terrestrial natural environment providing by JESD89A, and the red triangle from TRIUMF Neutron Facility. Spallation neutron source is produced by spallation reaction. Spallation reaction is a process in which an energetic light particle (e.g. proton, neutron) bombards on heavy atomic nuclei and results in large increasing of neutron yield and small number of protons. The SER of electronic device can be calculated by two parameters: the SEU cross section and the particle energy spectrum at a given location [JEDEC, 2006]. In addition, the device's SER

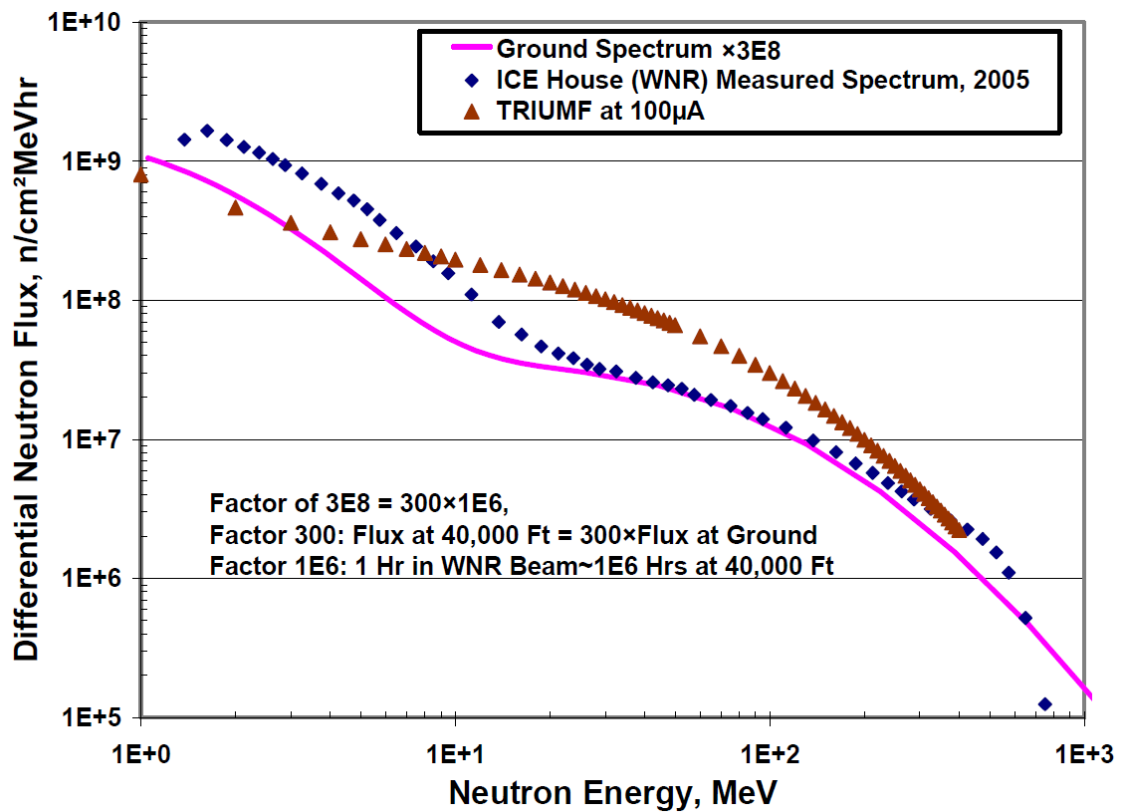


Fig. 1.9 Neutron beam spectra from Los Alamos, TRIUMF, and terrestrial [JEDEC, 2006]

varies with the location. The particle type and particle energy are significant for the value of SEU cross section. In ASER testing, the SEU cross section can be measured except for particle fluence. The particle fluence can be calculated with Monte Carlo simulation.

1.4 Monte Carlo simulation for single event effect studies

A Monte Carlo method is used for characterizing SEE by some given physics models of particle interactions with the matter. MC method is an amount of random or pseudo random values to do calculation many times, then obtain the probability of event occurrence.

Some popular codes or toolkits such as MCNP, GEANT4, FLUKA, and Tripoli, are used for simulating nuclear reactors including neutron transport, and neutron interactions with matter.

Los Alamos National Laboratory (LANL) developed Monte Carlo N-Particle (MCNP) code which is used to simulate neutron, photon, electron, or coupled neutron/photon/electron

transportation and generation [LANSCE, nd]. MCNPX (MCPX eXtended), Monte Carlo radiation transport code which is used to simulation almost all types of particles and energies on the basis of Fortran90 [LANSCE, nd; Prokofiev et al., 2014]. It breaks through the limitations of MCNP which can only simulate a few particles such as neutron, photon, and electron.

And GEANT GEometry ANd Tracking (Geant4), is another software package for simulating passage of particles through matter, which is designed by CERN ¹. Geant4 toolkit is also based on Monte Carlo method, and implemented in C++ programming language with using object oriented technology. Geant4 project started in 1994, completed preliminary research in 1998 and formally established in 1999. Now it becomes one of toolkits for simulating matters of modern particle and nuclear physics experiments. Geant4 is the first successful software package which uses object-oriented technology to design and develop modern particle and nuclear physics experiment. Enormous experiment simulations are based on Geant4. The application of Geant4 is not only distributed in the particle and nuclear physics but also considering the various aspects of requirements including space science, medical physics, cosmic ray physics, and radiation physics. Geant4 toolkit can be used to predict frequency or probability of single event upsets occurred on electronic devices. In addition, Geant4 based simulation could quantify the interaction effects in high energy physical processes, such as particle energy, flux, and energy deposition, through particle radiant energy. Geant4 is an open source in contrast with MCNPX code.

Truscott et al. used Classical Cascade and Binary Cascade models of Geant4 and MULASSIS² to predict neutron deposition spectra with using Ortec detector under simulated irradiation environment on the basis of TRIUMF NIF facility and TSL facility [Truscott et al., 2006, 2003; Weller et al., 2010]. The electron energy deposition in different materials are simulated with Geant4 toolkit [Batic et al., 2013]. Geant4 can be also used for investigating characterizations of heavy ion induced SEB or SEGR in power

¹CERN : The European Organization for Nuclear Research

²MULASSIS: A software uses Geant4 toolkit to simplify input parameters with one-dimensional shield and incident particle for modeling geometry, and particle interaction with matter.

MOSFETs [Ferlet-Cavrois et al., 2012]. Cai and Platt have shown how to use Geant4 version 4.9.3 to simulate neutron interaction and charge collection by using charged couple device [Cai and Platt, 2011]. Cai as a member of research group of University of Central Lancashire (UCLan) who used Geant4 toolkit to simulate a similar neutron response to real natural memory device [Cai, 2010]. Monte Carlo Simulation of SEE has been researched by Vanderbilt University in USA, QinetiQ in UK, the Aix-Marseille Université [Lei et al., 2005; Turowski et al., 2008; Weller et al., 2010], as well as UCLan [Weller et al., 2010].

The simulations of spallation neutron source will be modeled according to WNR at LANSCE and ANITA facility at TSL. The reference physics models for high energy proton interaction with the matter are string model [Geant4 Collaboration, ndb]. The available physics models such as *QGSP_BERT_HP*¹, *QGSP_BIC_HP*² are applied to spallation reaction. Version 9.6, 10.0 were released on official website on [Geant4 Collaboration, nda], which has been used in this research.

1.5 Aims and calculations

This project is to extend work of Platt and Zhang. A local beam monitoring system was successfully developed for measuring neutron dosimetry during SEE accelerated testing of electronic device with using Silicon photodiode [Zhang, 2013; Zhang et al., 2009]. However such silicon photodiode is sensitive to gamma-ray, as well as neutrons.

This work is aimed to characterize neutron and gamma fields at LANSCE WNR and TSL ANITA neutron sources with using Monte Carlo method. Geant4 version 4.9.6 is used to simulate preliminary WNR and ANITA naked neutron source and calculate neutron and gamma fields in Chapter 3, for instance, neutron yield, energy spectra, neutron spatial distribution, gamma yield, and gamma dose rate with binary intra-nuclear cascade and bertini intra-nuclear cascade models. The result with binary intra-nuclear cascade model gives a good agreement of neutron spectra obtained from measurement data between 0.1 MeV and 20 MeV.

¹QGSP: quark-gluon string model, BERT: bertini, HP: high precision neutron package

²BIC: binary

In Chapter 4, Geant4 version 10.0 is used to simulate ANITA neutron facility with more details for obtaining a closer quantitative agreement with measurement. The details of ANITA spallation neutron source with attaching shielding component, bending magnet, collimator, and detector systems will be considered. In addition to understanding spallation reaction, interactions of neutrons with matter and photons with matter, validating of Geant4 simulation models of ANITA neutron source. Analysis of neutron and gamma fields at the Close User Position (CUP) and Standard User Position (SUP) of ANITA facility with 3 cm, 10.2 cm, and 30 cm collimators will be the primary focus. The simulation results of direction components of neutrons at the CUP position will be used to compare with TSL analytical data, time of flight spectra and neutron beam profile will be compared with measurement data from the paper [Prokofiev et al., 2014] for validating ANITA modelling. Results of neutron spectra above 10 MeV with binary INC cascade model at this time is about 30% less than measurement data at the SUP, and around 33% less at the CUP. Furthermore, the gamma flux and gamma dose rate at the CUP and SUP will be calculated for investigate radiation field of ANITA facility. For example, the predicted gamma dose rates of 3 cm collimator with binary INC model are approximately $17.32mSvh^{-1}$ at the SUP and $378.0mSvh^{-1}$ at the CUP, respectively.

Chapter 2

Monte Carlo method for neutron spallation source

In order to understand how single event effects induced by neutrons at the sea level, Monte Carlo method to characterize neutron and gamma field at simulated Accelerating Soft Error Rate (ASER) testing was used for this work. Monte Carlo (MC) method becomes one of modern solutions to study neutron transport. Monte Carlo method is based on an amount of statistical tests, which has been used in some nature random processes, for example particle decay, particle transport process. In accordance with the rule of probability and statistics from practical problems, we can do random sampling test and calculate statistics with using computer. Figure 2.1 shows that Geant4 Monte Carlo simulation toolkit is a means of calculating neutron fluence rate and gamma dose at accelerated SER testing. In neutron beam monitoring SEE testing, Zhang pointed out the semiconductor detector is sensitive to gamma ray when it is applied to measure local neutron fluence [Zhang, 2013]. It is possible by a large number of numerical simulation experiments to verify radiation sources responding to the detector in neutron beam monitoring experiment [Zhang, 2013] and understand physical mechanism of the interaction between neutron and matter.

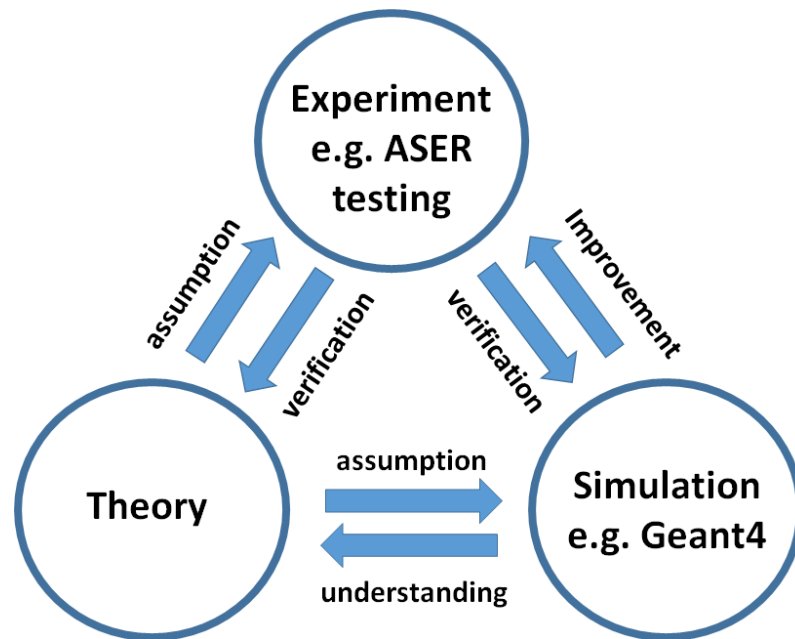


Fig. 2.1 Role of Monte Carlo simulation

2.1 Nuclear spallation reaction

In natural environment, it is likely to occur spallation reaction in atmosphere caused by high energy cosmic rays. The “nuclear spallation” word was created by Glenn T. Seaborg, who gave the description of nuclear spallation phenomenon [Serber, 1947]. Nuclear spallation reaction is a nuclear reaction in which an energetic light projectile (e.g. proton, neutron) impinges on a heavy target nucleus (e.g. tungsten, uranium), and results in the emission of an amount of hadrons or fragments [Russell, 1990]. In addition, secondary particles (for example, neutrons, protons) are able to interact with the target nucleus and produce more neutrons, known as intranuclear cascade. Each proton is capable of producing 25-30 neutrons by using uranium target [Schopper, 1993]. The spallation neutron source is based on this approach.

The earliest neutron source is radionuclide neutron source, which a radionuclide to undergo decay through (α, n) , (γ, n) reaction or spontaneous fission with releasing neutrons. Afterwards neutron source produced by nuclear fission chain reaction, which provides high neutron flux and wide neutron energy spectrum. A comparison with nuclear fission chain reaction approach, spallation reaction way can generate a pulsed neutron beam, a wider

neutron energy spectrum, and more neutrons, especially for high energy neutrons¹ (greater than 20 MeV) [Russell, 1990], see Table 2.1. Furthermore, fission reaction releases more heat than spallation reaction does, and limitation of reactor cooling technology results in limitation of maximum neutron flux. Another difference between spallation and fission is residual nucleus after the reaction, the mass number of spallation products is continuous and down to 120 but the mass number of fission products is between 60 and 120 [Russell, 1990].

The nuclear spallation can be considered as several stages: Intra-Nuclear Cascade (INC), pre-equilibrium, evaporation (or fission), and de-excitation, as shown in Figure 2.2. The target nucleus now is in highly excited state after it absorbs the projectile. Neutrons, protons, and pions that emerge from excited target nucleus with a certain kinetic energy (greater than 20 MeV), and they may collide with another nucleus again and then emerge more hadrons (for instance, neutrons, protons) from the nucleus, which is a cascade of collisions or further spallation reactions [Russell, 1990]. The higher energy neutrons are produced in intra-nuclear cascade process, and have roughly similar direction with primary incident proton's direction. The process of excited target nucleus losses itself high energy by promptly evaporating particles (mainly neutron), is known as evaporation process. Only protons left in residual nucleus so that a proton will transform into a neutron through beta decay (by emission of β particle). The fission reaction will compete with evaporation process if the mass of target nucleus is high enough [Russell, 1990]. For low energy neutrons, they are generated in the de-excitation process.

Table 2.1 Characteristic of neutron sources [Russell, 1990]

Comparison item	Radionuclide	Reactor reaction	Spallation reaction
neutron generation	(α, n) , (γ, n) , spontaneous fission	nuclear fission chain reaction	high energy proton induced spallation reaction
reaction way	continuous	continuous	pulsed
energy spectrum	narrow	wide	wider
deposited energy	~ 3 MeV	~ 180 MeV	~ 32 MeV

¹It can generate about 2.5 neutrons per fission event in accordance with fission chain way, and consume 1 neutron to sustain the fission reaction.

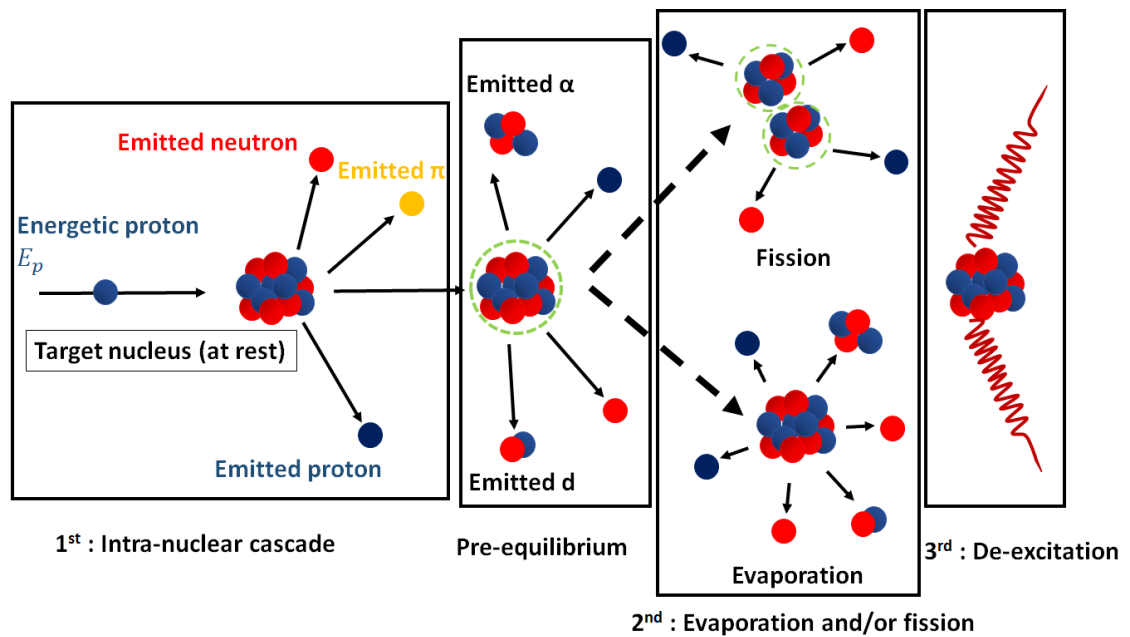


Fig. 2.2 The scheme of spallation reaction of high energy proton with heavy nuclei [Russell, 1990]. A bundle of nucleon represents heavier target nucleus, proton in blue, neutron in red, pion in yellow, and red wave presents gamma ray.

2.2 Neutron interactions with matter

Neutrons are neutral particles so that they do not loss energy via Coulomb interaction with orbital electrons. A neutron mainly transfers itself energy dependent upon the following mechanisms: elastic scattering, inelastic scattering, neutron capture, fission, and nuclear reaction [Alpen, 1998; Rinard, 1991]. The scope names of neutron are classified on basis of itself energy, as shown in Table 2.2.

Table 2.2 Neutron classification [Carron, 2006]

Scope name	Energy range /MeV
Cold neutron	$0 - 25 \times 10^{-9}$
Thermal neutron	25×10^{-9}
Slow neutron	$1 \times 10^{-3} - 10 \times 10^{-3}$
Resonance neutron	$0.01 - 0.3$
Intermediate neutron	$0.3 - 1$
Fast neutron	$1 - 20$
Relativistic neutron	> 20

The process of elastic scattering (n, n) between neutrons (before and after collision) and the target nucleus, obeys the energy conservation law and the law of momentum

conservation. The energy lost by neutron and transferred to the target nucleus ΔE can be calculated by Equation (2.1) [Alpen, 1998].

$$\Delta E = E_n \frac{4M_t M_n}{(M_t + M_n)^2} \cos^2 \theta \quad (2.1)$$

Where E_n represents initial neutron energy. M_t and M_n represent the target nucleus mass, and neutron mass. θ represents the angle of the recoiled target nucleus with respect to incident neutron direction¹ and ϕ represents the angle of the scattering neutron with respect to incident neutron direction, see Figure 2.3a.

At $\theta = 0^\circ$ and $\phi = 180^\circ$, the maximum energy ΔE_{max} transferred to the recoiled target nucleus is shown in Equation (2.2). A means atomic weight (ratio of target nucleus mass to neutron mass). According to Equation (2.2), it implies that if $A = 1$ (target is hydrogen atom), neutron is able to lose all energy and transfers it to the target nucleus. Therefore, water is a good moderating material. If $A = 207$ (target is lead), the maximum energy transferred to the lead target is only 1.9% of the incoming neutron energy.

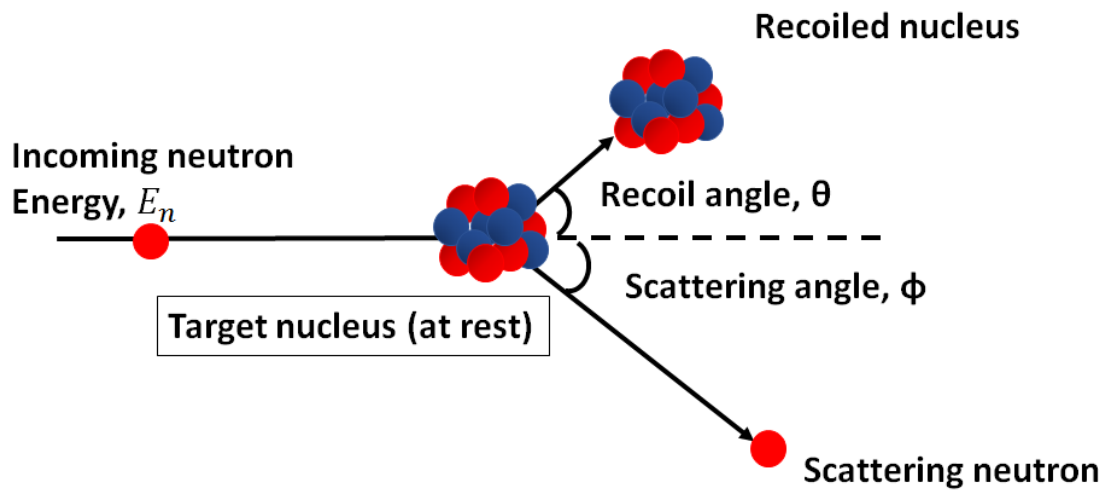
$$\Delta E_{max} = \frac{4AE_n}{(1+A)^2} \quad (2.2)$$

where $A = \frac{M_t}{M_n}$

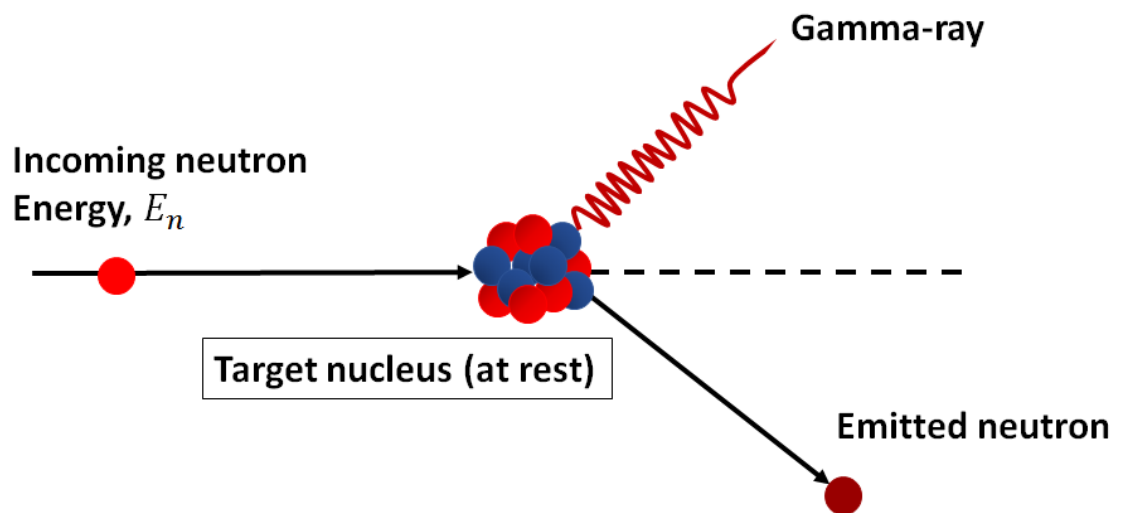
Inelastic scattering (n, n') is a process in which an energetic neutron is captured by target nucleus and then formed a compound nucleus. Such compound nucleus is in excited state so that a gamma photon and a neutron (not the same one with incoming neutron) will be emitted soon from the nucleus to get stable, as shown in Figure 2.3b. The kinetic energy of incoming neutron is greater than the total kinetic energy of emitted neutron and nucleus. If the energy transfer to the target nucleus is not high enough to place the nucleus into excited state, inelastic scattering is not likely to happen.

The number of protons and neutrons in the target nucleus remains the same after a neutron colliding with the target nucleus in the consideration of neutron scattering (include elastic and inelastic). However, the incoming neutron itself energy and direction would be

¹refer to the laboratory system of coordinates that assumes the target nucleus is at rest in lab



(a) Elastic scattering



(b) Inelastic scattering

Fig. 2.3 Neutron interactions with matter: scattering

changed, as well as that of the target nucleus. Neutron capture is a process in which the target nucleus absorbs a neutron and forms a heavier nucleus, thereby emits partial energy in the form of gamma photon.

Fission (n, f) is a nuclear reaction process in which the heavier target nucleus (for example, uranium nucleus) is hit by the incoming lighter particle (for example, neutron) and split into two massive fragments (nearly equal mass) with releasing neutrons and one or more than one prompt gamma ray, as shown in Figure 2.4. The neutron induced fission was first observed by Hahn and Strassman in 1938 [Patel, 1991]. ^{238}U is used in neutron detection technique which has a certain fission (n, f) cross section for charged particles production.

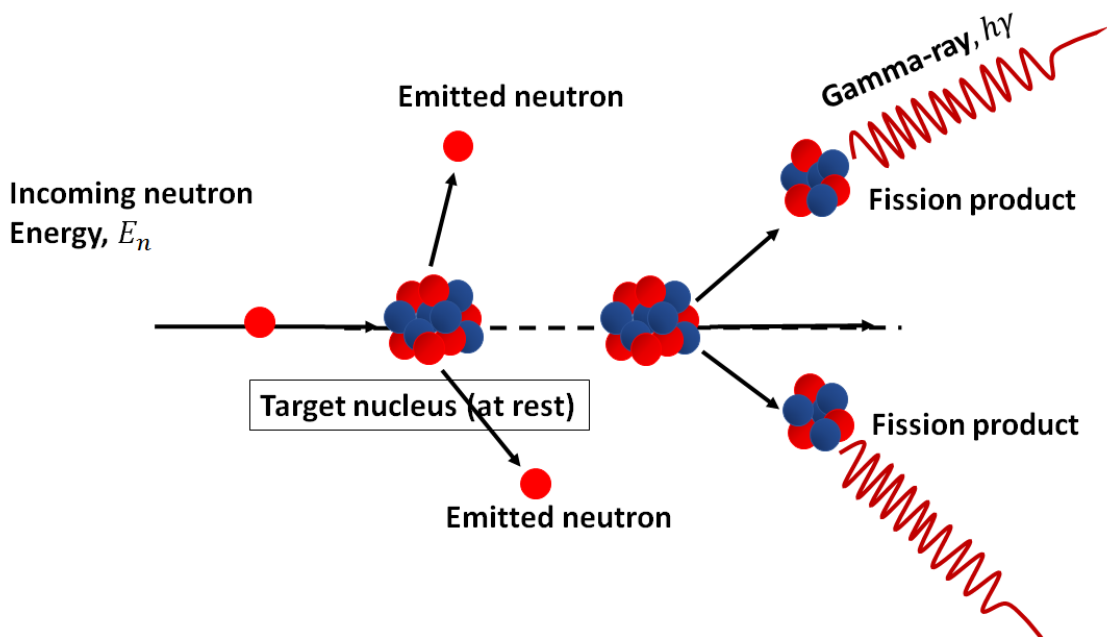


Fig. 2.4 The mechanism of neutron fission

2.3 Photons interactions with matter

Photons can be considered as neutral particles, which lose energy via the following mechanisms: photoelectric effect, Compton scattering, and pair production.

Heinrich Hertz discovered Photoelectric phenomena (PE) in 1887, who found electrons with a kinetic energy ejected from a metal surface after irradiation with ultraviolet light.

Figure 2.5 shows the absorption process of photoelectric effect. A photon transfers all energy to an electron which allows that electron turns to freedom by overcoming the electron's binding energy. Such free electron is called photoelectron, whose kinetic energy is given by Equation (2.3) [Alpen, 1998]. At the same time, a vacancy is created in atom resulting in an electron transition which loses energy. Such energy releases in the form of photon emission (Fluorescence) or electron emission (Auger effect) [Alpen, 1998].

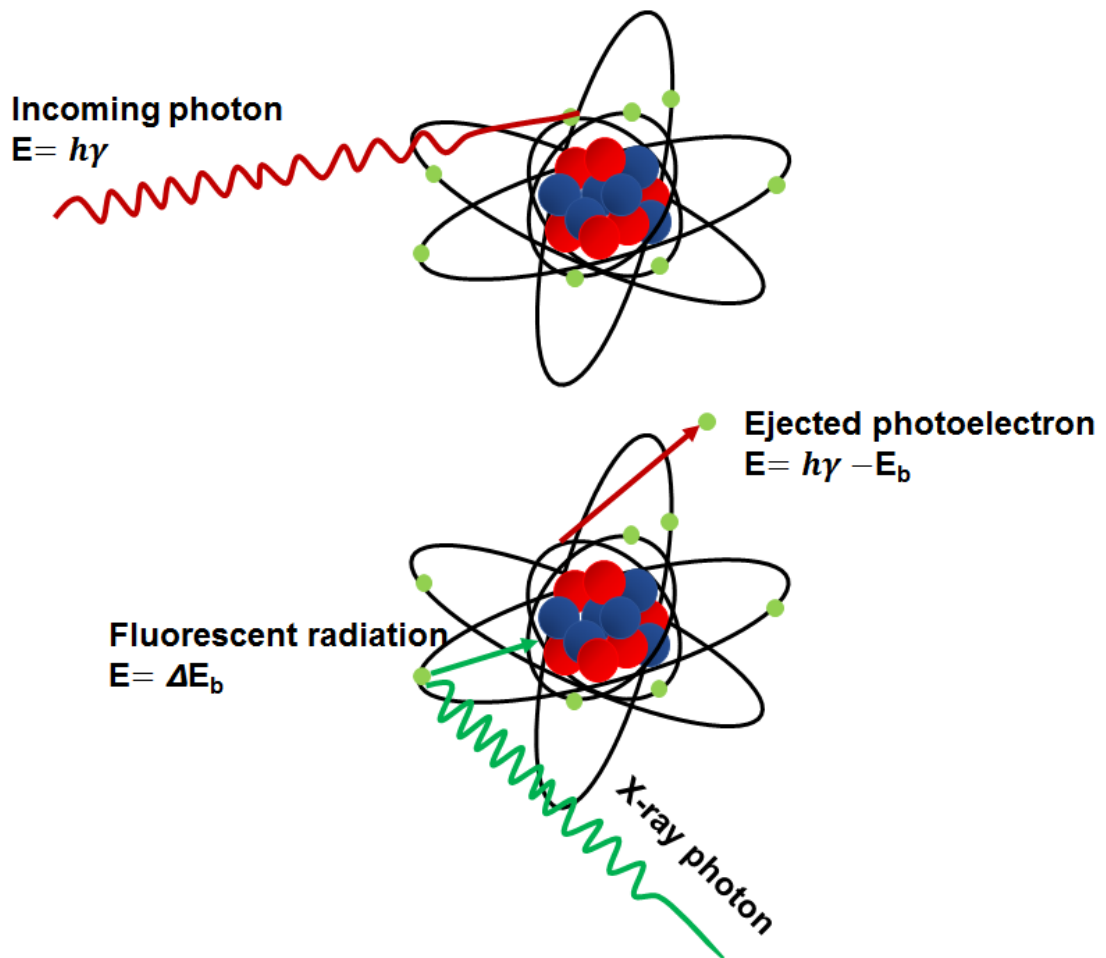


Fig. 2.5 The mechanism of photoelectric effect. The green solid circle represents the electrons bounded at atomic shell. A bundle of nucleon is shown as two parts: protons in blue and neutrons in red.

$$E_e = h\gamma - E_b \quad (2.3)$$

Where E_e represents kinetic energy of photoelectron, $h\gamma$ represents incident energy of photon, and E_b represents electron's binding energy.

The probability of photoelectric effect is dependent upon photon energy and atomic number of a material. The higher probability of photoelectric effect is likely to acquire if a higher atomic number material or the appropriate photon energy (just above electron's binding energy) is used.

Compton effect was discovered by Arthur Compton in 1923 [Compton, 1923]. Compton effect is a phenomenon of wavelength of the x-ray or gamma ray varies with the changes of itself scattering angle. Compared with photoelectric effect, photon will not completely disappear. The photon transfers partial energy to the electron rather than transfer all to electron. The emitted electron is known as Compton electron, whose energy is given by Equation (2.4) [Alpen, 1998].

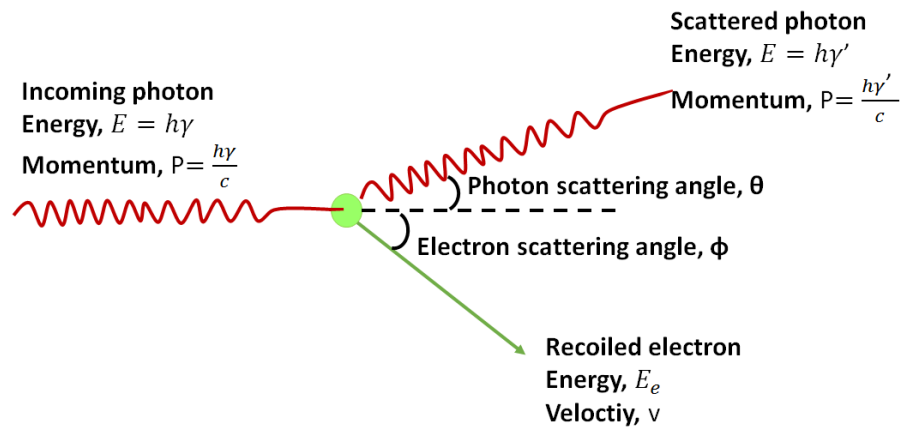


Fig. 2.6 The mechanism of Compton scattering [Alpen, 1998]. The green solid circle represents the electron. θ angle represents off-axis angle of photon with respect to incident photon direction. ϕ angle represents off-axis angle of recoiled electron with respect to incident photon direction.

$$E_e = h\gamma - h\gamma' \quad (2.4)$$

Where E_e represents energy of recoiled Compton electron, $h\gamma$ represents incident energy of photon, and $h\gamma'$ represents scattered photon energy.

According to conservation of momentum in Compton scattering between gamma-ray photon and electron (considered to be at rest in the beginning), scattered photon energy

and recoiled electron energy are given in Equation (2.5) [Alpen, 1998].

$$\begin{aligned} E_e &= h\gamma \frac{\alpha(1 - \cos \theta)}{1 + \alpha(1 - \cos \theta)} \\ h\gamma' &= h\gamma \frac{1}{1 + \alpha(1 - \cos \theta)} \end{aligned} \quad (2.5)$$

where $\alpha = \frac{h\gamma}{m_0c^2}$, $h\gamma$ represents incoming photon energy, and m_0c^2 represents rest energy of the electron, which is commonly 0.511 MeV.

If $\theta = 180^\circ$, recoiled electron will gain the maximum energy from the photon. The Compton electron is able to gain energy up to 95.30% of incoming photon if the incoming photon energy is 5.11 MeV. However, if the incoming photon energy is only 5.11 keV, then the maximum energy of Compton electron is 1.96% of incoming photon. It illustrates that transferred energy fraction will be low if the incoming photon energy is low (less than 100 keV). If the incoming photon (at least greater than 100 keV) rises, the transferred energy fraction will go up.

Pair production is an interaction between gamma and the nucleus of an atom, as shown in Figure 2.7. The phenomena of pair production, which gamma ray with energy greater than $2mc^2$ might give the birth of two electrons (positive, and negative) with a certain kinetic energy [Hubbell, 2006]. The reverse process of pair production, which two gamma ray photons with energy of 0.511 MeV in the opposite direction are created when the positron collides with a free electron, is known as annihilation radiation [Alpen, 1998]. Equation (2.6) shows the threshold of photon energy to induce pair production is 1.022 MeV. The probability of pair production increases with the increasing of incident photon energy and atomic number of the material.

$$h\gamma - 1.022 \text{ MeV} = E_{e+} + E_{e-} \quad (2.6)$$

Where $h\gamma$ represents the energy of incoming photon, 1.022 MeV is equivalent to total rest energies of two electrons. E_{e+} and E_{e-} represent kinetic energy of positron and electron, respectively.

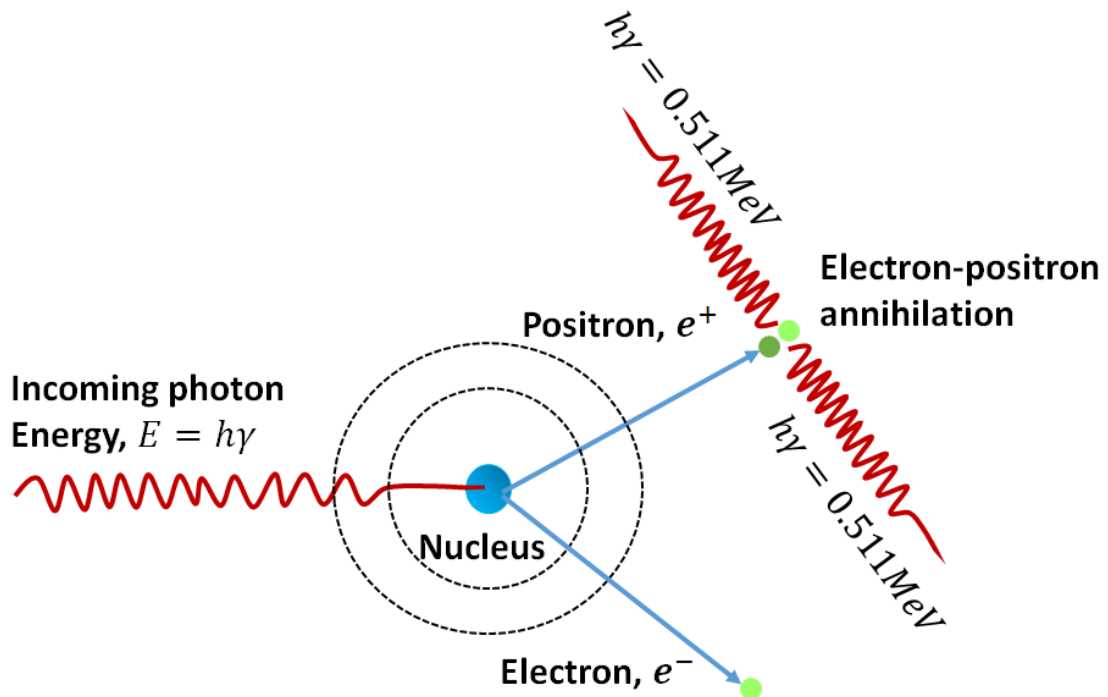


Fig. 2.7 The mechanism of pair production [Alpen, 1998]. The blue solid circle, dark green solid circle, and shiny green solid circle represent nucleus, positron, and electron, respectively.

2.4 A brief modelling with using Geant4 toolkit

Geant4 (GEometry ANd Tracking) toolkit is developed by CERN (European Organization for Nuclear Research), which is written in object-oriented C++ language. This software is mainly applied to simulate high energy particle transportation through matter, using Monte Carlo method. It provides users with a completed detection toolkit including geometry, detector response, run, event, track, graph display, and user interface. The significant applications are listed as follows : particle physics, nuclear physics, accelerator design, space engineering and medical physics.

Table 2.3 shows the Geant4 version and release date since this work began. The version 9.5 of Geant4 was used for installing Geant4 toolkit on Linux operation system and building existing Geant4 application examples. The preliminary Spallation Neutron Source (SNS) model based on LANSCE, WNR Target 4 made full use of Geant4 toolkit version 9.6 to calculate radiation fields. Besides that, the model of preliminary spallation neutron source based on TSL ANITA facility used Geant4.9.6 for calculating neutron flux

and estimating gamma dose. The model of SNS at ANITA facility, supplemented with components such as collimator, shielding, as well as bending magnet to calculate radiation fields at Standard User Position with Geant4.10.0.

Table 2.3 Geant4 version and release date

Item	version	date	Application
Geant4	9.5	December 2011	
Geant4	9.6	December 2012	Preliminary SNS
Geant4	10.0	December 2013	SNS at ANITA

Geant4 is aimed to investigate physical problems, which encapsulate a full set of C++ classes. The interface classes in Geant4 toolkit can be used to overload and implement user's needs by creating concrete class. The simplest Geant4 example requires three mandatory classes to register, which are `G4VUserDetectorConstruction`, `G4VUserPhysicsList`, and `G4VUserPrimaryGeneratorAction` [Agostinelli et al., 2003; Allison et al., 2006]. In addition, other optional classes for instance, `G4UserRunAction`, `G4UserEventAction`, `G4UserStackingAction`, `G4UserTrackingAction`, and `G4UserSteppingAction` can be used in Geant4 simulation [Agostinelli et al., 2003; Allison et al., 2006]. In the spallation neutron source model, the following concrete classes were created, for instance, `DetectorConstruction`, `PhysicsList`, and `PrimaryGeneratorAction`, as shown in Figure 2.8, they are derived from `G4VUserDetectorConstruction`, `G4VUserPhysicsList`, and `G4VUserPrimaryGeneratorAction` respectively.

The `G4VUserDetectorConstruction` is used for specifying geometry so that the derived class "`DetectorConstruction`" is created. "`DetectorConstruction`" implemented whole equipments space (e.g. cylinder target, thin shell detectors, cubic space facility), constituent material or substance (e.g. tungsten, air), and register sensitive detectors through `Construct()` method. Figure 2.9 shows portions of code written in `Construct()` of SNS at ANITA facility. Two detectors are placed at two positions (standard user position and front face of collimator), which are filling with vacuum, see line 159-183. `G4VUserPrimaryGeneratorAction` is used to initialize primary event, therefore the derived "`PrimaryGeneratorAction`" can be used to create primary incident particle with kinetic energy (e.g. proton with 800 MeV

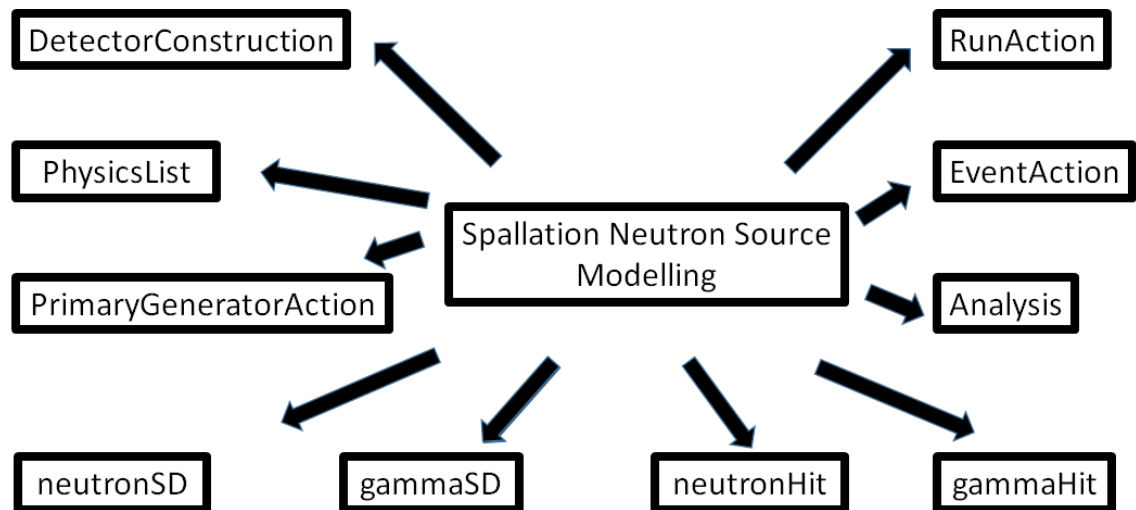


Fig. 2.8 Spallation neutron source modelling frame

```

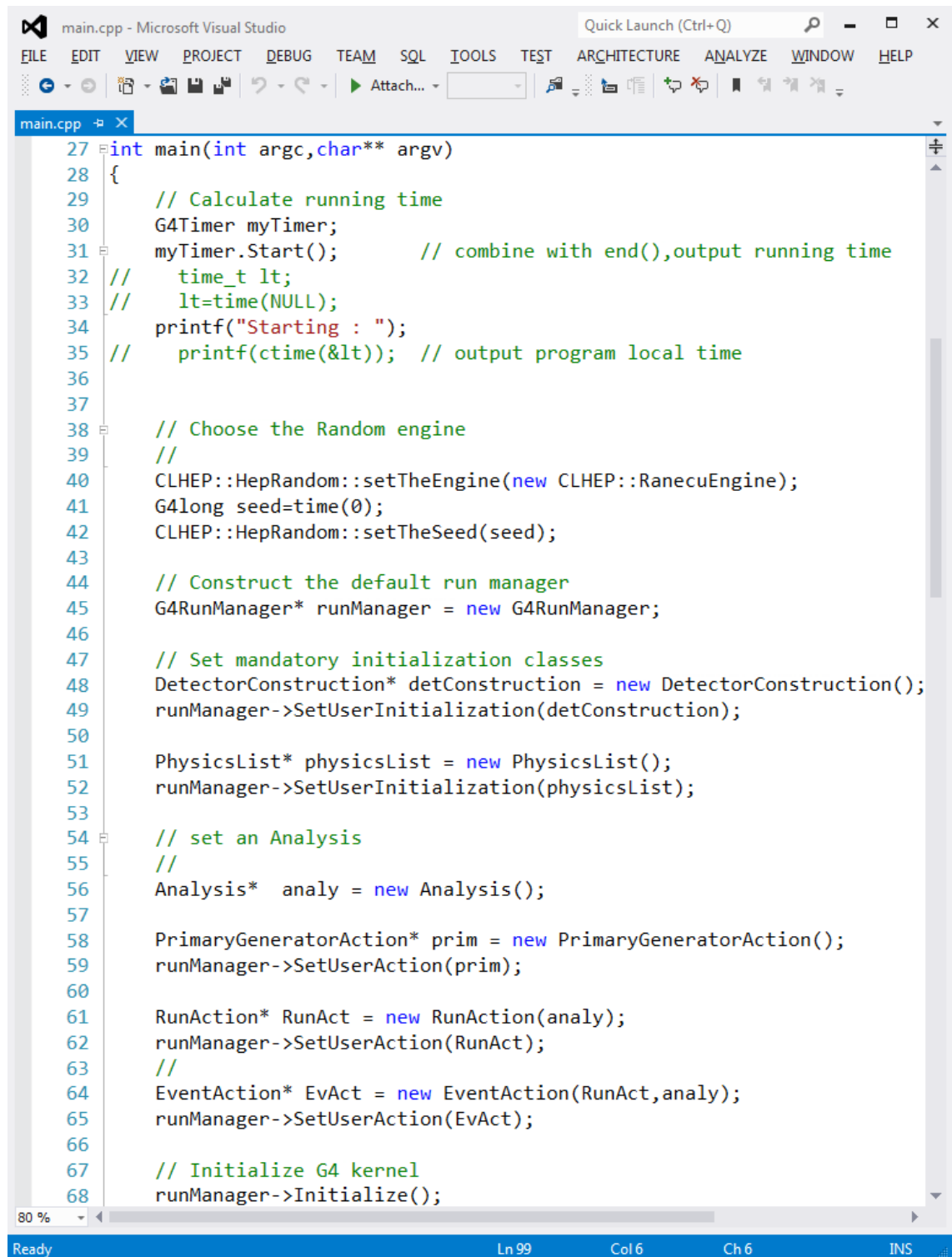
151 // Detector construction
152 //
153 G4cout << "#                               #" << G4endl ;
154 G4cout << "#   Building the < Sensitive Detectors > ... #" << G4endl ;
155 G4cout << "#                               #" << G4endl ;
156
157 // SUP position
158 //
159 G4Box* SUPSol = new G4Box("SUP",150*mm,150*mm,0.5*mm);
160 SUPLog = new G4LogicalVolume (SUPSol,VacuumMat,"SUP");
161 G4double SsDetectorPosZ = TARGETHEIGHT + 750*mm + 0.5*mm;
162 new G4PVPlacement(0, // Rotation matrix pointer
163                 G4ThreeVector(0*mm,0*mm,SsDetectorPosZ), // Translation vector
164                 SUPLog, // Logical volume
165                 "SUP", // Name
166                 WorldLog, // Mother volume
167                 false, // Unused boolean
168                 0,
169                 CheckOverlap);
170
171 // Front face of Collimator
172 //
173 G4Box* FrontFaceSol = new G4Box("FrontFace",COLLIMATORWIDTH/2,COLLIMATORHEIGHT/2,0.5*mm);
174 FrontFaceLog = new G4LogicalVolume (FrontFaceSol,VacuumMat,"FrontFace");
175 SsDetectorPosZ = TARGETHEIGHT + 867*mm - 0.5*mm;
176 new G4PVPlacement(0, // Rotation matrix pointer
177                 G4ThreeVector(0*mm,-APERTUREYMOV,SsDetectorPosZ), // Translation vector
178                 FrontFaceLog, // Logical volume
179                 "FrontFace", // Name
180                 WorldLog, // Mother volume
181                 false, // Unused boolean
182                 0,
183                 CheckOverlap);
184
100 %
Ready Ln1 Col1 Ch1 INS

```

Fig. 2.9 DetectorConstruction() code for SNS at ANITA facility

in LANSCE WNR, and with 180 MeV in TSL ANITA), incident direction, and initial vertex positions via `GeneratePrimaries()` method. `G4VUserPhysicsList` is used to define all particles and physical interactions and processes. Therefore, the derived "PhysicsList" class is applied to construct all particles involved to spallation neutron source (for example, proton, neutron and γ), and nuclear debris (for example, α and other heavier nucleus) via `ConstructParticle()` method. The processes construction can be registered to particles by using pure virtual method of `ConstructProcess()`.

Figure 2.10 shows core code of own `main()` function for preliminary spallation neutron source at the WNR and the ANITA facility. In the main function, running time is recored (line 30-34), random engine is chosen for generating pseudo-random number (line 40-42), objects of three mandatory classes (`DetectorConstruction`, `PhysicsList`, and `PrimaryGeneratorAction`) are created and passed their pointer to the run manager. Besides, the objects of user action classes are created and used for data. In preliminary SNS model, "RunAction" and "EventAction" are derived from `G4UserRunAction` and `G4UserEventAction`. Run, Event, and Step are representing different concepts. Run refers to a cycle of program execution, for example, `BeamOn()` function executes from the start to the end, is known as a Run. Event, for example, refers to whole transport process of the particle. Step refers to the part between two collision points of the particle. The relation among them is $\text{Run} > \text{Event} > \text{Step}$. In another word, a Run contains multiple events, and an event contains multiple steps. The next Event will begin until all Steps in the previous Event are completed. Similarly, the next Run will begin until all Events in the previous Run are completed. These optional user actions used to meet extra demands, such as tracking specified secondaries or killing secondaries. "neutronSD" and "gammaSD" are created for recording specified Event information (neutrons and gamma photons passing through two sensitive detectors). Sensitive detector registration is implemented in `Construct()` function of `DetectorConsturction` class. All data that we concerned will be recorded in "neutronHit" and "gammaHit" derived from `G4VHit` class. Analysis is created for selecting different output format, such as ROOT, XML, and CSV.



```
main.cpp - Microsoft Visual Studio
Quick Launch (Ctrl+Q)
FILE EDIT VIEW PROJECT DEBUG TEAM SQL TOOLS TEST ARCHITECTURE ANALYZE WINDOW HELP
main.cpp
27 int main(int argc, char** argv)
28 {
29     // Calculate running time
30     G4Timer myTimer;
31     myTimer.Start(); // combine with end(), output running time
32     // time_t lt;
33     // lt=time(NULL);
34     printf("Starting : ");
35     // printf(ctime(&lt)); // output program local time
36
37
38     // Choose the Random engine
39     //
40     CLHEP::HepRandom::setTheEngine(new CLHEP::RanecuEngine);
41     G4long seed=time(0);
42     CLHEP::HepRandom::setTheSeed(seed);
43
44     // Construct the default run manager
45     G4RunManager* runManager = new G4RunManager;
46
47     // Set mandatory initialization classes
48     DetectorConstruction* detConstruction = new DetectorConstruction();
49     runManager->SetUserInitialization(detConstruction);
50
51     PhysicsList* physicsList = new PhysicsList();
52     runManager->SetUserInitialization(physicsList);
53
54     // set an Analysis
55     //
56     Analysis* analy = new Analysis();
57
58     PrimaryGeneratorAction* prim = new PrimaryGeneratorAction();
59     runManager->SetUserAction(prim);
60
61     RunAction* RunAct = new RunAction(analy);
62     runManager->SetUserAction(RunAct);
63     //
64     EventAction* EvAct = new EventAction(RunAct, analy);
65     runManager->SetUserAction(EvAct);
66
67     // Initialize G4 kernel
68     runManager->Initialize();
```

80 % Ready Ln 99 Col 6 Ch 6 INS

Fig. 2.10 Core code of the main() function for preliminary SNS

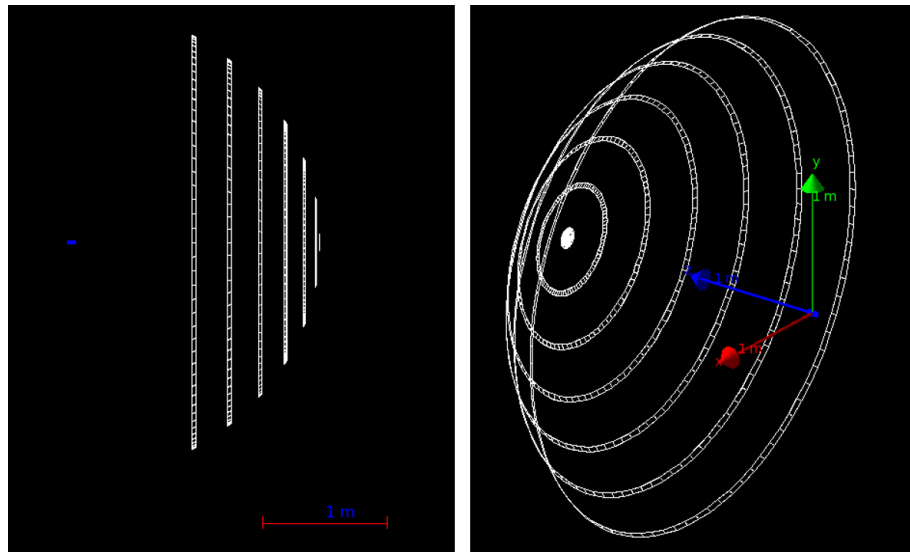


Fig. 2.11 Preliminary spallation neutron source model at ANITA facility. The dark green solid represents the tungsten target. The white lines represent concentric circles attached on detector, which acts as a neutron detector (counter)

Figure 2.11 shows the geometry of preliminary SNS layout at ANITA facility including the target and detector. The thickness of spherical neutron detector is 1 mm. The left one is a lateral view of preliminary SNS model, the little blue is the target and white lines show those emitted neutrons passing through neutron detector with angles of 1° , 10° , 20° , 30° , 40° , 50° , and 60° with respect to primary incident proton direction. The right one shows an oblique aerial view of the model with xyz axes. In comparison of preliminary SNS model at ANITA facility and that at WNR, the distance between detector and the target is different, the ANITA model is about 2.5 m and the WNR model is about 20 m.

In the simulation, it is aimed to calculate the number of neutrons passing through detector. In the real world, the total number of neutron products cannot be measured by detector in spallation neutron source. However, it is capable of calculating charged reaction products resulting from neutron interaction with matter (elastic scattering, inelastic scattering, absorption, and nuclear reaction), see Section 2.2.

In the simulation, the number of neutrons (photons) per unit area, known as neutron (photon) fluence, can be calculated directly. In the real world, fluence ($d\phi$) refers to the number of particles radiant energy on a unit surface area over the given period of time [JEDEC, 2006], $d\phi = \frac{N}{A}$ (unit: ncm^{-2}). The neutron yield ϕ_{Y_n} (unit: $np^{-1}sr^{-1}$)

represents the number of neutron productions per proton incident per solid angle, see the following Equation 2.7.

$$\phi_{Y_n} = \frac{N_n}{N_p \Omega} \quad (2.7)$$

Where N_n is the number of neutrons, N_p is the number of protons, and Ω is the solid angle. The solid angle refers to a dimensionless unit, known as steradian *sr*.

Flux ($d\dot{\phi}$ or $\frac{d\phi}{dt}$) refers to the time rate of fluence [JEDEC, 2006], shown in Equation 2.8, and its unit is $cm^{-2}s^{-1}$.

$$\frac{d\phi}{dt} = \frac{N}{At} \quad (2.8)$$

In the real world, N is the number of particles, A is the area being radiant, and t is the length of time. Therefore neutron flux unit is $ncm^{-2}s^{-1}$, here n stands for "neutron". If γ takes the place of n , then photon (gamma) flux unit will be expressed as $\gamma cm^{-2}s^{-1}$.

Differential flux ($\frac{d\phi}{dE}$) is defined as time rate of flux per unit energy [JEDEC, 2006], and its unit is $cm^{-2}s^{-1}MeV^{-1}$.

$$\frac{d\phi}{dE} = \frac{N_n}{AtE} \quad (2.9)$$

Differential flux is expressed in energy deviation, and E is the energy range in *MeV*. Thus, unit of differential neutron flux can be expressed in $ncm^{-2}MeV^{-1}s^{-1}$.

N_{SEU} , the number of SEU events observed, which can be estimated with cross-section (σ) and particle fluence (ϕ).

$$\sigma = \frac{N_{SEU}}{\phi} \quad (2.10)$$

If neutron induced SEU and Thin-Film Breakdown Counter (TFBC) as neutron detector, cross-section refer to the possibility of neutron interaction with ^{238}U , and its unit is cm^{-2} . Wherer ϕ is the neutron fluence. The neutron fluence can be calculated by SNS at ANITA facility model and folded with $^{238}U(n, f)$, thus the number of SEU events induced by neutron is known. Chapter 4 introduces the comparisons of simulated and experimental TOF spectra at the Close User Position.

2.4.1 Physics list chosen

In Section 2.1 and 2.2, it analyzed major physics processes in spallation neutron source. It is significant to familiar with processes because the categories of processes in this case decide the choice of physics lists used. According to Geant4 website under User Support, Physics lists 10.b [Geant4 Collaboration, ndb], “reference physics lists” are listed. Table 2.4 shows the naming convention of Geant4 physics list used in preliminary SNS model. The

Table 2.4 Geant4 physics list abbreviation

Abbreviation	Mean	Energy
<i>QGSP</i>	quark gluon string model	$>\sim 20\text{ GeV}$
<i>BIC</i>	binary cascade model	$<\sim 10\text{ GeV}$
<i>BERT</i>	bertini cascade model	$<\sim 10\text{ GeV}$
<i>HP</i>	high precision neutron model	$<\sim 20\text{ MeV}$

string model is used for high energy hadron interactions, and “reference physics list” is considered as starting point to validate for spallation neutron source. Truscott used Geant4 toolkit for prediction of neutron energy deposition spectra from neutron-nuclear reactions at TSL neutron facility (quasi-monoenergetic beam) and TRIUMF neutron facility (NIF, atmospheric neutron spectrum) with Geant4 binary cascade and Geant4 classical cascade models [Truscott et al., 2006]. A comparison of prediction with measurement result shows a good agreement from [Truscott et al., 2006]. It illustrated that the classical cascade and binary cascade models are useful for modelling intranuclear cascade. For classical cascade model, the energy range is between 40 MeV and 5 GeV and it is less accurate compared with binary cascade model for modelling intranuclear cascade [Truscott et al., 2006]. Haggmann reported that Monte Carlo Transport Code would be able to simulate cosmic ray shower [Haggmann et al., 2007]. The result of neutron spectrum at sea level from Geant4 gives a good agreement with MCNPX calculation between 0.1 MeV and 1×10^4 MeV with using 1000 GeV incident proton, see Figure 2.12. The spallation neutron source facilities wish to create neutron spectrum at aircraft altitude or at sea level, and result of neutron spectrum from MCNPX gives a good agreement with measurement data

from 1×10^4 MeV to 1×10^6 MeV, see Figure 2.13. Geant4 is able to apply in accelerated SEE testing for investigating neutron spectra between 0.1 MeV and 1×10^4 MeV.

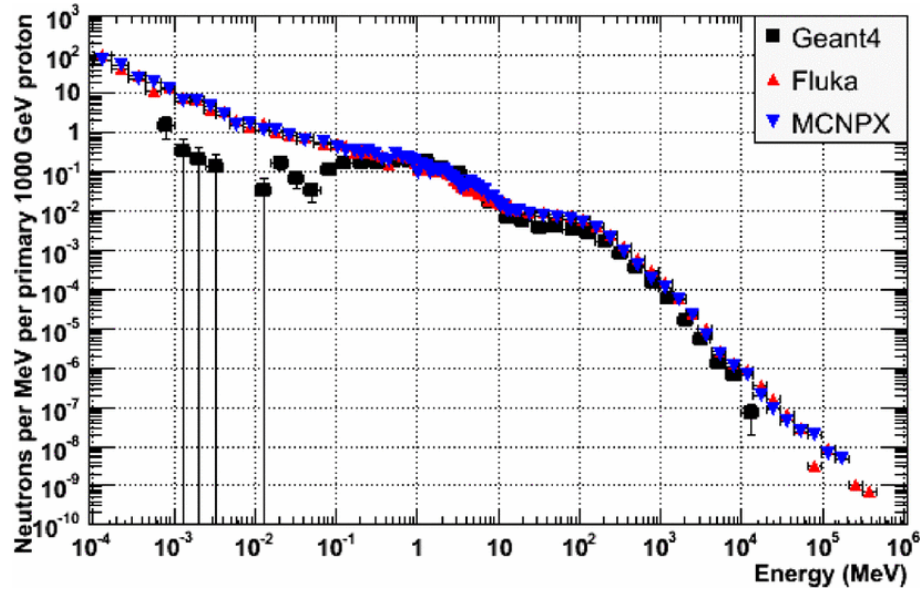


Fig. 2.12 A comparison of neutron spectra at sea level with Geant4 and MCNPX after air shower [Hagmann et al., 2007].

In addition, “Physics Reference Manual” under Documentation from Geant4 web page, binary cascade model is used for 800 MeV proton interaction with Aluminum [Geant4 Collaboration, ndb]. Beside, “Physics Reference Manual” suggested bertini cascade model for modelling intranuclear cascade. Bertini cascade model includes pre-equilibrium, evaporation, fission, and nucleus explosion models [Geant4 Collaboration, ndb]. Therefore, binary and bertini cascade models are useful to spallation neutron source.

QGSP_BERT_HP is like *QGSP_BERT*, and extra high precision neutron model (NeutronHP) is added. NeutronHP is used for neutrons with energy less than 20 MeV. *QGSP_BIC_HP* is same as *QGSP_BIC*, and NeutronHP is added. It would be appropriate for binary cascade model to simulate hadron-nucleon collision. Comparing *QGSP_BERT_HP* and *QGSP_BIC_HP*, binary cascade model is valid for proton, neutron, pion but bertini cascade model applies to more particles, such as gamma, kaon. *QGSP_BERT_HP* and *QGSP_BIC_HP* will be chose in preliminary modeling of spallation neutron source at LANSCE and ANITA.

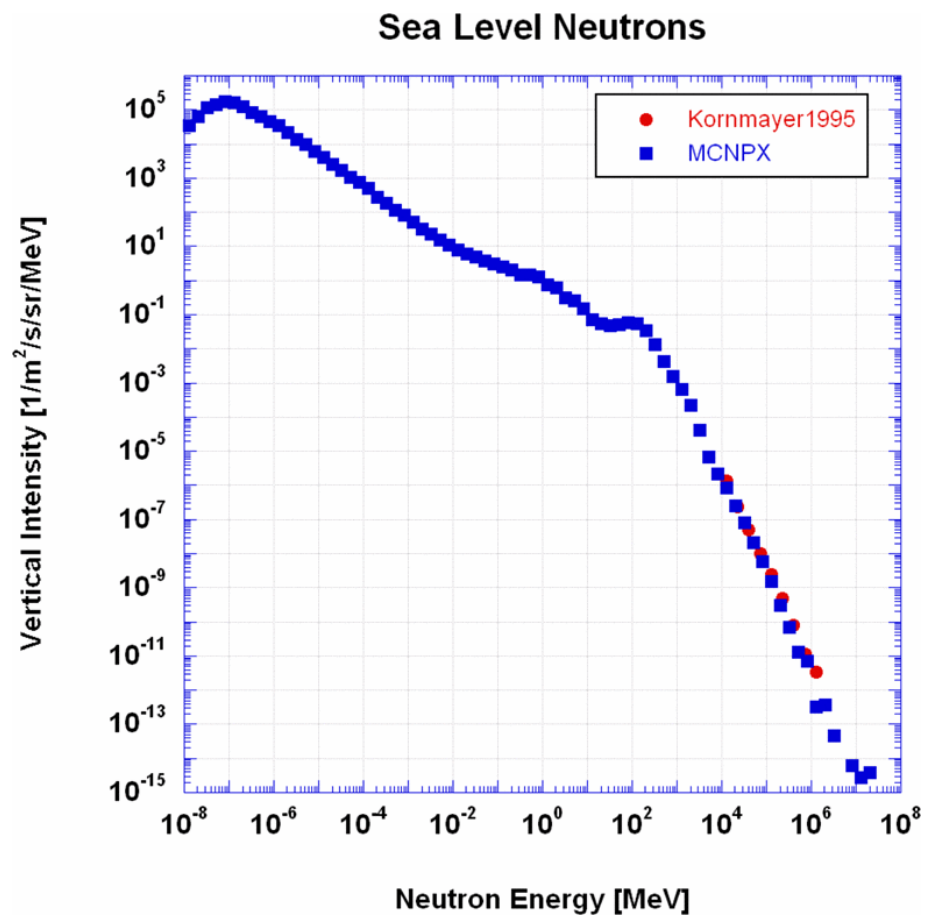


Fig. 2.13 A comparison of neutron spectra at sea level with MCNPX and Measurement [Hagmann et al., 2007].

2.4.2 Summary

Neutron and photon interactions with matter have been described through this Chapter, which are the basis of understanding physical phenomenon and interactions. Both binary intra-nuclear cascade model and bertini intra-nuclear cascade model with high precision neutron model will be used in preliminary neutron sources simulations at LANSCE and TSL. The preliminary simulations of two spallation neutron source facilities were conducted to investigate the behavior and transport of neutrons and photons at accelerated SEE testing with use of Geant4 toolkit in Chapter 3.

Chapter 3

Preliminary simulation of two spallation neutron sources

This chapter will show preliminary simulation of neutron and gamma fields at two spallation sources, which are at LANSCE and TSL. Model validation against independent calculations and measurements show reproduction of neutron spectra which were published at RADECS 2013 [Platt et al., 2013].

3.1 General description of the LANSCE WNR and TSL ANITA spallation sources and their models

Here are brief descriptions of the real spallation neutron source facilities. A schematic drawing shows detailed plan view of Target-4 flight paths at WNR, see Figure 3.1¹. Each Flight Path (FP) is named after the target and the direction of the flight path with respect to the incoming beam. For instance, 4FP90L indicates the neutron beam is produced at Target4 and its FP towards the left at an angle of 90° (90L). Target 4 provides the following flight paths, 4FP90L, 4FP30L, 4FP15L, 4FP15R, 4FP30R, 4FP60R. The spallation neutron source at Target 4 is produced due to the 800 MeV proton beam bombard on the tungsten

¹There are a few targets for different research purposes at LANSCE, such as Target 2 and Target 1 (Lujan Center). The preliminary simulation of the naked spallation neutron source at LANSCE was modeled after Target 4.

target. A broad spectrum of neutron beam with energies from about 0.1 MeV up to 800 MeV is obtained by time-of-flight (TOF) techniques. LANSCE calculation results are shown on online [LANSCE, nd]¹ and a unpublished LANSCE measurement data about neutron flux [Platt, 2012] will be used to validate Geant4 modelling of spallation neutron source at Target 4.

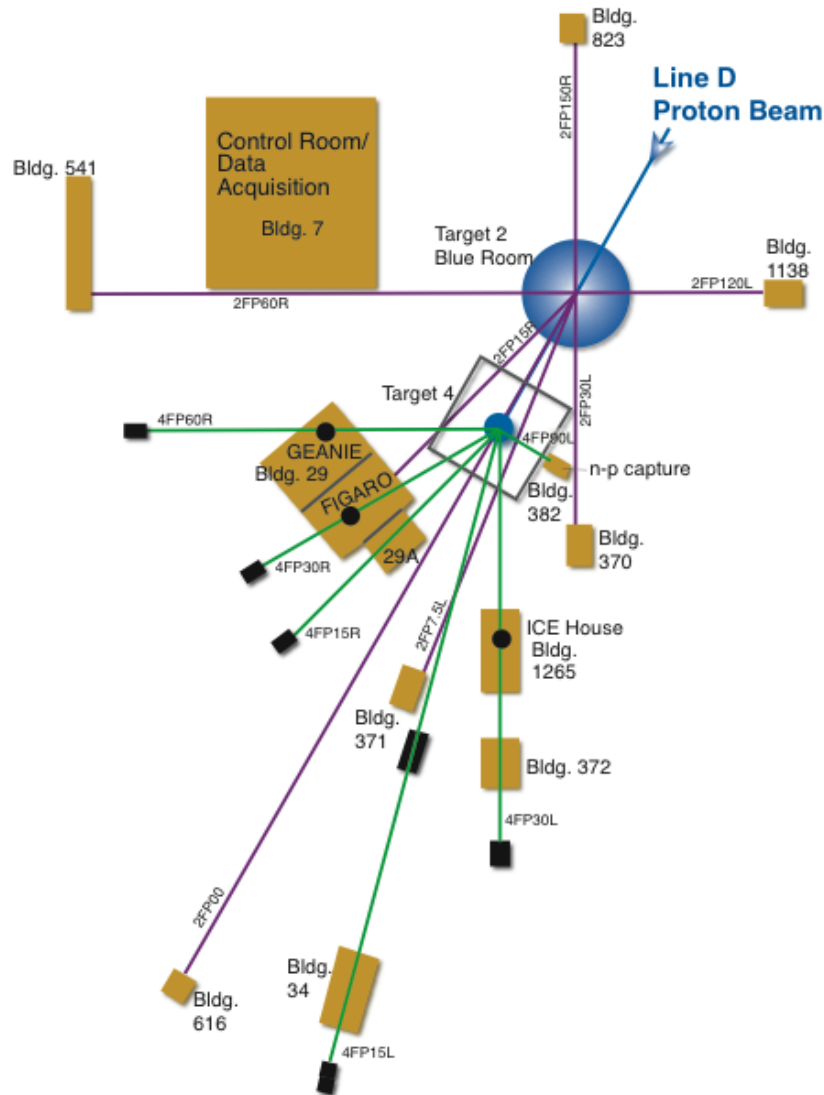


Fig. 3.1 Various flight paths of Target 4 at WNR facility. For examples, 4FP15L-A(20m), 4FP15L-B(90m), 4FP15R, 4FP30L-A(ICE House), 4FP30L-B, 4FP30R(ICE II), 4FP60R(GEANIE), and 4FP90L(TPC) [LANSCE, nd]

ANITA (Atmospheric-like Neutrons from thick TARGET), the neutron facility at The Svedberg Laboratory (TSL) provides spallation neutron source, but with different pa-

¹The calculation data were published online but now are no longer tabulated on the LANSCE website. They are reproduced in Appendix A.2 of this thesis

Table 3.1 Geant4 modelling parameters [Prokofiev et al., 2009, 2014; Wender and Lisowski, 1987]

Parameters	LANSCE	ANITA	Unit
target length	7.0	2.4	cm
target diameter	3.0	5.0	cm
proton energy	800	180	MeV
flight path length	20	2.5	m

Table 3.2 Simulated detector parameters

Detector Parameters	LANSCE	ANITA	Unit
Neutron detector inner radius	19.999	2.499	m
Neutron detector outer radius	20.000	2.500	m
Gamma detector inner radius	20.000	2.500	m
Gamma detector outer radius	20.001	2.501	m

parameter in comparison with WNR spallation source, see Table 3.1. The simulation of ANITA neutron field with Geant4 code and analytical model derived from MCNPX calculations [Prokofiev et al., 2009] will be compared to validate Geant4 modelling.

The geometrical model of spallation neutron sources at LANSCE and TSL is based on the arrangement shown in Figure 3.2. This is similar to SNS model of Figure 2.11 in Chapter 2. The big cube in black was the biggest object in the simulation and filled with air. The geometric centre of the cylindrical tungsten target in grey was placed at the origin of the Cartesian coordinate system. The proton beam is axially incident to the target, that blue sphere shell is aiming to record neutrons and photons information, for instance, position, momentum, kinetic energy. The blue sphere shell contains two simulated detectors: neutron detector and gamma detector. The gamma detector size is slightly bigger than the neutron detector and is next to neutron detector, see Table 3.2.

The simulation of LANSCE was carried out by 5 million incident protons with kinetic energy of 800 MeV. Neutron and gamma fields were calculated at the off-axis angle of $15^\circ \pm 1^\circ$, $30^\circ \pm 1^\circ$, $60^\circ \pm 1^\circ$, and $90^\circ \pm 1^\circ$ ¹ and 20 m from the tungsten target for LANSCE WNR neutron source. Geant4 simulation of ANITA was run with 205 million protons with

¹Here $90^\circ \pm 1^\circ$ indicates 89-90 degree because the modelling is only recorded up to 90° .

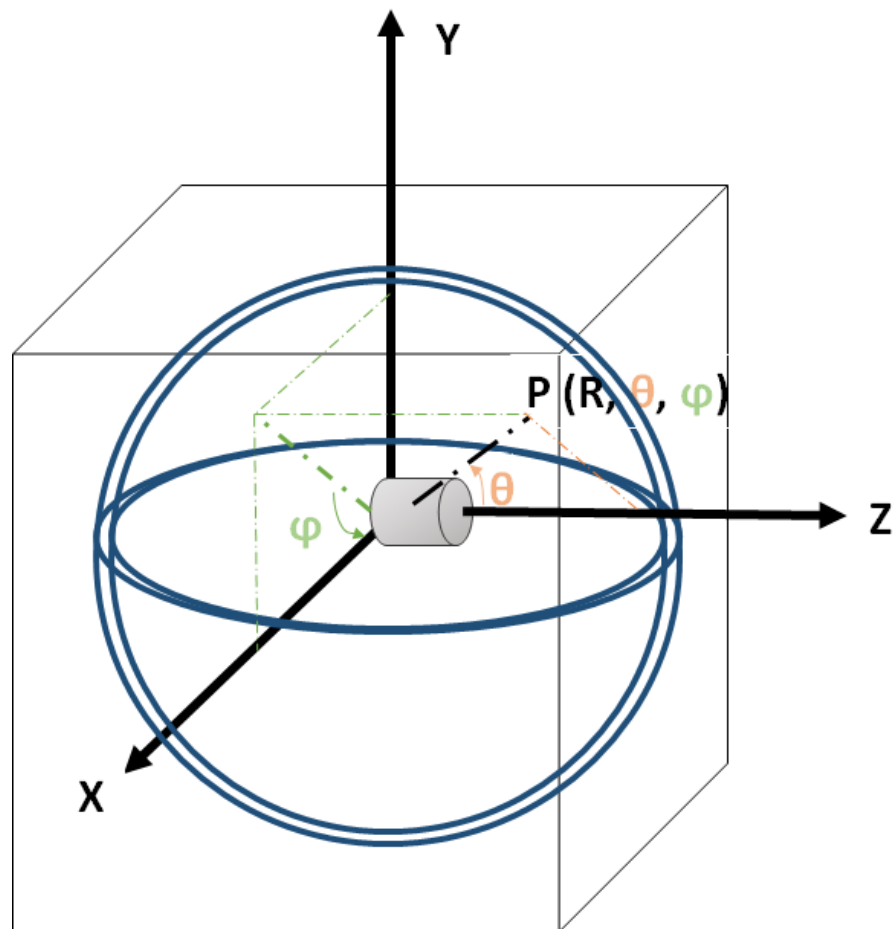


Fig. 3.2 Geometry drawing of spallation neutron source. $P(r, \theta, \varphi)$ represents a point on shell in spherical coordinates. R , θ , and φ indicate respectively radial distance, polar angle, and azimuthal angle.

kinetic energy of 180 MeV. Neutron and gamma fields were analysed at 2.5 m from the tungsten target on-axis (0° - 1.5°).

The number of incident protons reaches more than million because it determines production of neutrons in a period time. The phenomenon of a few events with low possibility occasionally were detected in the astrophysics measurement can be quantified with event rate or ratio of two event types [Gehrels, 1986]. In order to obtain an accurate and reliable result, a sufficient number of events are needed. According to Appendix B.1 and B.2, it illustrates the upper and lower confidence limits derived from Poisson statistics at some specified Confidence Level (CL) [Gehrels, 1986]. The number of events increases from 10 to 100, the upper uncertainty will be reduced (from 42.7% to 11.0%) for $CL = 0.8413$ (Gaussian statistics $1\sigma = 0.8413$). If the number of incident proton is close to one million, thus counting uncertainty is about 0.1%, which can be ignored.

The number of incoming protons used for SNS model at ANITA was larger than that used for LANSCE model, that is because the solid angle in two cases is different. The unit of neutron yield is neutron per proton per steradian ($np^{-1}sr^{-1}$). For example, the solid angle of ANITA model on axis 0° - 1.5° (0.0022 sr) that can capture neutrons is smaller than that of LANSCE at the off-axis angle of $30^\circ \pm 1^\circ$ (0.0540 sr). The solid angle ratio of LANSCE to ANITA is about twenty five times. It means the number of incoming protons used for ANITA at least 25 times as much as LANSCE.

The reason of physics list choices were described in Section 2.4.1 in Chapter 2. Binary and bertini internuclear cascade models were used in WNR and ANITA models, and *QGSP_BERT_HP* and *QGSP_BIC_HP* physics lists were selected to find out the differences between these two intra-nuclear cascade models.

3.2 Neutron field calculations

Since there will be many comparisons of neutron field from the Geant4 modelling with independent LANSCE measurements and calculation data in the following section, it is better to use Bertini and binary rather than *QGSP_BERT_HP* and *QGSP_BIC_HP*

physics list. Likewise, LANSCE experimental data is referred to as measurement and LANSCE calculation is referred to as calculation in Section 3.2.1.

3.2.1 Neutron field calculations at LANSCE WNR

Figure 3.3 shows the integral neutron and differential neutron yield versus energy at LANSCE WNR, ICE House (4FP30L). The calculated neutron yield above 10 MeV is $0.21 \text{ n p}^{-1} \text{ sr}^{-1}$ using the Bertini model and $0.19 \text{ n p}^{-1} \text{ sr}^{-1}$ using the binary model at the off-axis angle of 30° , see following Table 3.3. The number of neutrons above 10 MeV is very close to about $0.20 \text{ n p}^{-1} \text{ sr}^{-1}$ no matter whichever model is applied. LANSCE calculation results made and published¹ by LANSCE [LANSCE, nd] show a yield above 10 MeV of $0.216 \text{ n p}^{-1} \text{ sr}^{-1}$. LANSCE measurement data [Platt, 2012] give neutron yield above 10 MeV of $4.5 \times 10^5 \text{ n cm}^{-2} \text{ s}^{-1}$. In order to directly compare the LANSCE measurement results with others, the measurement data have to be normalized to $\text{n p}^{-1} \text{ sr}^{-1}$ by using Equation (3.1).

$$N = \frac{0.5 \times (\int_{10\text{MeV}}^{\infty} \phi(E)_{\text{bertini}} dE + \int_{10\text{MeV}}^{\infty} \phi(E)_{\text{binary}} dE)}{\int_{10\text{MeV}}^{\infty} \phi(E)_{\text{measure}} dE} \quad (3.1)$$

Here $\phi(E)$ ² particularly represents the density of neutrons per unit energy. Therefore, neutron yield above 10 MeV at 30° of the binary model ($0.21 \text{ n p}^{-1} \text{ sr}^{-1}$) and the Bertini model ($0.19 \text{ n p}^{-1} \text{ sr}^{-1}$) are used to calculate normalization factor N , in which $N = 4.44 \times 10^{-7} \text{ cm}^2 \text{ sp}^{-1} \text{ sr}^{-1}$.

The relation between normalization factor N and implied current I , as shown in Equation (3.3), can be inferred on the basis of Equation (3.2). In this case, the average neutron yield above 10 MeV from the Geant4 simulation should be assumed to have the

¹These were published online but are no longer tabulated on the LANSCE website. They are reproduced in Appendix A Table A.2 of this thesis

²Generally, this symbol stands for differential flux in the accelerated soft error rate testing, which means the time rate of total amount of particle per unit area per energy (for example, $\text{ncm}^{-2} \text{ s}^{-1} \text{ MeV}^{-1}$) [JEDEC, 2006]

same effect on neutron flux provided by LANSCE measurements.

$$I = \frac{N_p e}{t} \quad (3.2)$$

$$\Omega = \frac{A}{r^2}$$

Where N_p represents the number of protons, and e represents the electron charge (1.602×10^{-19} C). Ω represents the solid angle. A is the segment area inside the hemisphere. r represents flight path length (20 m).

The implied current I used for measurement could be worked out by using Equation (3.3).

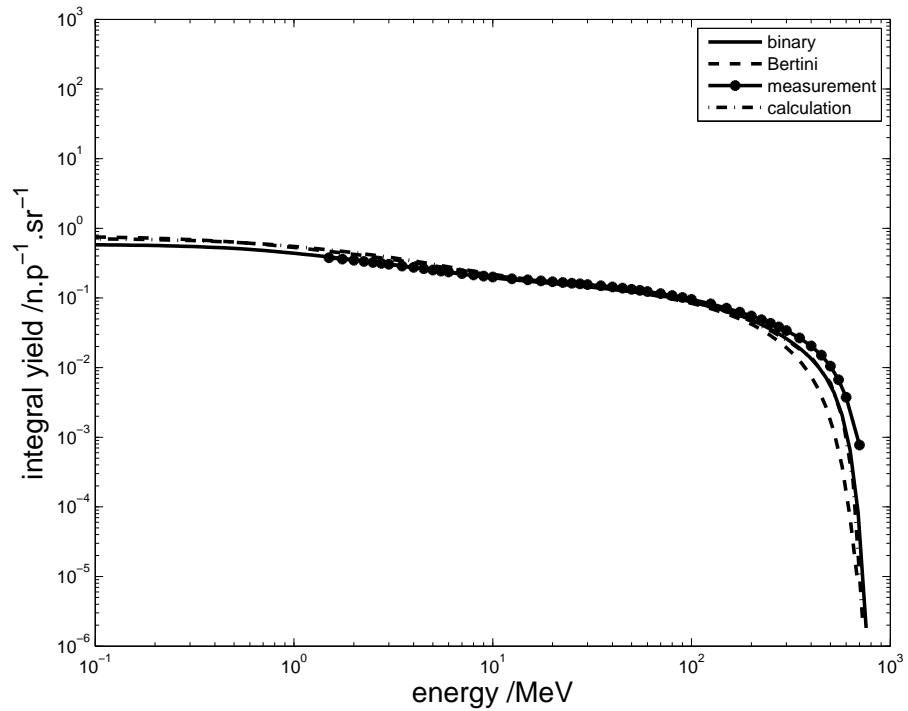
$$N = \frac{r^2 \times e}{I} \quad (3.3)$$

I stands for an average proton current to target of $1.44 \mu\text{A}$; allowing for interruptions to the beam this is consistent with the nominal proton current during the experiment ($1.8 \mu\text{A}$) [Platt et al., 2013].

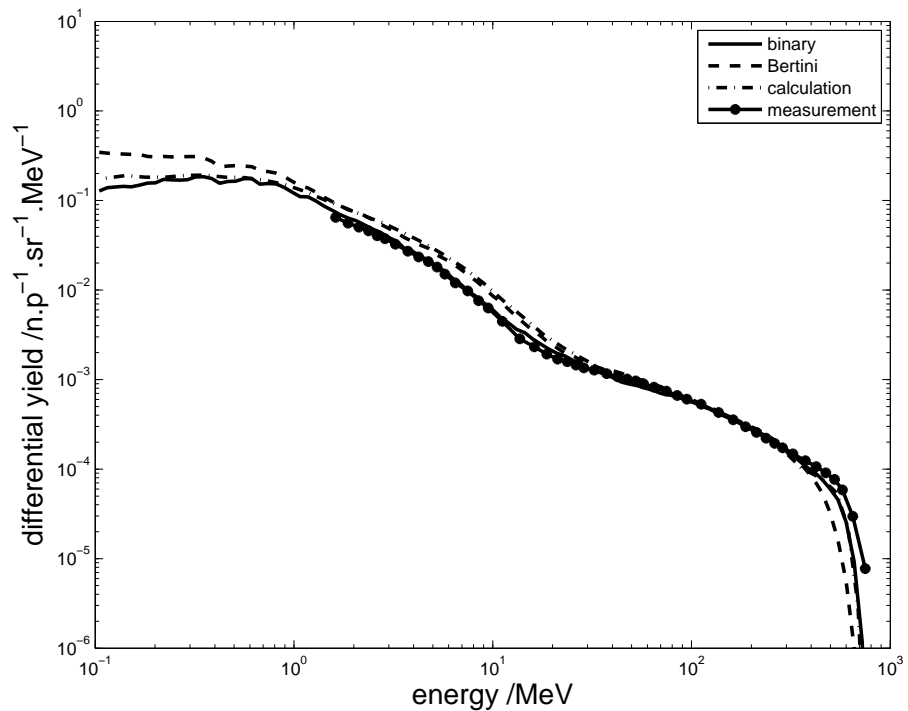
Comparison of the binary with the measurement one, they matched very well between 1 MeV and 100 MeV, as shown in Figure 3.3. And the binary is consistent with the calculation result with energies above 50 MeV and below 1 MeV. The Bertini result and calculation one is overlapped above 1 MeV until to 50 MeV. The neutron yield with energy above 100 MeV of the measurement curve is the highest among other curves.

Figure 3.4 shows neutron flux at 30° in the lethargy scale. This is given more details about neutron yield per steradian for each result, for example, the area under the spectra curve represent neutron flux from a certain energy to another energy.

Firstly, two peaks are shown in neutron energy spectra of measurement data. In the spallation reaction, these two peaks are called intra-nuclear cascade peak in higher energy and evaporation peak in lower energy. Intra-nuclear cascade peak is induced by spallation reaction of the tungsten target material, bombarded by 800 MeV proton beam. This results in emission of many secondaries, such as neutrons, pions, protons, alpha particles with high energies. And the evaporation peak is induced by deexcitation mechanism of the target nucleus (at high excited state) and fission. Both mechanisms are capable of producing



(a) Integral



(b) Differential

Fig. 3.3 Neutron yield at LANSCE WNR, ICE House (4FP30L). “calculation” represents Los Alamos calculation of WNR neutron flux at ICE House, see Table A.2 shown in Appendix A [LANSCE, nd]. “measurement” represents Los Alamos experimental measurement of neutron flux at ICE Hous in 2005, see Table A.1 shown in Appendix A [Platt, 2012].

a large amount of low (around 1 MeV) energy neutrons. Both binary and Bertini model have these two peaks, as well as the LANSCE calculation result. For the high energy peak which is located around 100 MeV, four curves are overlapped at $0.06 \text{ n p}^{-1} \text{ sr}^{-1}$. However, binary, Bertini, LANSCE calculation, and measurement results are shown different peak values at the low energy, which are $0.13 \text{ n p}^{-1} \text{ sr}^{-1}$, $0.17 \text{ n p}^{-1} \text{ sr}^{-1}$, $0.16 \text{ n p}^{-1} \text{ sr}^{-1}$, and $0.11 \text{ n p}^{-1} \text{ sr}^{-1}$. And each low peak is located in different energy bins, Bertini is more close to LANSCE calculation result, binary is more approach to measurement results. It is clear that binary results are consistent with measurement result with energy above 1 MeV in this lethargy scale than in log-log scale. It proves that binary cascade model is much more likely for LANSCE WNR neutron source. Although measurement result with energy below 1 MeV is missing, binary result still matches with calculation result very well with energy between 0.1 MeV to 1 MeV. However, both the Bertini results and LANSCE calculation results appear to overestimate the neutron yield in the low energy peak.

The uncertainty of WNR measurement data with neutron energy up to 20 MeV is around 5% [Wender et al., 1993]. The uncertainty of neutron yield with energy above 20 MeV is poorly known [Wender et al., 1993] because of fission cross sections of $^{238}\text{U}(n, f)$. Especially for neutrons with energy greater than 250 MeV, the neutron yield uncertainty is about 10% [Wender et al., 1993]. The average uncertainty in differential neutron yield is about 2.2% from binary and about 2.0% from bertini.

Figure 3.5 represents Geant4 simulated neutron yield spectrum in the lethargy scale depends on off-axis angle of the flight path with respect to the proton beam at LANSCE WNR Target4. Figure 3.5a and Figure 3.5b both reveal that neutron yield above 10 MeV increases with the decrease in off-axis angle and neutron yield below 10 MeV increases with the increase of deviation angle, see Table 3.3. This result is consistent with the Los Alamos calculation result, see Figure A.1 shown in Appendix A. Neutron yield below 10 MeV from the Bertini model is higher than that from the binary model. In addition, neutron yield above 10 MeV from the Bertini model is roughly the same as from the binary model, although for the binary model there is even no high energy peak at 90° off axis.

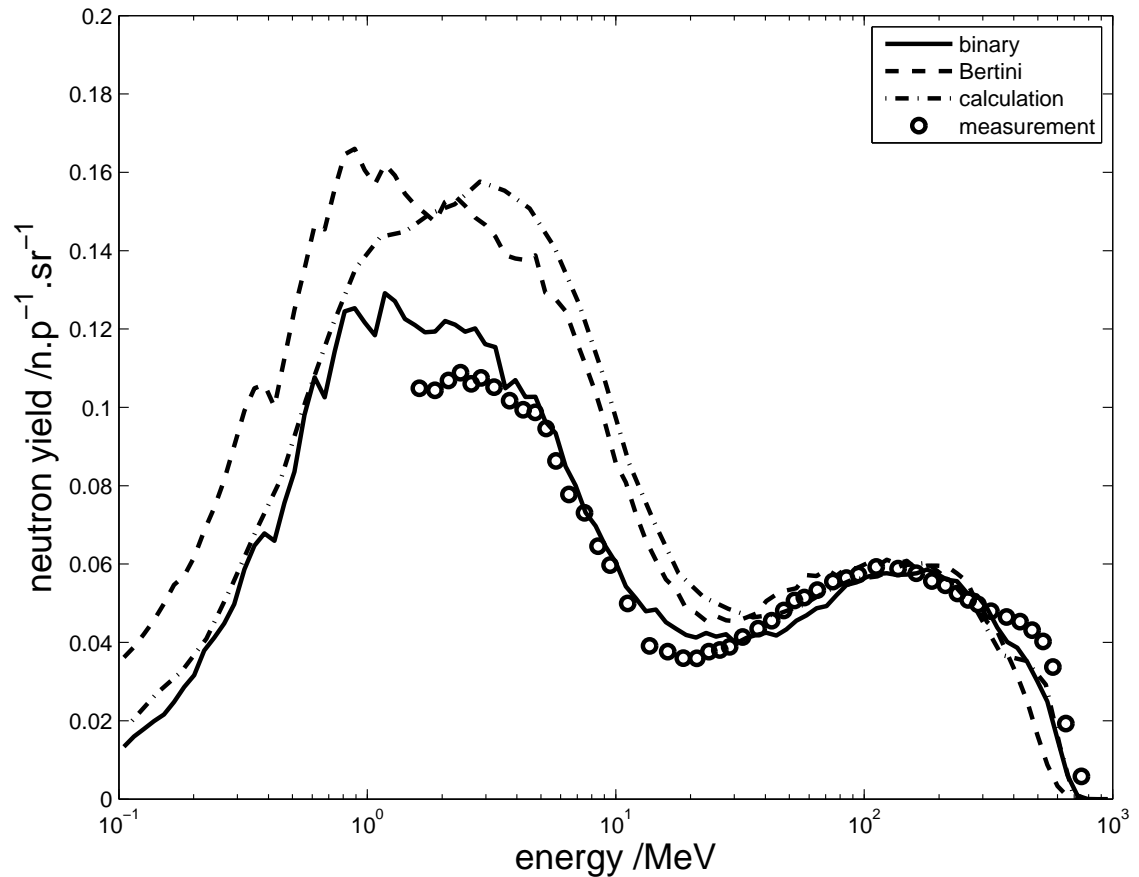
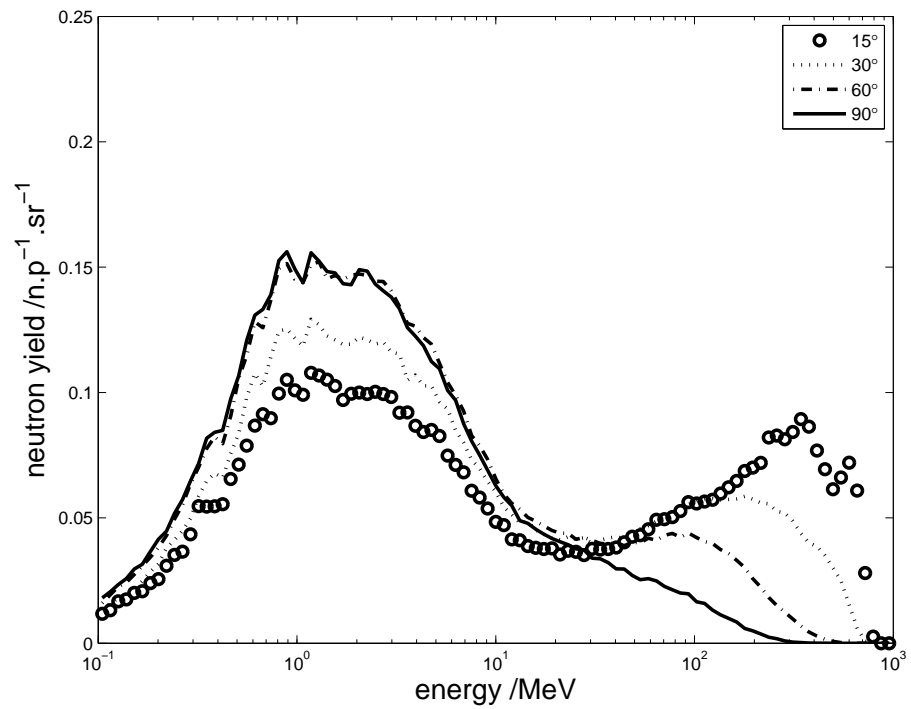
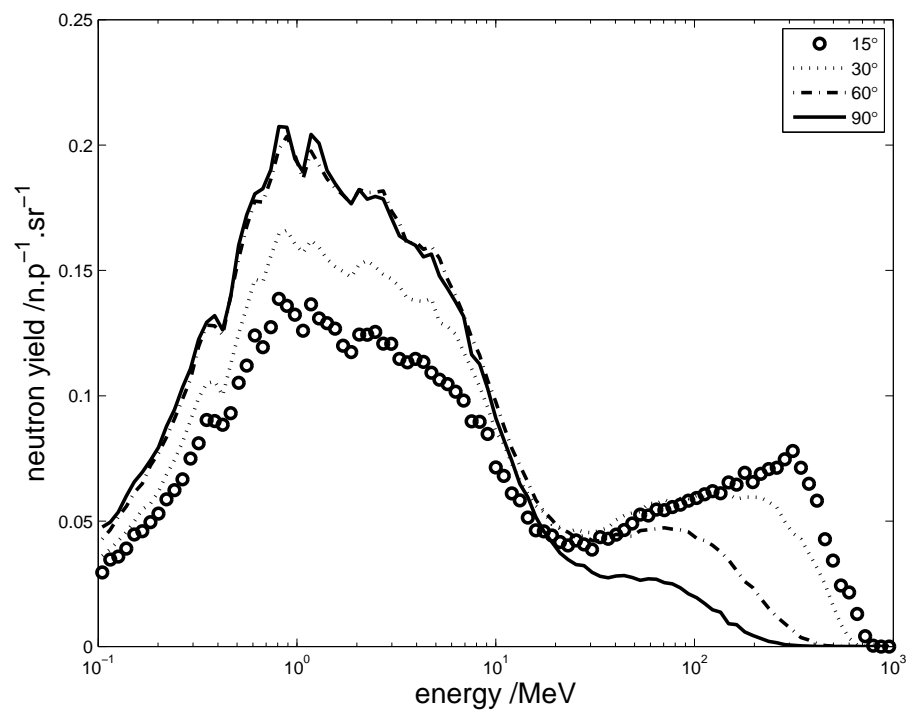


Fig. 3.4 Neutron yield spectrum in the lethargy scale at LANSCE WNR, ICE House (4FP30L) [LANSCE, nd; Platt, 2012]. Neutron field is calculated by Geant4 modelling with two intra-nuclear cascade models, one is binary (solid line), the other is Bertini (dashed line). The dash-dotted line represents Los Alamos calculation of WNR neutron flux at ICE House, which is 20 meters away from the tungsten target, see Table A.2 shown in Appendix A [LANSCE, nd]. The circle mark specifier represents Los Alamos experimental measurement of neutron flux at ICE Hous in 2005, see Table A.1 shown in Appendix A [Platt, 2012].



(a) Binary



(b) Bertini

Fig. 3.5 Neutron yield in lethargy scale at LANSCE

Table 3.3 Integral neutron yield above 10 MeV, below 10 MeV, and for all energies, with respect to off-axis angles

model	15° $\text{n p}^{-1} \text{sr}^{-1}$	30° $\text{n p}^{-1} \text{sr}^{-1}$	60° $\text{n p}^{-1} \text{sr}^{-1}$	90° $\text{n p}^{-1} \text{sr}^{-1}$
Bertini: above 10 MeV	0.223	0.208	0.147	0.093
binary: above 10 MeV	0.234	0.192	0.135	0.087
Bertini: below 10 MeV	0.451	0.544	0.650	0.655
binary: below 10 MeV	0.324	0.388	0.463	0.466
Bertini: total	0.674	0.752	0.797	0.748
binary: total	0.558	0.580	0.597	0.553

Table 3.4 Ratio comparison of projected area of the target to neutron flux at about 1 MeV with respect to the off-axis angles, the sequence was 90°, 60°, 30°, and 15°

Items	90°:60°	60°:30°	30°:15°
Projected area ratio	0.97	1.31	1.36
Flux ratio (Bertini)	1.01	1.19	1.21
Flux ratio (binary)	1.01	1.19	1.20

It is interesting to see that the neutron flux below 10 MeV with flight path angle 90° approaches to that at 60°. However, neutron flux below 10 MeV at 60° is much greater than that at 30°, as well as neutron flux comparison of 30° and 15°. The ratio of the flux at two angles (e.g. 90°:60°, 60°:30°, 30°:15°, and 15°:0°) at around 1 MeV is calculated for Bertini model and binary model, see Table 3.4. There is another item shown in Table 3.4, projected area ratio, which is used to find a relation between neutron flux and off-axis angle. The projected area of the target from the view of each off-axis angle is calculated, see Table A.4 shown in Appendix A. The neutron flux ratio is consistent with the projected area ratio, which means neutron flux below 10 MeV of each off-axis angle might depend upon projected area of the target from the view of that off-axis angle. The neutron yield above 10 MeV of each off-axis angle is not strongly influenced by projected area since high energy neutrons go straight through the target.

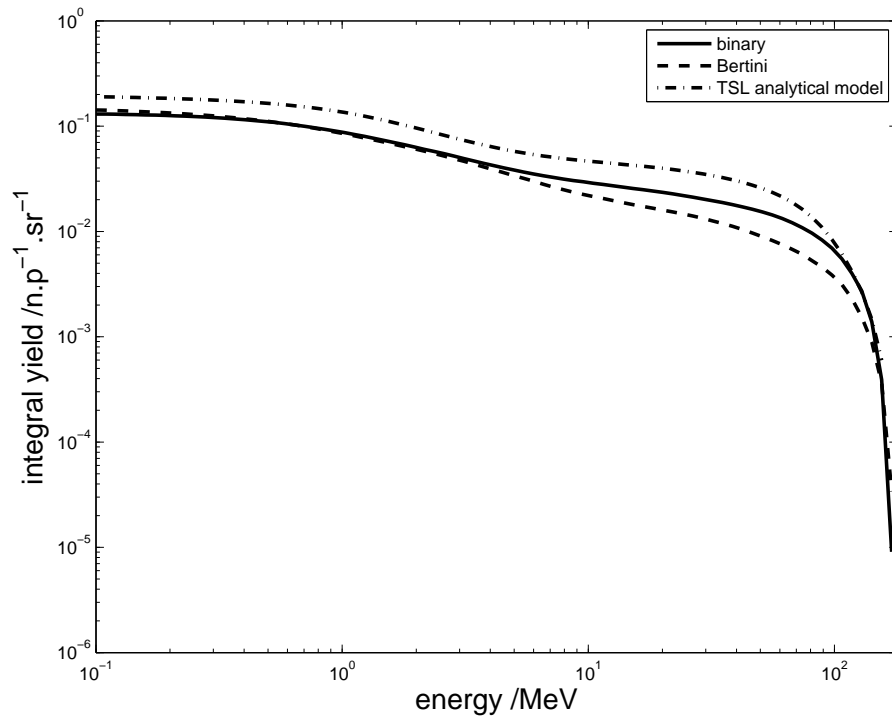
3.2.2 Neutron field calculations at TSL ANITA

The neutron field is observed at 2.5 m from the tungsten target, on-axis with respect to the proton beam for TSL ANITA. The physics list for preliminary SNS model at ANITA is the same as used in preliminary SNS model at WNR. The following TSL analytical model is using MCNPX code with bertini intra-nuclear cascade model and evaporation model for ANITA neutron field. This TSL analytical model data is close to experiment data, which is the combination result of Monte Carlo calculation and parametrized results [Prokofiev et al., 2009].

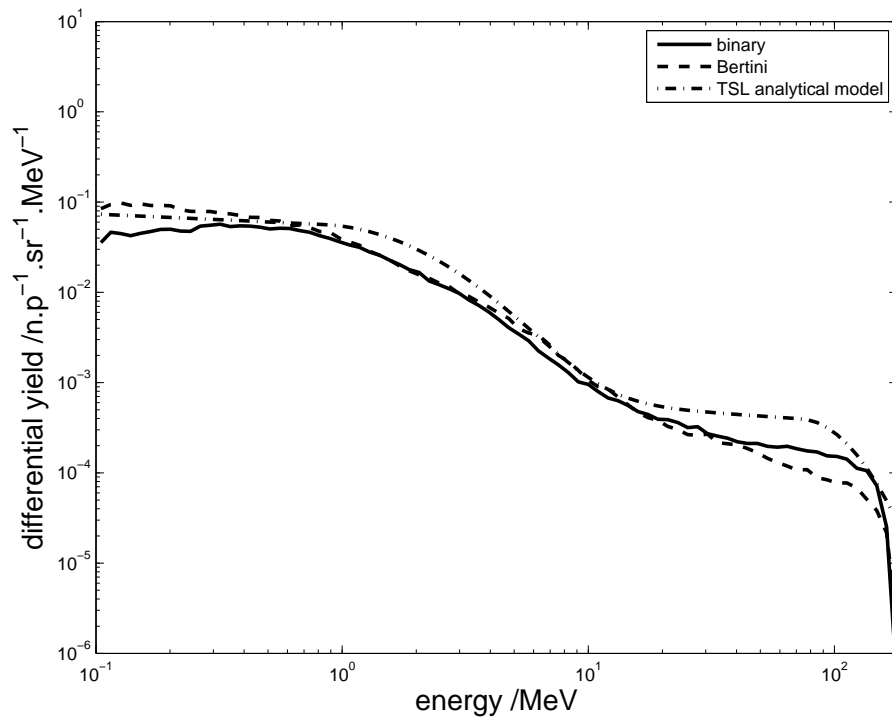
Figure 3.6a shows the integral neutron yield, and Figure 3.6b shows the differential neutron yield at TSL ANITA, the neutron yield above 1 MeV from the binary and Bertini model both are lower than ANITA analytical data given in [Prokofiev et al., 2009] with proton current 200 nA but the shape is similar. The ANITA analytical data can be converted from neutron flux in $\text{ncm}^{-2}\text{s}^{-1}$ to neutron yield in $\text{np}^{-1}\text{sr}^{-1}$ by using Equation (3.3). It is obvious that binary model data is more closer than Bertini model data to analytical model curve. The neutron yield with energy greater than 10 MeV is $0.029\text{np}^{-1}\text{sr}^{-1}$ for binary model, which is about 63% of the analytical model result ($9.3 \times 10^5\text{ncm}^{-2}\text{s}^{-1}$ at $2 \times 10^{-7}\text{A}$, $0.047\text{np}^{-1}\text{sr}^{-1}$).

The average uncertainty of differential neutron yield calculation of preliminary SNS at ANITA facility is around 4.5% according to binary cascade model and around 4.4% according to bertini cascade model.

Figure 3.7 shows the comparison of normalised neutron yield in lethargy scale from binary and Bertini model. These three neutron spectra curves are normalized to 1 above 10MeV, which used to discuss the shapes of neutron yield. As above, the shape of binary data has a better agreement with analytical data than the Bertini model does. The normalized neutron yield below 1 MeV of both the binary and Bertini seem to be greater than neutron yield from analytical data shown in Figure 3.7. A comparison of Bertini data with TSL analytical data shows that a less yield given by Bertini modelling in the intra-nuclear cascade peak.



(a) Integral



(b) Differential

Fig. 3.6 Neutron yield spectrum at ANITA facility, in TSL. Data marked binary represents Geant4 binary intra-nuclear cascade model used in preliminary SNS at ANITA. Bertini represents bertini cascade model used in preliminary SNS at ANITA. Data marked as TSL analytical model refers to the analytical calculation results from TSL, which is published in [Prokofiev et al., 2009]

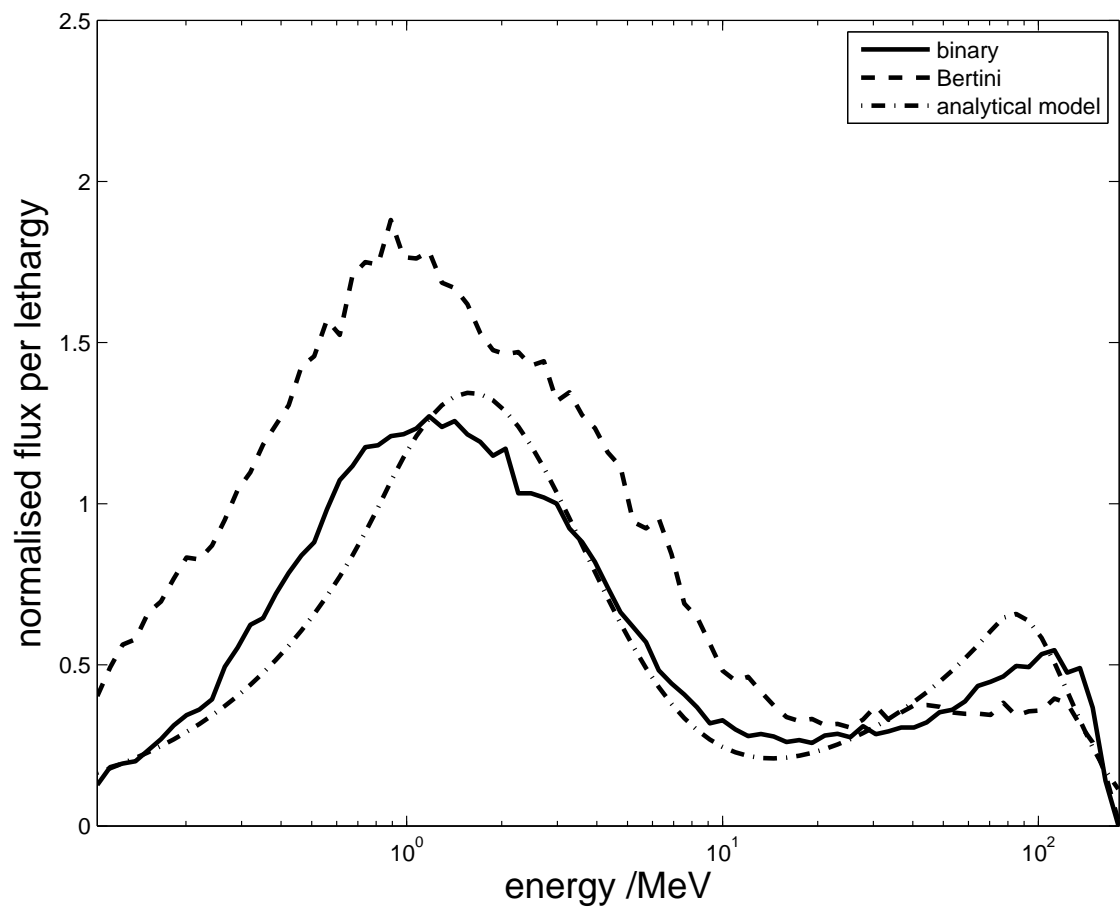


Fig. 3.7 Normalised neutron yield in the lethargy scale at TSL ANITA. Normalization is to 1 above 10 MeV

Table 3.5 Ratios of evaporation peak to intra-nuclear cascade peak

Name	binary	Bertini	TSL analytical model
ratio	2.340	5.467	2.108

The ratios of evaporation peak value to intra-nuclear cascade peak value of each curve are shown in Table 3.5. Here the binary and Bertini model shows neutron field at 2.5 m from the tungsten target induced by a naked spallation neutron source. This ANITA neutron source modelling is much simpler than TSL ANITA simulation results shown in paper [Prokofiev et al., 2009]. In TSL simulation, collimator and shielding were considered in modelling so that it might be the reason why binary and Bertini results of absolute neutron yield are lower than TSL analytical results. In next chapter, more complex modelling of ANITA facility will be represented to illustrate the collimator and shielding effect on neutron yield at the SUP position.

3.3 Gamma field calculations

Gamma field was calculated during the same simulation with neutron field calculation application. In this section, the prediction of gamma spectra will be shown for both LASNCE WNR and TSL ANITA, as well as gamma dose rate. The term gamma absorbed dose, D_g , refers to the radiant energy deposited in a unit mass. Thus, gamma absorbed dose rate, \dot{D}_g , is defined as the radiant energy deposited in a unit mass in period time, its unit : Gys^{-1} . The calculation of gamma dose rate according to Equation (3.4) [Kwon et al., 1980].

$$\dot{H} = \int_0^{\infty} DF_g(E)\phi_g(E) dE \approx \sum_{n=0}^{\infty} DF_g(E)\phi_g(E)\Delta E \quad (3.4)$$

Where \dot{H} refers to rontgen equivalent dose(rem h^{-1}), which is the enegy deposited per unit mass in human tissue or organ (equivalent biological damage done to human tissue). The difference between equivalent dose and absorbed dose is one object is matter and the other object is biology. DF_g refers to gamma ray flux-to-dose-rate conversion factor

($\text{rem h}^{-1}/\gamma\text{cm}^{-2}\text{s}^{-1}$) [Kwon et al., 1980]. And gamma flux ($\gamma\text{cm}^{-2}\text{s}^{-1}$) is represented by ϕ_g , and energy only from 0.01 MeV up to 15.0 MeV.

The radiation weighting factor (W_R), which is like a bridge used for conversion of equivalent dose and absorbed dose. Here the γ weighting factor (Gray to Sievert) is 1 so that \dot{H} can be converted to absorbed dose D .

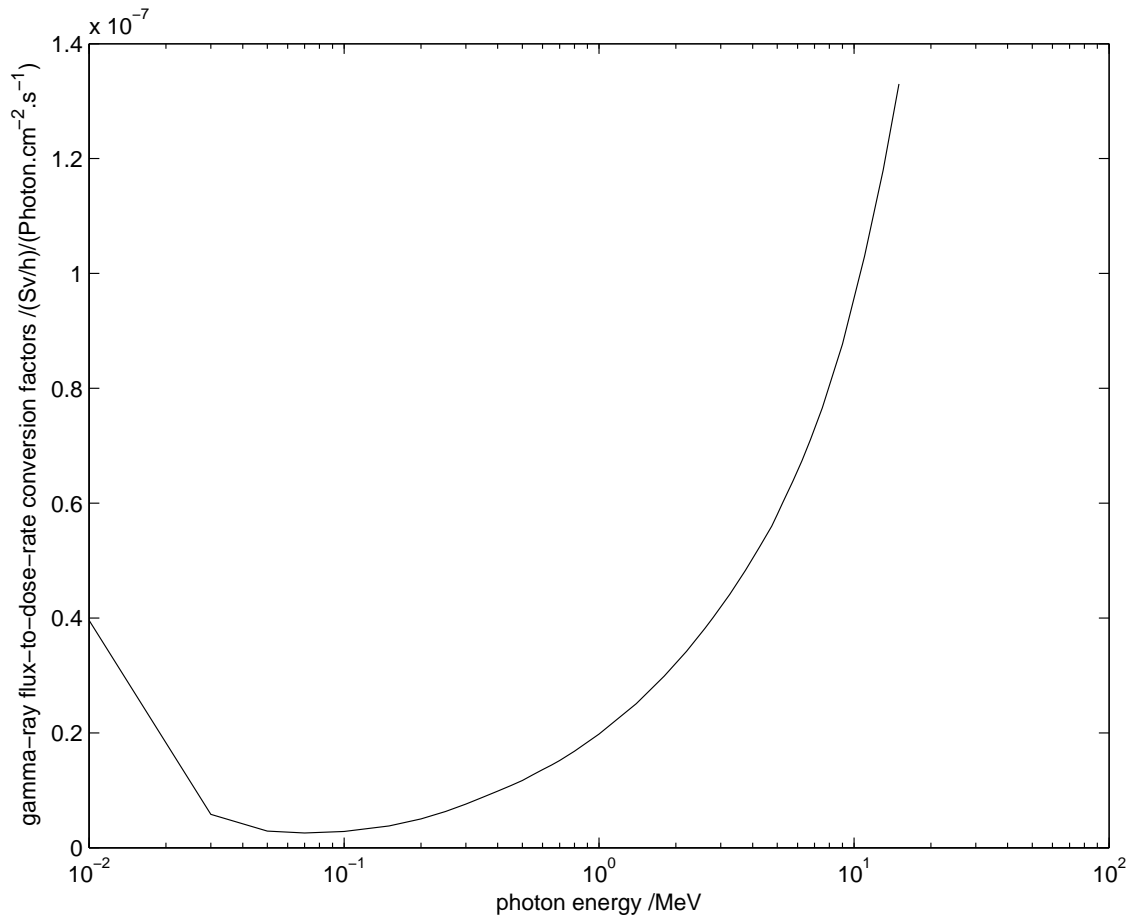


Fig. 3.8 gamma ray flux to dose rate conversion factor [Kwon et al., 1980]

Figure 3.8 shows a relationship of photon energy against gamma-ray-dose-rate conversion factors [Kwon et al., 1980], the conversion factor value is known for each photon energy. Differential gamma fluence rate is calculated with using same energy bin shown in Figure 3.8. The calculation of gamma dose rate is done by multiplying differential gamma flux with gamma-ray-dose-rate conversion factors.

3.3.1 Gamma field calculations at LANSCE WNR, ICE House (4FP30L)

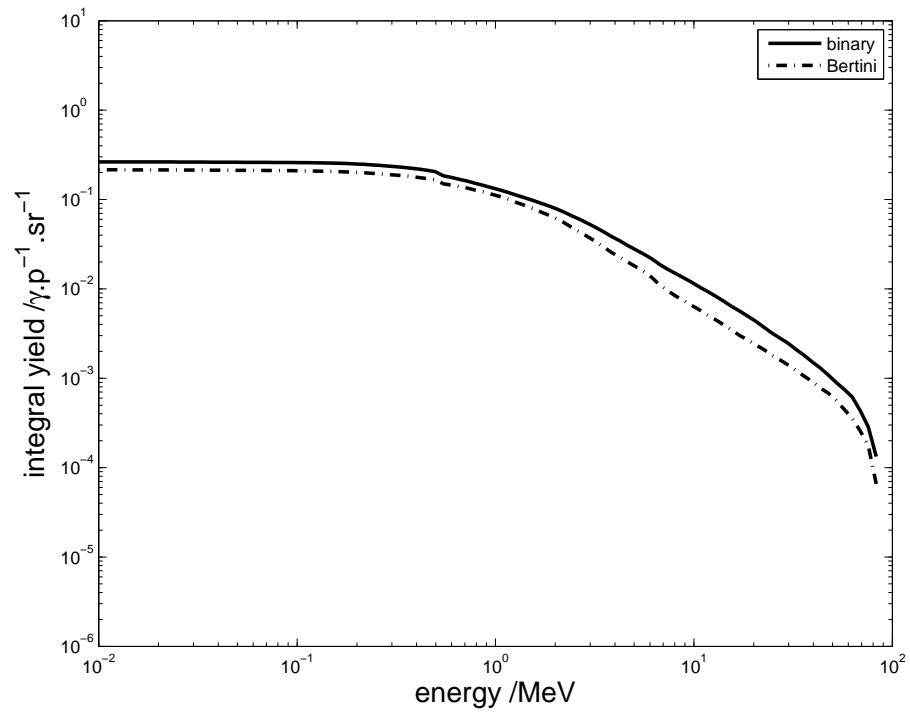
Figure 3.9 shows integral and differential photon yield spectra at LANSCE WNR, ICE House (4FP30L). The photon yield spectrum is a continuous spectrum between 0.1 MeV and 100 MeV, and is a flat spectrum below 0.1 MeV. The only peak appears at around 0.5 MeV in both binary and Bertini curve shown in Figure 3.9b, as a result of electron positron annihilation at 0.511 MeV. The photon yield above 0.5 MeV reduces with the energy increasing by a power law with exponent greater than 2.

The dose rate at LANSCE WNR of flight path angle of 15°, 30°, 60°, and 90° could be calculated by reference to [Kwon et al., 1980] with using Equation (3.4) and information shown in Figure 3.8, which are 15.4 mSvh⁻¹(1.54 rem h⁻¹), 16.8 mSvh⁻¹(1.68 rem h⁻¹), 21.6 mSvh⁻¹(2.16 rem h⁻¹), and 21.2 mSvh⁻¹ (2.12 rem h⁻¹) with operating current of 1.44×10^{-6} A at WNR, LANSCE. The gamma dose rate increases with the increase of deviation angle, that is by coincidence a relation between neutron yield with energy less than 10 MeV and off-axis angle.

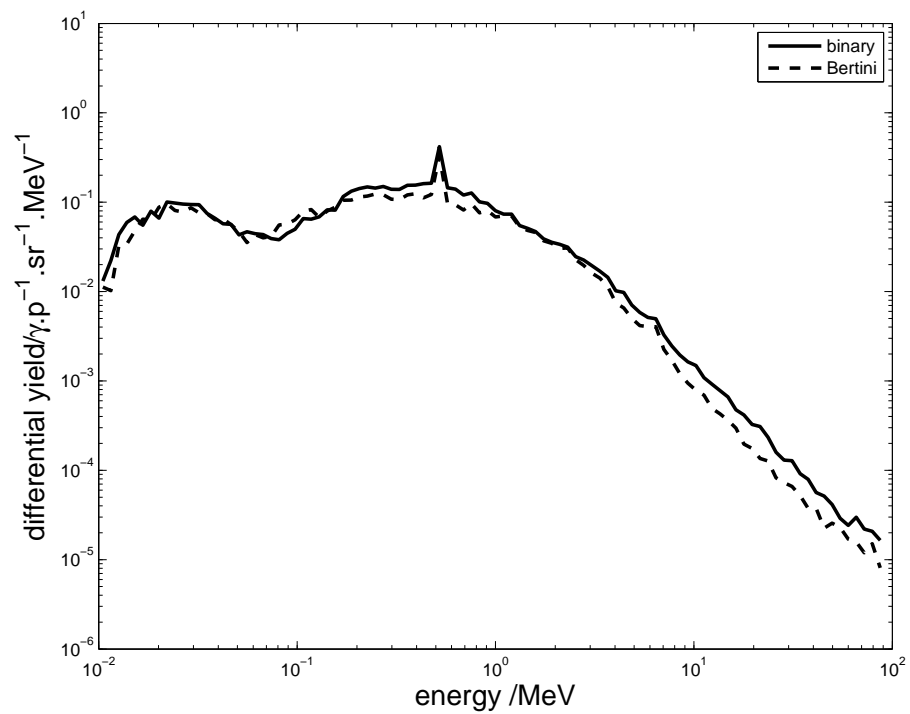
The average uncertainty of differential gamma yield calculation of preliminary SNS at WNR facility is around 6.3% according to binary cascade model and around 7.5% according to bertini cascade model. The uncertainty of gamma yield is higher than that of neutron yield because the number of gamma detected is smaller than neutrons.

3.3.2 Gamma field calculations at TSL ANITA

As seen in the results in Section 3.3.1, a peak at about 0.5 MeV appears again in ANITA case but not so clear as shown in Figure 3.9b. The photon yield below 0.1 MeV is flat which means few amount of photon with energy below 0.1 MeV, see Figure 3.10b. Furthermore, the photon yield spectrum is a continuous spectrum between 0.1 MeV and 10 MeV. The peaks appear below 0.1 MeV are attributed to statistical noise. The integral yields between 0.1 MeV and 10 MeV are approximately 0.26 $\gamma p^{-1} sr^{-1}$ and 0.046 $\gamma p^{-1} sr^{-1}$ at LANSCE ICE House and TSL ANITA in each case.

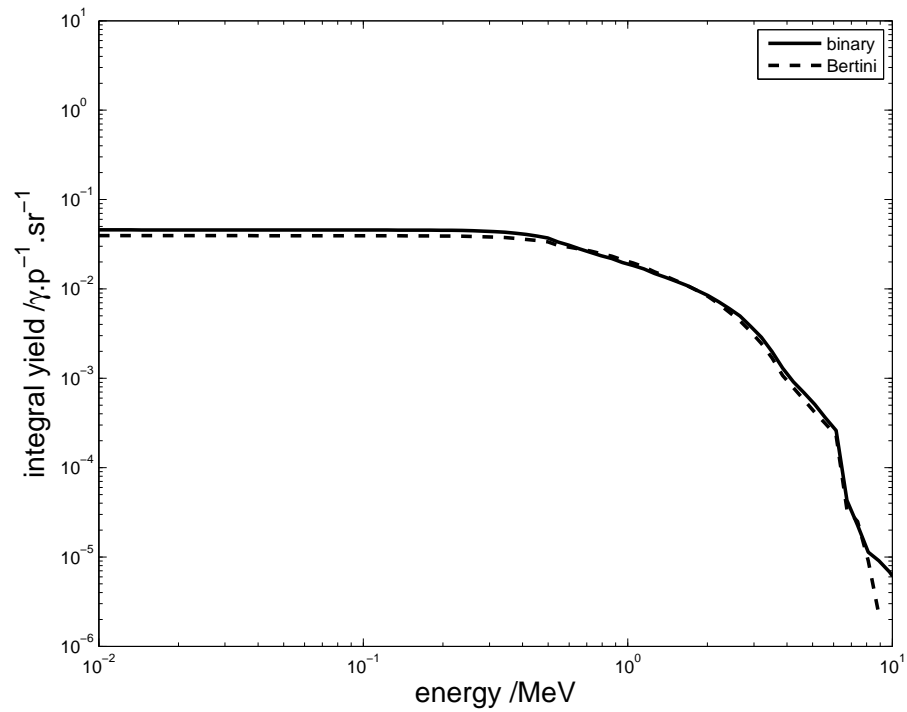


(a) Integral

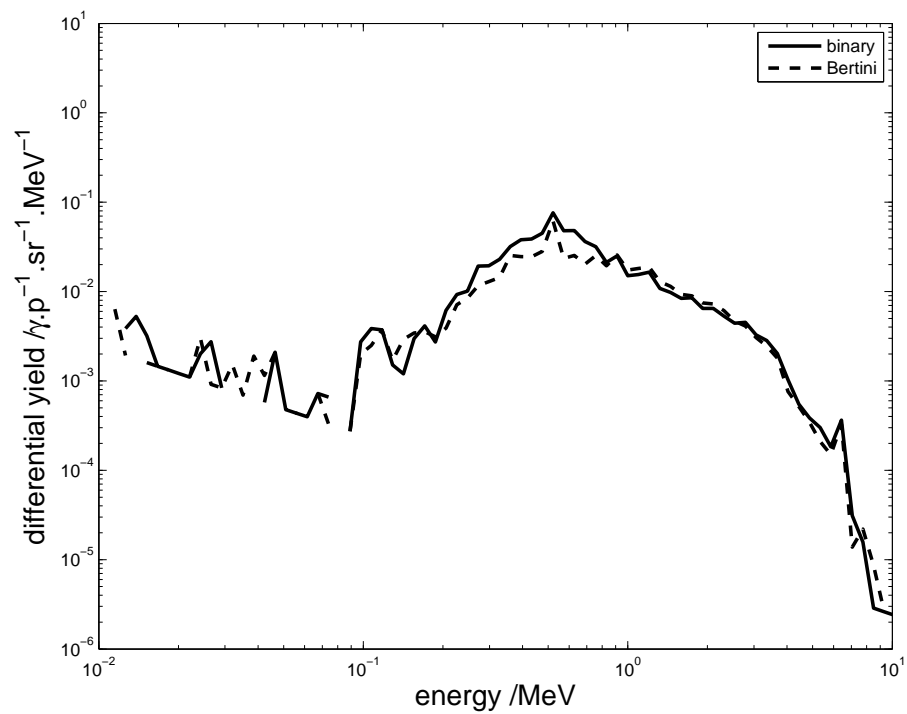


(b) Differential

Fig. 3.9 Photon yield spectrum at LANSCE WNR, ICE House (4FP30L)



(a) Integral



(b) Differential

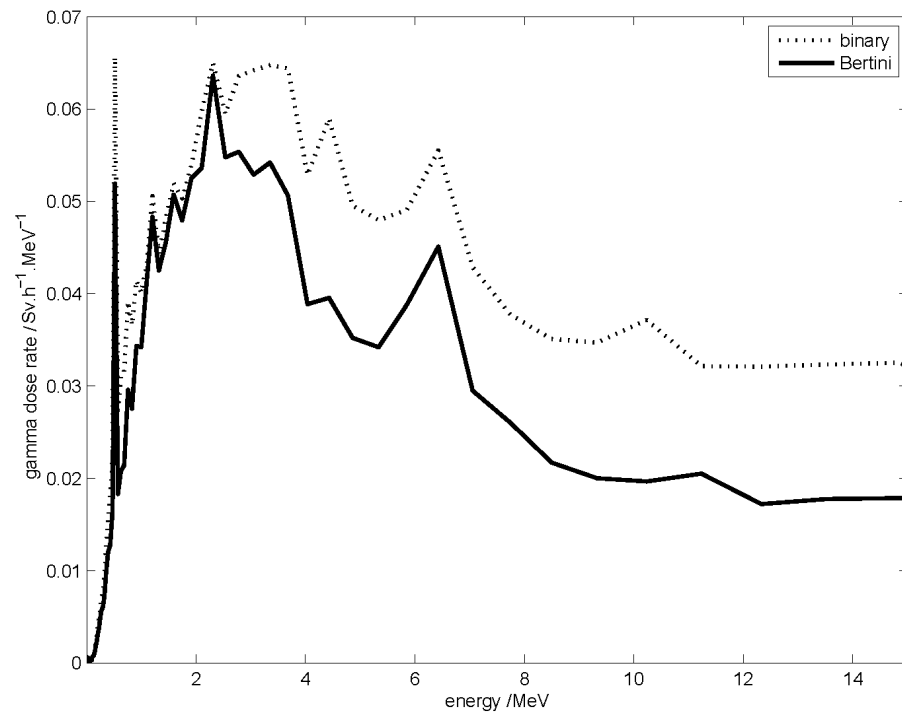
Fig. 3.10 Photon yield spectra at TSL ANITA

Gamma dose rate at 2.5 m away from the tungsten target was calculated by reference to [Kwon et al., 1980] with using standard operating current during the experiment (200 nA) [Prokofiev et al., 2009]. To calculate gamma dose rate by using Equation (3.4), which is 18.0 mSvh^{-1} (1.80 remh^{-1}) for bertini model and 16.8 mSvh^{-1} (1.68 remh^{-1}) for binary model.

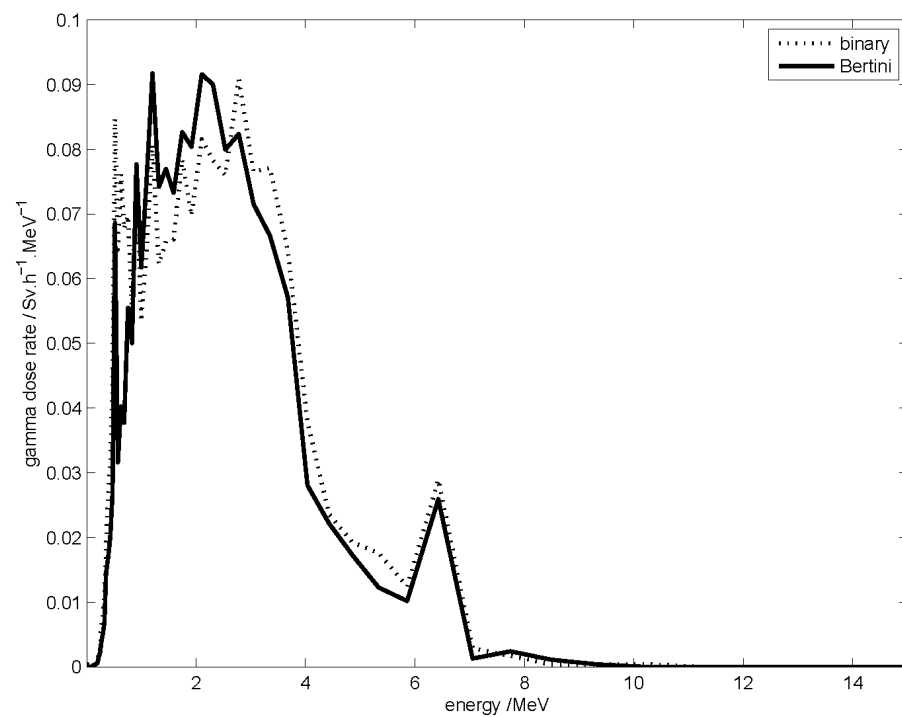
Figure 3.11 shows predicted absorbed dose versus energy at LANSCE ICE House and TSL ANITA. Two models applied in calculation of gamma dose rate for preliminary SNS at ANITA facility and WNR facility. A comparison of dose rate at ANITA and WNR (assuming both with binary cascade model), a few common energy peaks appeared in both cases, which are at 0.571 MeV, 1.238 MeV, 2.381 MeV, and 6.571 MeV. It proves that a few same physical interactions about gamma production occurring during spallation neutron source. These specific energy peaks correspond to the specified interactions. The gamma dose rate at LANSCE is dominated by continua from 0.01 MeV to 14.5 MeV or even higher. However, gamma dose rate at ANITA is dominated by continua between 0.01 MeV and about 10 MeV, which is shorter than LANSCE. The high dose rates at TSL ANITA are concentrate on the photon energy between 0.1 MeV and 4 MeV. A comparison of binary and bertini model, gamma dose rate spectrum are similar at preliminary SNS model at ANITA facility. However, gamma dose rate spectrum are different at preliminary SNS model at WNR facility. For gamma dose rate calculation, it illustrates that results from binary and from bertini cascade model are similar with incident particle energy less than 180 MeV, but different with incident particle energy greater than 180 MeV.

3.4 Summary

This chapter shows preliminary simulation of two naked spallation neutron sources at LANSCE WNR and TSL ANITA. The spallation neutron source modelling is validated by comparing with measurements and independent calculation data. Geant4 modelling results from the binary model are more closely to measurement results from the LANSCE ICE House and TSL ANITA in each case compared to results from the Bertini model.



(a) LANSCE WNR



(b) TSL ANITA

Fig. 3.11 Prediction of dose rate versus energy at the WNR ICE House and TSL ANITA

Binary model gives a good representation of neutron spectra obtained from LANSCE measurements, but absolute neutron yield is less than TSL analytical results. It might be influenced by incomplete geometry construction in the simulation. Chapter 4 will present ANITA neutron source modelling using the Geant4 *QGSP_BIC_HP* physics list with attaching more geometry components. It is the first time to calculate gamma spectra at spallation neutron source used for accelerated SEE testing. A continuum gamma spectrum between 0.01 MeV and 100 MeV at LANSCE with a peak at 0.5 MeV is predicted, as well as ANITA (between 0.01 MeV and 10 MeV).

Chapter 4

Detailed calculation of neutron and gamma fields in the ANITA facility at TSL

Chapter 3 introduced simulation of spallation neutron sources at LANSCE and TSL used for accelerated SEE testings, and Geant4 modelling results were validated by experimental and calculation data where these are available. Chapter 4 will show modelling of the ANITA facility using Geant4 toolkit and discuss the characterization of the neutron and gamma ray fields (yield, fluence rate, energy spectra, and spatial distribution) at the Close User Position (CUP) and the Standard User Position (SUP) of the ANITA.

This chapter firstly shows geometry construction of the ANITA facility modelling. Then the calculation and analysis of neutron fields at the CUP and the SUP will be reported in 4.2. In 2014, Prokofiev et al. published a paper about neutron field at the ANITA facility and showed experimental data of neutron field at the CUP and the CUP-TOF position [Prokofiev et al., 2014]. The comparisons about spectral neutron fluence (for different collimator aperture sizes), time of flight spectra, and neutron beam profiles between Prokofiev et al. work [Prokofiev et al., 2014] and Geant4 simulation results are shown in Section 4.2. The SUP area has been chosen to measure and analyze neutron

fields [Prokofiev et al., 2009], just like the CUP. The final section in Chapter 4 will present gamma field characterizations at the CUP and the SUP.

4.1 Geant4 modelling of the ANITA facility

This paragraph aims to explain that all sources used in this simulation work are from unpublished work of ANITA facility construction provided by Prokofiev [Prokofiev, 2013]. Additionally, two papers introduce irradiation positions (the CUP and the SUP) at the ANITA neutron facility at TSL [Prokofiev et al., 2009, 2014]. Focusing on a spallation neutron source produced at the ANITA facility for accelerated soft error rate testing, this work introduces modelling of the ANITA facility with using Geant4 toolkit to study neutron and gamma fields at the CUP and the SUP.

In Figure 4.1, the real ANITA facility shows that the bending magnet, shielding area and target region are in a concrete cave. The collimator is just embedded in the concrete wall. Besides the neutron beam produced by the ANITA facility, TSL also provides a Quasi-Monoenergetic neutron (QMN) beam from the lithium target. Magnetic pole is used for QMN source to remove residual protons. Compared with the real ANITA facility, there is no concrete wall, lithium target, TV camera or vacuum pipe in the simulated ANITA facility. The main five parts of the ANITA facility are modelled in the simulation work and introduced in the following section.

Simulation is based on the real ANITA facility at the TSL and geometry construction is divided into five parts in simulation work: Part I: Bending magnet, Part II: Shielding components, Part III: Target region, Part IV: Collimator, and Part V: Detection system, see Figure 4.2. The modelling simplifies geometry of the real ANITA facility and reduces time consuming in high performance computer execution.

Figure 4.3 shows a close up view of the target region. Dark red, yellow, and blue represent tungsten, cooling water, and stainless steel material, respectively. The solid target structure is made of a cylinder of tungsten with 2.4 cm in length, whose side surfaces were surrounded by cooling water tubes embedded in stainless steel to reduce

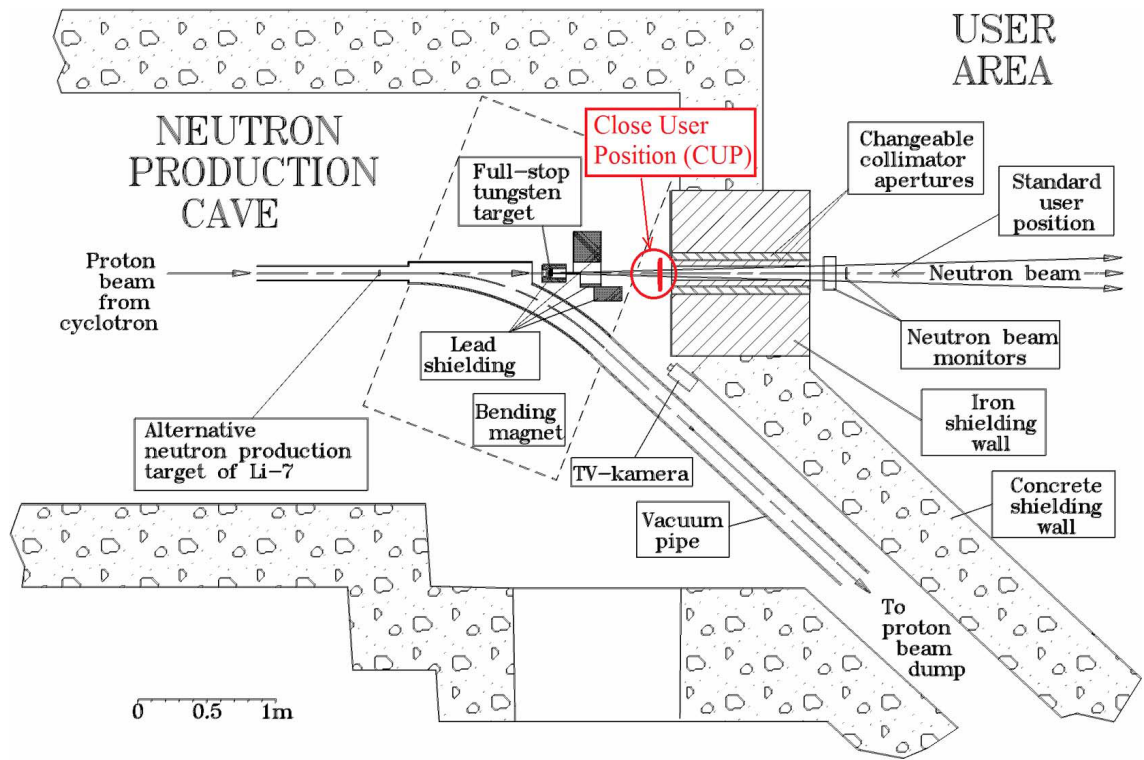


Fig. 4.1 Real ANITA and QMN facilities overview seen from above [Prokofiev et al., 2014]

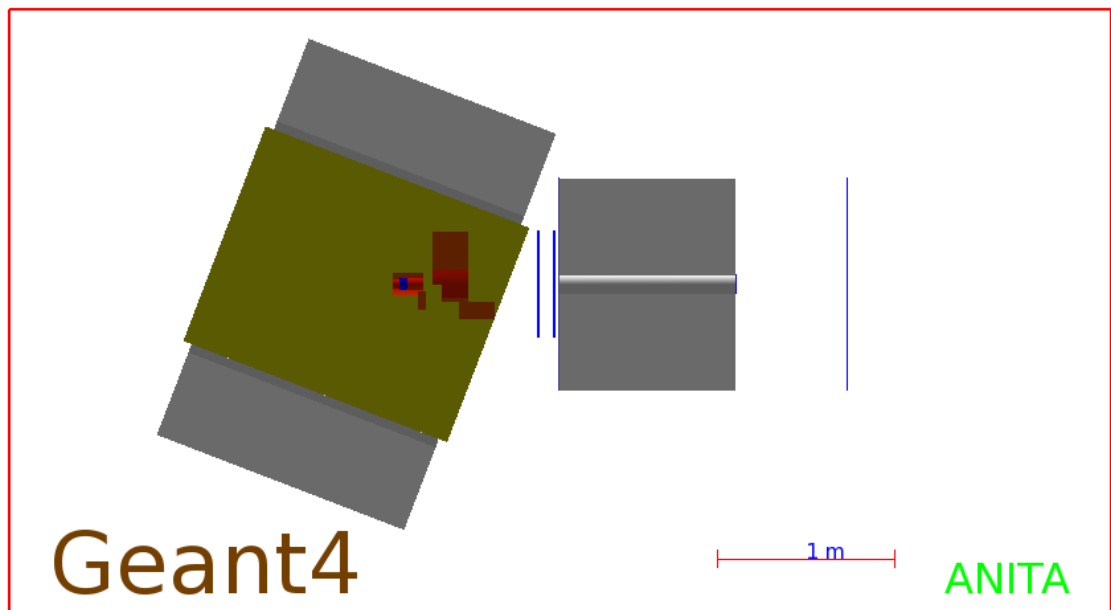


Fig. 4.2 Simulated ANITA facility overview seen from above (yellow: bending magnet ; red: shielding components; blue: target cooling jacket (enclosing the target); grey: collimator; blue: detection system)

high temperature when running experiments in the lab. In addition, the target is surrounded by a secondary outer layer stainless steel and lead shielding. A second lead shielding object is placed further away from the target, between the first shielding object and the collimator. Figure 4.4 takes a downstream view of the secondary shielding. Then the detection system is shown in Figure 4.5, which consists of 5 simulated detectors which are located at different positions. Figure 4.5 shows the whole ANITA facility from the side, the collimator is in grey on the right side of the Figure 4.5, and detectors are shown in blue. The detection system detects all neutrons and photons passing through the detectors at the CUP, CUP-TOF¹, FF, TE and SUP. The details of detectors are shown in the Table 4.1. All simulated detectors are very thin and with a large cross sectional area, except the TE detector. The radius of the TE detector matches the aperture size of the collimator, which varies from 3 cm diameter to 30 cm diameter.

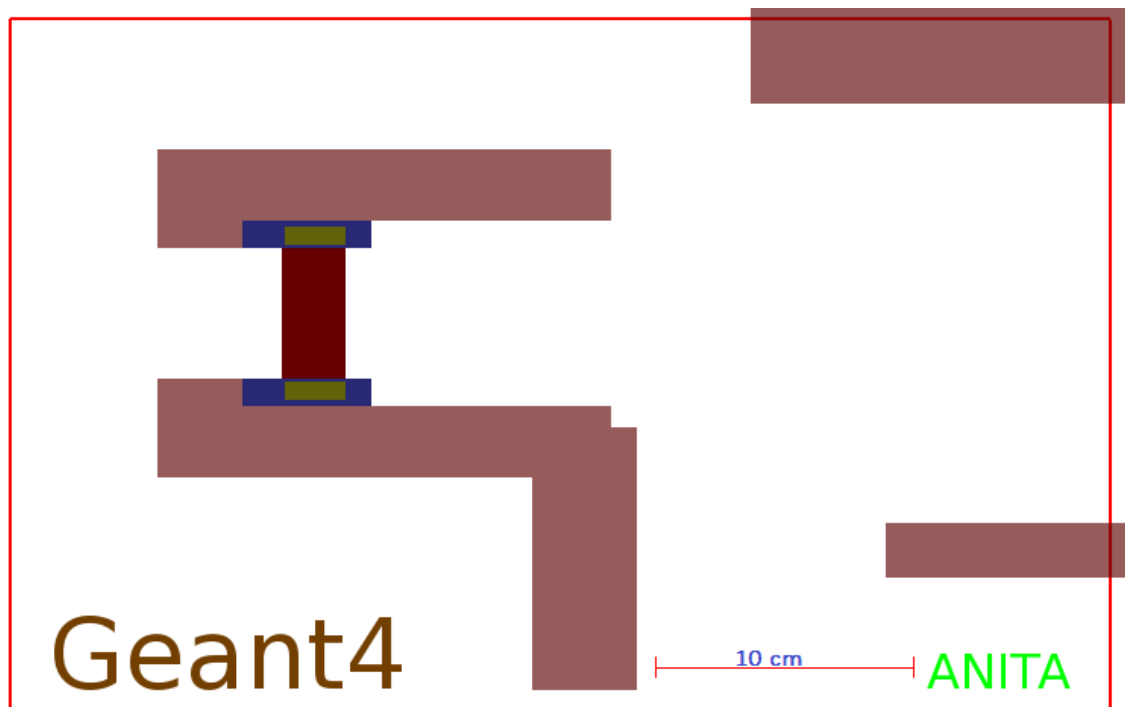


Fig. 4.3 Simulated ANITA facility close up view seen of target region from above (dark red: tungsten target; yellow: cooling water; blue: stainless steel; red: lead shielding)

¹CUP-TOF is the position of placing a thin film breakdown counters (TFBC). In accelerated SER testing at TSL, TFBC mounted on Trolley sled (used for mounting devices under testing) which is located at the distance of 84 cm downstream of the W target; CUP is located 9 cm in front of CUP-TOF position

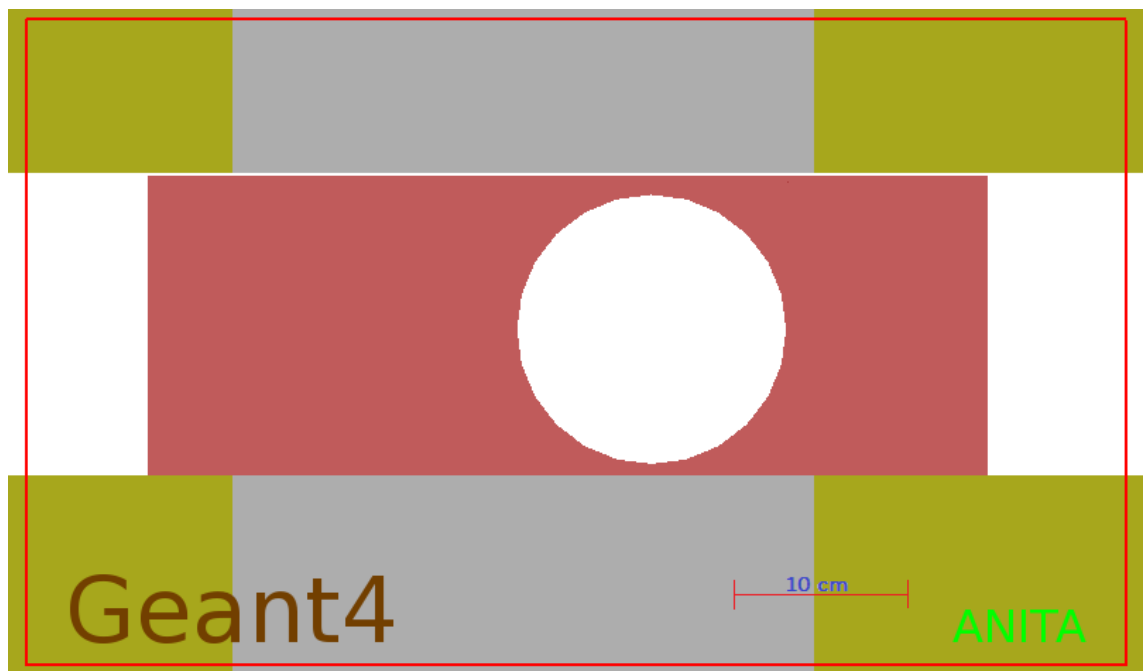


Fig. 4.4 Simulated ANITA facility looking downstream from the target area (grey: bending magnet; yellow: copper coil; red: lead shielding)

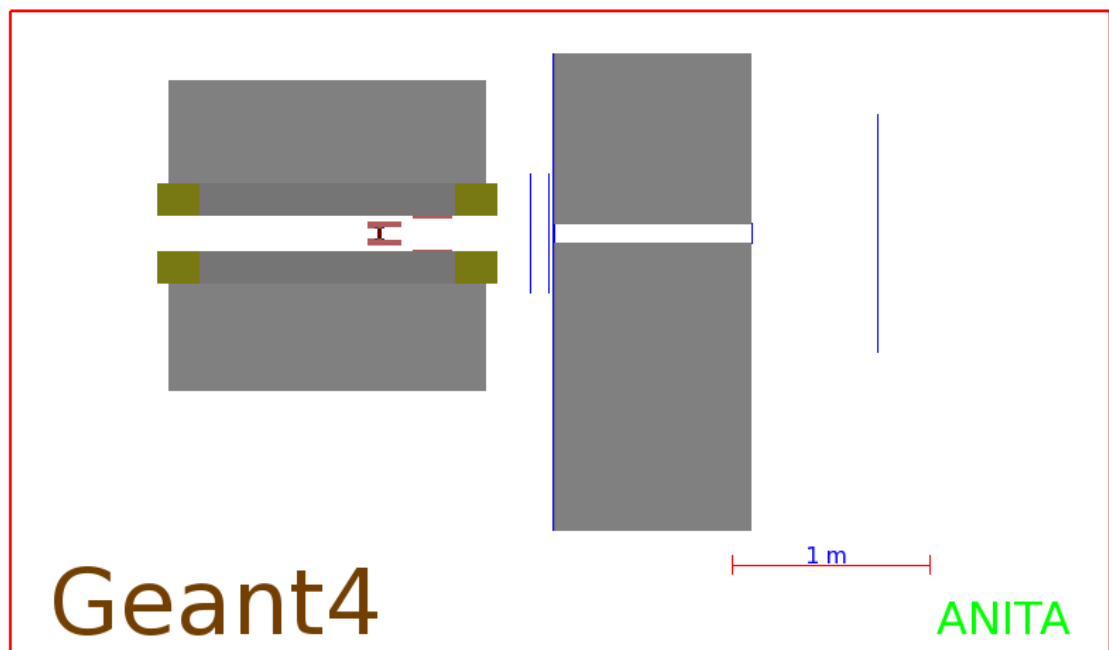


Fig. 4.5 Simulated ANITA facility overview seen from the side

Table 4.1 Detection systems

Detector name	Size /cm	Location from Target /cm	Ref
CUP	60 60 0.1	75	[Prokofiev et al., 2014]
CUP-TOF	60 60 0.1	84	[Prokofiev et al., 2014]
FF	120 240 0.1	86.6	
TE	aperture size	186.7	
SUP	120 120 0.1	250	[Prokofiev et al., 2009]

In addition, the iron collimator, shown in grey in Figure 4.5, is 1 m thickness with a changeable aperture size in diameter such as 3 cm, 10.2 cm and 30 cm. Section 4.2 will show the differences of neutron and gamma fields among these three collimators. The bending magnet is made of iron, shown in grey, which is the same material used in the collimator. The copper coils shown in yellow, winding around the middle section of the magnetic pole, see Figure 4.6. It is obvious that the bending magnet is not symmetrical looking upstream towards the target station.

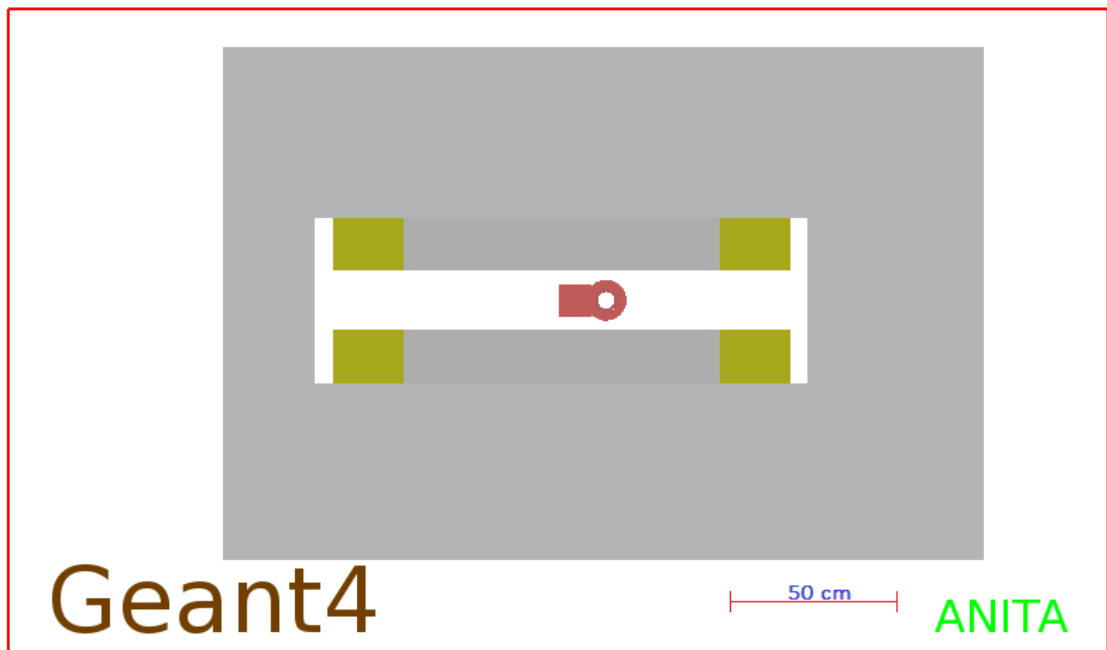


Fig. 4.6 Simulated ANITA facility looking upstream towards the target area with the target remove

In this simulation work, 110 million protons with 180 MeV were tracked and stopped in the tungsten target¹. Neutrons and photons were detected by the 5 simulated detectors. Three of them are placed at CUP, CUP-TOF, and SUP, and two of them are placed at FF and TE, see Table 4.1 (Data from FF and TE are not used in this Chapter). The properties such as time of flight (arrival in the detector from protons arrival at the target), positions in Cartesian coordinate system, kinetic energy and momentum of each particle would be recorded.

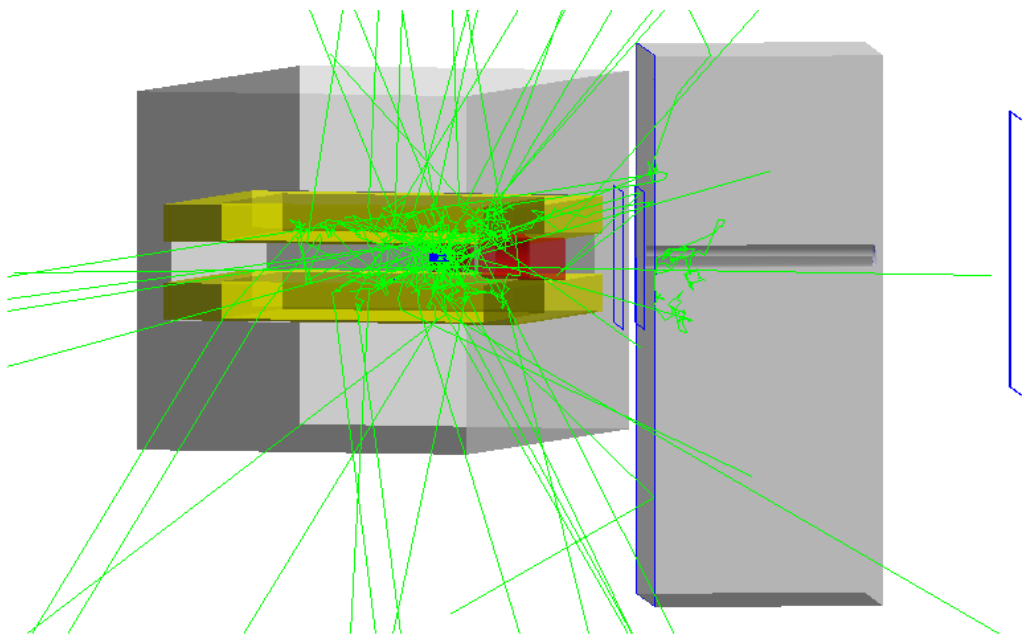


Fig. 4.7 Geant4 modelling of a neutron beam with atmospheric like spectrum at TSL ANITA. The green lines represent the neutron trajectories; left-block in grey represents bending magnet; grey block on the right represents collimator; blue frames represent detectors constructed in the modelling; sandwich material in yellow represents copper coils; red block represents lead shielding; little blue block represents target cooling jacket (enclosing the target)

Figure 4.7 displays an example of a simulation of a spallation neutron source with a few tracks of neutrons shown in green lines (50 events of 180 MeV proton). It reveals neutrons fly in all directions and some of neutrons are bounced back towards the source by shielding material.

¹The number of protons is fine for the results at CUP and CUP-TOF, but not enough for the results at SUP

Table 4.2 Umbra and penumbra dimensions at the standard user position

collimator diameter /cm	umbra radius /cm	penumbra radius /cm
3	1.5	2.86
10.2	5.98	7.68
30	19.24	20.93

4.2 Neutron fields at the Close User Position and the Standard User Position of the ANITA facility

To analyze neutron field, an upper limit is used for calculating neutron fluence at energies above all neutrons, only above 1 MeV, and only above 10 MeV are considered. Neutrons with energies above 10 MeV are very significant because they are the most likely to cause SEE by indirect ionization. It is also interesting to observe neutrons with energies between 1 MeV and 10 MeV, they are capable of inducing SEE in sensitive semiconductor devices but with less event rate than the neutrons above 10 MeV [Platt et al., 2010]. The data for all neutrons are obtained through a mass of simulations. For the sake of analysis, neutron energy thresholds have been considered as all neutrons, above 1 MeV, and above 10 MeV in this chapter. It is interesting to find out the difference of neutron fluence in umbra and penumbra regions at the standard user position. The umbra and penumbra regions are calculated and dependent upon collimator apertures, see Table 4.2. According to the results from Chapter 3, *QGSP_BIC_HP* was used in updated SNS model at ANITA facility¹.

4.2.1 Spatial distribution of neutron field at the CUP and the SUP

This section shows spatial distribution at the CUP with different neutron energy for different size collimators. The CUP detector is considered as a square in the x-y plane, being subdivided into 20×20 , $3 \text{ cm} \times 3 \text{ cm}$ equal squares in the x-y plane.

The spatial distribution of neutron yield at the CUP of 3 cm collimator with energies above all neutrons, above 1 MeV, above 10 MeV are shown in Figure 4.8. It shows that

¹updated SNS model at ANITA facility: it is not same as preliminary SNS model at ANITA facility, it adds 5 more components

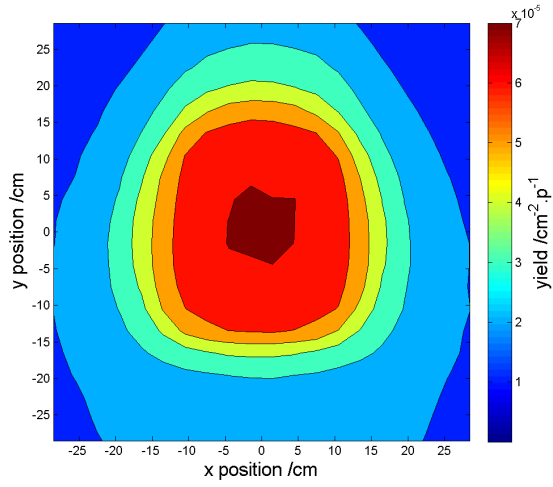
neutrons penetrating the CUP detector are distributed in the centre, which shows the highest number of neutrons is between -5 cm and 5 cm in both x-axis and y-axis. In addition, the lowest neutron yield is dispersed over edges of the detector. Neutrons are not evenly distributed at the CUP of the ANITA facility. However, neutrons recorded in the detector are not all directly from the target, as will be discussed in Section 4.2.3. A comparison of 4.8a and 4.8c in Figure 4.8, neutron with energy above 10 MeV has a high density yield in the centre. And above properties either appear in Figure 4.9 and Figure 4.10.

Figure 4.9 shows the spatial distribution of neutron yield at the CUP with 10.2 cm collimator. A comparison of Figure 4.8b and Figure 4.9b shows that the spatial distribution and neutron yield do not change a lot, which illustrates neutrons with energy above 1 MeV do not influence on 3 cm and 10 cm collimators. The neutrons above all energy change a little, seen from the changes in color and distribution. It is obvious that collimator aperture size does affect neutron yield with energy below 1 MeV. The neutron yield decreases at the centre with radius of 5 cm.

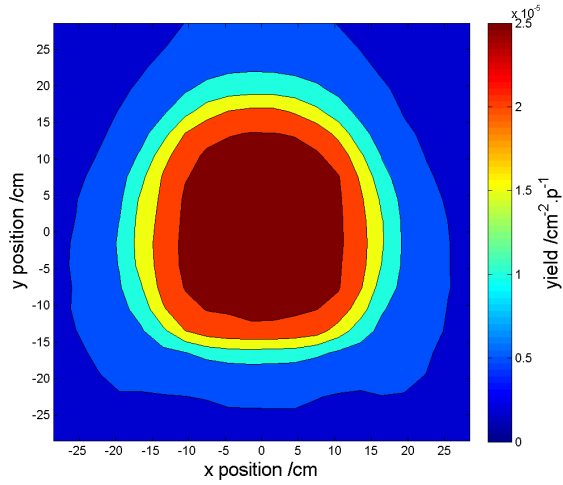
Figure 4.10 shows the spatial distribution of neutron yield at the CUP with 30 cm collimator. A comparison of Figure 4.8a, Figure 4.9a, and Figure 4.10a: the neutron yield above all neutrons decreases with the increase of collimator aperture size.

The dark red color representing neutron yield of $7 \times 10^{-5} \text{ n cm}^{-2} \text{ p}^{-1}$ above all can be seen as a concentrated circle in Figure 4.8a, lighter color and a bigger circle in Figure 4.9a, and disappeared in Figure 4.10a. A comparison of Figure 4.8c, Figure 4.9c, and Figure 4.10c shows that the shape and color of concentrated circles are close to each other. It illustrates the number of neutrons with energy greater than 10 MeV is quite similar and independent on collimator size. From all neutrons above 1 MeV, as the collimator aperture size increases, the neutron yield decreases a little bit at the CUP (see changes in distribution or concentrated circle size).

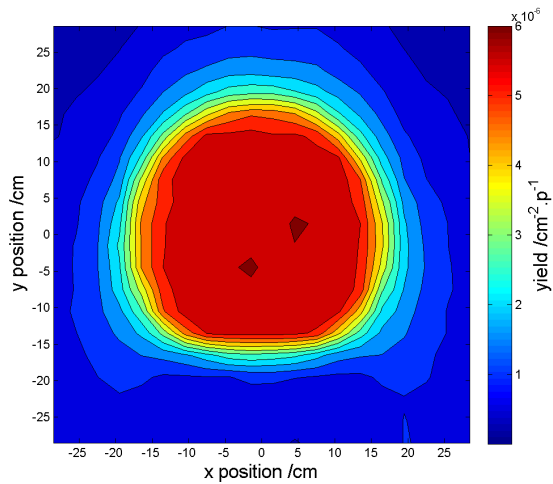
After neutron penetrating collimators, neutrons can be detected at the SUP. Figure 4.11, Figure 4.12, and Figure 4.13 show neutron yield spatial distribution at the SUP. The SUP detector is divided into 120×120 , $1 \text{ cm} \times 1 \text{ cm}$ equal squares in the x-y plane.



(a) all neutrons

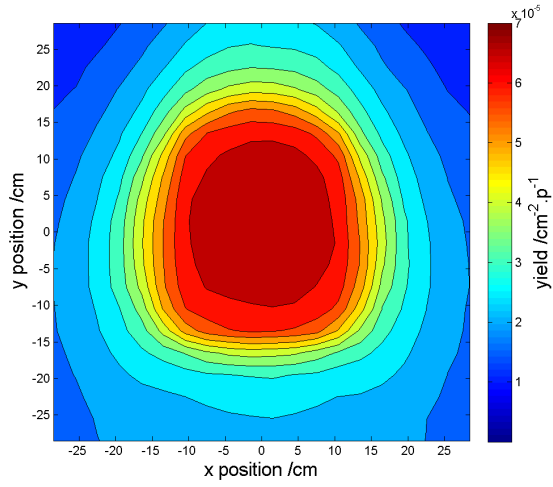


(b) neutrons above 1 MeV

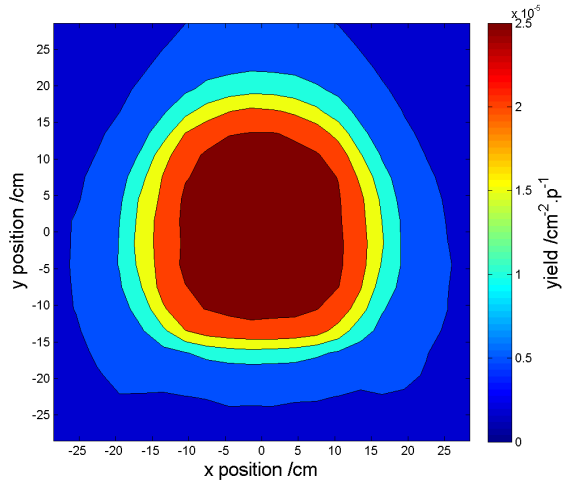


(c) neutrons above 10 MeV

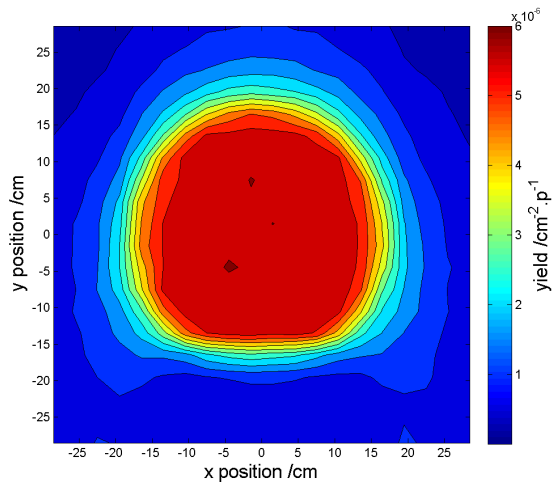
Fig. 4.8 Neutron spatial distribution at the CUP with 3 cm collimator



(a) all neutrons

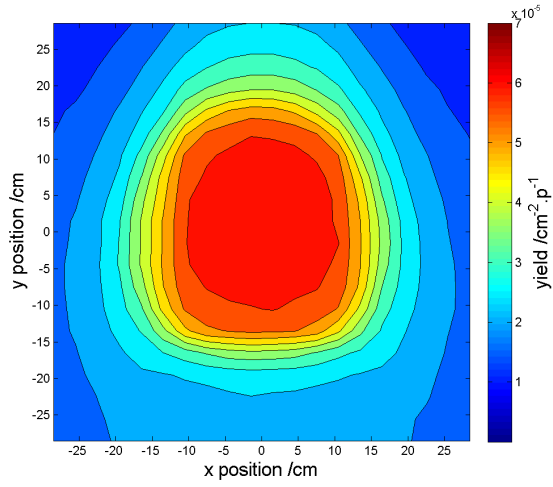


(b) neutrons above 1 MeV

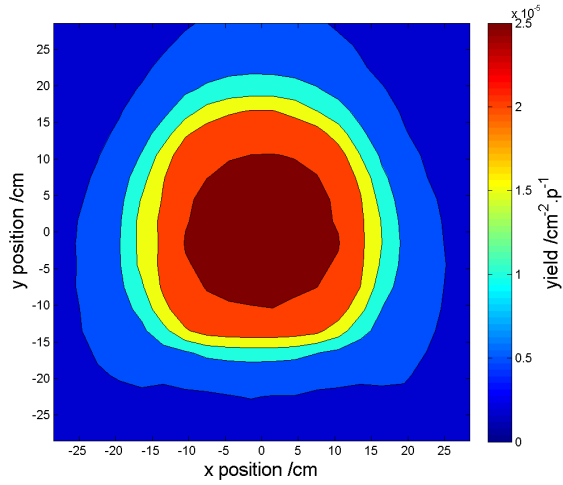


(c) neutrons above 10 MeV

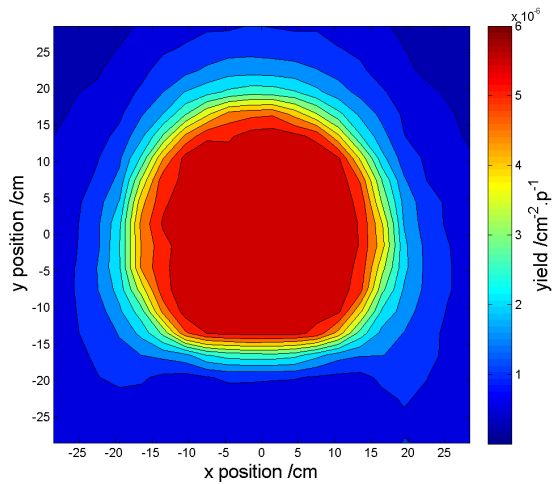
Fig. 4.9 Neutron spatial distribution at the CUP with 10.2 cm collimator



(a) all neutrons



(b) neutrons above 1 MeV



(c) neutrons above 10 MeV

Fig. 4.10 Neutron spatial distribution at the CUP with 30 cm collimator

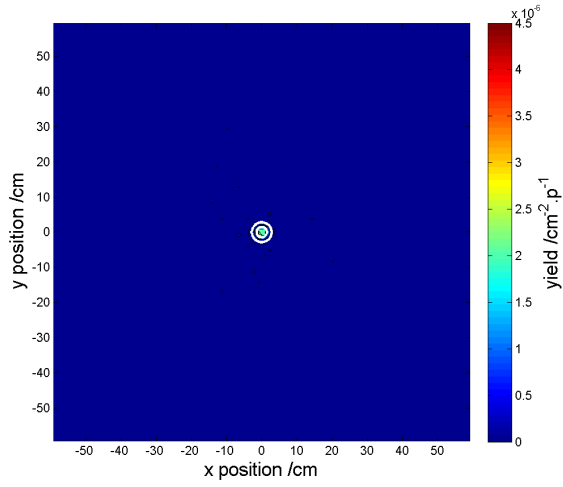
A comparison of Figure 4.11 a and Figure 4.8a, it is obvious that neutron distribution is smaller at the SUP than the CUP and number of neutrons decreases. That is because the collimator has a shielding effect for neutrons through elastic, inelastic scattering, or nuclear interaction.

The following Figure 4.11, Figure 4.12, Figure 4.13 show neutron yield distribution with 3 cm, 10.2 cm and 30 cm collimators. There two white circles show the penumbra and umbra region on the SUP detector for each case. Most of neutrons are penetrating in the umbra region. The neutron yield with energy above 1 MeV and 10 MeV both are very very low with 3 cm collimator, see Figure 4.11.

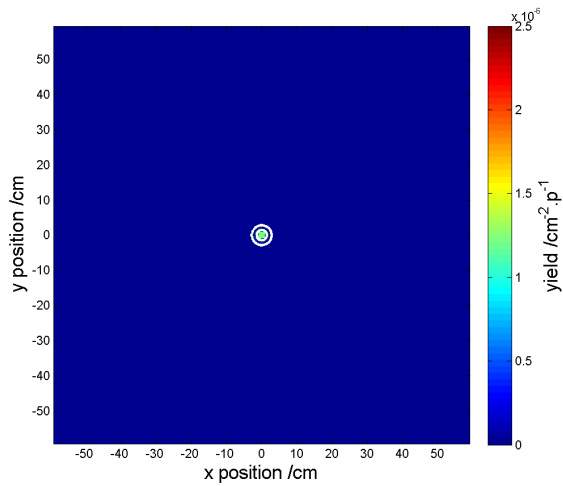
For 10.2 cm collimator case (see Figure 4.12), the number of neutrons increases when applying large collimator aperture size. It shows that neutron yield at the SUP is dependent on collimator size. It is obvious that a few number of neutrons is penetrating in the penumbra region. According to comparison result of Figure 4.11, Figure 4.12 and Figure 4.13, it proves that collimator size indeed has an effect on neutron yield with energy below 10 MeV at the SUP. The neutron fluence rate at the SUP decreases with reduction in collimator size, see comparison of Figure 4.12b and Figure 4.13b. In addition, when the collimator size increases to 30 cm, neutrons are capable of arriving at outside of the penumbra region.

4.2.2 Calculation of effective radius

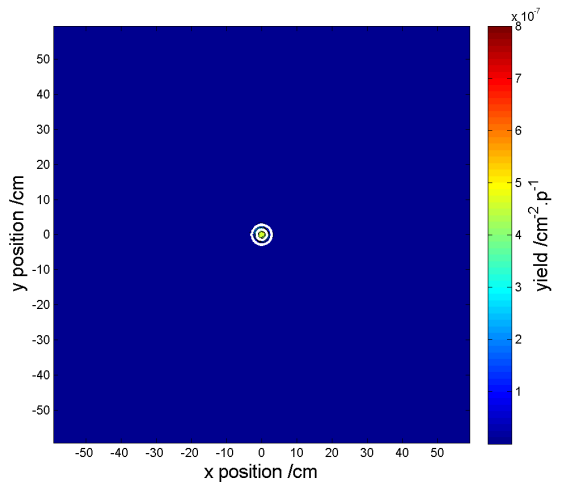
The spatial distribution of neutrons yield at the CUP and SUP of the ANITA facility with three different collimators is analyzed in the previous section. The ANITA facility modelling contains three cases, including 3 cm, 10.2 cm, and 30 cm collimators, which are constructed and used in simulation testing of 110 million primary protons. Figure 4.14 shows all neutron at the CUP with 3 cm, 10.2 cm, and 30 cm collimators. The simulated CUP detector is divided into 900 equal area concentric circles on the basis of geometric centre. The enclosed region between two concentric circles is 3.146 cm^2 .



(a) all neutrons

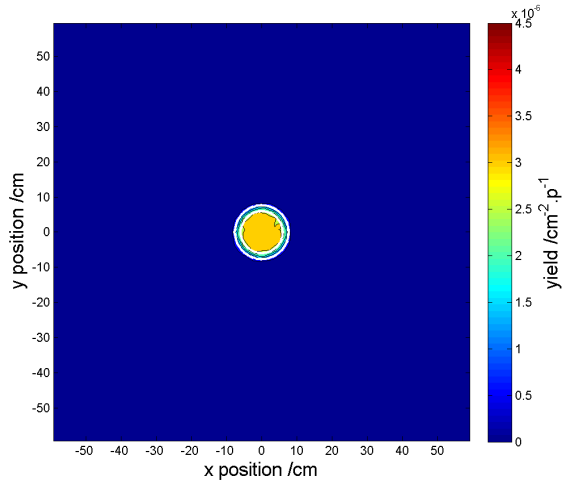


(b) neutrons above 1 MeV

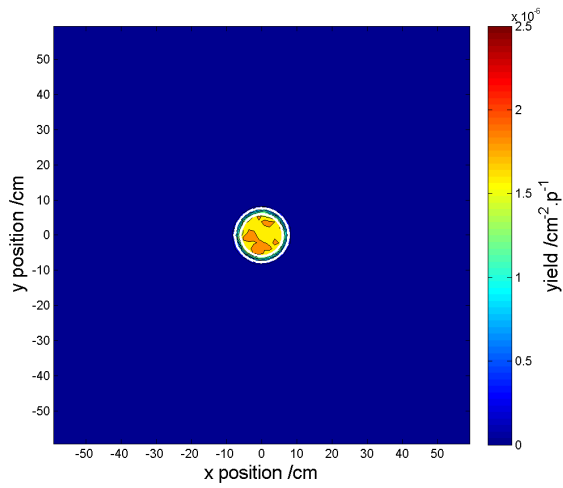


(c) neutrons above 10 MeV

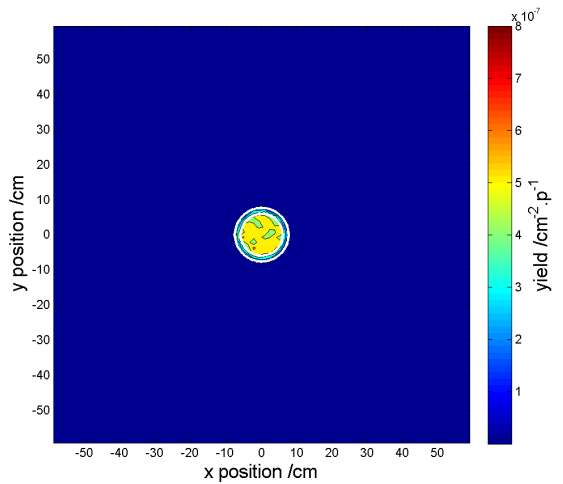
Fig. 4.11 Neutron spatial distribution at the SUP with 3 cm collimator



(a) all neutrons

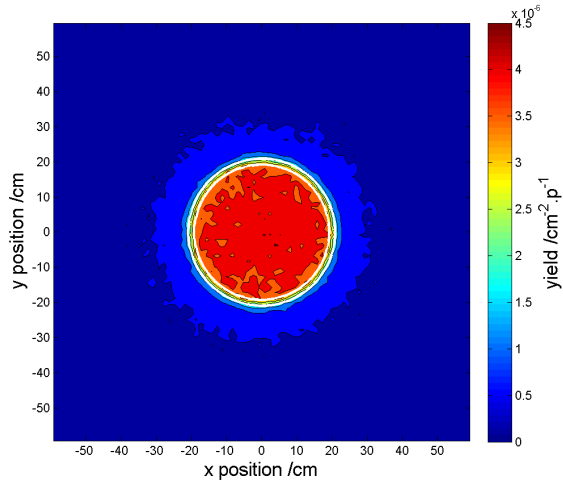


(b) neutrons above 1 MeV

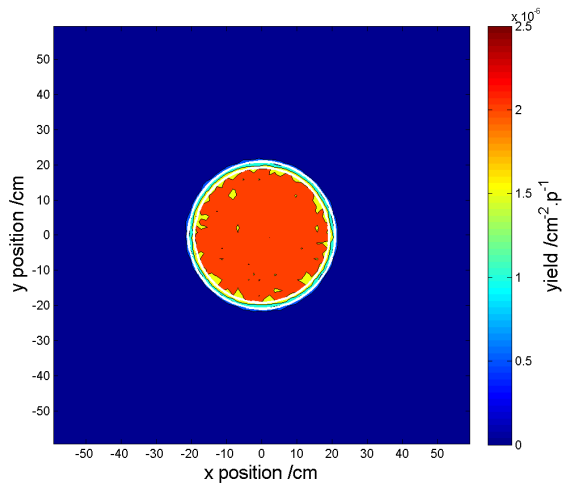


(c) neutrons above 10 MeV

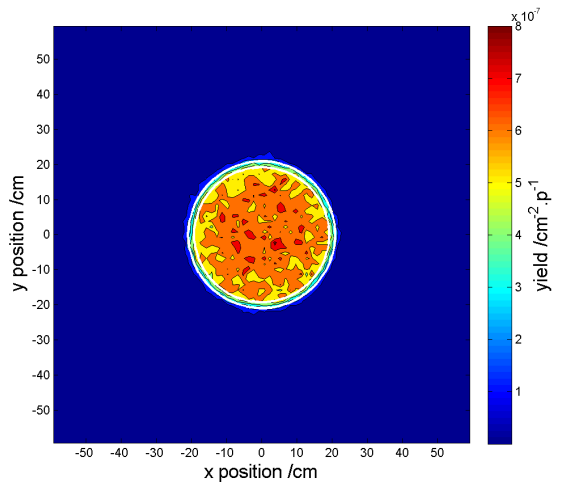
Fig. 4.12 Neutron spatial distribution at the SUP with 10.2 cm collimator



(a) all neutrons



(b) neutrons above 1 MeV

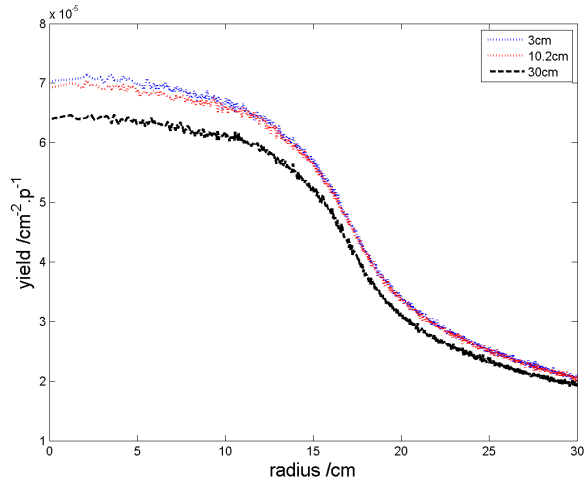


(c) neutrons above 10 MeV

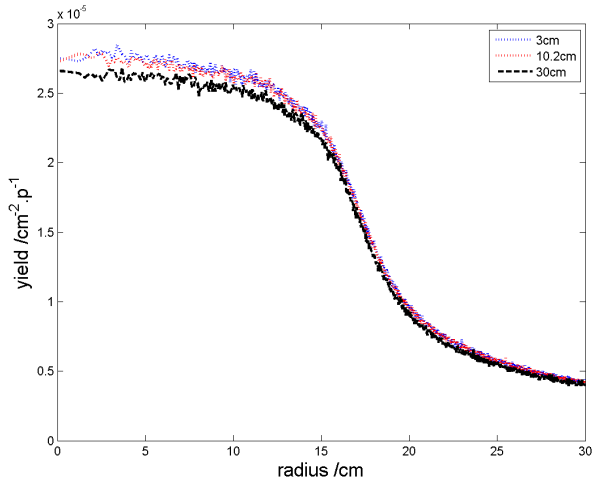
Fig. 4.13 Neutron spatial distribution at the SUP with 30 cm collimator

From Figure 4.14a, it shows the total neutron yield of 3 cm collimator is the highest among all collimators with the radius less than 10 cm. A comparison of 3 cm with 10.2 cm collimator with the radius greater than 10 cm shows that the neutron yield is almost the same. The backscattered neutrons from frontal wall (also called collimator) are mainly located within the circle of 10 cm radius of the CUP detector. The difference between 3 cm and 10.2 cm collimator is smaller than that between 3 cm and 30 cm collimator. The number of neutrons with 30 cm collimator is about 7.14% less per unit area than that of 3 cm collimator within 5 cm radius. It illustrates that the number of backscattered neutrons with 30 cm is less than those of 3 cm and 10 cm collimators. The 30 cm collimator aperture is big enough to let neutrons pass through it. Focusing on the similarities, when radius gets close to 15 cm, neutron yield of three collimators falls steeply in each case. This shows that the effective radius of the CUP is about 15 cm, as shown in Figure 4.14b and Figure 4.14c. Neutron yields with energy greater than 1 MeV for 3 cm and 10.2 cm collimators are quite similar, which illustrates these two collimators have the similar effect on neutron with energy greater than 1 MeV. For 30 cm collimator, the number of neutrons is about 3.64% less per unit area than that of 3 cm collimator within 5 cm radius. In addition, collimator size has a strong influence on neutron fluence having energy less than 1 MeV. It is clear that collimator size with no effect to the neutron yield with energy above 10 MeV from Figure 4.14c. Although the statistical noise increases with reduction in radius, multiple baselines are overlapped at $5.9 \times 10^{-6} \text{ n cm}^{-2} \text{ p}^{-1}$. It can prove that high energy neutron from spallation reaction with energy greater than 10 MeV are directly passing through the CUP detector and the collimator aperture, with little scattering angle.

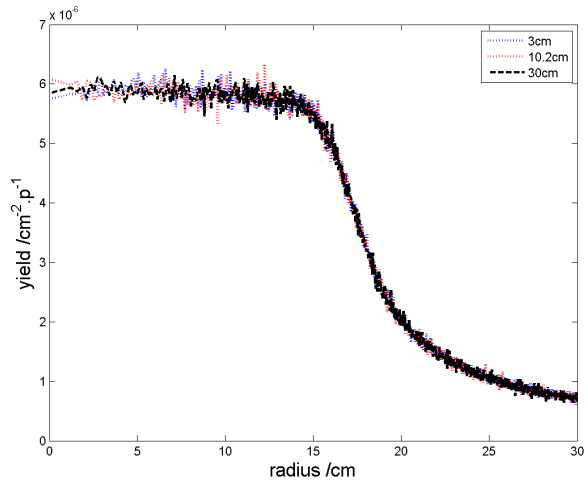
Figure 4.15 shows that neutron yield at the SUP above 10 MeV remains at about the same value inside of each umbra area for three collimators. In another word, the neutron intensity under the umbra region is the greatest in each case. And neutron yield begins to reduce steeply from umbra radius until to penumbra radius for 3 cm collimator. For both of 10.2 cm collimator and 30 cm collimator cases, neutron yield continues to fall after penumbra radius. Comparing 3 cm collimator and 10.2 cm collimator, neutron yield above 10 MeV is almost the same ($5.25 \times 10^{-7} \text{ cm}^{-2} \text{ p}^{-1}$) under the umbra region. The neutron



(a) all neutrons



(b) neutrons above 1 MeV



(c) neutrons above 10 MeV

Fig. 4.14 Radius effect of neutrons at the CUP with 3 cm, 10.2 cm, and 30 cm collimators

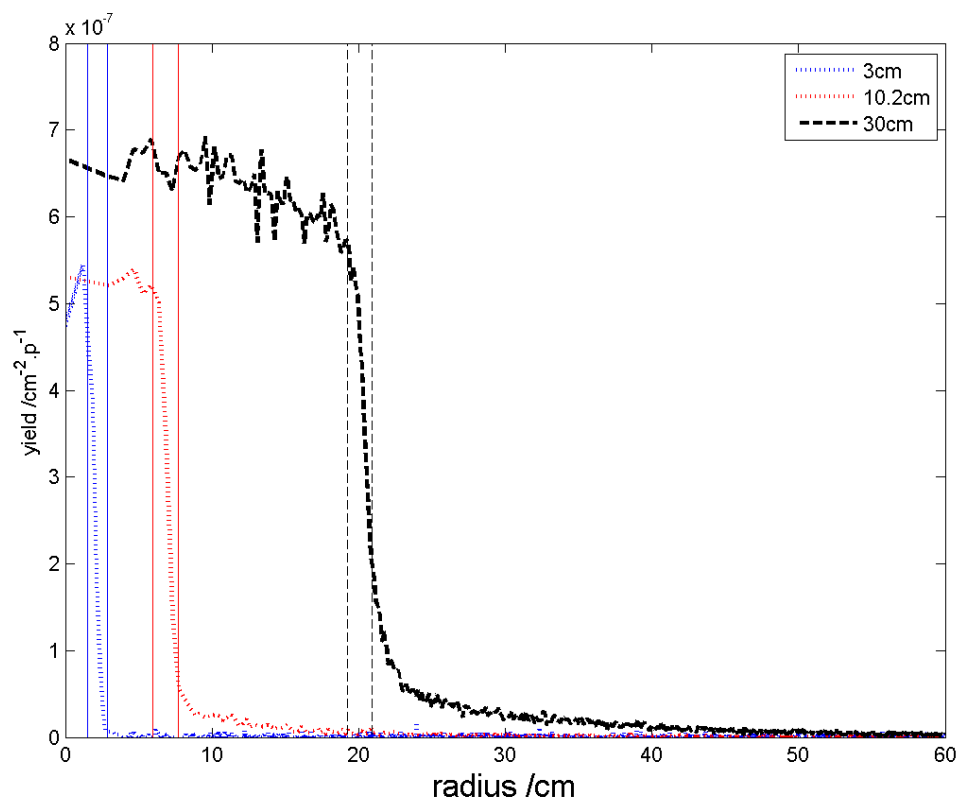


Fig. 4.15 Radius effects for neutrons above 10 MeV at the SUP. The vertical blue solid line, red solid line, and black dashed line represent the radius of umbra and penumbra of 3 cm, 10.2 cm, and 30 cm collimators, respectively

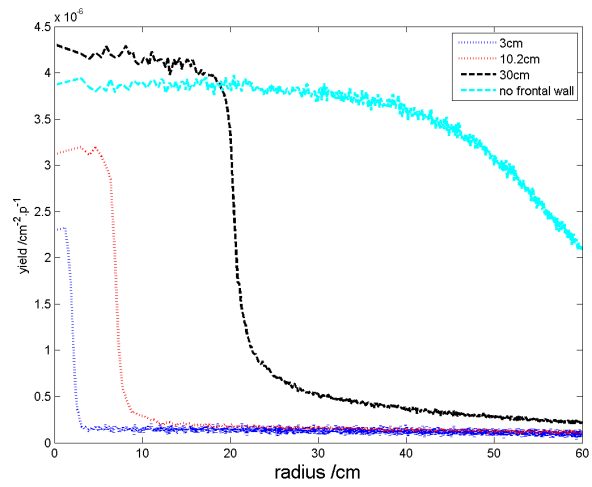
yield of 30 cm collimator is about 23.81% higher than 3 cm and 10.2 cm collimator at the SUP.

A comparison of Figure 4.15 with Figure 4.14c shows that neutron yield above 10 MeV of 3 cm collimator and 10.2 cm collimator at the SUP is about 11.2 times less than at the CUP, which is because of the $1/R^2$ law calculation. It is consistent with the ratio factor 11.7 given by [Prokofiev et al., 2014], neutron flux above 10 MeV at the ANITA-CUP to the ANITA-SUP field. However, the neutron yield above 10 MeV of 30 cm collimator at the SUP is about 9.1 times less than that at the CUP. For 30 cm collimator case, it verifies that a mass of neutrons ¹ above 10 MeV must hit or scatter with collimator inner wall, which results in neutron production.

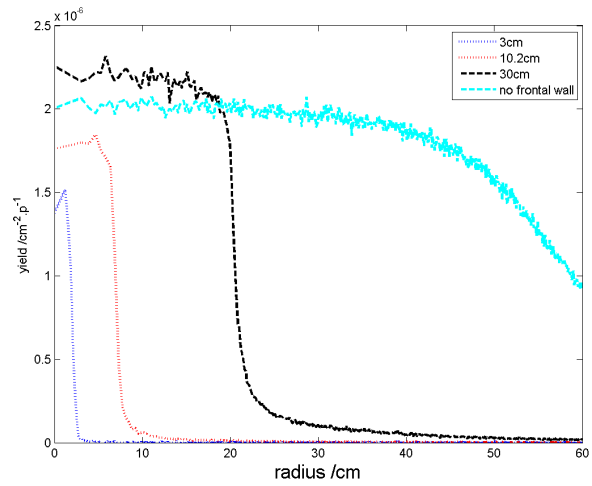
Figure 4.16 shows neutron yield versus radius at the SUP with no collimator, 3 cm, 10.2 cm, and 30 cm collimators. Compared with Figure 4.15, more information about yield for all neutrons, neutron yield above 1 MeV, and neutron yield of no collimator is given. The neutron yield of each collimator is basically a constant in the umbra region, as shown Figure 4.16.

The neutron yield of no collimator remains constant until the radius increases up to 40 cm, and then starts to slowly decrease from 40 cm. The neutron yield of 30 cm collimator is higher than that of no collimator within radius of 20 cm in Figure 4.16c, which once again proves a previously inference (extra neutrons is due to inner wall of 30 cm collimator). It is seen from Table 4.3 that the neutron yield is proportional to collimator aperture size with energy below 10 MeV under the umbra at the SUP. For 3 cm collimator, the neutron yield between 1 MeV and 10 MeV is the highest among these 3 energy ranges, and is about 1.857 times over than yield above 10 MeV and about 1.170 times over than yield below 1 MeV. For other 2 collimator sizes, main distribution under the umbra region is attributed to the neutron yield below 1 MeV.

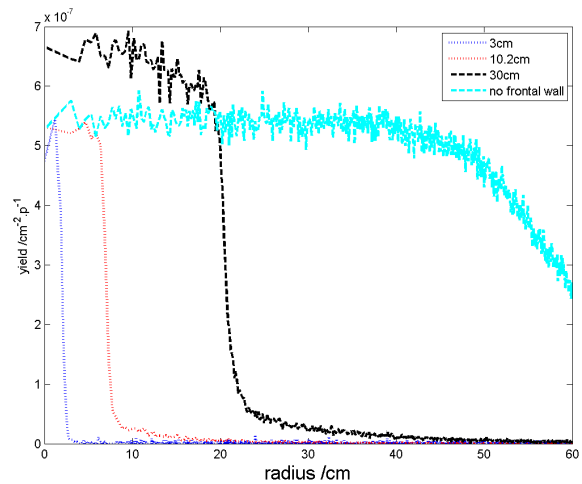
¹it infers that flight path angle of neutrons above 10 MeV is bigger than 0.7256 sr, taking 3 cm collimator as an example.



(a) all neutrons



(b) neutrons above 1 MeV



(c) neutrons above 10 MeV

Fig. 4.16 Radius effect of neutrons at the SUP with no collimator, 3 cm, 10.2 cm, and 30 cm collimators

Table 4.3 Neutron yield under the umbra region at the standard user position

collimator /cm	below 1 MeV / $1 \times 10^{-6} \text{ ncm}^{-2} \text{ p}^{-1}$	between 1 and 10 MeV / $1 \times 10^{-6} \text{ ncm}^{-2} \text{ p}^{-1}$	above 10 MeV / $1 \times 10^{-6} \text{ ncm}^{-2} \text{ p}^{-1}$
3	0.833	0.975	0.525
10.2	1.394	1.248	0.525
30	1.962	1.555	0.650

4.2.3 Spectral neutron fluence at the CUP and the SUP for different collimator size

Neutron fluence data at the CUP, in the lethargy plot, are shown in Figure 4.17. In this case, a circle of radius 9 cm is chosen on the simulated CUP detector center for analyzing neutron field at the CUP. Neutron fluence will not change too much with area chosen unless the radius is greater than about 15cm, as shown in Figure 4.14. From Figure 4.17, it is obvious that the number of neutrons having energy greater than 10 MeV is not changing with collimator size. However, collimator size has an effect for neutron energy below 10 MeV. The smaller the aperture of collimator is, the more neutrons below 10 MeV appear.

To compare directly neutron fluence in lethargy scale with Prokofiev's results [Prokofiev et al., 2014], it is better to choose equal linear space in energy bin. Figure 4.18a is slightly different from Figure 4.17 on energy bins chosen, as well as on position chosen. A comparison of Figure 4.17 and Figure 4.18a, it is shown that the highest neutron yield of 3 cm collimator is 1.17 times higher than that of 30 cm collimator at the CUP, while the ratio at the CUP-TOF position is 1.36 times. Thus it can be seen neutron yield at the CUP is slightly different with that at the CUP-TOF position.

In order to make the comparison clear, 3 cm collimator is taken as an example to analyze and explain Figure 4.18a. It is shown peaks (0.35,1.732), (0.65,2.337), (0.95,1.681), and (1.15,1.666) with neutron energy below 10 MeV with 3 cm collimator. In addition, the neutron yield above 10 MeV begins to overlap with other dimension collimators and reaches a maximum about $0.229 \times 10^{-5} \text{ n cm}^{-2} \text{ p}^{-1}$ at around 100 MeV, which is very close to the Prokofiev's result ($0.252 \times 10^{-5} \text{ n cm}^{-2} \text{ p}^{-1}$) shown in [Prokofiev et al.,

2014]. Four main peaks of neutron yield below 10 MeV appear in Figure 4.18a, but Geant4 simulation data of neutron yield with energy below 10 MeV are lower than the ANITA data, as shown in [Prokofiev et al., 2014] in terms of 3 cm collimator, which are (0.35,2.172), (0.65,2.931), (0.95,1.897), and (1.15,2.000). The ratio of maximum neutron yield below 10 MeV to maximum value above 10 MeV are 10.2 times (from the Geant4 simulation data) and 11.6 times (from [Prokofiev et al., 2014]). As for other dimension collimators, it is clear to see four main peaks below 10 MeV and the shape of each are quite similar. In addition, they have the same neutron yield above 10 MeV. It illustrates that neutron yield below 10 MeV increases with reduction in collimator aperture size and yield above 10 MeV is not influenced by collimator aperture size. A comparison of 3 cm collimator and 10.2 cm collimator, they are very close and almost start from the same point (0.1, 0.5) and four main peaks of 10.2 cm collimator just slightly lower than that of 3 cm collimator. Therefore, the difference in neutron yield for the collimator aperture size between 3 cm and 10.2 cm will not be greater than $\pm 2.93\%$.

It is not difficult to find that the shape of Figure 4.18a seems to appear in the earlier Chapter 3. The evaporation peak below 10 MeV has been split in four and the intranuclear cascade peak above 10 MeV is still there comparing Figure 4.18a with Figure 3.7. The neutron yield below 10 MeV is about 2 times higher than that above 10 MeV at the SUP, as shown in Figure 3.7. The neutron yield below 10 MeV with no frontal wall is about 5 times higher than that above 10 MeV at the CUP, as shown in Figure 4.18a. This is caused by interaction of neutrons with shielding material. The neutron yield below 10 MeV with 3 cm collimator is about 10 times higher than that above 10 MeV at the CUP, which is due to interaction of neutrons with shielding material and neutron backscattering by collimator.

Figure 4.19 shows a comparison of simulated neutron fluence rate at the CUP with Geant4 and MCNPX. It shows a good agreement between Geant4 simulated results and TSL analytical fit from Prokofiev et al. [2014]. The evaporation peak at around 1 MeV (the fit cannot reproduce the structure in this energy region) and intra-nuclear cascade peak at around 100 MeV are obvious to justify. The intra-nuclear cascade peak from Geant4 simulation drifts towards higher energy rather than 100 MeV.

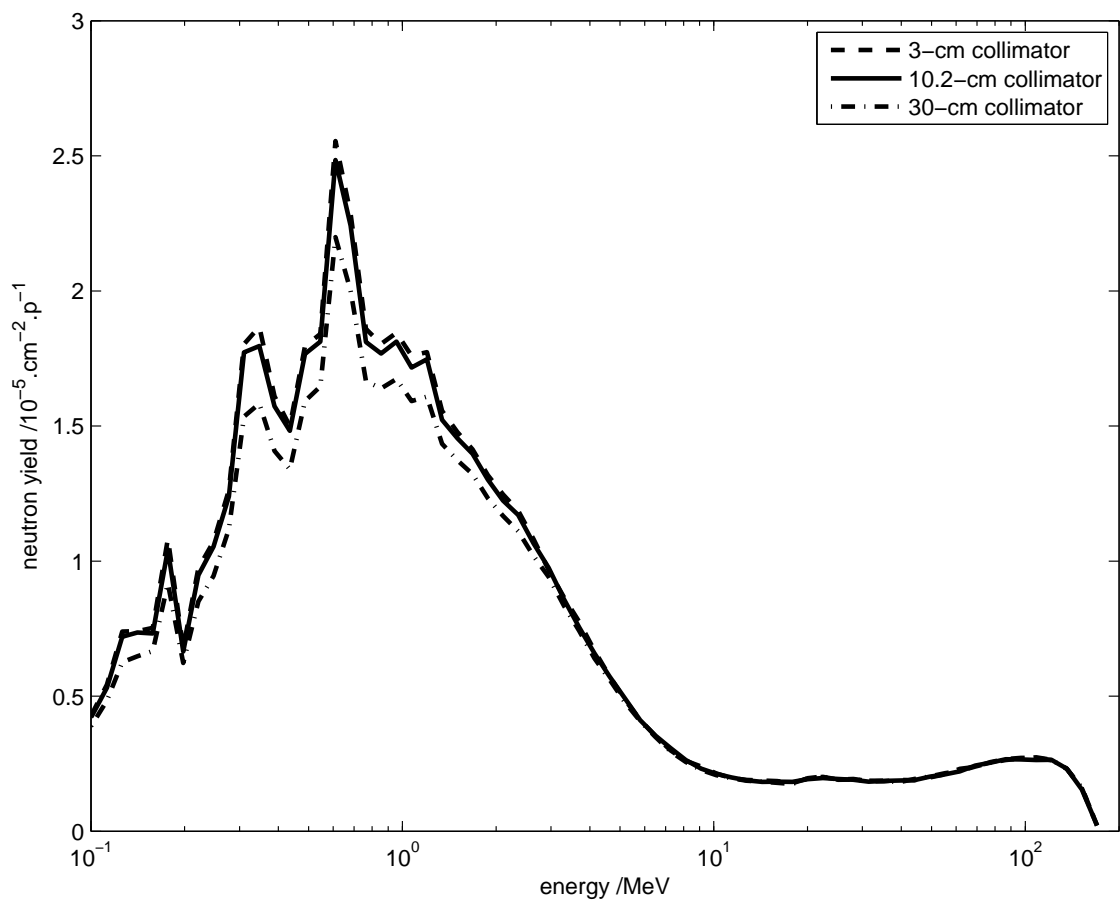
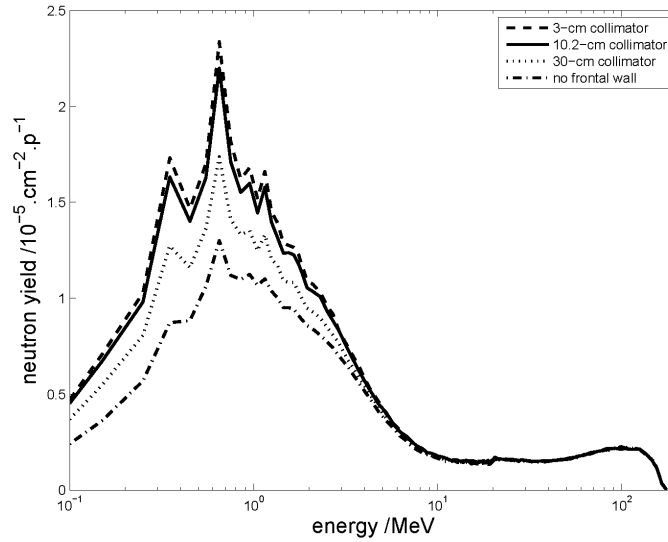
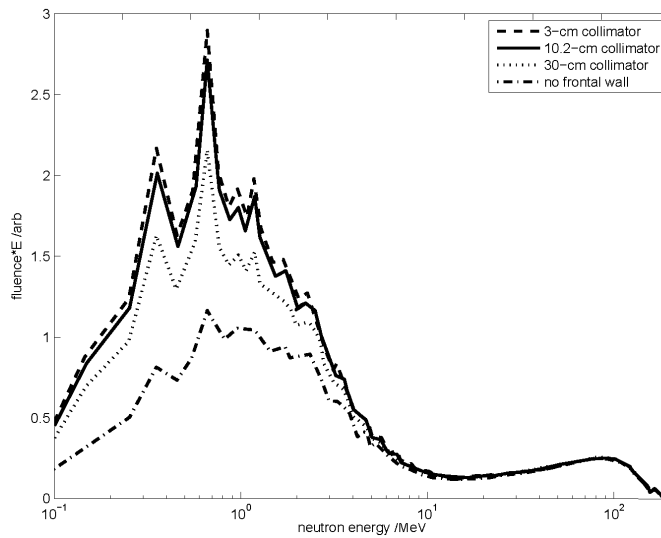


Fig. 4.17 Simulated spectral fluence at the CUP for 3 cm, 10.2 cm, and 30 cm collimators



(a) Geant4 modelling



(b) TSL MCNPX modelling [Prokofiev et al., 2014]

Fig. 4.18 Simulated spectral fluence at the CUP-TOF position for 3 cm, 10.2 cm, 30 cm and no collimator. The dashed line, solid line, and dotted line represent the neutron yield of collimator with diameter 3, 10.2, and 30 cm. The dash-dotted line represents modelling with no collimator attached.

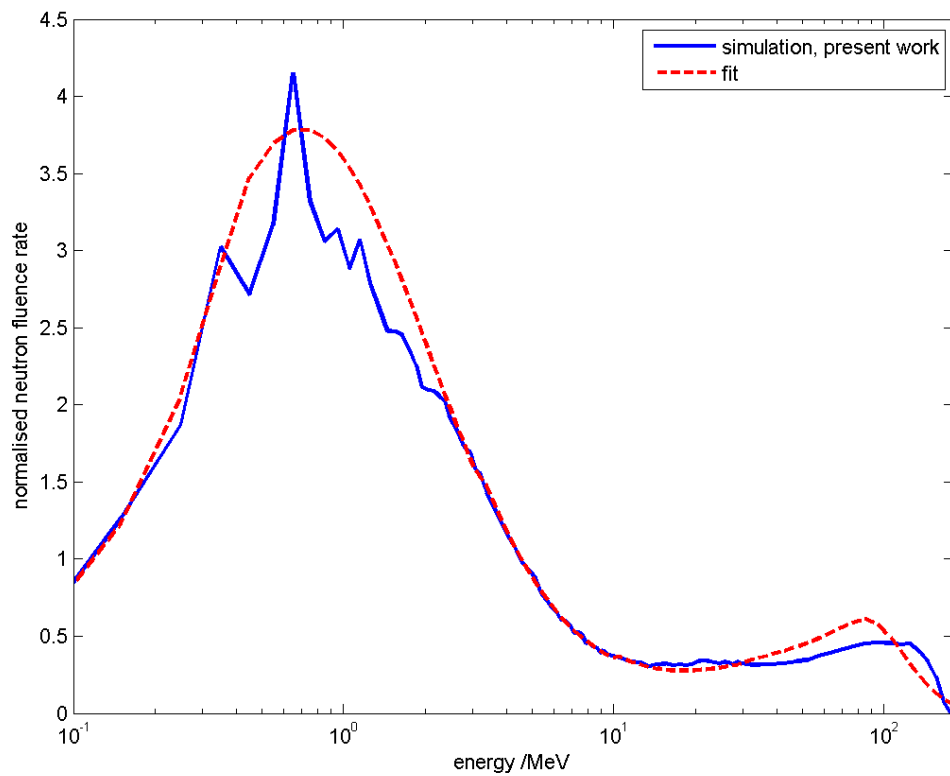


Fig. 4.19 Comparison of neutron fluence rate at the CUP with 10.2 cm collimator, normalized to 1 above 10 MeV. fit: from TSL analytical data, which is published [Prokofiev et al., 2014]. simulation, present work: from Geant4 calculation of SNS model at ANITA facility.

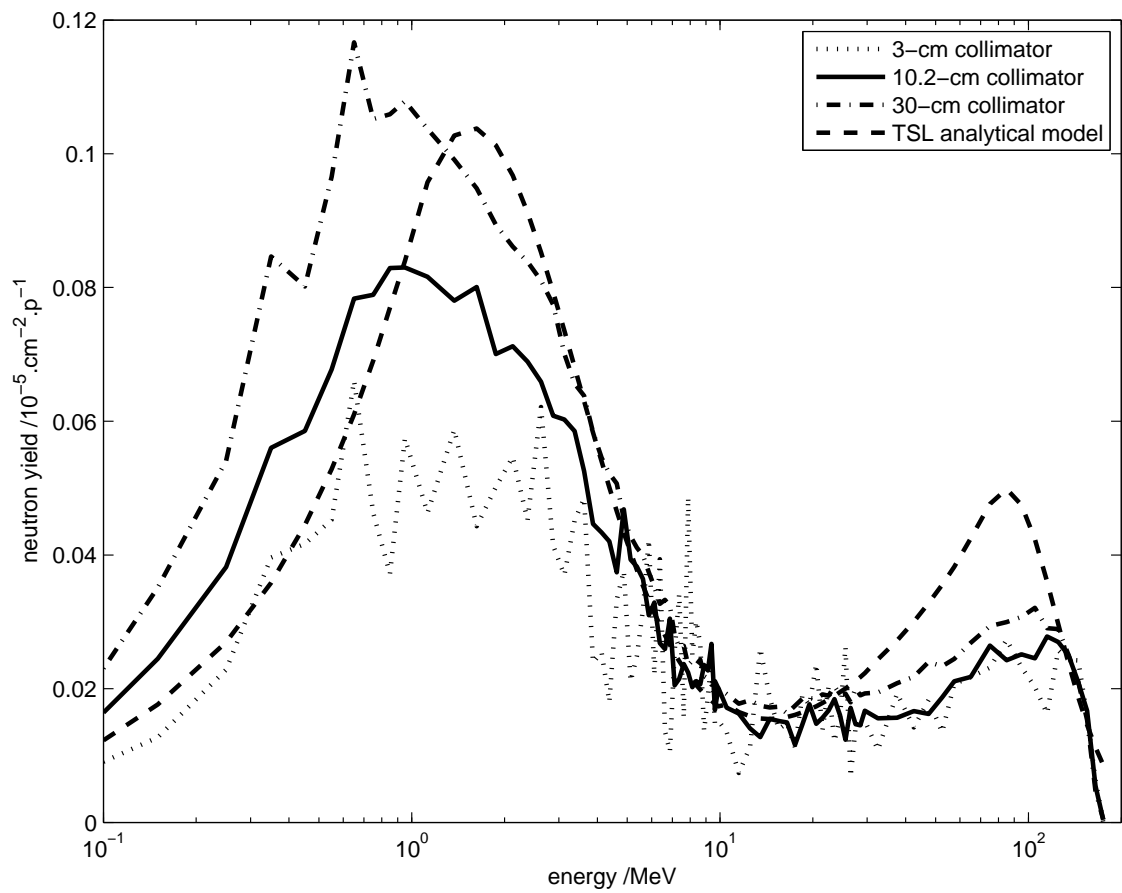
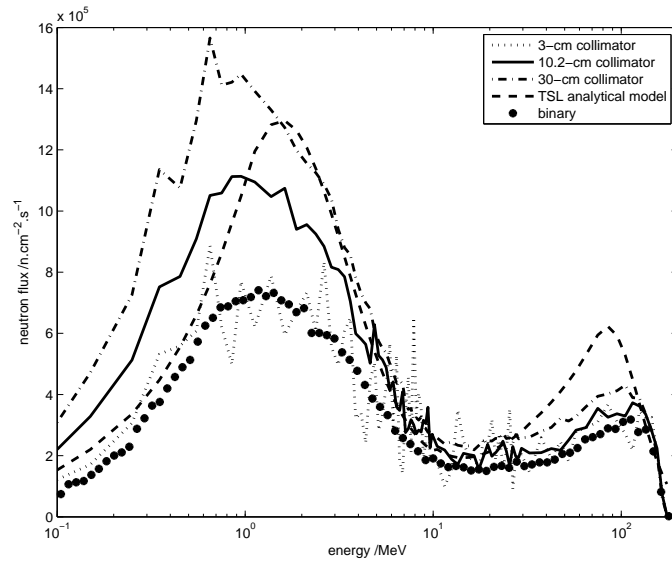


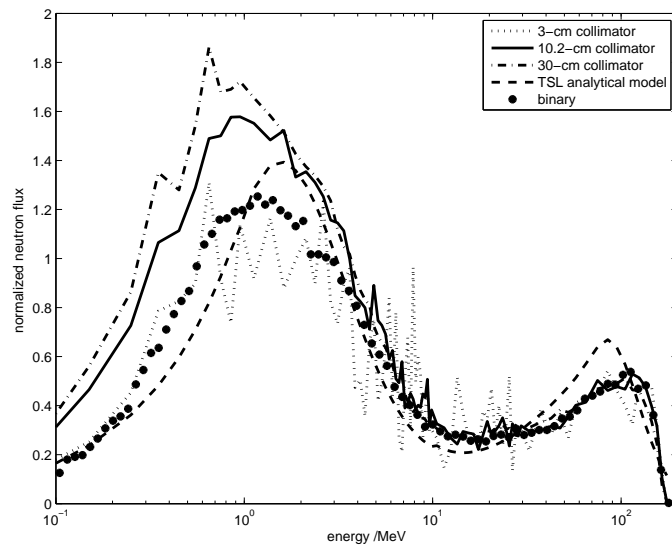
Fig. 4.20 Simulated spectral yield at the SUP for 3 cm, 10.2 cm, and 30 cm collimators

Figure 4.20 shows neutron yield with different dimension collimators at the SUP, based on same energy bin, and the results of 3 cm collimator is very noisy comparing with other two dimension collimators. The neutron yield of 3 cm collimator is the lowest among collimators, as shown in Figure 4.16a, which results in high statistical noise. It is seen that cascade peak is around 100 MeV and evaporation peak is around 1 MeV at the SUP. Neutron yield above 10 MeV with 3 cm collimator is close to 10.2 cm collimator, which is about $2.585 \times 10^{-7} \text{ n cm}^{-2} \text{ p}^{-1}$. For 30 cm collimator, neutron yield is higher than other two collimator size, one is $3.113 \times 10^{-7} \text{ n cm}^{-2} \text{ p}^{-1}$ (cascade peak), the other one is $11.67 \times 10^{-7} \text{ n cm}^{-2} \text{ p}^{-1}$ (evaporation peak). In addition, neutron yields below 10 MeV with 10.2 cm collimator and 3 cm collimator are $8.298 \times 10^{-7} \text{ n cm}^{-2} \text{ p}^{-1}$, and $5.717 \times 10^{-7} \text{ n cm}^{-2} \text{ p}^{-1}$, respectively. The neutron yield below 10 MeV with 30 cm collimator is 1.4 times higher than that with 10.2 cm collimator, and 2.04 times higher than that with 3 cm collimator at the SUP. The neutron yield shown in Figure 4.21a is about 8.86 times less than the yield shown in Figure 4.18a in terms of 3 cm collimator, which satisfies with the $1/R^2$ law ($2.5^2/0.84^2 = 8.858$). It also fits with previous analysis for Figure 4.16.

Figure 4.21a shows five curves of absolute neutron flux spectra at the SUP which are 3 cm, 10.2 cm, 30 cm collimator, no collimator (binary), and TSL analytical one. It is better to use unified units ($\text{n cm}^{-2} \text{ s}^{-1}$) for an analysis of these results. As can be seen from Figure 4.21a, the result of absolute neutron flux with 3 cm collimator is close to that of binary model although 3 cm collimator results have statistical noise. The result of neutron flux above 10 MeV with 10.2 cm collimator is slightly higher than that of binary model and about 50% higher than binary model at evaporation peak. The neutron flux above 1 MeV with 10.2 cm collimator is more closer to the TSL analytical model curve than binary and 3 cm collimator do. In addition, Figure 4.21a shows good agreement between 30 cm collimator and TSL analytical model with neutron energy greater than 10 MeV. Although the intranuclear cascade peak value of 30 cm collimator is 30% lower than TSL analytical one, it is a slightly higher than 10.2 cm collimator. For neutron flux below 1 MeV, only the 10.2 cm and 30 cm collimator results are greater than the TSL analytical data, other cases



(a) without normalizing



(b) normalized

Fig. 4.21 Comparison of neutron flux at the SUP for 3 cm, 10.2 cm, 30 cm collimators, and no collimator (binary) with TSL analytical model. The dotted line, solid line, and dash-dotted line represent the neutron flux for 3 cm, 10.2 cm 30 cm collimator, respectively. The dashed line represent the results of neutron flux for the standard ANITA SUP field. The circle mark and star mark represent neutron flux at the SUP with only naked target. One is shown the raw data (without normalizing). The other (normalized) shows the neutron flux normalized to 1 above 10 MeV

Table 4.4 Neutron flux above 10 MeV at the SUP

modelling unit	TSL analytical /n cm ⁻² s ⁻¹	3 cm /n cm ⁻² s ⁻¹	10.2 cm /n cm ⁻² s ⁻¹	30 cm /n cm ⁻² s ⁻¹
neutron flux	9.3×10^5	6 765e5	7.057×10^5	8.407×10^5

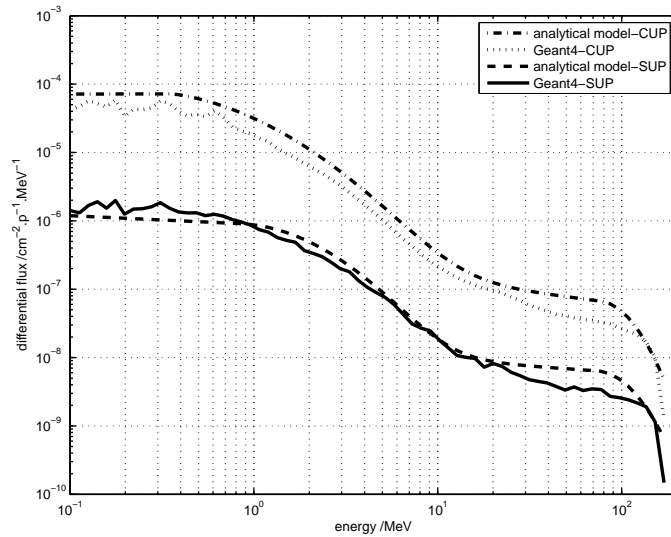
Table 4.5 Ratios of evaporation peak to intranuclear cascade peak

	preliminary	TSL analytical	3 cm	10.2 cm	30 cm
ratio	2.330	2.108	2.149	2.935	3.279

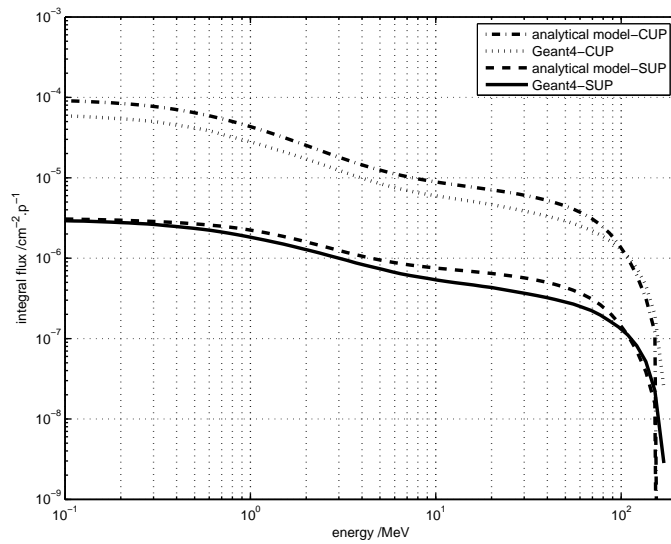
are basically consistent with TSL analytical data. Overall, the result of ANITA modelling with collimator and shielding attached is more similar with TSL analytical data than the modelling of spallation neutron source.

In Table 4.4, it is shown the absolute neutron flux above 10 MeV calculated using the 3 cm collimator, 10.2 cm collimator, and 30 cm collimator are about 72.74%, 75.88%, and 90.40% of the TSL analytical data (9.3×10^5 n cm⁻² s⁻¹) that inferred from [Prokofiev et al., 2009].

A comparison of neutron yield normalized to 1 above 10 MeV among the binary and TSL analytical model is shown in Chapter 3 Figure 3.7. Table 4.5 shows more complete data on ratio of evaporation peak to intranuclear cascade peak. In terms of ratio between evaporation peak and intranuclear cascade peak, it shows ratio of 3 cm collimator is the nearest to that of TSL analytical model. However, the statistical noise is high so that the ratio is not reliable. Figure 4.21b shows the shapes of the naked spallation neutron source modelling (binary) and three dimension collimators (3 cm, 10.2 cm, and 30 cm) unencumbered by considerations of absolute neutron flux. It shows the neutron flux below 1 MeV from the 10.2 cm, and 30 cm collimators are higher than the TSL analytical data. In addition, the neutron flux below 1 MeV from 3 cm collimator and binary model are more close to the TSL analytical data. To compare with absolute neutron flux from Table 4.4, it is known that neutron flux below 1 MeV is less than neutron spectra shown in Figure 4.21b.



(a) Differential



(b) Integral

Fig. 4.22 Comparison of Geant4 simulated spectral fluence with analytical model at the SUP and the CUP with 10.2 cm collimator [Prokofiev et al., 2009, 2014]

Figure 4.22 shows differential and integral neutron yield with 10.2 cm collimator comparing with TSL analytical data at the CUP and SUP. Comparing differential neutron yield at the SUP with the CUP, shapes are quite similar at two positions but neutron yield at the SUP is less than that at the CUP. The calculated ratio of neutron yield from the Geant4 modelling data above 10 MeV at the CUP to the SUP is about 10, as shown in Figure 4.22b. In addition, the calculated ratio of neutron yield above 10 MeV at the SUP from the Geant4 modelling data to the TSL analytical data is about 0.722, which is about 72.2% of the TSL analytical data at the SUP. This ratio is consistent with the result (75.88%) that calculated according to Table 4.4. The neutron yield above 10 MeV at the CUP from the Geant4 modelling data is about 66.7% TSL analytical data.

4.2.4 Components distribution to CUP

In Section 4.2.3, it is known that neutron yield below 10 MeV increased with reduction in diameter of the collimator at the CUP. It is interesting to know how much probability of neutrons originating from the target (with no interaction with collimator), how many neutrons being scattered by collimator frontal wall, and how many neutrons from other components, for instance, shielding components, bending magnet component. It is more convenient to define neutron field at the CUP as following three components, Direct Component (DC), Frontal Wall Component (FWC), and Surroundings Component (SC), using the same names as in [Prokofiev et al., 2009].

The following Figure 4.24 shows neutron yield with the 3 cm collimator at the CUP which is divided into three components. The neutrons from frontal wall components could be filtered by direction ¹. The neutrons components can be calculated by Equation (4.1) if neutron position (x, y, z) and direction (u, v, w) are known. The equation is deduced according to Figure 4.23. Here $z = 84$ cm for the CUP-TOF position, z is determined by detector position. If $R \leq 2.5$ (radius of the target, in cm), it can be inferred that neutrons are originating from the target. Otherwise, neutrons are from the surrounding component.

¹neutron momentum (u,v,w) gives direction information. It is known that primary protons are travelling along +z axis. w will be a negative number if neutrons are scattered from the frontal wall component

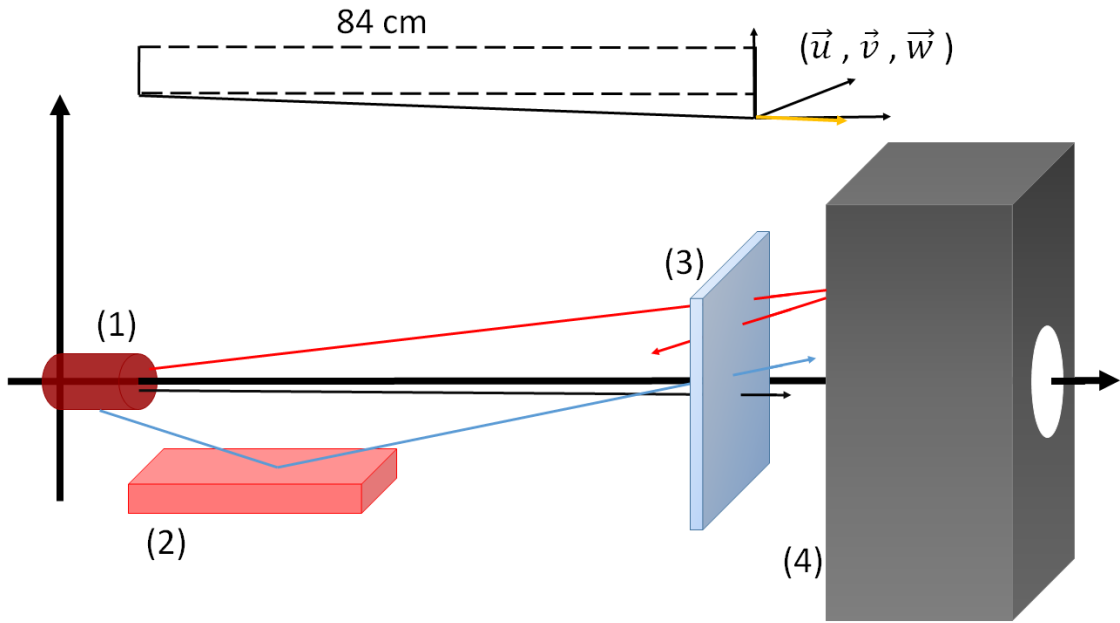


Fig. 4.23 Schematic diagram of neutron direction. (1), (2), (3), and (4) represent the tungsten target, part of shielding, CUP-TOF detector, and collimator. In addition, black line, red line, and blue line stand for a DC neutron, FWC neutron, and SC neutron.

$$R^2 = (y - M \times v)^2 + (x - M \times u)^2 \quad (4.1)$$

where $M = \frac{z}{w}$

Figure 4.24 shows that DC has two peak values, the first one is about 0.5 (at about 1 MeV) and the second one is about 0.26 (at about 100 MeV). DC dominates neutron yield at the CUP-TOF position at the energy between 1 MeV and 10 MeV. FWC dominates neutron yield at the CUP-TOF position at the energy less than 1 MeV, as well as SC. However, SC stretches up to energy around 100 MeV.

Geant4 modelling results and TSL results are shown in [Prokofiev et al., 2014], the things they have in common are that DC dominates neutron yield at the CUP-TOF position at the energy between 1 MeV and 10 MeV, FWC vanishes out at around 10 MeV. The differences are that both FWC and DC from the Geant4 modelling are lower than that of TSL result but SC is just the opposite, see Table 4.6.

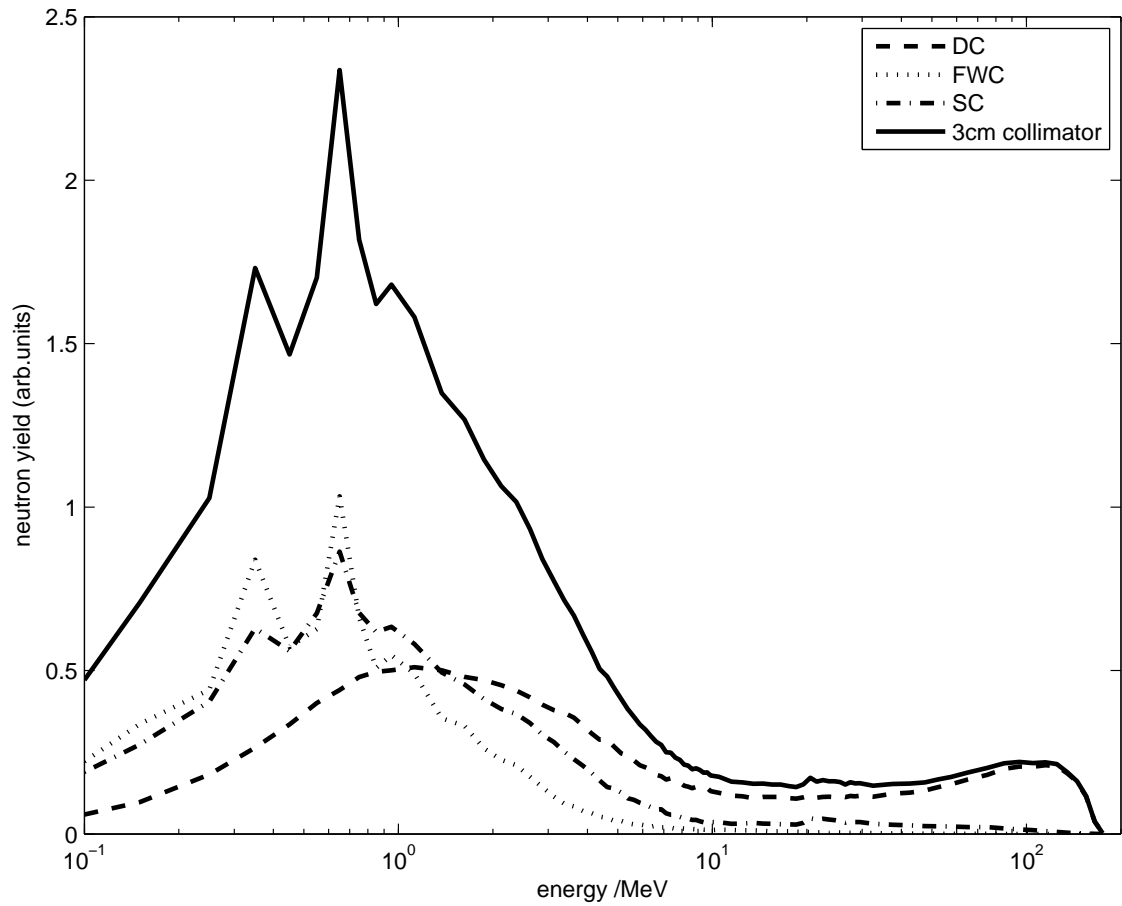


Fig. 4.24 Simulated neutron yield with 3 cm collimator at the CUP-TOF position and three components. The dashed line, dotted line, dash-dotted line represent neutrons directly from the target, frontal wall component, and surroundings component, respectively. The solid line represents the sum of the DC, FWC, and SC components, which is the neutron yield with 3 cm collimator at the CUP-TOF position, in the lethargy scale.

Table 4.6 Three components percentage over neutron yield below 10 MeV with 3 cm collimator at the CUP-TOF position

component	DC	SC	FWC
Geant4 modelling	21.35%	37.08%	43.81%
TSL modelling	30.96%	23.81%	53.33%

4.2.5 Time of flight spectra of fission events $^{238}\text{U}(n, f)$

In the real life, neutron cannot be counted like the simulation do because it cannot induce ionization directly. However, neutrons can be recorded according to charged-secondary particle produced by neutron interaction with nucleus which is likely to cause ionization. The dominant reactions of neutron interaction with matter are nuclear fission, scattering (elastic and inelastic), captures, and radiative capture. The Thin-Film Breakdown Counter (TFBC) was used in TSL ANITA for spallation neutron source [Prokofiev et al., 2014] to measure the number of events of neutron interaction with uranium(238). In another word, the ionization chamber of $^{238}\text{U}(n, f)$ is the basis of cross-section measurement. In Geant4 modelling, the number of neutrons at the CUP-TOF position and the SUP are calculated. In order to compare Geant4 simulation results with experimental results from the TSL ANITA, $^{238}\text{U}(n, f)$ cross-section [Carlson et al., 2009] was used to evaluate the number of fission events. Figure 4.25 shows $^{238}\text{U}(n, f)$ cross-section versus neutron energy [Carlson et al., 2009], which helps with obtaining time of flight spectrum of $^{238}\text{U}(n, f)$ fission events. In addition, the cross-section of $^{238}\text{U}(n, f)$ reaction was used to calculate neutron energy between 1 MeV and 200 MeV.

Figure 4.26 exhibits data processing of time of flight spectra at the CUP-TOF position, a few time correction were done for obtaining time-of-flight spectra from the raw modelling data, for instance, folding with $^{238}\text{U}(n, f)$ cross-section, frame overlap events. Figure 4.26d shows time of flight spectra of $^{238}\text{U}(n, f)$ fission events in TFBC at the CUP-TOF position. Here time of flight starts from proton emission until to neutron being detected at the CUP-TOF position. According to raw data, time range is chosen from 0 to 180 ns due to the following reason. At the beginning, the time range is chosen from 0 up to 800 ns with 799 bins and neutron yield above 180 ns is likely to decline only slowly and the number of neutrons per unit area is about 10.82% of the highest peak. In addition, TOF spectra of fission events in TFBC at the CUP-TOF position shown in paper [Prokofiev et al., 2014], which gives micropulse period of 45 ns (a quarter of 180 ns). Therefore, the time bin now

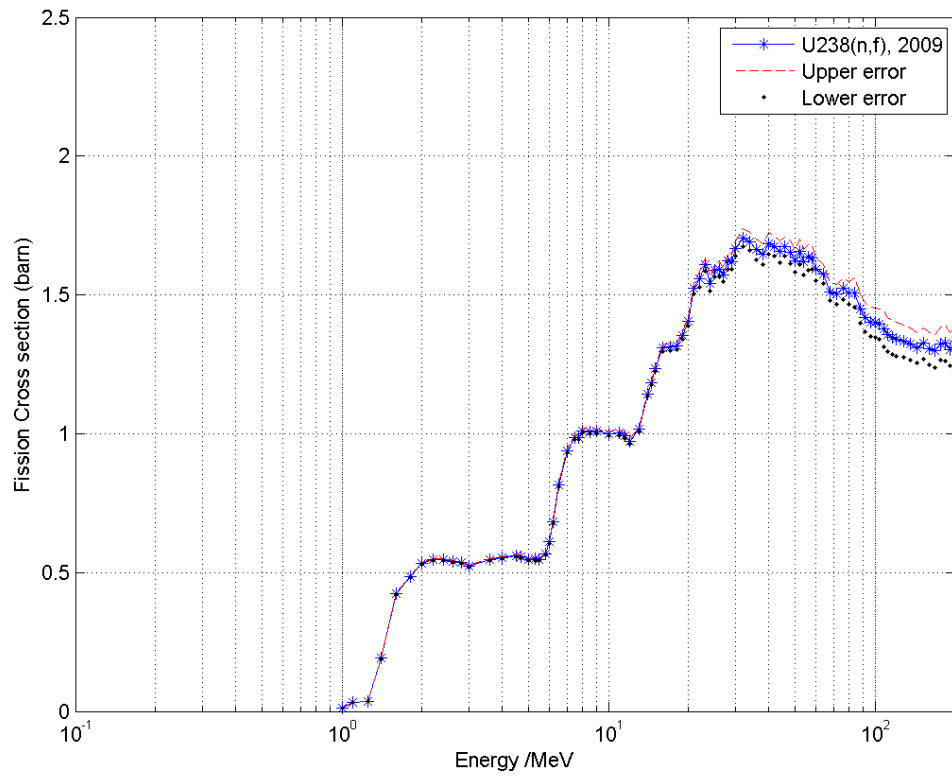
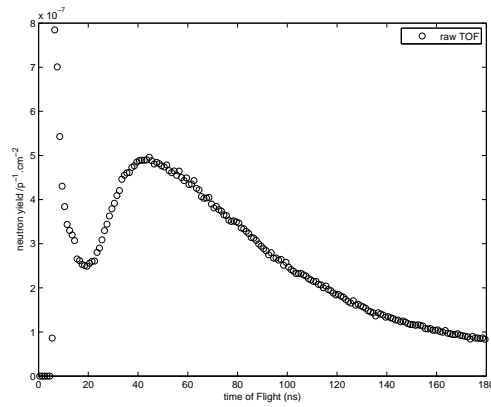
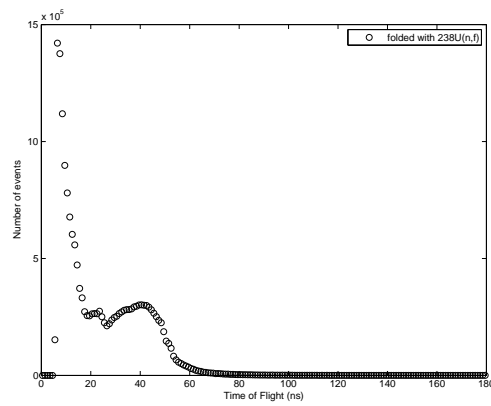


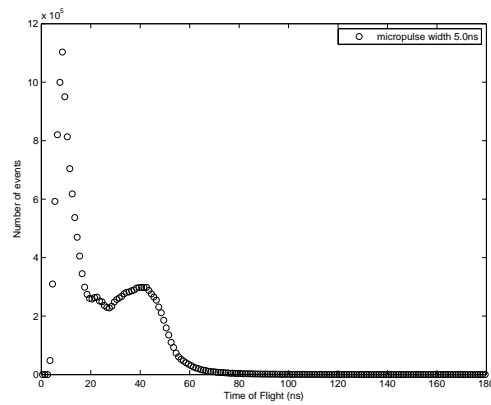
Fig. 4.25 $^{238}\text{U}(n, f)$ cross-section [Carlson et al., 2009]



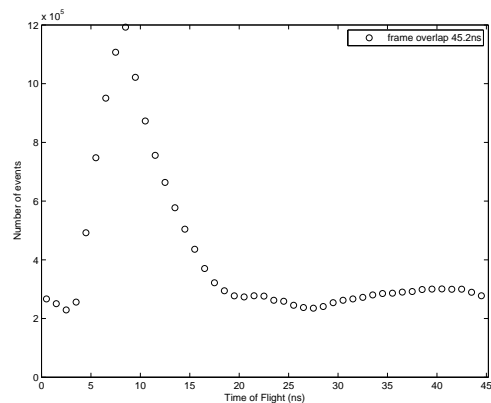
(a) Raw TOF



(b) folded with $^{238}\text{U}(n, f)$



(c) micropulse width 5 ns



(d) frame overlap 45.2 ns

Fig. 4.26 Time of flight spectrum at the CUP-TOF position, with 3 cm collimator

is from 0 to 180 ns with 180 bins (1 second per bin). The two peaks (6.5, $7.846e-7$) and (44.5, $4.96e-7$) are very significant, high neutron flux is concentrated on 6.5 ns and 44.5 ns.

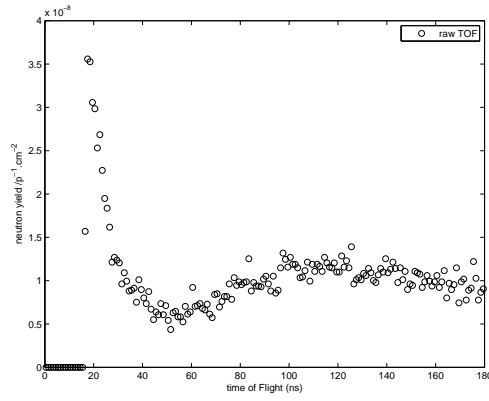
Then the number of fission events can be calculated by using raw data shown in Figure 4.26a. After folding with cross-section of $^{238}\text{U}(n, f)$ [Carlson et al., 2009], the number of fission events are known, as shown in Figure 4.26b. The macro-pulse repetition period is 45.2 ns, and each macro-pulse has micro-pulse structure of 5 ns¹. Therefore, those overlap neutrons originated with 5 ns between pulses at the TSL ANITA (the slow neutrons from a preceding pulse and fast neutrons are able to be detected at the same time). Figure 4.26d shows the result of frame overlap by using modulus operator of micro-pulse in each macro-pulse.

Figure 4.26d predicts about 6.25 ns (FWHM) for charged secondaries losing energies in sensitive volume of TFBC and the FWHM is about 7.2 ns from the TSL simulation results [Prokofiev et al., 2014]. The ratio of peak to baseline on the number of fission events is 4.286 (Geant4 modelling) and 4.286 (TSL simulation), which agree quite well. The fission TOF spectrum is dominated by a prominent peak at $ToF \simeq 8.57$ ns, which correspond to the high energy peak at around 100 MeV in Figure 4.24.

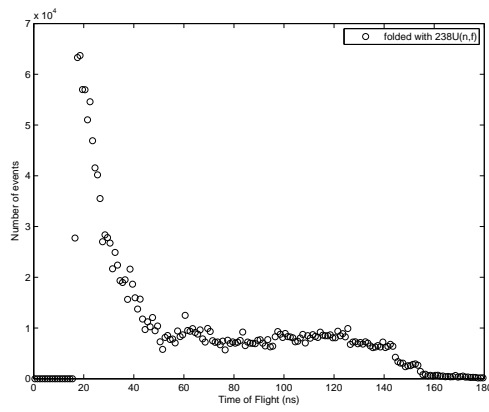
Figure 4.27 shows the process of how TOF spectra obtained according to raw data. The time range is chosen from 0 up to 180 ns with 180 bins (1 second per bin). The raw data are folding with $^{238}\text{U}(n, f)$ cross-section and then overlapped neutrons originated with micro-pulse 5 ns between each macro-pulse repetition period 45.2 ns. The frame overlap events are corrected by fitting micro-pulse in each macro-pulse period.

Figure 4.27d shows about 14.29 ns (FWHM) for charged secondaries losing energies in sensitive volume of TFBC and the FWHM is about 14 ns from the TSL simulation results [Prokofiev et al., 2009]. The ratio of peak to baseline on the number of fission events is 3.179 (Geant4 modelling) and 3.333 (TSL simulation), which agree quite well. The fission TOF spectrum is dominated by a prominent peak at $ToF \simeq 19.5$ ns, which correspond to the high energy peak at around 100 MeV in Figure 4.20.

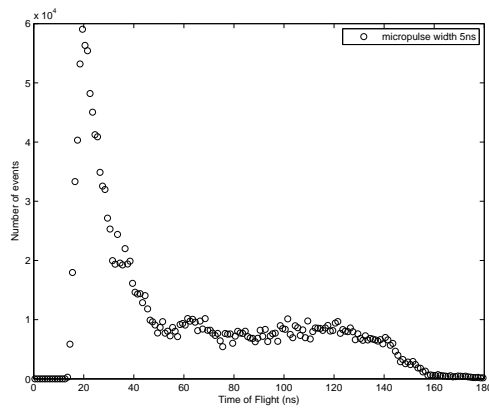
¹The information is obtained from Alexander V. Prokofiev through email



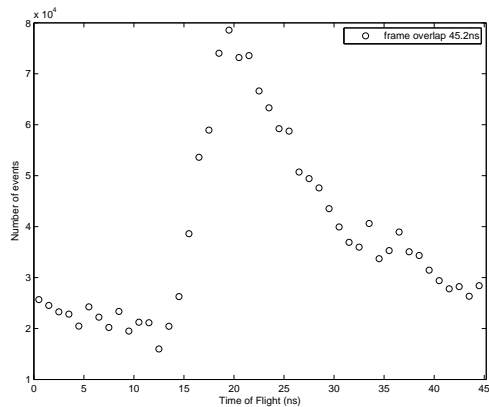
(a) Raw TOF



(b) folded with $^{238}\text{U}(n, f)$



(c) micropulse width 5 ns



(d) frame overlap 45.2 ns

Fig. 4.27 Time of flight spectrum at the SUP, with 10.2 cm collimator

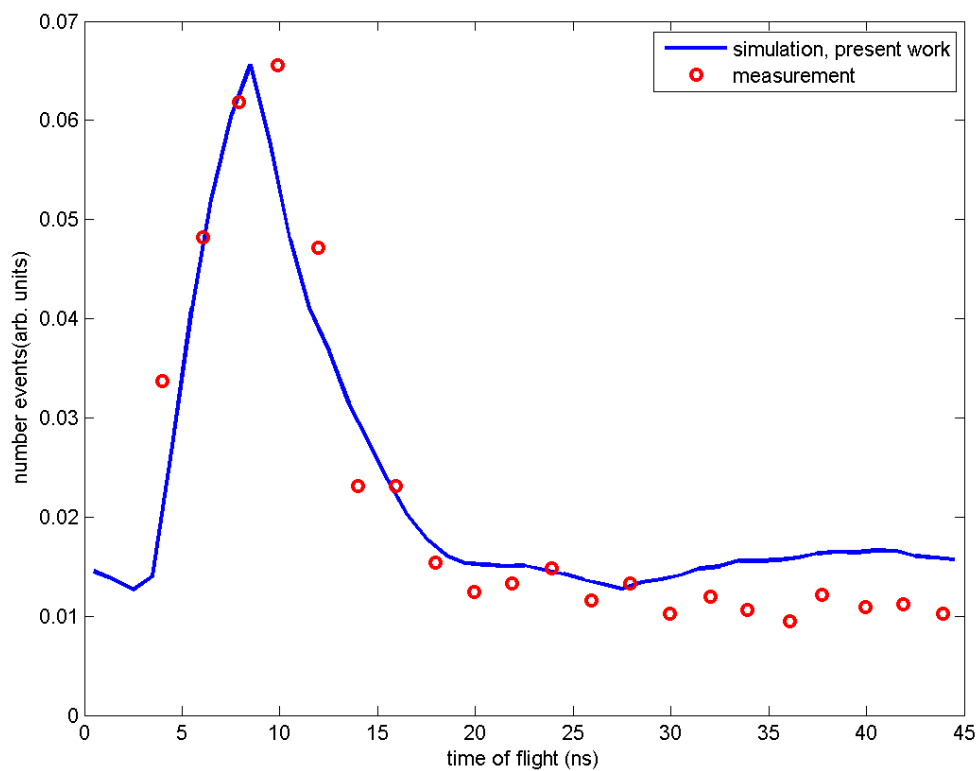


Fig. 4.28 Comparison of experimental [Prokofiev et al., 2014] and Geant4 simulated TOF spectra folding with $^{238}\text{U}(n, f)$ fission at the CUP-TOF position. measurement: from TSL measurement, which is published [Prokofiev et al., 2014]. simulation, present work: from Geant4 calculation of SNS model at ANITA facility.

Figure 4.28 shows a comparison of simulated time of flight spectrum and experimental one at CUP-TOF position with 3 cm collimator. The shape of simulated results agrees well with experiment data. The continuum beyond about 30 ns, corresponding to neutrons below about 40 MeV. It illustrates the event number of neutrons with energy less than 40 MeV in the calculation results are higher than that in the experimental results. Thus, the number of neutrons with energy greater than 40 MeV is less than that in the experimental results due to normalization.

4.2.6 Neutron beam profiles at the CUP, and SUP

Several special positions in the central area at the CUP, $60\text{ cm} \times 60\text{ cm}$, are chosen to calculate neutron flux with using Geant4 toolkit. The measured data are available for 11 positions in the neutron field in the vertical axis (along trolley sled) and 3 positions in the horizontal axis [Prokofiev et al., 2014]. The real measurement positions in the horizontal axis are less than that in the vertical axis because of the dimensions of the trolley sled. However, Geant4 modelling has no such practical limitation for calculating neutron beam profiles at the CUP. In Geant4 modelling, 50 equally spaced positions in the horizontal axis from -30 cm to 30 cm , and similarly 50 equally spaced positions in the vertical axis from -30 cm to 30 cm are considered, which form the cross shape (in x-y plane) at the CUP.

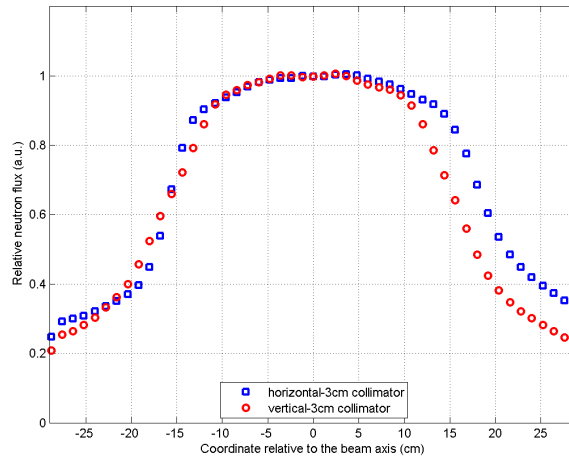
The neutron beam profiles above all neutrons, above 1 MeV, and above 10 MeV with 3 cm collimator at the CUP are shown in Figure 4.29. The displacement from the origin (0, 0) is represented in the X-axis, and the ratio of neutron flux at each position to that at the origin is presented in the Y-axis. The neutron flux in the centre at the CUP is the highest and the relative neutron flux is about 1 from the whole view. A common among these figures is a boundary (10 cm away from the origin) exists where relative neutron flux suddenly decreases. Another common is that the shape of vertical profile presents a symmetric distribution and the shape of horizontal profile shows an asymmetric distribution with a small shift. The shift and asymmetric distribution of neutron flux might be caused by a asymmetric setup of shielding components and bending magnet, as shown in Figure 4.4.

Comparing Figure 4.29a with Figure 4.29c, the relative flux above all neutrons in the vertical axis is around 0.7 with -15 cm displacement which is lower than relative flux above 10 MeV (0.9). The relative neutron flux in the vertical axis for all neutrons is 0.2 which is higher than that for neutrons above 10 MeV at the edge (0.1). It illustrates that neutron flux above all neutrons is higher than that above 10 MeV at the same displacement. The relative neutron flux above all neutrons is similar to Gauss normal distribution and relative neutron flux above 10 MeV presents a stable value between -10 cm and 10 cm.

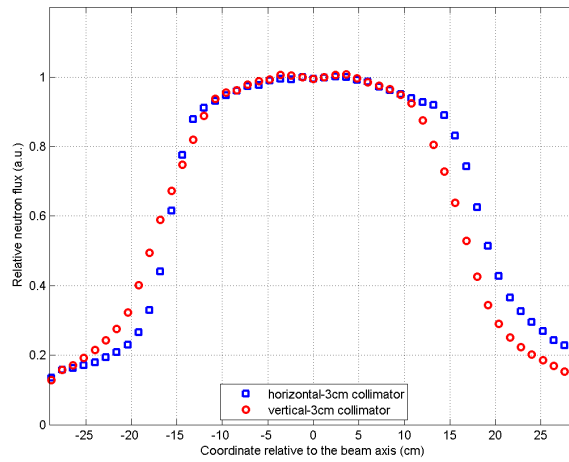
Figure 4.30 and Figure 4.31 show the neutron beam profiles with 10.2 cm collimator and with 30 cm collimator at the CUP and these two have a lot in common with Figure 4.29. The neutron beam profiles are significantly reduced from ± 10 cm in axes. The vertical profile is bilateral symmetry, but the horizontal profile is not symmetrical (relative neutron flux is higher in positive axis than negative axis).

Figure 4.32 shows the neutron beam profiles above 1 MeV, and above 10 MeV with 3 cm collimator at the SUP. The displacement from the origin (0, 0) is represented in the X-axis, and the ratio of neutron flux at each position to that at the origin is presented in the Y-axis. The neutron flux in the centre at the SUP is the highest and the relative neutron flux is about 1 more or less from the whole view. These figures have the same boundary (2 cm away from the origin) exists where relative neutron flux suddenly decreases. Comparing Figure 4.32a with Figure 4.32b, the shape of relative flux above 1 MeV in the vertical axis is quite similar with the shape of relative neutron flux above 10 MeV. The number of neutrons with energy between 1 MeV and 10 MeV is largely distributed on edge of the umbra region than neutrons above 10 MeV at the SUP. The width of neutron beam profile is dependent on the dimension of collimator by comparing Figure 4.32 with Figure 4.33.

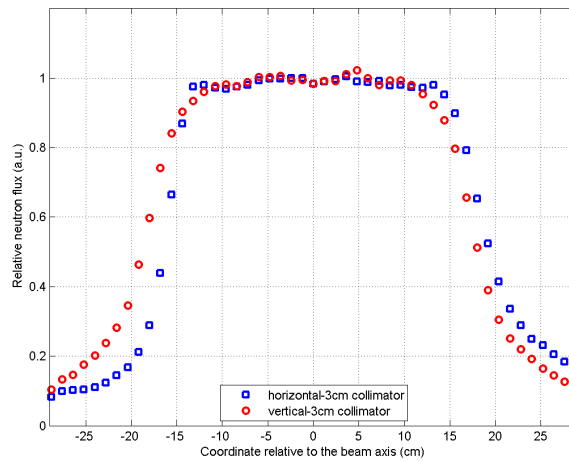
Figure 4.33 and Figure 4.34 both show high fluctuations in curves of neutron beam profile because of less number of neutrons in the region from -10 cm to 10 cm or -20 cm to 20 cm. These neutron beam profiles are normalized to 1 at itself center neutron flux. The fluctuation in curves represents the neutron flux outside of center region is more or less than the centre value. The number of neutrons does have an effect on fluctuation. See



(a) above all

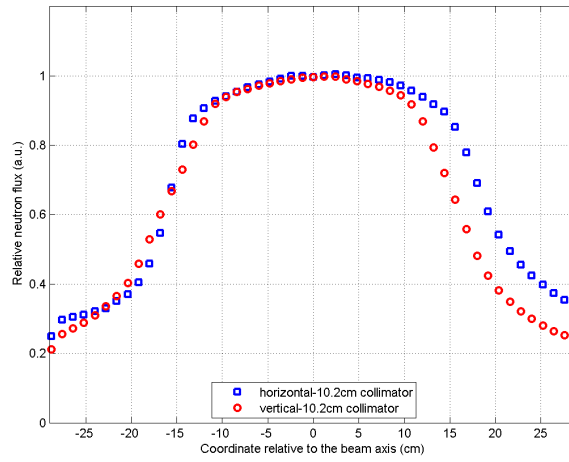


(b) above 1 MeV

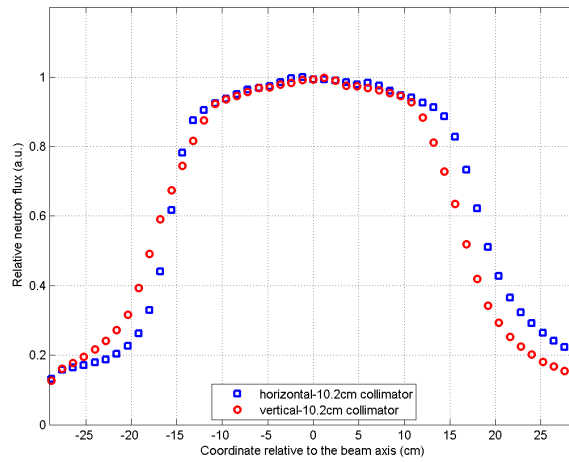


(c) above 10 MeV

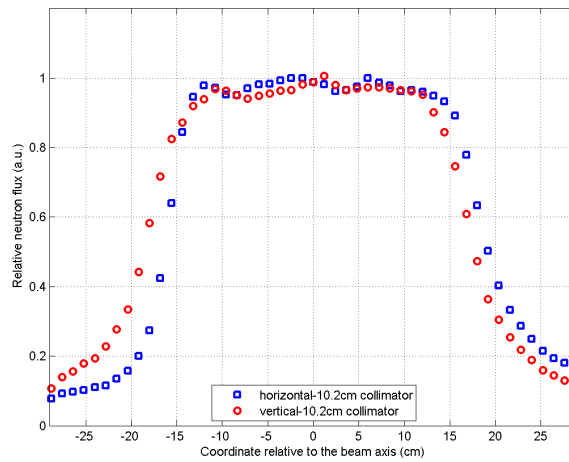
Fig. 4.29 Neutron beam profile at the CUP with 3 cm collimator. Red circles show positions in the vertical axis, and blue squares show positions in the horizontal axis.



(a) above all

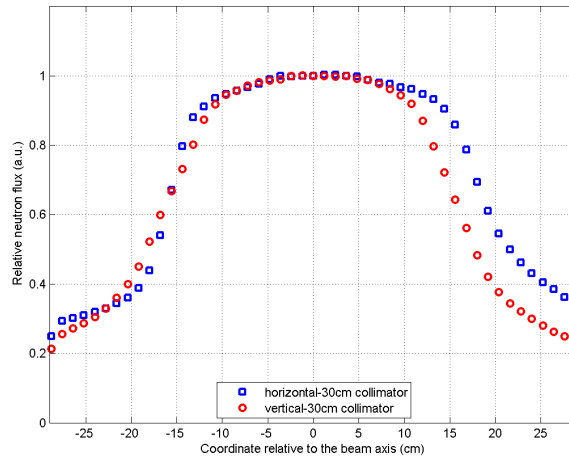


(b) above 1 MeV

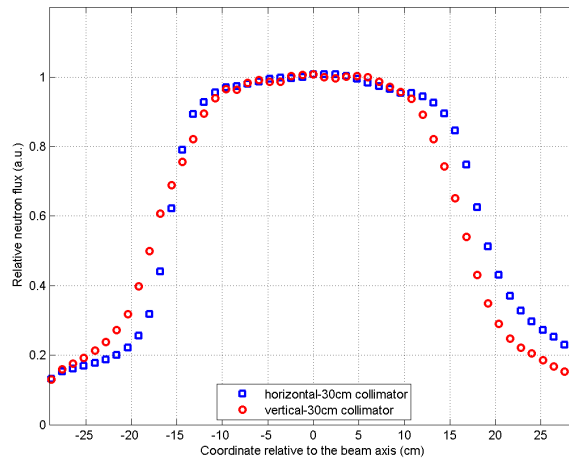


(c) above 10 MeV

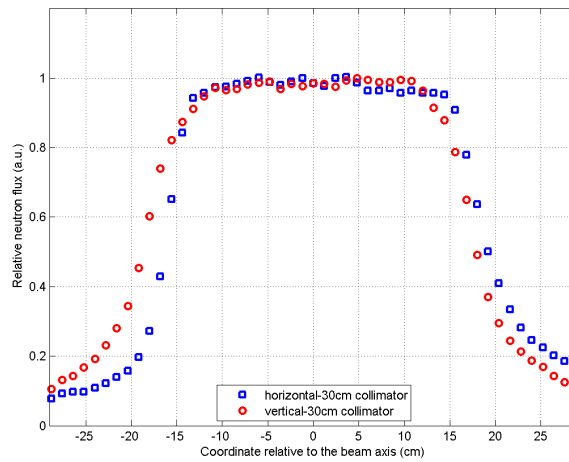
Fig. 4.30 Neutron beam profile at the CUP with 10.2 cm collimator. Red circles show positions in the vertical axis, and blue squares show positions in the horizontal axis.



(a) above all

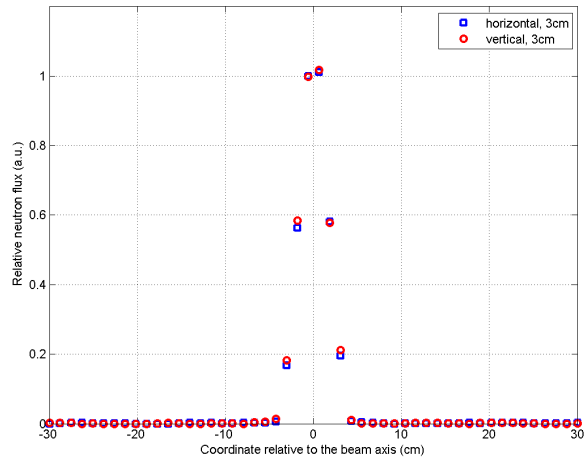


(b) above 1 MeV

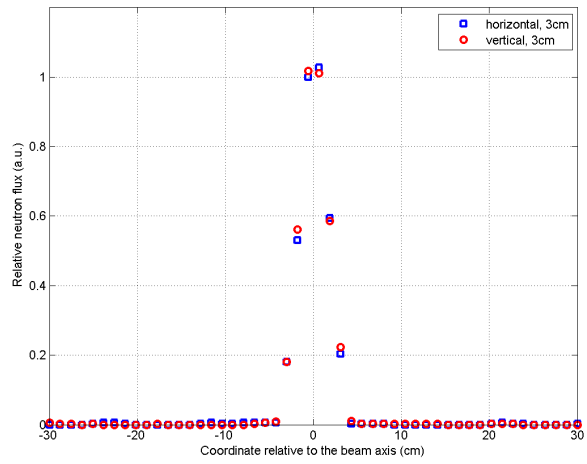


(c) above 10 MeV

Fig. 4.31 Neutron beam profile at the CUP with 30 cm collimator. Red circles show positions in the vertical axis, and blue squares show positions in the horizontal axis.



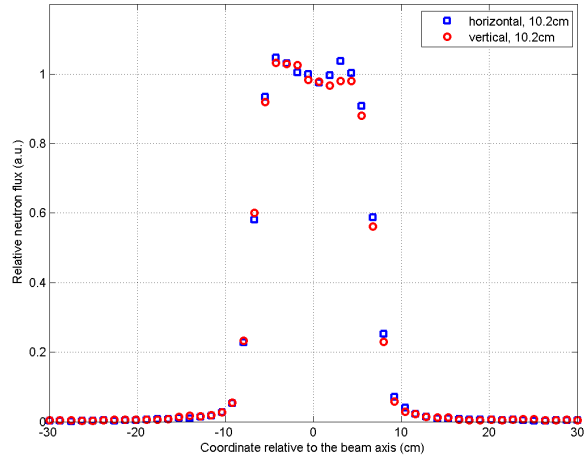
(a) above 1 MeV



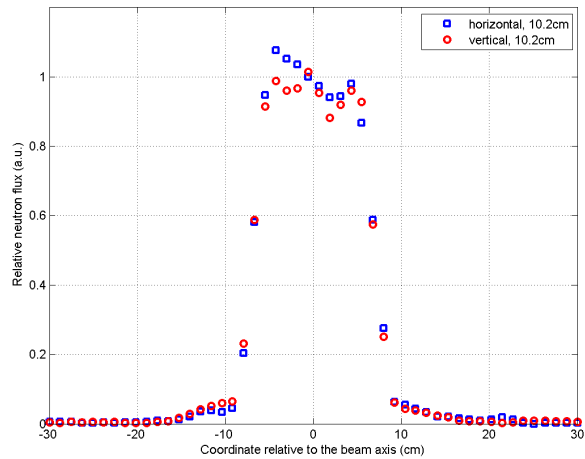
(b) above 10 MeV

Fig. 4.32 Neutron beam profile above 1 MeV, and above 10 MeV at the SUP with 3 cm collimator. Red circles show positions in the vertical axis, and blue squares show positions in the horizontal axis.

any neutron beam profile at the CUP, the fluctuation is not obvious due to a large number of neutrons.



(a) above 1 MeV

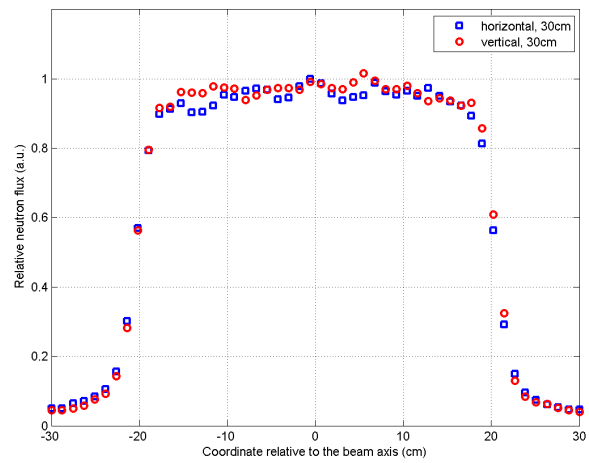


(b) above 10 MeV

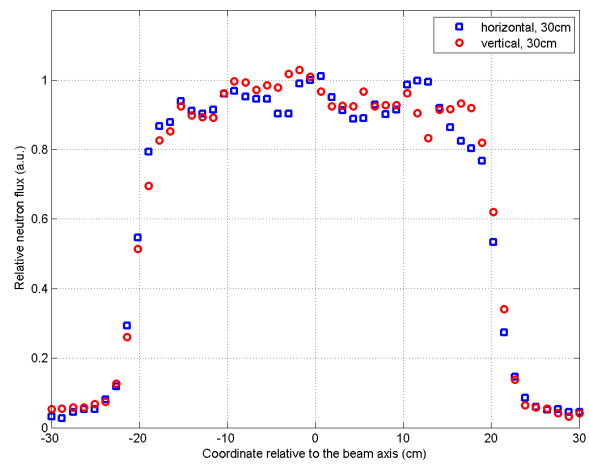
Fig. 4.33 Neutron beam profile at the SUP with 10.2 cm collimator. Red circles show positions in the vertical axis, and blue squares show positions in the horizontal axis.

4.2.7 Neutron beam spatial profiles folding with $^{238}\text{U}(n, f)$ cross-section at the CUP-TOF, and SUP

Figure 4.35 shows horizontal and vertical neutron beam profiles folding with $^{238}\text{U}(n, f)$ cross-section at the CUP-TOF position with different dimension collimators. The fission event is obtained by folding $^{238}\text{U}(n, f)$ cross-section with neutron flux. Here, 50 equally



(a) above 1 MeV



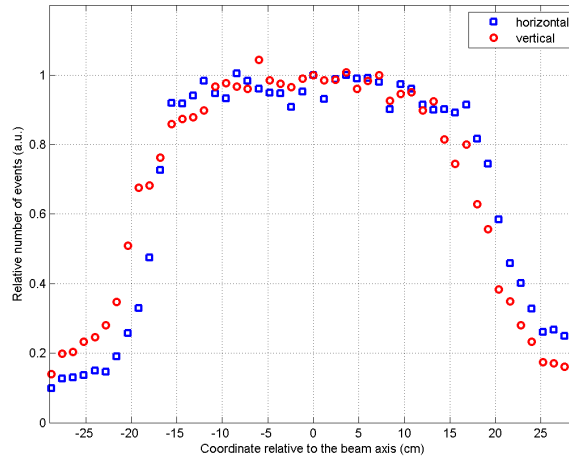
(b) above 10 MeV

Fig. 4.34 Neutron beam profile at the SUP with 30 cm collimator

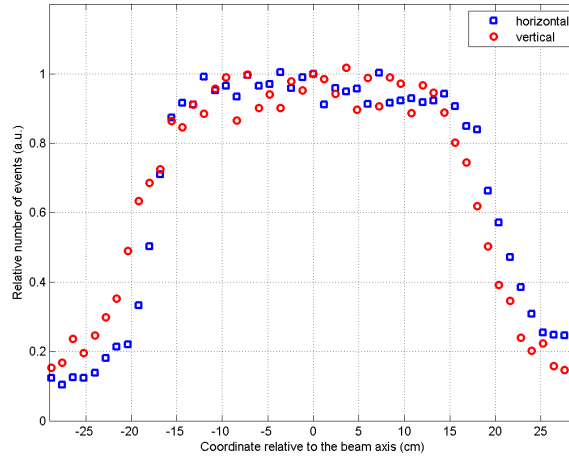
spaced positions in the horizontal axis from -30 cm to 30 cm, and 50 equally spaced positions in the vertical axis from -30 cm to 30 cm are considered at the CUP-TOF position to calculate neutron flux in Geant4 modelling. The TFBC whose radius of 0.45 cm was used to measure fission events during accelerated SEE testing at ANITA facility. In order to ensure the same as real experimental condition, a circle of radius 0.45 cm centred on each position is chosen at CUP-TOF position for analyzing neutron beam profiles. Y-axis represents ratio of fission events at each position to that at the origin. Figure 4.35 shows that the shape of neutron beam profiles above all neutrons with 3 cm, 10.2 cm, and 30 cm collimators at the CUP-TOF position are very similar. The widths of both neutron beam profiles, horizontal and vertical, are very similar with each dimension of collimator at the CUP-TOF position. It illustrates the relative fission events are independent on dimension of collimator at the CUP-TOF position. The neutron field has been found to be the highest and uniform within a 15 cm radius at the CUP-TOF position.

The neutron beam profiles of horizontal and vertical from [Prokofiev et al., 2014] show a sharply decrease between 10 cm (-10 cm) and 20 cm (-20 cm). The experimental results and Geant4 modelling data both show the start point of sharply decreasing is at ± 10 cm. However, the decreasing rate from the experimental data is faster than that from Geant4 modelling data reference to Figure 4.35. The relative neutron flux in the vertical axis from the ANITA experimental data is 0.329 (0.362) at displacement of -15 cm (15 cm). And the relative flux above all neutrons in the vertical axis from the Geant4 modelling data is around 0.85 (0.75) as displacement equal to -15 cm (15 cm), which is higher compared with ANITA experimental results. This Geant4 modelling result is able to do some predictions about neutron flux distribution at the CUP-TOF position.

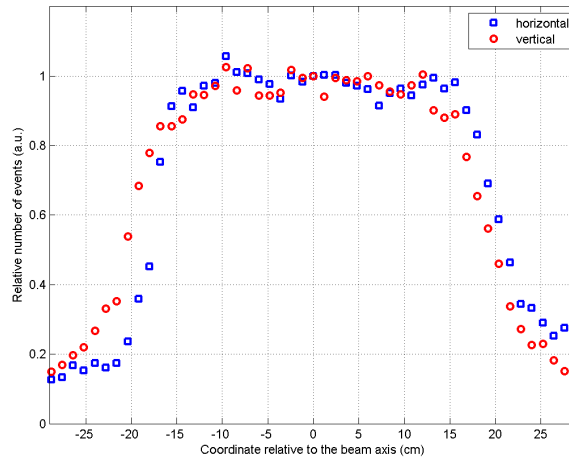
A comparison of neutron beam vertical profile from measurement and calculation results at the CUP-TOF position with 10.2 cm collimator, is shown in Figure 4.36. The number of neutron counts from Geant4 simulation is folded in energy with $^{238}\text{U}(n, f)$ cross-section. The number of fission events of $^{238}\text{U}(n, f)$ (due to neutrons) is consistent with measurement data. However, the simulated neutron beam vertical profile is broader than measurement data and the sharp cut-off beyond 11 cm. The composite of realistic copper



(a) 3 cm collimator



(b) 10.2 cm collimator



(c) 30 cm collimator

Fig. 4.35 Neutron beam profiles folding with $^{238}\text{U}(n, f)$ cross-section at the CUP-TOF position with 3 cm, 10.2 cm, and 30 cm collimators

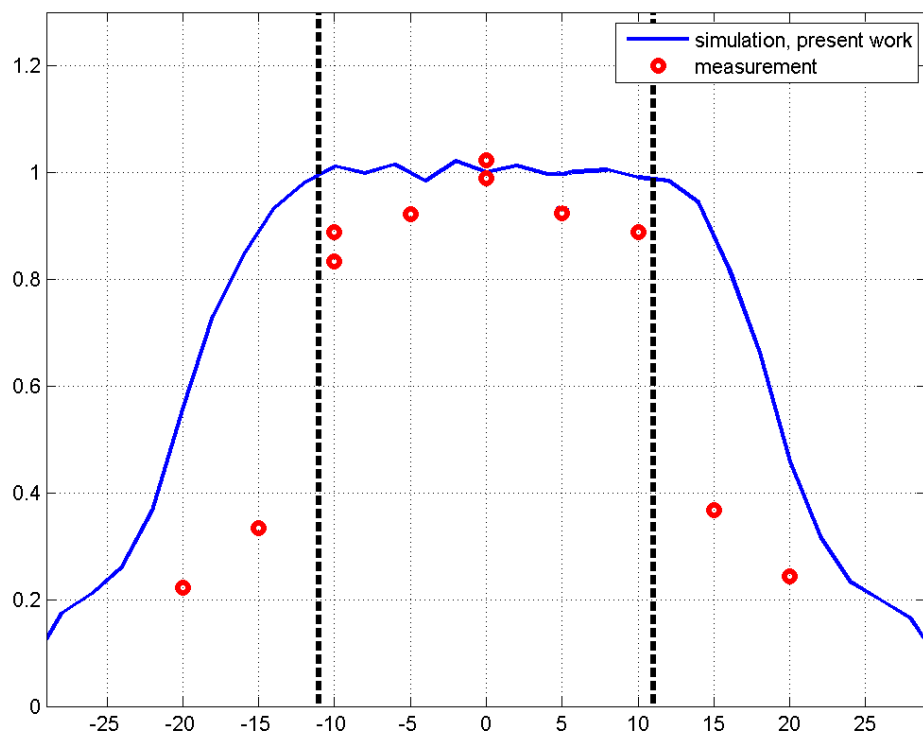


Fig. 4.36 Comparison of neutron beam vertical profile at the CUP-TOF position with 10.2 cm collimator. measurement: from TSL measurement, which is published [Prokofiev et al., 2014]. simulation, present work: from Geant4 calculation of SNS model at ANITA facility.

coil is different from the composite in modelling, which may cause neutron penetration is too high in simulation result. In the real ANITA facility, cooling water pipes are filling in the copper coils, which means hydrogen atoms are filling in copper coils. The high cross-section is able to cutting down the number of neutrons at the CUP-TOF.

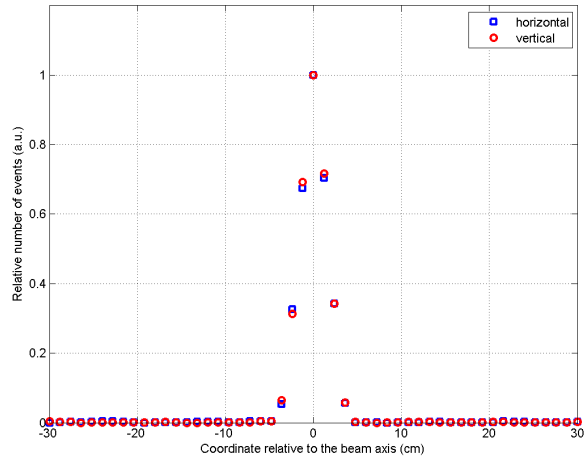
Figure 4.37 shows neutron beam profiles folding with $^{238}\text{U}(n, f)$ cross-section at the SUP. It is shown that the widths of neutron beam profile in the horizontal axis and in the vertical axis are dependent upon the dimension of collimator. The widths of neutron beam profiles, horizontal and vertical, are varying with umbra radius of each collimator.

4.3 Gamma field at the Close User Position and the Standard User Position of the ANITA facility

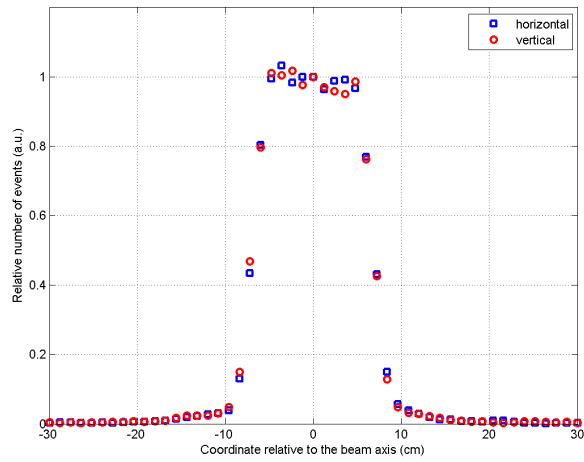
4.3.1 Gamma spatial distribution at the CUP and SUP

From the previous Section 4.2.1, spatial distribution of neutrons at the CUP and SUP were discussed according to contour plot. Again, Figure 4.38, Figure 4.39, and Figure 4.40 show photons spatial distributions at the CUP with 3 different collimators. For different collimator cases, This paragraph takes 3 cm collimator as an example to discuss the spatial distribution at different energy levels (above 0 MeV, 1 MeV, and 10 MeV) with exactly the same one used in Section 4.2.1 for neutron spatial distribution. The CUP was divided into 60×60 , $1 \text{ cm} \times 1 \text{ cm}$ equal squares in the x-y plane and high statistical noise is easy to see at the edge of the contour plot. But, it is obvious that photons yield with energy above 10 MeV is relatively small at the CUP in any collimator case. Comparing Figure 4.38b with Figure 4.38a, photons with energy below 1 MeV reduce greatly. Photon spatial distribution is quite similar with neutron spatial distribution at the CUP, which the highest yield concentrates in the centre and very few at the edge.

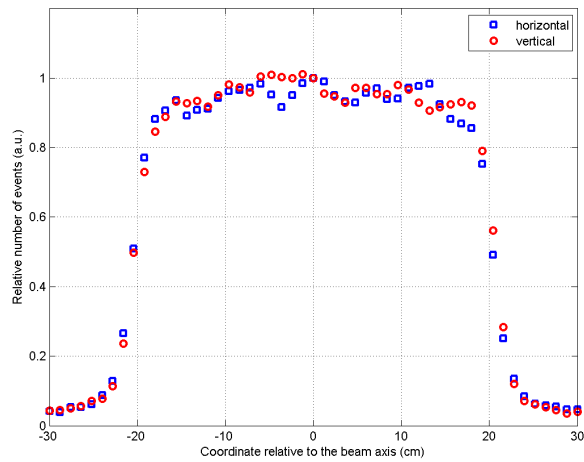
Comparing Figure 4.38a and Figure 4.40a, it shows that collimator size has an influence on photon yield at the CUP, which the collimator size is bigger and there is more photons at the CUP. A comparison of Figure 4.38b and 4.40b shows that photons above 1 MeV with



(a) 3 cm collimator



(b) 10.2 cm collimator



(c) 30 cm collimator

Fig. 4.37 Neutron beam profile folding with $^{238}\text{U}(n, f)$ cross-section at the SUP with 3 cm, 10.2 cm, and 30 cm collimators

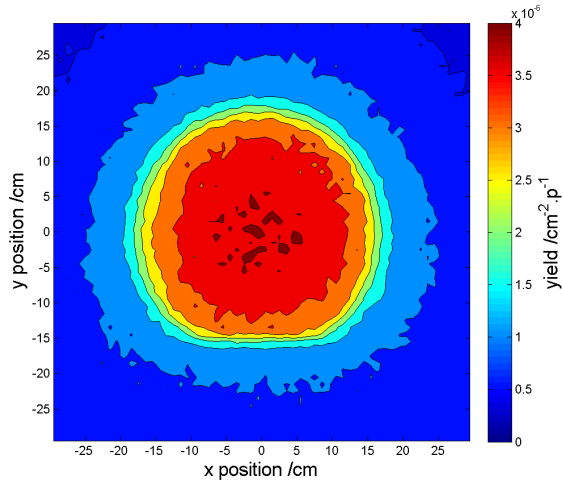
3 cm collimator is higher than that of 30 cm collimator, which means the extra photons production due to the difference in collimator size. The extra photons may be produced by neutron interaction with the collimator or from gamma scattering. It is easy to find out not only photons above 1 MeV but also photons above 0 MeV, collimator size had an impact on photon yields at the CUP. In addition, the photon yield is one order smaller than the neutron yield contribution at the CUP with the same collimator.

Now look at the photon spatial distribution at the SUP with 3 collimator cases. There are 60×60 , $2 \text{ cm} \times 2 \text{ cm}$ equal squares all over the SUP region. Figure 4.41 shows very few photons have been detected with 3 cm collimator and the highest photons yield is limited in umbra region and a low photon yield appears at the edge of penumbra region at the SUP, as well as in Figure 4.42 and Figure 4.43. The all photons yield at the SUP is more than one order smaller than that at the CUP. The photon yield above 10 MeV is very low in any collimator, see Figure 4.41c, Figure 4.42c, and Figure 4.43c. A comparison of Figure 4.43a with Figure 4.41a shows photon yield with 30 cm collimator is higher than that with 3 cm collimator at the SUP. It illustrates that the bigger the collimator size is, the higher the photon yield is at the SUP. This conclusion contrasts with that at the CUP, where a higher photon yield is induced by a smaller collimator. In terms of neutron spatial distribution, neutron yield above 1 MeV and above 10 MeV are rich and distributed at the CUP and the SUP. However, photon yield above 10 MeV are of scarcity and uneven distribution.

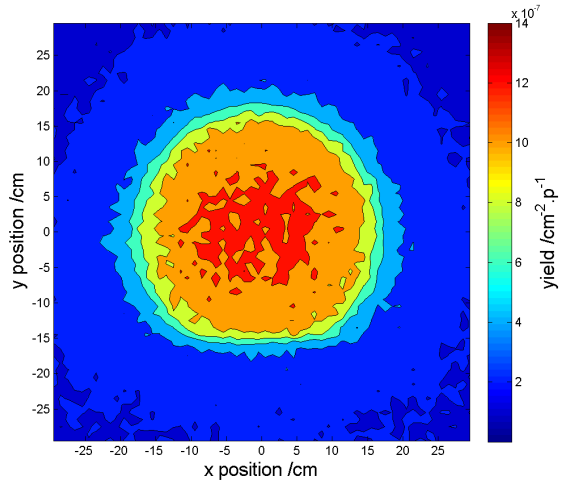
Figure 4.43c, Figure 4.42c and Figure 4.41c appear black dots because of the following two reasons, the number of photons with energy above 10 MeV at the SUP is small, and the default color of tick mark for these contour plots is black. In fact, the black parts in figures are not dots, they are enclosing lines.

4.3.2 Calculation of effective radius for γ ray at the CUP and SUP

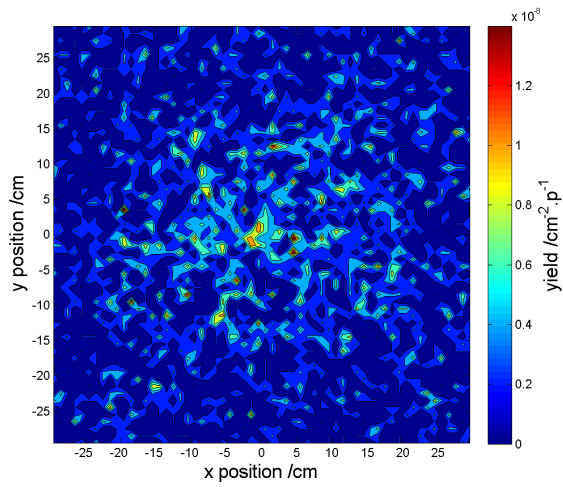
According to γ spatial distribution analysis, photon yield above 10 MeV is very low so that γ analysis was divided into considering all photons, and only above 1 MeV. Figure 4.44



(a) all photons

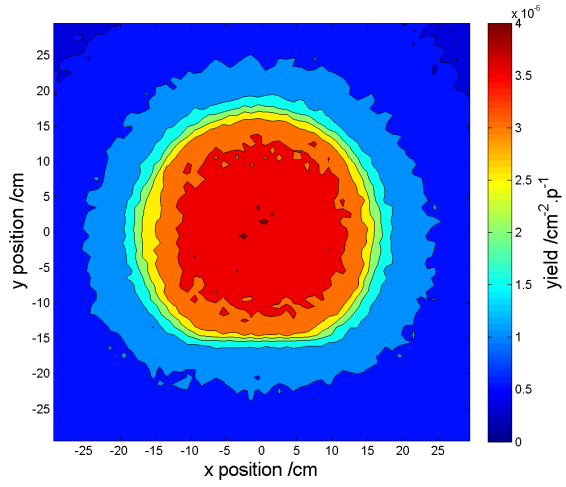


(b) photons above 1 MeV

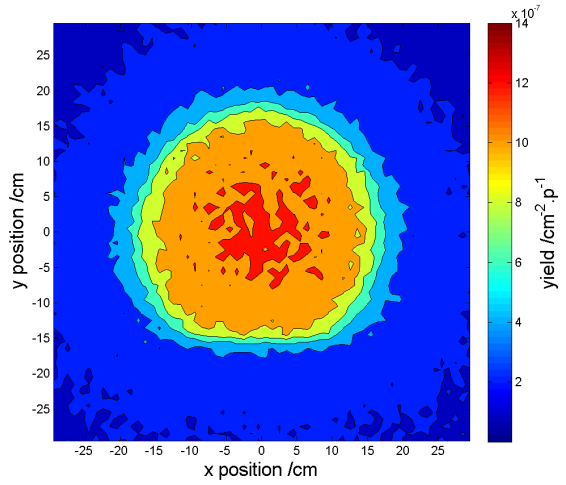


(c) photons above 10 MeV

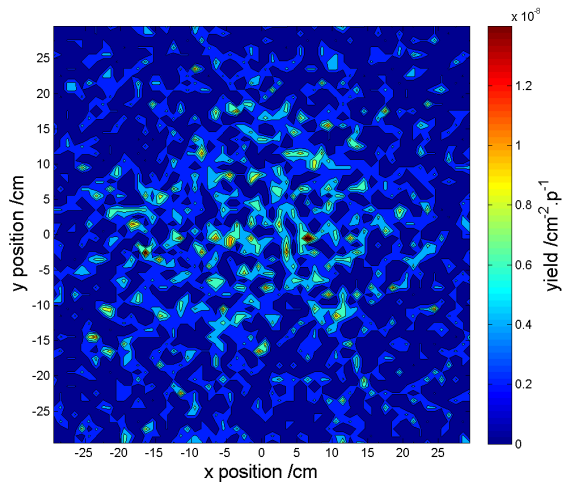
Fig. 4.38 Gamma spatial distribution at the CUP with 3 cm collimator



(a) all photons

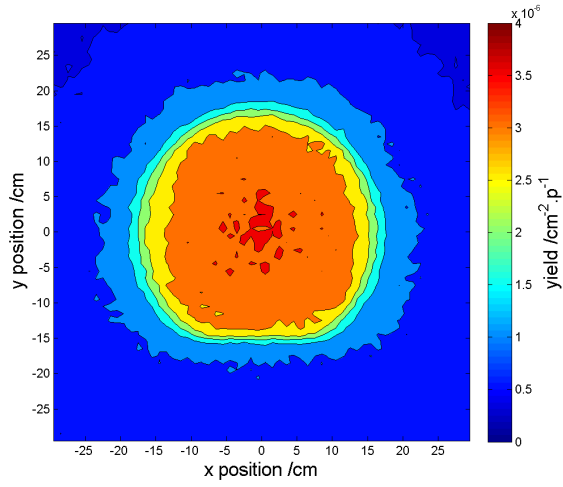


(b) photons above 1 MeV

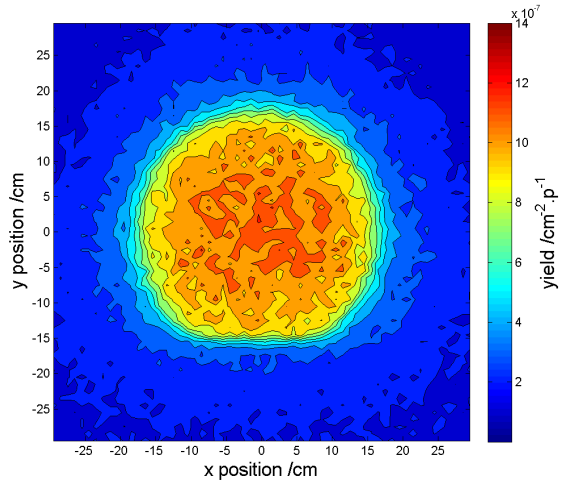


(c) photons above 10 MeV

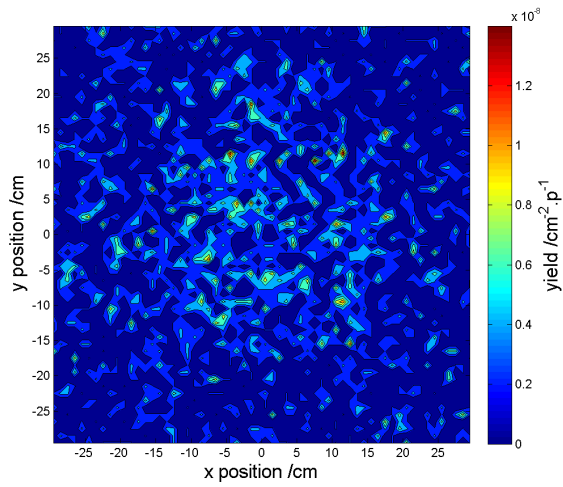
Fig. 4.39 Gamma spatial distribution at the CUP with 10.2 cm collimator



(a) all photons

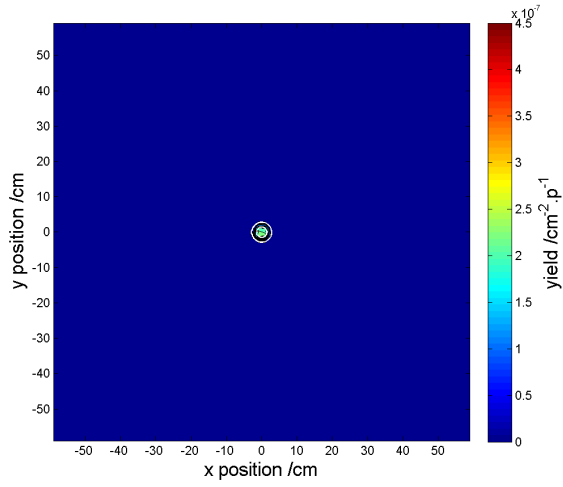


(b) photons above 1 MeV

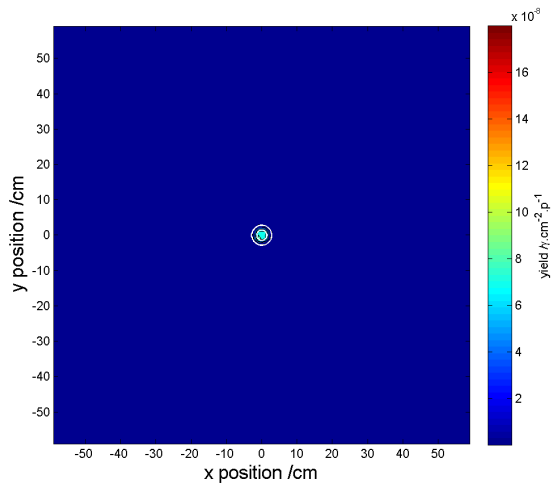


(c) photons above 10 MeV

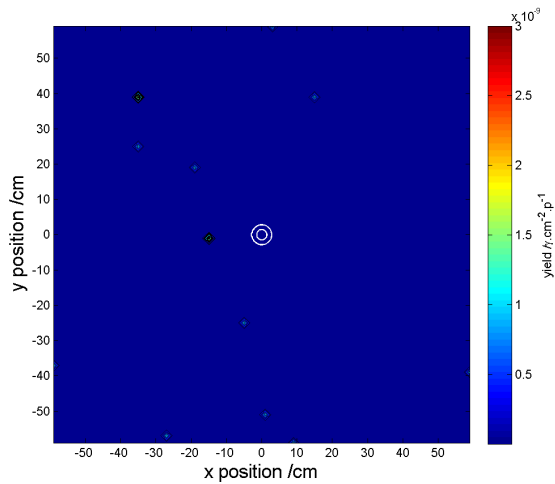
Fig. 4.40 Gamma spatial distribution at the CUP with 30 cm collimator



(a) all photons

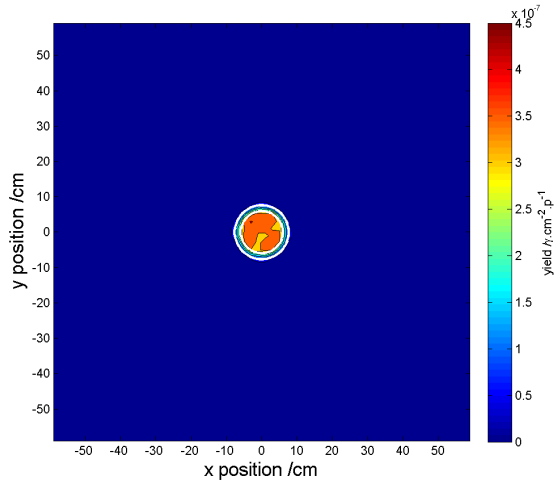


(b) photons above 1 MeV

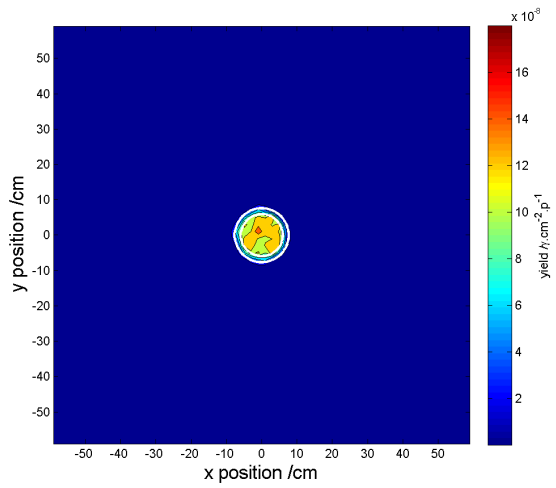


(c) photons above 10 MeV

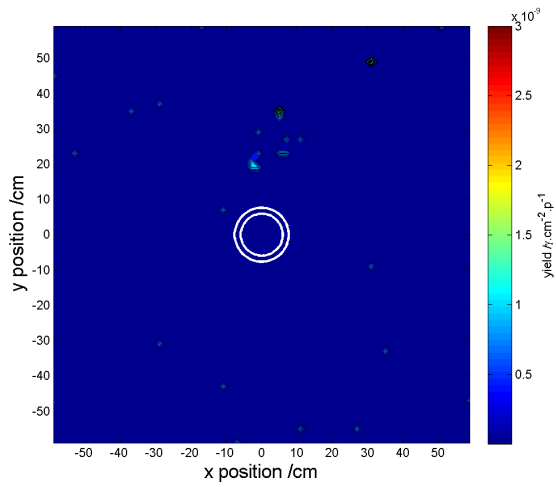
Fig. 4.41 Gamma spatial distribution at the SUP with 3 cm collimator



(a) all photons

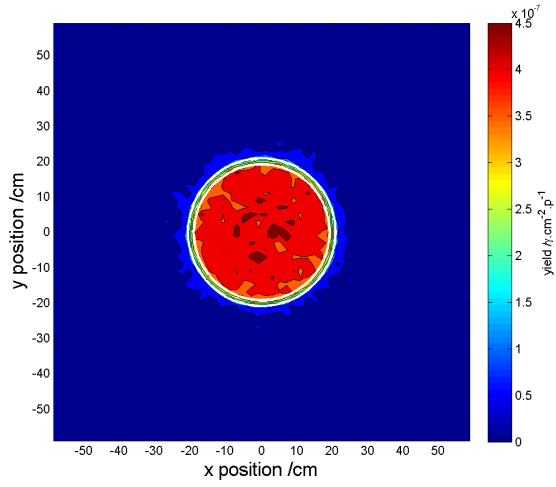


(b) photons above 1 MeV

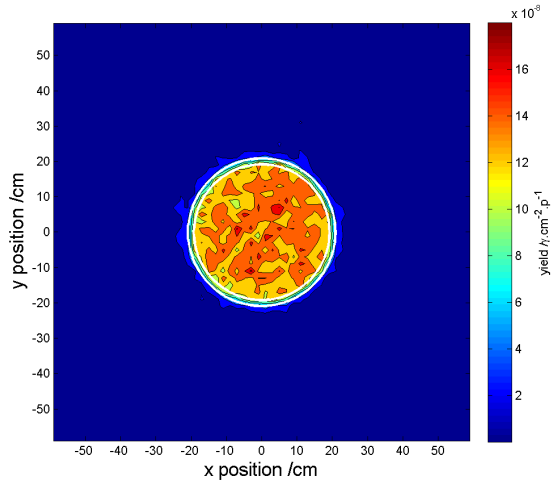


(c) photons above 10 MeV

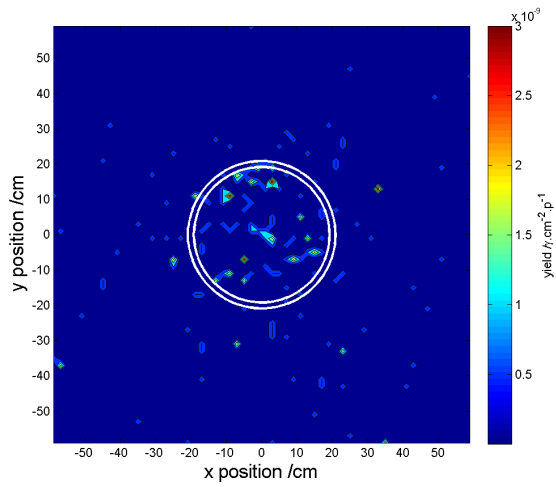
Fig. 4.42 Gamma spatial distribution at the SUP with 10.2 cm collimator



(a) all photons



(b) photons above 1 MeV



(c) photons above 10 MeV

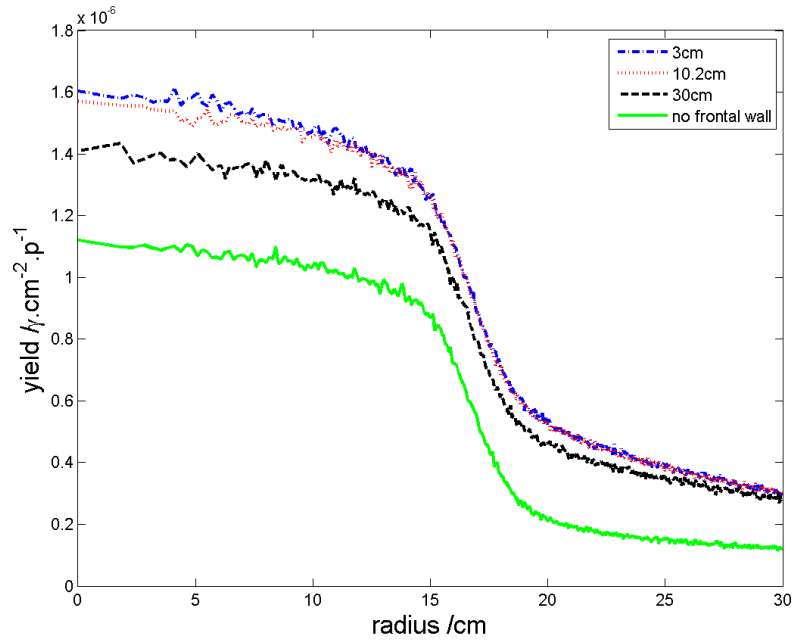
Fig. 4.43 Gamma spatial distribution at the SUP with 30 cm collimator

shows variation of γ yield with the change of the radius over all CUP with 4 collimator cases. The CUP was divided into 400 concentric circles with equal area 7.069 cm^2 . In Figure 4.44 and Figure 4.45, no frontal wall means no collimator is constructed in the simulation or could be seen as collimator aperture size is infinity. Figure 4.44a shows that when effective radius is less than 15 cm, the all photons yield has undergone a process of gentler linear decline. For different collimator cases, they have an approximate factor of decline rate, -1.43×10^{-8} . For example, Equation (4.2) shows the relation between radius (less than 15 cm) and photon yield. When effective radius is greater than 15 cm, the photon yield falls steeply until 20 cm and then begins to steady again for any collimator. In Figure 4.44, a conclusion is once again proved that photon yield is inversely proportion to collimator aperture size at the CUP.

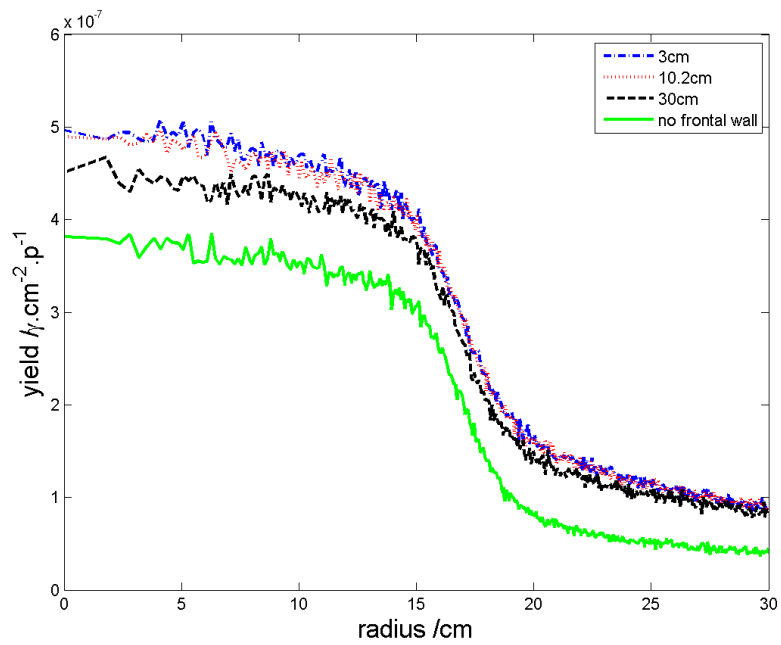
For photons with energy greater than 1 MeV, they have similar curve shapes with curves shown in Figure 4.44a but about 3 to 3.2 times less in γ yield. In addition to the above features, the photon yield above 10 MeV with 3 cm is close to that with 10.2 cm collimator at the CUP.

$$Y(R) = -1.43 \times 10^{-8}R + 1.15 \times 10^{-6} \quad (4.2)$$

In the modelling, the maximum area can be used at the SUP is $120 \text{ cm} \times 120 \text{ cm}$ in the x-y plane. There are 3600 concentric circles with same area of 3.14 cm^2 at the SUP of 3 cm collimator. For 10.2 cm, 30 cm, and no collimator cases, each SUP was divided into 400 concentric circles with equal area of 28.27 cm^2 . For Figure 4.45a and Figure 4.45b, Figure 4.45b is chosen as an example to illustrate γ yield at the SUP. Three sets of parallel lines in blue, red, and black represent umbra radius and penumbra radius of 3 cm, 10.2 cm, and 30 cm collimator. The photon yield of each collimator at the SUP keeps a constant, if the effective radius is not bigger than umbra radius. And photon yield starts to reduce rapidly from umbra radius to penumbra radius and then achieves stable low baseline. But photon yield with 30 cm collimator is not the same as 3 cm and 10.2 cm collimator when effective radius is greater than penumbra radius. The photon yield is proportion to



(a) all γ



(b) γ above 1 MeV

Fig. 4.44 Radius effect of gamma at the CUP with 3 cm, 10.2 cm, and 30 cm collimators

Table 4.7 γ yield for each collimator at the CUP

Collimator size /cm	above 1 MeV / $10^{-6} \text{ cm}^{-2} \text{ p}^{-1}$	above 0.1 MeV / $10^{-6} \text{ cm}^{-2} \text{ p}^{-1}$
3	4.93	15.73
10.2	4.86	15.27
30	4.44	13.80

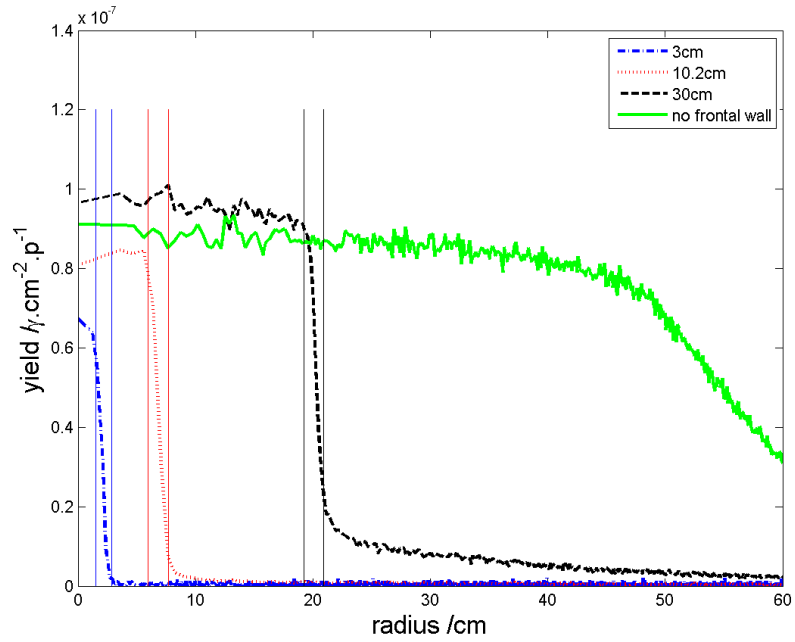
Table 4.8 γ yield for each collimator in umbra region at the SUP

Collimator size cm	above 1 MeV $10^{-7} \gamma \text{ cm}^{-2} \text{ p}^{-1}$	above 0.1 MeV $10^{-7} \gamma \text{ cm}^{-2} \text{ p}^{-1}$
3	2.3	6.7
10.2	2.8	8.3
30	3.2	9.4

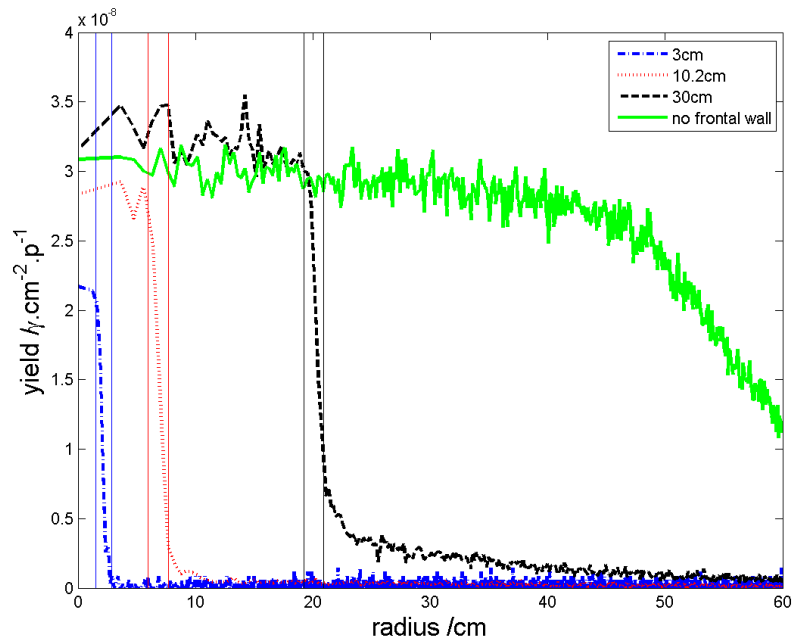
collimator size at the SUP in umbra region of each collimator, see Table 4.8. No frontal wall case can be considered as a collimator with infinite aperture hole and photon yield must be the highest at the SUP. However, the photon yield of no frontal wall is lower than that of 30 cm collimator in a radius of 20 cm in Figure 4.45, it illustrates that photon production did happen in flight of passing collimator. They are probably from neutron interactions with the inner side of the collimator. As the collimator wide open, more low energy neutrons are possible to enter the collimator. Another possibility is gamma scattering with collimator material.

4.3.3 Photon spectra at the CUP and SUP

Figure 4.46 shows differential photon spectra at the CUP and SUP with 3 collimators. Two peaks, one is at about 0.5 MeV and the other is at about 6 MeV both can be observed at the CUP and SUP. The low energy peak is the result of annihilation of the electron and positron, which cause gamma ray photons production at 0.511 MeV. A comparison of γ yield at the CUP and the SUP, photon yield at the SUP is about 10 time less than that at the CUP. Figure 4.46b shows that 3 cm collimator has the lowest photon yield compared with the other collimators at the SUP. Photon yield with energies between 0.1 MeV and 1 MeV is near to 100 times more than that energies above 1 MeV at the CUP. Photons are



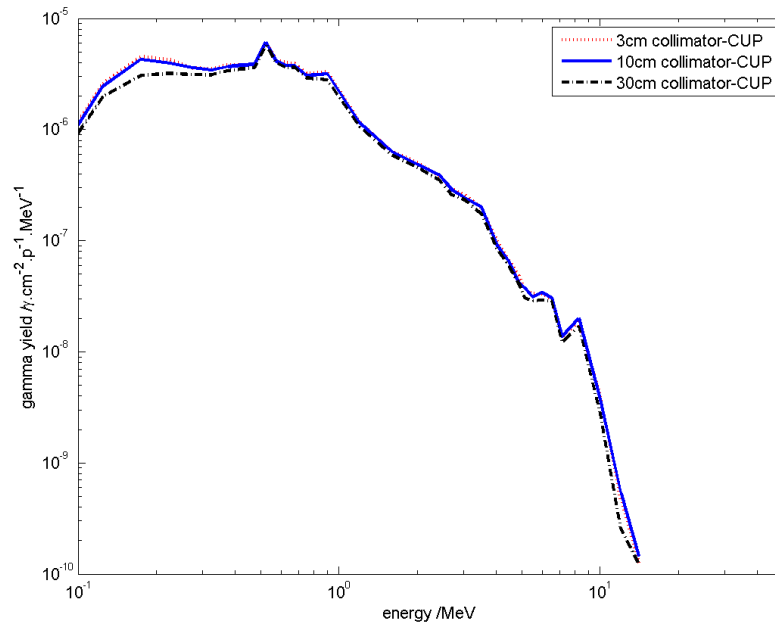
(a) all γ



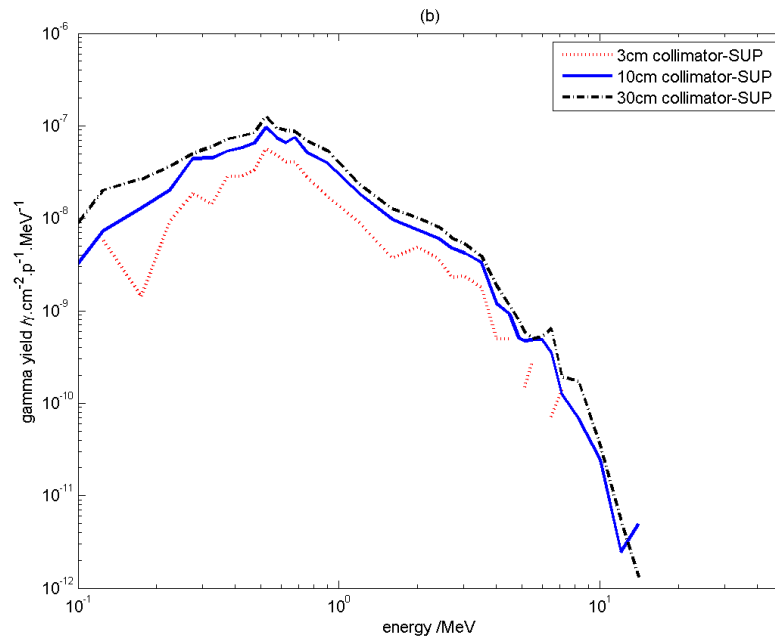
(b) γ above 1 MeV

Fig. 4.45 Radius effect of gamma at the SUP with 3 cm, 10.2 cm, and 30 cm collimators

different with neutrons, an amount of neutrons with energies is above 10 MeV but most of these photons with energy between 0.1 MeV and 1 MeV.

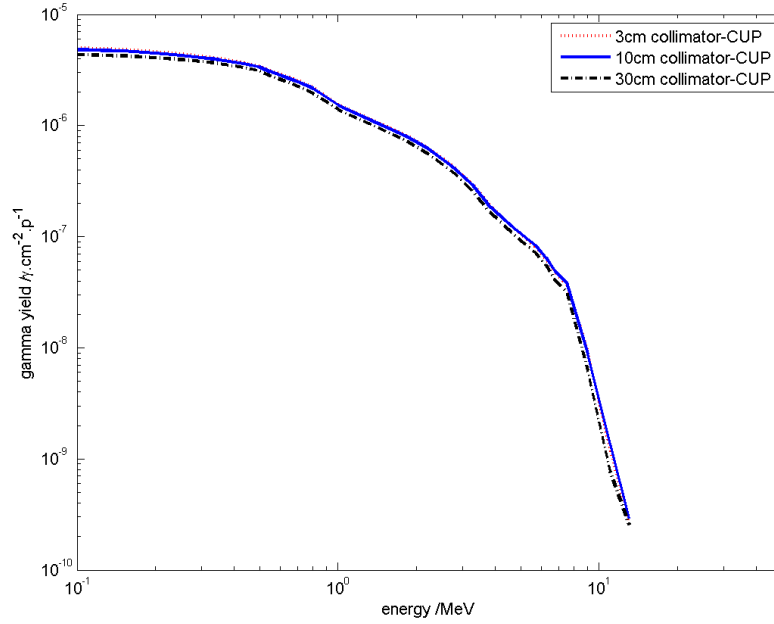


(a)

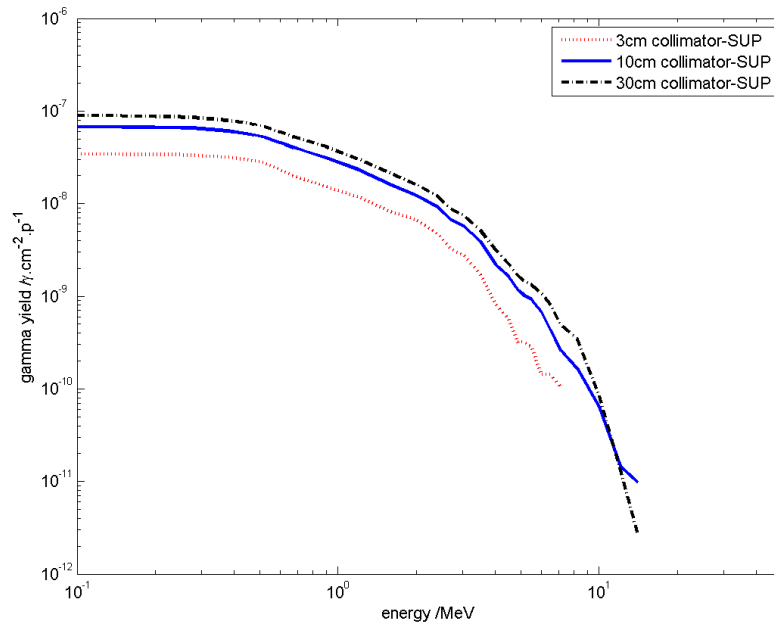


(b)

Fig. 4.46 Comparison of differential photon yield at the CUP and SUP



(a)



(b)

Fig. 4.47 Comparison of integral photon yield at the CUP and SUP

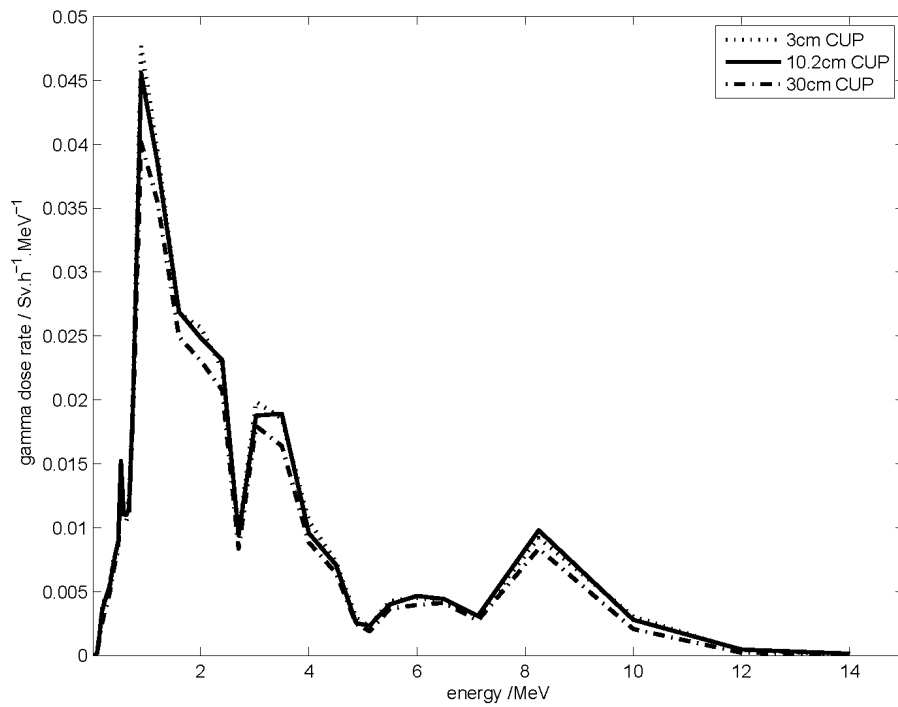
Table 4.9 γ dose rate for each collimator at the CUP and SUP

collimator diameter /cm	CUP /mSvh ⁻¹	SUP /mSvh ⁻¹
3	378.0	17.32
10.2	369.4	20.90
30	336.4	23.65

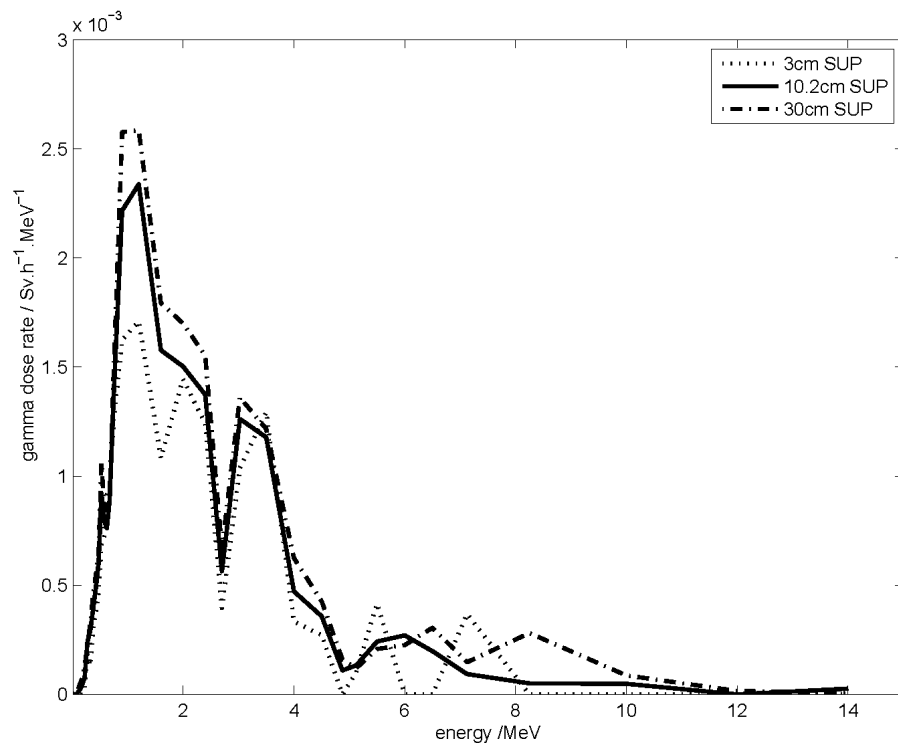
Figure 4.47 displayed integral photon spectra at the CUP and SUP. The photon spectra at the SUP with 3 cm collimator, it is dominated by energy within about 7 MeV at the SUP, see Figure 4.47b.

Calculation of γ dose rate is done by knowing γ ray flux-to-dose-rate conversion factors [Kwon et al., 1980]. The relation of photon energy and γ ray flux-to-dose-rate conversion factors is shown in Chapter 3, Figure 3.8. Table 4.9 shows the results of γ dose rate at the CUP and the SUP for 3 cm, 10.2 cm, and 30 cm collimators. We calculate the γ dose rate at the CUP (75 cm) and at the SUP (250 cm) with operating current (215 nA). The upper limits of gamma dose rate at the CUP and at the SUP are approximately 170 mSv h⁻¹ (17 rad h⁻¹) reported by Prokofiev et al [Prokofiev et al., 2014], and 40 mSv h⁻¹ (4 rad h⁻¹) from [Prokofiev et al., 2009]. The Geant4 simulation results of gamma dose rate at the CUP show a conflict with measurements data.

Figure 4.48 shows absorbed dose versus energy at the CUP and SUP with different dimension of collimator. Figure 4.48a presents similar dose shape for each collimator at the CUP. The result of dose at the CUP from the 3 cm and the 10.2 cm collimators are very close to each other but dose from the 30 cm collimator is lower than that from 10.2 cm. The dose at the CUP is inversely proportional to aperture size of collimator at 1 MeV. However, dose at the SUP is increased with increasing aperture of collimator. 3 cm collimator has a higher noise than other two dimensions of collimator because of the number of neutrons is less. A high dose peak at around 8.02 MeV is visible with 30 cm collimator at the SUP but it disappears with 10.2 cm collimator at the SUP. It illustrates that the dose is dependent on collimator size at the SUP.



(a) CUP



(b) SUP

Fig. 4.48 Dose versus energy at the CUP and SUP with 3 cm, 10.2 cm, and 30 cm collimators

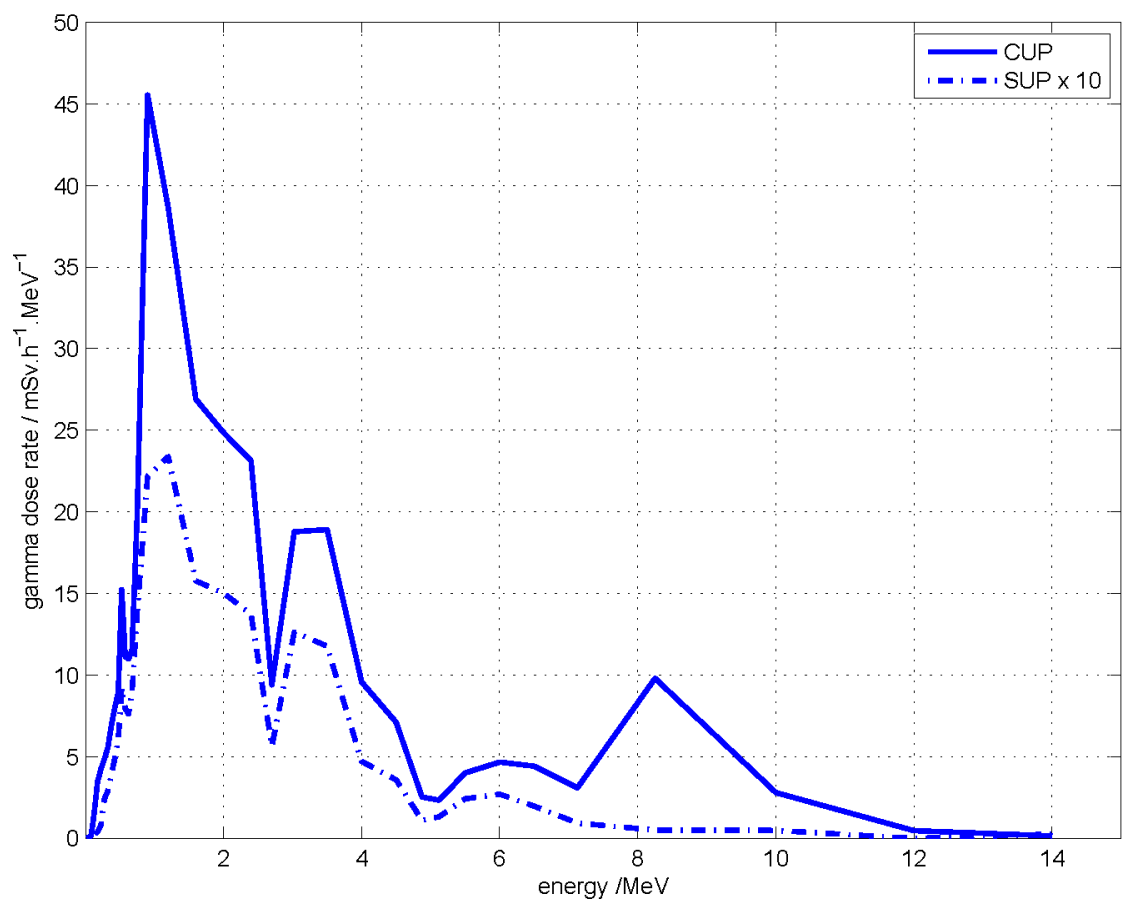


Fig. 4.49 Comparison of gamma dose rate at the SUP and the CUP

Figure 4.49 shows the comparison of gamma dose spectrum at the SUP and the CUP. It is obvious that specified energy peaks at around 1.5 MeV, 3 MeV, 6 MeV and 8 MeV appear in this structure. They are not coincidence peaks. It was discussed in Section 3.3.2 of Chapter 3. It is likely to have specified reactions occurred from spallation target, for example, annihilation radiation. For gamma, it is still not very clear about what happen in spallation target, we still calculate and analyze gamma radiation field. The calculation of gamma dose rate at the CUP is about 17 times greater than that at the SUP, is somewhat greater than $\frac{1}{R^2}$.

4.4 Summary

Chapter 4 shows spallation neutron sources model at TSL ANITA (more components added) with binary intra-nuclear cascade model. The comparisons of neutron flux at the CUP and SUP, comparisons between simulated data and analytical data at the SUP (CUP), between previous simulated data and present simulated data are presented. In addition, neutron and gamma spatial distributions are listed. The comparison of simulated neutron spectrum (TOF, beam profile) with measurement data are discussed. The predictions of gamma dose rate spectrum at the CUP and SUP were shown in this chapter.

Chapter 5

Conclusions

5.1 Summary of results

This work is aimed to calculate neutron and gamma fields at two spallation neutron sources using Geant4 simulation toolkit.

In Chapter 3, the neutron yield above 10 MeV at 30° from the Binary model is $0.192 \text{ n p}^{-1} \text{ sr}^{-1}$, which is more closer to LANSCE measurement result of $0.1998 \text{ n p}^{-1} \text{ sr}^{-1}$ than Bertini does ($0.208 \text{ n p}^{-1} \text{ sr}^{-1}$). The neutron yield from the bertini model is more closer to independent LANSCE calculation data than binary model does. According to the binary model, the neutron yields above 10 MeV with respect to off-axis angles of 15°, 60°, 90° at LANSCE neutron source are $0.234 \text{ n p}^{-1} \text{ sr}^{-1}$, $0.135 \text{ n p}^{-1} \text{ sr}^{-1}$, and $0.087 \text{ n p}^{-1} \text{ sr}^{-1}$. An intranuclear cascade peak and evaporation peak at around 100 MeV and 1 MeV are visible on neutron yield spectra in lethargy scale. The neutron yield below 10 MeV of each off-axis angle is influenced by projected area of the target but the neutron yield above 10 MeV is independent on projected area of the target.

The absolute neutron yield from the binary model ($0.029 \text{ n p}^{-1} \text{ sr}^{-1}$) above 10 MeV at ANITA neutron source is about 63% of the TSL analytical result ($0.047 \text{ n p}^{-1} \text{ sr}^{-1}$). However, the shape of normalized neutron yield of the binary model is quite similar to analytical one. It is considered that the missing geometry components (collimator, shielding component, bending magnet, and detector system) are likely to influence on neutron field

calculation. Model validation against measurements and independent calculation data show a good agreement of neutron yield using the *QGSP_BIC_HP* model so that only *QGSP_BIC_HP* model is used in complex ANITA simulation.

The effective radius effect at the CUP is no more greater than 15 cm for each dimension collimator. The appropriate radius for investigating neutron yield at the SUP is within umbra radius. The following results of neutron yield are calculated within effective radius at each position. The absolute neutron flux above 10 MeV at the SUP with 3 cm, 10.2 cm, and 30 cm collimators are about 72.74%, 75.88%, and 90.40% of the TSL analytical data ($9.3 \times 10^5 \text{ n cm}^{-2} \text{ s}^{-1}$), which are indeed even better than that of naked spallation neutron modelling. However, absolute neutron yield is somewhat less than the TSL measurements.

The neutron yield below 10 MeV at the CUP is dependent on dimension of collimator, which increasing with reduction in aperture of collimator size. In contrast, the neutron yield above 10 MeV at the CUP is independent upon dimension of collimator. The neutron yield above 10 MeV with 3 cm or 10.2 cm collimator at the CUP is 11.2 times higher than that at the SUP, which is consistent with ratio factor 11.7 times given by [Prokofiev et al., 2014]. For 30 cm collimator, the neutron yield at the CUP is 9.1 times higher than that at the SUP. The shape of Geant4 simulated time of flight spectrum at the CUP-TOF position is similar to ANITA calculation TOF spectrum. The FWHM of Geant4 TOF spectrum is 6.25 ns, which is very close to 7.2 ns from ANITA calculation data [Prokofiev et al., 2014]. The ratio of peak to baseline of the number of fission events from the Geant4 modelling is the same as TSL simulation (ratio value is 4.3). The shapes of Geant4 simulated neutron beam profile at the CUP-TOF position with 3 cm, 10.2 cm, and 30 cm collimators folding with $^{238}\text{U}(n, f)$ cross-section are close to the neutron beam profile shape shown in [Prokofiev et al., 2014], which was used to validate Geant4 modelling of ANITA neutron source. The photon spectra at LANSCE WNR and TSL ANITA show a visible peak at 0.5 MeV, and this peak is due to electron-positron annihilation at 0.511 MeV. The energy-integral gamma yield from 0.1 MeV up to 10 MeV is $0.26 \text{ } \gamma p^{-1} \text{ sr}^{-1}$ at LANSCE WNR and $0.046 \text{ } \gamma p^{-1} \text{ sr}^{-1}$ at TSL ANITA, see Chapter 3.

The integral gamma yields above 0.1 MeV with 3 cm, 10.2 cm, and 30 cm collimators, are approximately $1.57e-5 \gamma p^{-1} cm^{-2}$, $1.53e-5 \gamma p^{-1} cm^{-2}$, and $1.38e-5 \gamma p^{-1} cm^{-2}$ at the CUP. The integral gamma yields, above 0.1 MeV with 3 cm, 10.2 cm, and 30 cm collimators are approximately $6.7e-7 \gamma p^{-1} cm^{-2}$, $8.3e-7 \gamma p^{-1} cm^{-2}$, and $9.4e-7 \gamma p^{-1} cm^{-2}$ under the umbra region at the SUP.

The gamma dose rates, at the SUP with 3 cm, 10.2 cm, and 30 cm collimators are approximately $17.32 \text{ m Sv h}^{-1}$, $20.90 \text{ m Sv h}^{-1}$, and $23.65 \text{ m Sv h}^{-1}$, which are consistent with the upper limit dose rate amount of 40 m Sv h^{-1} [Prokofiev et al., 2009]. However, the gamma dose rates at the CUP with 3 cm, 10.2 cm, and 30 cm collimators are approximately $378.0 \text{ m Sv h}^{-1}$, $369.4 \text{ m Sv h}^{-1}$, and $336.4 \text{ m Sv h}^{-1}$, and are larger than the upper limit dose rate amount of 170 m Sv h^{-1} provided by [Prokofiev et al., 2014].

5.2 Contributions to knowledge

In this work, a preliminary Geant4 simulations of spallation neutron sources at LANSCE WNR and TSL ANITA were performed by *QGSP_BIC_HP* and *QGSP_BERT_HP* models, which were contributed to the paper [Platt et al., 2013] published at RADECS 2013. The Geant4 *QGSP_BIC_HP* model shows a good agreement with LANSCE experimental results on neutron yield. In addition, calculation of gamma yield and prediction of gamma dose at LANSCE were done by using *QGSP_BIC_HP* physics list for the first time. The gamma fields are dominated by continua between 0.1 MeV and 10 MeV, with integral yields approximately $0.26 \gamma p^{-1} sr^{-1}$.

Geant4 modelling of ANITA spallation neutron source is used to characterize neutron field at the CUP and SUP positions. The simulated time of flight spectrum at the CUP-TOF was calculated by folding with $^{238}\text{U}(n, f)$ cross-section, whose shape is close to that from the independent ANITA calculation results. The result of neutron beam profiles gives more information on the horizontal direction at the CUP.

Gamma yield shows a continuum spectra between 0.1 MeV and 10 MeV and a prompt peak at 0.5 MeV. It is the first time to predict gamma dose rate at the CUP and SUP at

ANITA neutron source. The prediction of gamma dose rate at the SUP is consistent with the upper limit gamma dose rate from measurements.

5.3 An evaluation of the limitations of work

The absolute neutron yield above 10 MeV from the Geant4 modelling is lower than that from the TSL ANITA calculation results, but the absolute neutron yield below 10 MeV from Geant4 modelling is higher than TSL ANITA calculation results, as shown in Chapter 4. The limitation is provided by *QGSP_BIC_HP* model since it is a High Precision (HP) neutron package for neutron transport from thermal energy (0.025 eV) up to 20 MeV. There is a node point exist at 20 MeV, see Figure 4.17. The accuracy of the modelling needs to be improved until simulation results are nearly the same as measurement results.

The method to distinguish neutron components at the CUP-TOF position is belong to mathematical way. It could be improved by optimizing the code, for instance, record previous step and the step before the previous step of the neutron and determine the direction according to the physical volumes each step belongs to. It will be a high precision method to know the contributions to the CUP neutron field.

Gamma dose prediction and gamma field calculations were done using Geant4 toolkit, but the data was not experimentally validated in this work. Future work may focus on this.

Geant4 is used to model neutron SEE test facility at TSL. A preliminary Monte Carlo simulation of radiation fields at standard user position is published in [Platt et al., 2013]. The aim of that work is to understand whether semiconductor detector is either sensitive to gamma ray. The latest work is to investigate whether calculation results will be closer to measurement result after adding more geometry components in models. Neutron fluence rate, neutron energy spectrum, time of flight spectrum, neutorn beam profile and spatial distribution are described in this thesis. Gamma dose rate and spatial distribution are predicted in here. It will give more comprehensive set of characterization of radiation fields at ANITA facility.

The simulation of spallation neutron source is a good approach for calculation of radiation fields in accelerated SEE testing. SEE testing is significant for measure soft error rate of electronic device. For future work, through simulation method, it is possible to predict neutron flux at any new place we interested in during accelerated SEE testing. If the devices under SEE testing is required to place in environment of neutron flux up to $10 \times 10^7 \text{ n cm}^{-2} \text{ s}^{-1}$, it is convenient to calculate neutron flux at any particular place in SEE test facility.

References

- Adams, J. (1983). Radiation effects in microelectronics for space instruments. *IEEE Transactions on Nuclear Science*, 30(1):481–484.
- Agostinelli, S., Allison, J., and Amako, K. (2003). Geant4 a simulation toolkit. *Nuclear Instruments and Methods in Physics Research Section A: Accelerators, Spectrometers, Detectors and Associated Equipment*, 506(3):250–303.
- Allison, J., Amako, K., and Apostolakis, J. (2006). Geant4 developments and applications. *IEEE Transactions on Nuclear Science*, 53(1):270–278.
- Alpen, E. L. (1998). *Radiation Biophysics*. Academic Press, second edition.
- Autran, J., Roche, P., Borel, J., Sudre, C., Castellani-Coulie, K., Munteanu, D., Parrassin, T., Gasiot, G., and Schoellkopf, J.-P. (2007). Altitude SEE Test European Platform (ASTEP) and first results in CMOS 130 nm SRAM. *IEEE Transactions on Nuclear Science*, 54(4):1002–1009.
- Autran, J., Roche, P., Sauze, S., Gasiot, G., Munteanu, D., Loaiza, P., Zampaolo, M., and Borel, J. (2008). Altitude and underground real-time SER characterization of CMOS 65nm SRAM. In *Proceedings of the eighth European Workshop on Radiation and Its Effects on Components and Systems*, pages 519–524.
- Autran, J.-L. and Munteanu, D. (2015). *Soft Errors: From Particles to Circuits*. CRC Press.
- Autran, J. L., Serre, S., Semikh, S., Munteanu, D., Gasiot, G., and Roche, P. (2012). Soft-error rate induced by thermal and low energy neutrons in 40 nm SRAMs. *IEEE Transactions on Nuclear Science*, 59(6):2658–2665.

- Batic, M., Hoff, G., Pia, M. G., Saracco, P., and Weidenspointner, G. (2013). Validation of Geant4 simulation of electron energy deposition. *IEEE Transactions on Nuclear Science*, 60(4):2934–2957.
- Binder, D., Smith, E. C., and Holman, A. B. (1975). Satellite anomalies from galactic cosmic rays. *IEEE Transactions on Nuclear Science*, 22(6):2675–2680.
- Blackmore, E. W., Dodd, P. E., and Shaneyfelt, M. R. (2003). Improved capabilities for proton and neutron irradiations at TRIUMF. In *2003 IEEE Radiation Effects Data Workshop Record*, pages 149–155.
- BSI (2012). Process management for avionics. atmospheric radiation effects. accommodation of atmospheric radiation effects via single event effects within avionics electronic equipment. BS IEC 62396-1:2012.
- Cai, X. X. (2010). *Characterizing the influence of neutron fields in causing single-event effects using portable detectors*. PhD thesis, University of Central Lancashire.
- Cai, X. X. and Platt, S. P. (2011). Modeling neutron interactions and charge collection in the Imaging Single-Event Effects Monitor. *IEEE Transactions on Nuclear Science*, 58(3):910–915.
- Carlson, A. D., Pronyaev, V. G., Smith, D. L., Larson, N. M., Chen, Z., Hale, G. M., Hamsch, F.-J., Gai, E. V., Oh, S.-Y., Badikov, S. A., Kawano, T., Hofmann, H. M., Vonach, H., and Tagesen, S. (2009). International evaluation of neutron cross section standards. *Nuclear Data Sheets*, 110(12):3215–3324.
- Carron, N. J. (2006). *An Introduction to the Passage of Energetic Particles through Matter*. CRC Press.
- Compton, A. H. (1923). A quantum theory of the scattering of X-rays by light elements. *Physical Review*, 21:483–502.
- Dirk, J. D., Nelson, M. E., Ziegler, J. F., Thompson, A., and Zabel, T. H. (2003). Terrestrial thermal neutrons. *IEEE Transactions on Nuclear Science*, 50(6):2060–2064.
- Ferlet-Cavrois, V., Schwank, J., and Liu, S. (2012). Influence of Beam Conditions and Energy for SEE Testing. *IEEE Transactions on Nuclear Science*, 59(4):1149–1160.

- Fischer, T. A. (1987). Heavy-ion-induced gate-rupture in power MOSFETs. *IEEE Transactions on Nuclear Science*, 34(6):1786–1791.
- Frost, C. D., Ansell, S., and Gorini, G. (2009). A new dedicated neutron facility for accelerated SEE testing at the ISIS facility. In *Proceedings of the forty-seventh IEEE International Reliability Physics Symposium*, pages 952–955.
- Gaillard, R. (2011). *Soft Errors in Modern Electronic Systems*. Springer US.
- Geant4 Collaboration (n.d.a). Geant4 user’s guide: For application developers. <http://geant4.web.cern.ch/geant4/UserDocumentation/UsersGuides/ForApplicationDeveloper/html/index.html> Accessed: 2012-03-01.
- Geant4 Collaboration (n.d.b). Physics Reference Manual. <http://geant4.web.cern.ch/geant4/UserDocumentation/UsersGuides/PhysicsReferenceManual/fo/PhysicsReferenceManual.pdf> Accessed: 2012-02-02.
- Gehrels, N. (1986). Confidence limits for small numbers of events in astrophysical data. *Astrophysical Journal*, 303:336–346.
- Goldhagen, P. (2003). Cosmic ray neutrons on the ground and in the atmosphere. *MRS Bulletin*, 28:131–135.
- Guenzer, C. S., Wolicki, E. A., and Allas, R. G. (1979). Single event upset of dynamic RAMs by neutrons and protons. *IEEE Transactions on Nuclear Science*, 26(6):5048–5052.
- Hagmann, C., Lange, D., and Wright, D. (2007). Cosmic-ray shower generator (CRY) for Monte Carlo transport codes. In *2007 IEEE Nuclear Science Symposium Conference Record*, volume 2, pages 1143–1146.
- Hubbell, J. H. (2006). Electron-positron pair production by photons: A historical overview. *Radiation Physics and Chemistry*, 75(6):614–623.
- JAEA (n.d.). Japan Atomic Energy Agency, Takasaki Advanced Radiation Research Institute. http://www.taka.jaea.go.jp/index_e.html Accessed: 2015-08-09.

- JEDEC (2006). Measurement and reporting of alpha particle and terrestrial cosmic ray-induced soft errors in semiconductor devices. JESD89A.
- Koga, R., Penzin, S. H., Crawford, K. B., and Crain, W. R. (1997). Single event functional interrupt (SEFI) sensitivity in microcircuits. In *Proceedings of the fourth European Conference on Radiation and Its Effects on Components and Systems*, pages 311–318.
- Kwon, S. G., Ha, C. W., Moon, P. S., Kim, K. E., and Yook, C. C. (1980). Calculation of neutron and gamma-ray flux-to-dose rate conversion factors. *Journal of the Korean Nuclear Society*, 12(3):171–179.
- LANSCE (n.d.). Neutron and nuclear science (WNR) facility at LANSCE. <http://wnr.lanl.gov/> Accessed: 2012-03-10.
- Lei, F., Hands, A., Clucas, S., Dyer, C., and Truscott, P. (2005). Improvements to and validations of the QinetiQ Atmospheric Radiation Model (QARM). In *Proceedings of the eighth European Conference on Radiation and Its Effects on Components and Systems*, pages D3–1–D3–8.
- Martin, R. C., Ghoniem, N. M., Song, Y., and Cable, J. S. (1987). The size effect of ion charge tracks on single event multiple-bit upset. *IEEE Transactions on Nuclear Science*, 34(6):1305–1309.
- May, T. C. and Woods, M. H. (1978). A new physical mechanism for soft errors in dynamic memories. In *Proceedings of the sixteenth IEEE International Reliability Physics Symposium*, pages 33–40.
- Messenger, G. C. (1997). *Single event phenomena*. Chapman & Hall.
- Normand, E. and Dominik, L. (2010). Cross comparison guide for results of neutron SEE testing of microelectronics applicable to avionics. In *2010 IEEE Radiation Effects Data Workshop Record*.
- Patel, S. (1991). *Nuclear Physics An Introduction*. New Age International.
- Petersen, E. (2011). *Single Event Effects In Aerospace*. Wiley-IEEE Press.

- Pickel, J. and Blandford, J. (1978). Cosmic ray induced errors in MOS memory cells. *IEEE Transactions on Nuclear Science*, 25(6):1166–1171.
- Platt, S. (2012). Details of SER testing at WNR Facility at LANSCE in 2005. Private communication.
- Platt, S., Torok, Z., Frost, C. D., and Ansell, S. (2008). Charge-collection and single-event upset measurements at the ISIS neutron source. *IEEE Transactions on Nuclear Science*, 55(4):2126–2132.
- Platt, S. P., Hong, Q., Mein, S. J., and Zhang, L. H. (2013). Neutron and gamma fields at neutron spallation sources for single-event-effects testing. In *Proceedings of the fourteenth European Conference on Radiation and Its Effects on Components and Systems*.
- Platt, S. P., Prokofiev, A. V., and Cai, X. X. (2010). Fidelity of energy spectra at neutron facilities for single-event effects testing. In *Proceedings of the forty-eighth IEEE International Reliability Physics Symposium*, pages 411–416.
- Plompen, A., Chadwick, M. B., and Koning, A. J. (2005). *Neutron Activation Cross-Section Measurements from Threshold to 20 MeV for the Validation of Nuclear Models and their Parameters*, volume 37. Nuclear Energy Agency (NEA) of the Organisation for Economic Co-operation and Development (OECD).
- Prokofiev, A. (2013). Drawing of ANITA Neutron Facility at TSL. Private communication.
- Prokofiev, A. V., Blomgren, J., Majerle, M., Nolte, R., Rottger, S., Platt, S. P., Xiao, C. X., and Smirnov, A. N. (2009). Characterization of the ANITA neutron source for accelerated SEE testing at The Svedberg Laboratory. In *2009 IEEE Radiation Effects Data Workshop Record*, pages 166–173.
- Prokofiev, A. V., Passoth, E., Hjalmarsson, A., and Majerle, M. (2014). CUP-a new high-flux irradiation position at the ANITA neutron facility at TSL. *IEEE Transactions on Nuclear Science*, 61(4):1929–1936.
- Prokofiev, A. V., Pomp, S., Blomgren, J., Bystrom, O., Ekstrom, C., Jonsson, O., Reistad, D., Tippawan, U., Wessman, D., Ziemann, V., and Osterlund, M. (2005). A new

- neutron facility for single-event effect testing. In *Proceedings of the forty-third IEEE International Reliability Physics Symposium*, pages 694–695.
- PSI (n.d.). Paul Scherrer Institut, Proton Irradiation Facility. <https://www.psi.ch/> Accessed: 2015-09-01.
- Rinard, P. (1991). Neutron interaction with matter. In Reilly, D., Ensslin, N., and Smith, Jr., H., editors, *Passive Nondestructive Assay of Nuclear Materials*. U.S. Nuclear Regulatory Commission.
- Rocheman, S., Wrobel, F., Vaille, J.-R., Saigne, F., Weulersse, C., Buard, N., and Carriere, T. (2008). Neutron induced energy deposition in a silicon diode. *IEEE Transactions on Nuclear Science*, 55(6):3146–3150.
- Russell, G. J. (1990). Spallation physics an overview. In *Proceedings of the 11th Meeting of the International Collaboration on Advanced Neutron Sources*, pages 291–299.
- Schopper, H., editor (1993). *Advances of Accelerator Physics and Technologies*. World Scientific.
- Serber, R. (1947). Nuclear reactions at high energies. *Physical Review*, 72:1114–1115.
- STFC (n.d.). Science and Technology Facilities Council ISIS. <http://www.isis.stfc.ac.uk/> Accessed: 2014-03-01.
- Titus, J., Johnson, G., Schrimpf, R., and Galloway, K. (1991). Single-event burnout of power bipolar junction transistors. *IEEE Transactions on Nuclear Science*, 38(6):1315–1322.
- Torok, Z., Platt, S. P., and Cai, X. X. (2007). SEE-inducing effects of cosmic rays at the High-Altitude Research Station Jungfraujoch compared to accelerated test data. In *Proceedings of the ninth European Conference on Radiation and Its Effects on Components and Systems*.
- Truscott, P., Dyer, C., Frydland, A., Hands, A., Clucas, S., and Hunter, K. (2006). Neutron energy-deposition spectra measurements, and comparisons with Geant4 predictions. *IEEE Transactions on Nuclear Science*, 53(4):1883–1889.

- Truscott, P., Lei, F., Dyer, C., Quaghebeur, B., Heyndericks, D., Nierninen, P., Evans, H., Daly, E., Mohammadzadeh, A., and Hopkinson, G. (2003). MULASSIS - Monte Carlo radiation shielding simulation for space applications made easy. In *7th European Conference on Radiation and Its Effects on Components and Systems*, pages 191–196.
- TSL (n.d.). The Svedberg Laboratory, Uppsala University, Sweden. <http://www.tsl.uu.se>
Accessed: 2014-09-01.
- Turowski, M., Fedoseyev, A., Raman, A., and Warren, K. (2008). Single event upset modeling with nuclear reactions in nanoscale electronics. In *Mixed Design of Integrated Circuits and Systems, 2008. MIXDES 2008. 15th International Conference on*, pages 443–448.
- Wallmark, J. T. and Marcus, S. M. (1962). Minimum size and maximum packing density of nonredundant semiconductor devices. *Proceedings of the IRE*, 50(3):286–298.
- Waskiewicz, A. E. and Groninger, J. W. (1990). Burnout thresholds and cross section of power MOS transistors with heavy ions. Technical report, Rockwell International Corp.
- Weller, R. A., Mendenhall, M. H., Reed, R. A., Schrimpf, R. D., Warren, K. M., Sierawski, B. D., and Massengill, L. W. (2010). Monte Carlo simulation of single event effects. *IEEE Transactions on Nuclear Science*, 57(4):1726–1746.
- Wender, S. A., Balestrini, S., Brown, A., Haight, R. C., M.Laymon, C., Lee, T. M., Lisowski, P. W., McCorkle, W., Nelson, R. O., Parker, W., and Hill, N. W. (1993). A fission ionization detector for neutron flux measurements at a spallation source. *Nuclear Instruments and Methods in Physics Research Section A: Accelerators, Spectrometers, Detectors and Associated Equipment*, 336(1–2):226–231.
- Wender, S. A. and Lisowski, P. W. (1987). A white neutron source from 1 to 400 MeV. *Nuclear Instruments and Methods in Physics Research Section B: Beam Interactions with Materials and Atoms*, 24-25, Part 2:897–900.
- Zhang, L. H. (2013). *Neutron beam monitoring for single-event effects testing*. PhD thesis, University of Central Lancashire.

- Zhang, L. H., Platt, S. P., Edwards, R. H., and Allabush, C. (2009). In-situ neutron dosimetry for single-event effect accelerated testing. *IEEE Transactions on Nuclear Science*, 56(4):2070–2076.
- Ziegler, J. F. (1996). Terrestrial cosmic rays. *IBM Journal of Research and Development*, 40(1):19–39.
- Ziegler, J. F. (1998). Terrestrial cosmic ray intensities. *IBM Journal of Research and Development*, 42(1):117–140.
- Ziegler, J. F. and Lanford, W. A. (1979). Effect of cosmic rays on computer memories. *Science*, 206(4420):776–788.
- Ziegler, J. F. and Lanford, W. A. (1981). The effect of sea level cosmic rays on electronic devices. *Journal of Applied Physics*, 52(6):4305–4312.

Appendix A

Los Alamos calculation using MCNP(X) and measurement data

The neutron spectra obtained from measurement and independent calculation data are used for comparison purpose, which are shown in Appendix A.

Los Alamos measurement of WNR Target-4 neutron flux at ICE House (4FP30L)

The measurement data of neutron flux at WNR Target 4 station (ICE House, about 30° of the flight path with respect to the proton beam) in LANSCE are shown in Table A.1. These unpublished measurement data about neutron flux at WNR are provided by Dr S. P. Platt. It shows integral flux and differential flux from 1.25 MeV to 800 MeV. The mean energy represents the geometric mean of low and high energy.

Table A.1 Los Alamos measurement of WNR Target-4 neutron flux at ICE House (4FP30L)

low	high	mean	integral flux	differential flux	flux
/MeV	/MeV	/MeV	/ncm ⁻² s ⁻¹	/ncm ⁻² s ⁻¹ MeV ⁻¹	/ncm ⁻² s ⁻¹
1.25	1.5	1.369306394	880030.9639	119344.2625	29836.06562

Continued on next page

Table A.1 – continued from previous page

low	high	mean	integral flux	differential flux	flux
/MeV	/MeV	/MeV	/ncm ⁻² s ⁻¹	/ncm ⁻² s ⁻¹ MeV ⁻¹	/ncm ⁻² s ⁻¹
1.5	1.75	1.620185175	850194.8983	145714.0785	36428.51962
1.75	2	1.870828693	813766.3787	125558.8729	31389.71822
2	2.25	2.121320344	782376.6605	113384.441	28346.11026
2.25	2.5	2.371708245	754030.5502	103282.4793	25820.61982
2.5	2.75	2.62202212	728209.9304	91024.05109	22756.01277
2.75	3	2.872281323	705453.9176	84272.98398	21068.24599
3	3.5	3.240370349	684385.6716	73036.51145	36518.25572
3.5	4	3.741657387	647867.4159	61174.54606	30587.27303
4	4.5	4.242640687	617280.1429	52729.77642	26364.88821
4.5	5	4.74341649	590915.2547	46850.87146	23425.43573
5	5.5	5.244044241	567489.8189	40598.18272	20299.09136
5.5	6	5.744562647	547190.7276	33820.74075	16910.37038
6	7	6.480740698	530280.3572	27001.91657	27001.91657
7	8	7.483314774	503278.4406	21982.68632	21982.68632
8	9	8.485281374	481295.7543	17125.28905	17125.28905
9	10	9.486832981	464170.4652	14170.46524	14170.46524
10	12.5	11.18033989	450000	10055.20377	25138.00943
12.5	15	13.69306394	424861.9906	6430.985004	16077.46251
15	17.5	16.20185175	408784.5281	5231.080259	13077.70065
17.5	20	18.70828693	395706.8274	4331.473687	10828.68422
20	22.5	21.21320344	384878.1432	3814.963295	9537.408238
22.5	25	23.71708245	375340.735	3571.564254	8928.910636
25	27.5	26.2202212	366411.8243	3267.379851	8168.449627
27.5	30	28.72281323	358243.3747	3045.282286	7613.205715

Continued on next page

Table A.1 – continued from previous page

low	high	mean	integral flux	differential flux	flux
/MeV	/MeV	/MeV	/ncm ⁻² s ⁻¹	/ncm ⁻² s ⁻¹ MeV ⁻¹	/ncm ⁻² s ⁻¹
30	35	32.40370349	350630.169	2873.168153	14365.84077
35	40	37.41657387	336264.3282	2617.757634	13088.78817
40	45	42.42640687	323175.54	2416.183178	12080.91589
45	50	47.4341649	311094.6241	2285.025668	11425.12834
50	55	52.44044241	299669.4958	2175.208833	10876.04416
55	60	57.44562647	288793.4516	2015.30777	10076.53885
60	70	64.80740698	278716.9128	1852.920415	18529.20415
70	80	74.83314774	260187.7086	1670.194742	16701.94742
80	90	84.85281374	243485.7612	1496.227089	14962.27089
90	100	94.86832981	228523.4903	1360.186591	13601.86591
100	125	111.8033989	214921.6244	1193.067441	29826.68603
125	150	136.9306394	185094.9384	966.9156522	24172.8913
150	175	162.0185175	160922.0471	801.0228491	20025.57123
175	200	187.0828693	140896.4759	669.7589438	16743.97359
200	225	212.1320344	124152.5023	578.9644827	14474.11207
225	250	237.1708245	109678.3902	498.2070262	12455.17566
250	275	262.202212	97223.21455	436.4529053	10911.32263
275	300	287.2281323	86311.89192	389.5039821	9737.599553
300	350	324.0370349	76574.29237	333.1861054	16659.30527
350	400	374.1657387	59914.9871	279.7341843	13986.70921
400	450	424.2640687	45928.27789	240.3174943	12015.87471
450	500	474.341649	33912.40317	204.7019194	10235.09597
500	550	524.4044241	23677.3072	172.6382704	8631.913521
550	600	574.4562647	15045.39368	132.0831498	6604.157491

Continued on next page

Table A.1 – continued from previous page

low	high	mean	integral flux	differential flux	flux
/MeV	/MeV	/MeV	/ncm ⁻² s ⁻¹	/ncm ⁻² s ⁻¹ MeV ⁻¹	/ncm ⁻² s ⁻¹
600	700	648.0740698	8441.236193	67.00389316	6700.389316
700	800	748.3314774	1740.846877	17.40846877	1740.846877

Los Alamos calculation of WNR Target-4 neutron flux

LANSCE provided the calculated neutron spectra above 0.1 MeV of 15°, 30°, 60° and 90° and their uncertainties at Target-4 station, see Table A.2 and Table A.3.

Table A.2 Calculation of WNR Target-4 neutron flux at 15° and 30° ($\text{np}^{-1}\text{MeV}^{-1}\text{Sr}^{-1}$)

MeV	15°	+/-	30°	+/-
0.113	1.26E-01	5.85E-03	1.77E-01	3.95E-03
0.142	1.35E-01	5.40E-03	1.90E-01	3.65E-03
0.179	1.35E-01	4.82E-03	1.82E-01	3.18E-03
0.225	1.40E-01	4.36E-03	1.82E-01	2.83E-03
0.284	1.44E-01	3.96E-03	1.91E-01	2.59E-03
0.357	1.42E-01	3.50E-03	1.92E-01	2.31E-03
0.45	1.41E-01	3.10E-03	1.82E-01	2.01E-03
0.566	1.42E-01	2.77E-03	1.80E-01	1.78E-03
0.713	1.30E-01	2.37E-03	1.68E-01	1.53E-03
0.897	1.17E-01	2.00E-03	1.51E-01	1.30E-03
1.13	9.66E-02	1.62E-03	1.27E-01	1.06E-03
1.42	7.64E-02	1.29E-03	1.02E-01	8.44E-04
1.79	6.59E-02	1.06E-03	8.35E-02	6.82E-04
2.25	5.34E-02	8.53E-04	6.75E-02	5.46E-04
2.84	4.27E-02	6.80E-04	5.55E-02	4.42E-04
3.57	3.36E-02	5.38E-04	4.35E-02	3.48E-04
4.5	2.73E-02	4.32E-04	3.35E-02	2.72E-04
5.66	1.97E-02	3.27E-04	2.49E-02	2.09E-04
7.13	1.39E-02	2.45E-04	1.77E-02	1.57E-04
8.97	9.51E-03	1.81E-04	1.20E-02	1.15E-04

Continued on next page

Table A.2 – continued from previous page

MeV	15°	+/-	30°	+/-
11.3	6.26E-03	1.31E-04	7.59E-03	8.18E-05
14.2	4.00E-03	9.30E-05	5.00E-03	5.91E-05
17.9	2.61E-03	6.66E-05	3.22E-03	4.21E-05
22.6	2.13E-03	5.42E-05	2.28E-03	3.19E-05
28.4	1.59E-03	4.16E-05	1.71E-03	2.45E-05
35.7	1.30E-03	3.35E-05	1.30E-03	1.91E-05
45	1.05E-03	2.68E-05	1.05E-03	1.52E-05
56.6	8.59E-04	2.16E-05	8.76E-04	1.24E-05
71.3	7.47E-04	1.80E-05	7.47E-04	1.02E-05
89.7	5.93E-04	1.43E-05	6.25E-04	8.32E-06
113	5.53E-04	1.23E-05	5.03E-04	6.66E-06
142	4.69E-04	1.01E-05	4.20E-04	5.42E-06
179	3.93E-04	8.22E-06	3.37E-04	4.33E-06
225	3.24E-04	6.64E-06	2.46E-04	3.29E-06
284	2.67E-04	5.38E-06	1.69E-04	2.44E-06
357	1.88E-04	4.02E-06	1.03E-04	1.69E-06
450	9.76E-05	2.58E-06	7.84E-05	1.32E-06
538	9.08E-05	2.95E-06	5.43E-05	1.30E-06
613	1.38E-04	3.60E-06	2.20E-05	8.19E-07
688	9.64E-05	3.01E-06	2.95E-06	3.00E-07
763	1.57E-05	1.22E-06	3.04E-08	3.04E-08

Table A.3 Calculation of WNR Target-4 neutron flux at 60° and 90° ($\text{np}^{-1}\text{MeV}^{-1}\text{Sr}^{-1}$)

MeV	60°	+/-	90°	+/-
0.113	2.52E-01	3.20E-03	2.70E-01	2.19E-03
0.142	2.53E-01	2.86E-03	2.75E-01	1.97E-03
0.179	2.51E-01	2.54E-03	2.70E-01	1.74E-03
0.225	2.54E-01	2.28E-03	2.71E-01	1.55E-03
0.284	2.57E-01	2.04E-03	2.70E-01	1.38E-03
0.357	2.57E-01	1.82E-03	2.72E-01	1.23E-03
0.45	2.45E-01	1.58E-03	2.59E-01	1.07E-03
0.566	2.32E-01	1.37E-03	2.46E-01	9.32E-04
0.713	2.17E-01	1.18E-03	2.27E-01	7.98E-04
0.897	1.93E-01	9.96E-04	2.01E-01	6.69E-04
1.13	1.63E-01	8.14E-04	1.67E-01	5.44E-04
1.42	1.31E-01	6.51E-04	1.34E-01	4.34E-04
1.79	1.05E-01	5.19E-04	1.07E-01	3.46E-04
2.25	8.56E-02	4.18E-04	8.58E-02	2.76E-04
2.84	6.73E-02	3.31E-04	6.85E-02	2.20E-04
3.57	5.36E-02	2.63E-04	5.24E-02	1.71E-04
4.5	4.01E-02	2.03E-04	3.94E-02	1.32E-04
5.66	2.93E-02	1.54E-04	2.82E-02	9.98E-05
7.13	2.03E-02	1.15E-04	1.94E-02	7.37E-05
8.97	1.32E-02	8.24E-05	1.23E-02	5.24E-05
11.3	8.25E-03	5.80E-05	7.41E-03	3.62E-05
14.2	5.22E-03	4.11E-05	4.43E-03	2.50E-05
17.9	3.18E-03	2.84E-05	2.60E-03	1.69E-05
22.6	2.19E-03	2.12E-05	1.65E-03	1.22E-05

Continued on next page

Table A.3 – continued from previous page

MeV	60°	+/-	90°	+/-
28.4	1.53E-03	1.58E-05	1.11E-03	8.84E-06
35.7	1.17E-03	1.23E-05	7.98E-04	6.68E-06
45	9.39E-04	9.80E-06	6.02E-04	5.17E-06
56.6	7.57E-04	7.84E-06	4.48E-04	3.98E-06
71.3	5.95E-04	6.20E-06	3.22E-04	3.01E-06
89.7	4.60E-04	4.86E-06	2.14E-04	2.18E-06
113	3.57E-04	3.81E-06	1.35E-04	1.55E-06
142	2.52E-04	2.86E-06	7.13E-05	1.00E-06
179	1.62E-04	2.04E-06	3.24E-05	6.02E-07
225	9.02E-05	1.36E-06	1.14E-05	3.18E-07
284	4.22E-05	8.27E-07	2.82E-06	1.41E-07
357	1.47E-05	4.35E-07	5.37E-07	5.48E-08
450	2.69E-06	1.66E-07	2.67E-08	1.09E-08
538	3.00E-07	6.55E-08	1.00E-09	1.00E-09
613	1.00E-09	1.00E-09	1.00E-09	1.00E-09
688	1.00E-09	1.00E-09	1.00E-09	1.00E-09
763	1.00E-09	1.00E-09	1.00E-09	1.00E-09

Figure A.1 is plotted according to data in Table A.2 and Table A.3.

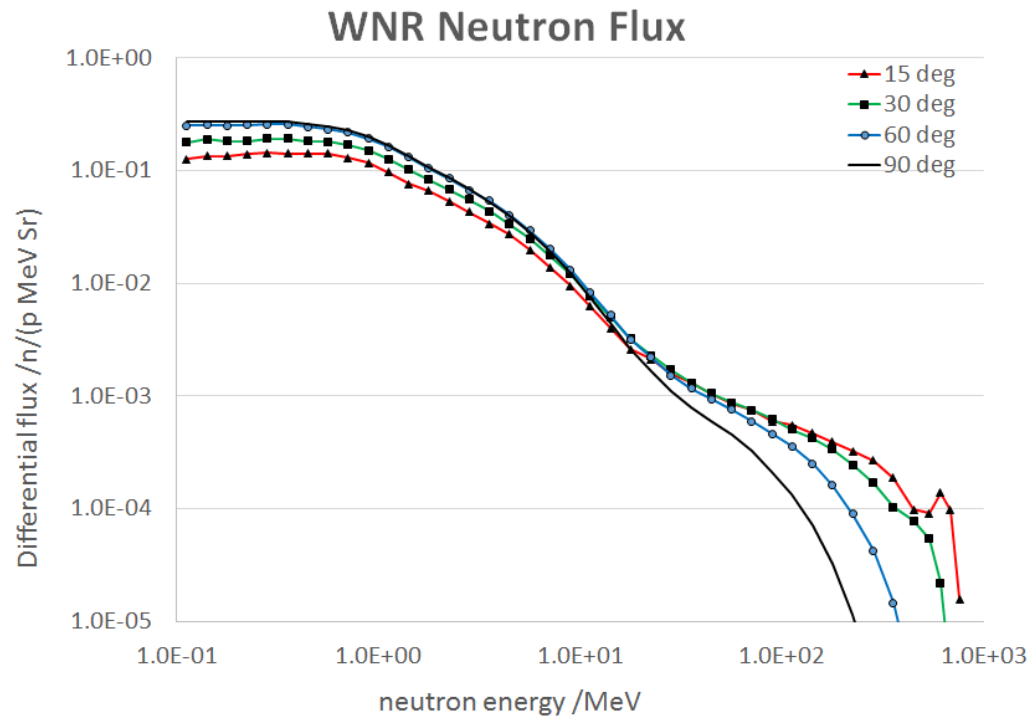


Fig. A.1 Calculated neutron yield spectra at LANSCE WNR Target4 LANSCE [nd]

Table A.4 Projected area of the target from the view of the off-axis angle of 90°, 60°, 30°, and 15°

off axis angle	$A_{front} / \text{cm}^{-2}$	$A_{side} / \text{cm}^{-2}$	$A_{total} / \text{cm}^{-2}$
90°	0	21	21
60°	3.534	18.187	21.721
30°	6.122	10.5	16.622
15°	6.828	5.435	12.263
0°	7.069	0	7.069

Appendix B

Uncertainty of counting

Confidence limit

Table B.1 and Table B.2 indicate confidence limits for small numbers of counts, which are dependent on Poisson statistics [Gehrels, 1986].

Table B.1 Poisson single sided upper limits

n	0.8413	0.9772	0.9987
	σ	2σ	3σ
0	1.841E+00	3.783E+00	6.608E+00
1	3.300E+00	5.683E+00	8.900E+00
2	4.638E+00	7.348E+00	1.087E+01
3	5.918E+00	8.902E+00	1.268E+01
4	7.163E+00	1.039E+01	1.439E+01
5	8.382E+00	1.182E+01	1.603E+01
6	9.584E+00	1.322E+01	1.762E+01
7	1.077E+01	1.459E+01	1.917E+01
8	1.195E+01	1.594E+01	2.069E+01
9	1.311E+01	1.727E+01	2.218E+01

Continued on next page

Table B.1 – continued from previous page

n	0.8413	0.9772	0.9987
	σ	2σ	3σ
10	1.427E+01	1.858E+01	2.364E+01
11	1.542E+01	1.987E+01	2.508E+01
12	1.656E+01	2.116E+01	2.651E+01
13	1.770E+01	2.243E+01	2.791E+01
14	1.883E+01	2.370E+01	2.931E+01
15	1.996E+01	2.495E+01	3.069E+01
16	2.108E+01	2.620E+01	3.206E+01
17	2.220E+01	2.744E+01	3.342E+01
18	2.332E+01	2.868E+01	3.476E+01
19	2.444E+01	2.990E+01	3.610E+01
20	2.555E+01	3.113E+01	3.744E+01
21	2.666E+01	3.234E+01	3.876E+01
22	2.776E+01	3.355E+01	4.007E+01
23	2.887E+01	3.476E+01	4.138E+01
24	2.997E+01	3.596E+01	4.269E+01
25	3.216E+01	3.716E+01	4.398E+01
26	3.326E+01	3.836E+01	4.528E+01
27	3.326E+01	3.955E+01	4.656E+01
28	3.435E+01	4.074E+01	4.784E+01
29	3.545E+01	4.192E+01	4.912E+01
30	3.654E+01	4.310E+01	5.039E+01
31	3.763E+01	4.428E+01	5.166E+01
32	3.872E+01	4.546E+01	5.292E+01
33	3.980E+01	4.663E+01	5.418E+01

Continued on next page

Table B.1 – continued from previous page

n	0.8413	0.9772	0.9987
	σ	2σ	3σ
34	4.089E+01	4.780E+01	5.543E+01
35	4.197E+01	4.897E+01	5.669E+01
36	4.306E+01	5.014E+01	5.793E+01
37	4.414E+01	5.130E+01	5.918E+01
38	4.522E+01	5.246E+01	6.042E+01
39	4.630E+01	5.362E+01	6.166E+01
40	4.738E+01	5.478E+01	6.289E+01
41	4.846E+01	5.593E+01	6.413E+01
42	4.953E+01	5.793E+01	6.536E+01
43	5.061E+01	5.824E+01	6.658E+01
44	5.168E+01	5.939E+01	6.781E+01
45	5.276E+01	6.054E+01	6.903E+01
46	5.383E+01	6.169E+01	7.025E+01
47	5.490E+01	6.283E+01	7.147E+01
48	5.598E+01	6.397E+01	7.268E+01
49	5.705E+01	6.512E+01	7.390E+01
50	5.812E+01	6.626E+01	7.511E+01
60	6.879E+01	7.760E+01	8.711E+01
70	7.941E+01	8.883E+01	9.896E+01
80	8.998E+01	9.998E+01	1.107E+02
90	1.005E+02	1.111E+02	1.223E+02
100	1.110E+02	1.221E+02	1.338E+02

Table B.2 Poisson single sided lower limits

n	0.8413	0.9772	0.9987
	σ	2σ	3σ
0	1.730E-01	2.300E-02	1.350E-03
1	7.080E-01	2.300E-01	5.290E-02
2	1.367E+00	5.690E-01	2.120E-01
3	2.086E+00	1.058E+00	4.650E-01
4	2.840E+00	1.583E+00	7.920E-01
5	3.620E+00	2.153E+00	1.175E+00
6	4.419E+00	2.758E+00	1.603E+00
7	5.232E+00	3.391E+00	2.068E+00
8	6.057E+00	4.046E+00	2.563E+00
9	6.891E+00	4.719E+00	3.084E+00
10	7.734E+00	5.409E+00	3.628E+00
11	8.585E+00	6.113E+00	4.191E+00
12	9.441E+00	6.828E+00	4.772E+00
13	1.030E+01	7.555E+00	5.367E+00
14	1.117E+01	8.291E+00	5.977E+00
15	1.204E+01	9.036E+00	6.599E+00
16	1.292E+01	9.789E+00	7.233E+00
17	1.380E+01	1.055E+01	7.877E+00
18	1.468E+01	1.132E+01	8.530E+00
19	1.557E+01	1.209E+01	9.193E+00
20	1.645E+01	1.287E+01	9.863E+00
21	1.735E+01	1.365E+01	1.054E+01
22	1.824E+01	1.444E+01	1.123E+01
23	1.914E+01	1.523E+01	1.192E+01

Continued on next page

Table B.2 – continued from previous page

n	0.8413	0.9772	0.9987
	σ	2σ	3σ
24	2.003E+01	1.603E+01	1.262E+01
25	2.093E+01	1.683E+01	1.332E+01
26	2.184E+01	1.764E+01	1.403E+01
27	2.274E+01	1.845E+01	1.475E+01
28	2.365E+01	1.926E+01	1.547E+01
29	2.455E+01	2.007E+01	1.619E+01
30	2.546E+01	2.089E+01	1.692E+01
31	2.637E+01	2.171E+01	1.765E+01
32	2.728E+01	2.254E+01	1.839E+01
33	2.820E+01	2.336E+01	1.913E+01
34	2.911E+01	2.419E+01	1.988E+01
35	3.003E+01	2.503E+01	2.063E+01
36	3.094E+01	2.586E+01	2.138E+01
37	3.186E+01	2.670E+01	2.214E+01
38	3.278E+01	2.753E+01	2.289E+01
39	3.370E+01	2.838E+01	2.366E+01
40	3.462E+01	2.922E+01	2.442E+01
41	3.555E+01	3.006E+01	2.519E+01
42	3.647E+01	3.091E+01	2.596E+01
43	3.739E+01	3.176E+01	2.673E+01
44	3.832E+01	3.261E+01	2.751E+01
45	3.924E+01	3.346E+01	2.829E+01
46	4.017E+01	3.431E+01	2.907E+01
47	4.110E+01	3.517E+01	2.985E+01

Continued on next page

Table B.2 – continued from previous page

n	0.8413	0.9772	0.9987
	σ	2σ	3σ
48	4.202E+01	3.602E+01	3.063E+01
49	4.295E+01	3.688E+01	3.142E+01
50	5.228E+01	4.553E+01	3.940E+01
60	6.165E+01	5.429E+01	4.754E+01
70	7.107E+01	6.313E+01	5.581E+01
80	8.053E+01	7.204E+01	6.418E+01
90	9.002E+01	8.102E+01	7.265E+01
100	1.110E+02	1.221E+02	1.338E+02

Appendix C

TSL facility

ANITA neutron facility

Figure C.1 shows real features at ANITA neutron facility. The large grey concrete blocks, black or red cables, a desk and iron collimator are shown in Figure C.1. The devices can be placed on the desk and neutron beam will be coming from the collimator (middle right of Figure C.1). The detector will be sent to the CUP by trolley sled through this hole, see Figure C.2.

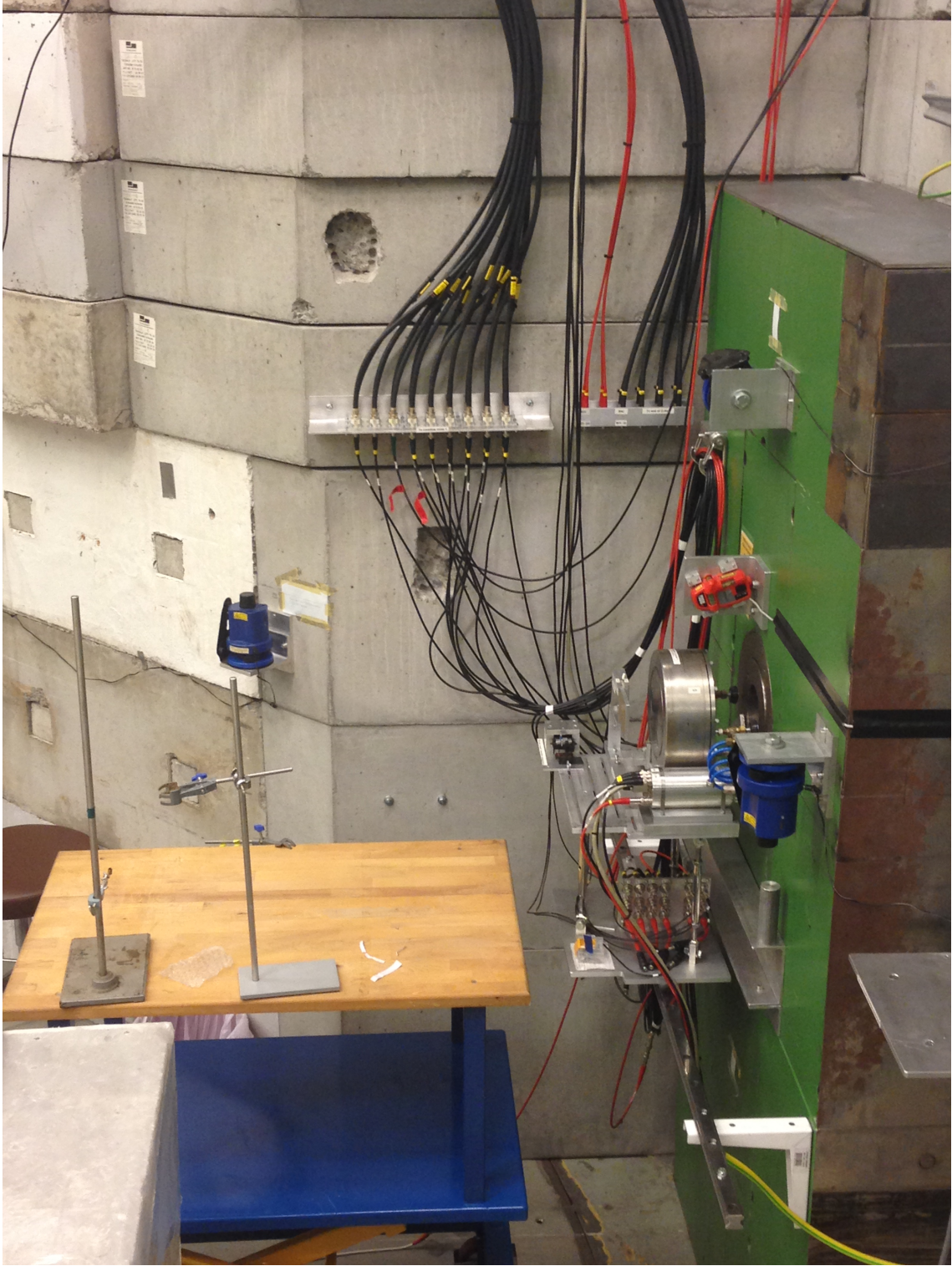


Fig. C.1 Standard User Position for devices under testing at ANITA facility in TSL

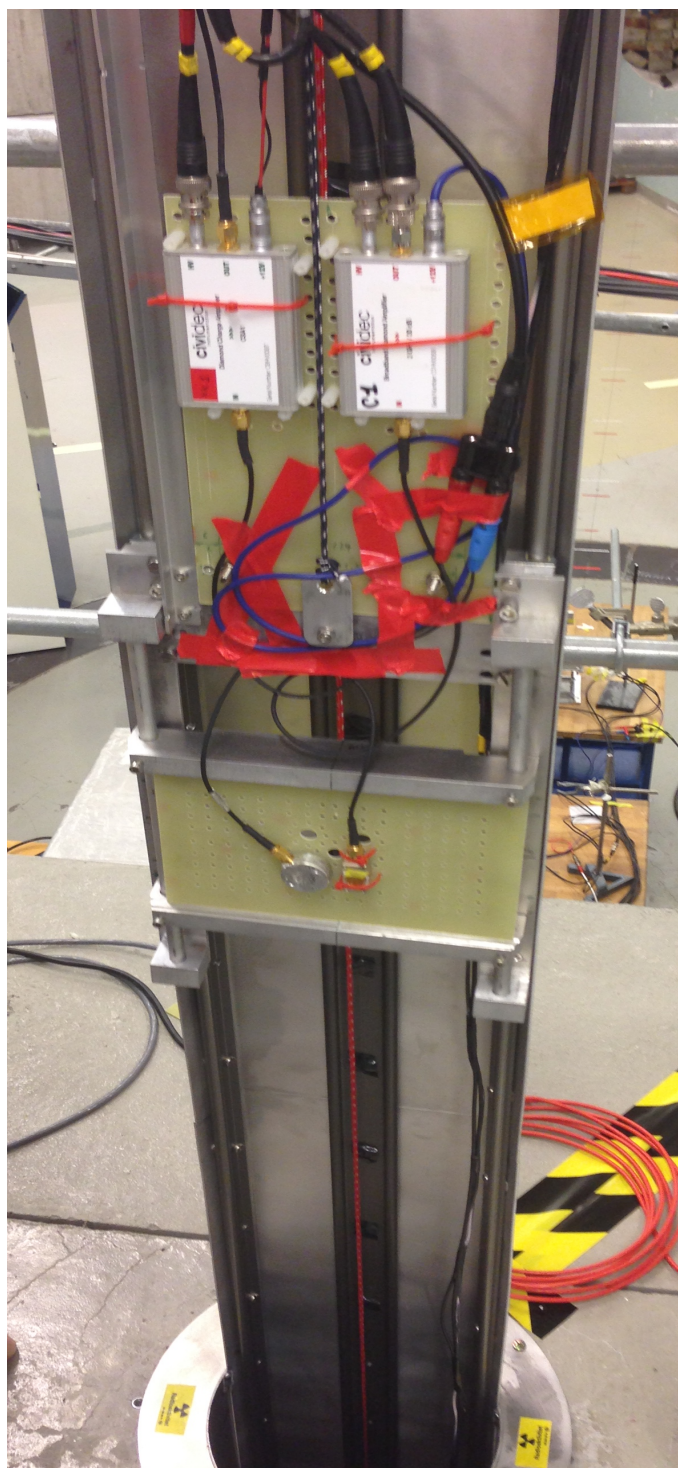


Fig. C.2 Right above over Closer User Position at ANITA facility in TSL. Two yellow boards installed on trolley sled and detectors are mounted on these boards. These devices were managed to take the trolley sled down to the CUP position through the hole.

Appendix D

WNR calculation data with using Geant4

Calculation of Target-4 neutron flux at WNR with binary INC cascade

Table D.1 and Table D.2 show Geant4 simulation data of neutron fluxes at 15°, 30°, 60°, and 90° with respect to the incident proton beam were calculated with binary INC cascade.

Table D.1 Geant4 calculation of WNR Target4 differential neutron yield at ICE House with binary INC cascade at 15° and 30° ($\text{np}^{-1}\text{Sr}^{-1}\text{MeV}^{-1}$)

MeV	15°	+/-	30°	+/-
0.104761575	0.12758	0.1227	0.13265	0.34514
0.1149757	0.13892	0.13405	0.14395	0.33783
0.126185688	0.14179	0.1371	0.14664	0.33391
0.138488637	0.14363	0.13912	0.14828	0.32986
0.151991108	0.14209	0.13781	0.1465	0.32815
0.166810054	0.14838	0.14421	0.15268	0.32766

Continued on next page

Table D.1 – continued from previous page

MeV	15°	+/-	30°	+/-
0.183073828	0.15618	0.15209	0.16038	0.31118
0.2009233	0.15733	0.15341	0.16134	0.30744
0.220513074	0.17206	0.16815	0.17606	0.31061
0.242012826	0.17021	0.1665	0.17401	0.30723
0.265608778	0.16882	0.16529	0.17242	0.30672
0.291505306	0.17069	0.1673	0.17415	0.30925
0.319926714	0.18334	0.17999	0.18675	0.30977
0.351119173	0.18424	0.18104	0.1875	0.29866
0.385352859	0.17596	0.17297	0.179	0.27457
0.422924287	0.15588	0.15319	0.15861	0.23674
0.464158883	0.16293	0.16031	0.1656	0.24243
0.509413801	0.16404	0.16153	0.16659	0.24513
0.559081018	0.17537	0.17289	0.17788	0.242
0.613590727	0.17547	0.1731	0.17787	0.23877
0.673415066	0.15226	0.15015	0.15439	0.21596
0.739072203	0.15459	0.15256	0.15664	0.21072
0.811130831	0.15352	0.15159	0.15547	0.2029
0.890215085	0.14076	0.139	0.14254	0.1865
0.977009957	0.12452	0.12294	0.12612	0.16436
1.072267222	0.11043	0.10901	0.11187	0.1464
1.176811952	0.10976	0.10841	0.11113	0.1377
1.291549665	0.0984	0.097178	0.099638	0.12327
1.417474163	0.086479	0.085385	0.087586	0.10903
1.555676144	0.077776	0.076786	0.078778	0.097478

Continued on next page

Table D.1 – continued from previous page

MeV	15°	+/-	30°	+/-
1.707352647	0.069788	0.068893	0.070694	0.087602
1.873817423	0.063692	0.062876	0.064519	0.078606
2.056512308	0.059349	0.058597	0.060111	0.074139
2.25701972	0.053651	0.052969	0.054343	0.068186
2.477076356	0.048165	0.047548	0.04879	0.061132
2.718588243	0.044196	0.043632	0.044768	0.054613
2.98364724	0.038923	0.038418	0.039436	0.049144
3.274549163	0.035232	0.034773	0.035697	0.043862
3.593813664	0.029179	0.028781	0.029584	0.03863
3.944206059	0.027119	0.026752	0.027491	0.034989
4.328761281	0.023709	0.023382	0.024041	0.031786
4.750810162	0.021619	0.021321	0.021922	0.029214
5.214008288	0.018477	0.018214	0.018745	0.024784
5.722367659	0.016322	0.016086	0.016562	0.022302
6.280291442	0.013521	0.013316	0.013729	0.019834
6.892612104	0.011609	0.011427	0.011793	0.017045
7.564633276	0.0096683	0.0095101	0.0098292	0.01464
8.302175681	0.0083963	0.0082556	0.0085395	0.012487
9.111627561	0.0070762	0.0069528	0.0072017	0.010472
10	0.006034	0.0059253	0.0061447	0.0085778
10.97498765	0.004948	0.004854	0.0050438	0.0073658
12.0450354	0.0042563	0.004173	0.0043411	0.0060476
13.21941148	0.0036291	0.0035557	0.0037039	0.0049974
14.50828778	0.0033351	0.0032679	0.0034035	0.0042009

Continued on next page

Table D.1 – continued from previous page

MeV	15°	+/-	30°	+/-
15.92282793	0.0028357	0.0027766	0.002896	0.0035225
17.475284	0.0024896	0.0024367	0.0025436	0.0030671
19.17910262	0.0021856	0.0021384	0.0022339	0.0025382
21.04904145	0.0019598	0.0019171	0.0020035	0.0022587
23.101297	0.0018358	0.0017963	0.0018761	0.0019698
25.35364494	0.0016364	0.0016008	0.0016727	0.0018435
27.82559402	0.0015128	0.0014802	0.0015462	0.0016403
30.53855509	0.0013021	0.0012732	0.0013316	0.0014862
33.51602651	0.0012279	0.0012011	0.0012553	0.0013829
36.78379772	0.0011385	0.0011139	0.0011637	0.0012882
40.37017259	0.001052	0.0010294	0.001075	0.0012524
44.30621458	0.00094213	0.00092172	0.00096299	0.0011792
48.6260158	0.00089108	0.00087213	0.00091044	0.0010954
53.36699231	0.00085378	0.00083608	0.00087186	0.0010084
58.57020818	0.00080136	0.00078498	0.00081807	0.00097602
64.28073117	0.00075761	0.00074241	0.00077311	0.00088565
70.54802311	0.00069864	0.00068471	0.00071285	0.00083031
77.42636827	0.00067251	0.00065947	0.00068581	0.0007368
84.97534359	0.00064344	0.00063126	0.00065586	0.00069395
93.26033469	0.00059342	0.00058226	0.0006048	0.00063209
102.3531022	0.00055411	0.00054381	0.0005646	0.00058781
112.3324033	0.00051169	0.00050224	0.00052131	0.00052878
123.2846739	0.00046782	0.0004592	0.0004766	0.0004958
135.3047775	0.00042307	0.00041525	0.00043105	0.00044393

Continued on next page

Table D.1 – continued from previous page

MeV	15°	+/-	30°	+/-
148.4968262	0.00038602	0.00037888	0.00039329	0.00040951
162.9750835	0.00035365	0.00034713	0.00036029	0.00036038
178.8649529	0.00032749	0.0003215	0.00033359	0.00033308
196.304065	0.00029281	0.0002874	0.00029831	0.00030359
215.443469	0.00025988	0.00025502	0.00026483	0.0002758
236.4489413	0.00023522	0.0002308	0.00023972	0.00024367
259.5024211	0.00020262	0.00019871	0.00020661	0.00021395
284.8035868	0.00018248	0.00017894	0.0001861	0.00017512
312.571585	0.0001558	0.00015268	0.00015899	0.00014458
343.0469286	0.00012768	0.00012498	0.00013044	0.00012488
376.4935807	0.0001065	0.00010414	0.00010891	9.86E-05
413.20124	9.35E-05	9.14E-05	9.56E-05	7.61E-05
453.4878508	7.71E-05	7.53E-05	7.90E-05	5.48E-05
497.7023564	6.05E-05	5.89E-05	6.21E-05	3.30E-05
546.2277218	4.56E-05	4.43E-05	4.69E-05	1.60E-05
599.4842503	2.56E-05	2.47E-05	2.65E-05	5.59E-06
657.9332247	9.26E-06	8.74E-06	9.82E-06	1.01E-06
722.0809018	1.19E-06	1.01E-06	1.40E-06	1.09E-07
792.4828984	2.47E-08	4.27E-09	8.16E-08	0

Table D.2 Geant4 calculation of WNR Target4 differential neutron yield at ICE House with binary INC cascade at 60° and 90° ($\text{np}^{-1}\text{Sr}^{-1}\text{MeV}^{-1}$)

MeV	60°	+/-
0.104761575	0.3371	0.35336
0.1149757	0.33024	0.34559
0.126185688	0.32671	0.34127
0.138488637	0.32303	0.33683
0.151991108	0.32164	0.33478
0.166810054	0.32146	0.33398
0.183073828	0.30541	0.31706
0.2009233	0.30196	0.31301
0.220513074	0.30535	0.31595
0.242012826	0.30224	0.31229
0.265608778	0.30196	0.31155
0.291505306	0.30469	0.31388
0.319926714	0.30541	0.31419
0.351119173	0.29458	0.3028
0.385352859	0.27083	0.27836
0.422924287	0.23343	0.2401
0.464158883	0.23924	0.24568
0.509413801	0.24206	0.24824
0.559081018	0.23909	0.24495
0.613590727	0.23601	0.24157
0.673415066	0.21346	0.2185
0.739072203	0.20836	0.21311
0.811130831	0.20069	0.20514

Continued on next page

Table D.2 – continued from previous page

MeV	60°	+/-
0.890215085	0.18448	0.18855
0.977009957	0.16254	0.1662
1.072267222	0.14476	0.14805
1.176811952	0.13619	0.13923
1.291549665	0.1219	0.12465
1.417474163	0.1078	0.11027
1.555676144	0.09637	0.098599
1.707352647	0.086599	0.088616
1.873817423	0.0777	0.079523
2.056512308	0.073298	0.074989
2.25701972	0.067417	0.068965
2.477076356	0.060437	0.061835
2.718588243	0.053985	0.055247
2.98364724	0.048576	0.049718
3.274549163	0.04335	0.044381
3.593813664	0.038171	0.039094
3.944206059	0.034572	0.035411
4.328761281	0.031406	0.03217
4.750810162	0.028867	0.029565
5.214008288	0.024479	0.025093
5.722367659	0.022025	0.022581
6.280291442	0.019585	0.020086
6.892612104	0.016825	0.017268
7.564633276	0.014445	0.014837

Continued on next page

Table D.2 – continued from previous page

MeV	60°	+/-
8.302175681	0.012315	0.012661
9.111627561	0.010322	0.010625
10	0.0084481	0.0087094
10.97498765	0.0072511	0.0074822
12.0450354	0.0059484	0.0061484
13.21941148	0.0049113	0.005085
14.50828778	0.0041256	0.0042776
15.92282793	0.0034566	0.0035896
17.475284	0.0030085	0.0031269
19.17910262	0.0024872	0.0025901
21.04904145	0.0022128	0.0023055
23.101297	0.0019289	0.0020115
25.35364494	0.0018058	0.001882
27.82559402	0.0016063	0.001675
30.53855509	0.0014554	0.0015178
33.51602651	0.0013544	0.0014119
36.78379772	0.001262	0.001315
40.37017259	0.0012278	0.0012776
44.30621458	0.0011564	0.0012025
48.6260158	0.0010744	0.0011168
53.36699231	0.00098914	0.001028
58.57020818	0.00095795	0.00099443
64.28073117	0.00086922	0.00090239
70.54802311	0.00081512	0.00084577

Continued on next page

Table D.2 – continued from previous page

MeV	60°	+/-
77.42636827	0.00072315	0.00075071
84.97534359	0.0006813	0.00070683
93.26033469	0.00062056	0.00064383
102.3531022	0.0005772	0.00059861
112.3324033	0.00051918	0.00053856
123.2846739	0.00048692	0.00050483
135.3047775	0.00043591	0.0004521
148.4968262	0.00040216	0.00041699
162.9750835	0.0003538	0.00036709
178.8649529	0.00032704	0.00033923
196.304065	0.00029808	0.00030919
215.443469	0.00027079	0.0002809
236.4489413	0.00023918	0.00024825
259.5024211	0.00020993	0.00021804
284.8035868	0.00017165	0.00017866
312.571585	0.00014157	0.00014765
343.0469286	0.00012221	0.00012761
376.4935807	9.63E-05	0.0001009
413.20124	7.42E-05	7.81E-05
453.4878508	5.33E-05	5.64E-05
497.7023564	3.19E-05	3.42E-05
546.2277218	1.53E-05	1.68E-05
599.4842503	5.16E-06	6.05E-06
657.9332247	8.40E-07	1.22E-06

Continued on next page

Table D.2 – continued from previous page

MeV	60°	+/-
722.0809018	5.66E-08	1.94E-07
792.4828984	0	4.55E-08
